

University of Nottingham
UK | CHINA | MALAYSIA

On-surface Chemistry: Directing and Controlling Chemical Interactions

Chris Judd

Thesis submitted to the University of Nottingham
for the degree of Doctor of Philosophy

September 2020

Abstract

On-surface synthesis, where molecular building blocks react together to produce covalently bonded products, offers the potential for the generation of structures via alternative routes to those performed within traditional solution-phase chemistry. However, a better understanding of the mechanistic process of on-surface reactions, obtained through surface analysis techniques such as scanning probe microscopy, is first required in order to develop these reactions.

Within this thesis, investigations into on-surface synthesis are primarily performed using scanning tunnelling microscopy techniques under ultra high vacuum conditions. These techniques are used to examine molecular structures formed on coinage metal surfaces, obtained via the on-surface Ullmann-like coupling reaction.

The effects of surface topography upon the synthesis of surface-confined structures are initially investigated. Ullmann coupling reactions of 4,4"-diiodo-m-terphenyl (DITP) on Ag(111) and Ag(110) are performed and the resulting structures characterised at each phase of the reaction. The dimensions of these structures and their adsorption geometries relative to the surface are then compared, finding that intermediate and product structure geometries are driven by their alignment to the surface.

Utilising a combination of normal incidence X-ray standing wave (NIXSW) technique and STM imaging, the adsorption of 1,3,5-tris(4-iodophenyl)benzene (TIPB) and DITP on Ag(111) is studied. NIXSW measurements of molecular structures in the metal organic and covalent phases of the Ullmann coupling reaction are used to determine vertical positioning of molecules relative to the bulk surface. Additionally, these results are used to determine the presence of metal adatoms within metal-organic structures. Further NIXSW measurements combined with STM imaging are then used to generate lateral adsorption models for molecular structures.

Building upon the observations of reactions upon 'atomically flat' surfaces, the concept of a molecular template is introduced and used to demonstrate a methodology for confining on-surface reactions. Large porphyrin macrocycles, consisting of 40 linked porphyrin units (c-P40) are used to confine the reaction of TIPB on Au(111). Covalently bonded structures are successfully produced within templates while exploring the limitations of this system, including thermal stability and the presence of contaminant species.

Additionally, the electronic properties of c-P40 nanorings are characterised. Quantum confinement effects are observed in stacks of porphyrin rings, including quantised energy levels and localisation of electron states. Measurements are supported by density functional theory (DFT) and extended tight binding (xTB) calculations. These results act to demonstrate the potential for stacks of c-P40 to act as molecular quantum rings.

The findings presented within this thesis offer additional understanding on the role certain factors play within on-surface reactions and provide details of potential methods which may be used to influence and control these reactions.

Acknowledgements

I'd first like to thank my supervisor Alex, without whom none of this would have been possible. Thank you for your advice and guidance. I'd also like to thank Phil as my second supervisor for his advice. Thank you to everyone in the Nanoscience group, in particular Ellie and Matt, for friendship and providing someone to whinge to when nothing worked. To everyone in C20 and the tea room, thank you for friendship, advice and wonderful distractions from work.

Outside the world of physics I want to thank my family, for the loving support they have always given me. Thank you to my friends throughout Nottingham for keeping me (mostly) sane through this long process, you guys are the best. Finally thanks to everyone in the ultimate frisbee community, UoN, Flyght and EMO, for playing this amazing sport with me while being amazing people.

List of Publications

1. *Ullmann Coupling Reactions on Ag(111) and Ag(110); Substrate Influence on the Formation of Covalently Coupled Products and Intermediate Metal-Organic Structures*, **Chris J. Judd**, Sarah L. Haddow, Neil R. Champness and Alex Saywell, *Sci. Rep.* **7**, 14541 (2017).

2. *An On-Surface Reaction Confined within a Porous Molecular Template*, **Chris J. Judd**, Neil R. Champness and Alex Saywell, *Chem. Eur.J.* **24**, 56–61 (2018).

3. *On-Surface Synthesis within a Porphyrin Nanoring Template*, **Chris J. Judd**, Dmitry V. Kondratuk, Harry L. Anderson and Alex Saywell, *Sci. Rep.* **9**, 9352 (2019).

4. *A molecular quantum ring formed from a π-conjugated macrocycle*, **Chris J. Judd**, Anton S. Nizovtsev, Rikke Plougmann, Dmitry V. Kondratuk, Harry L. Anderson, Elena Besley, Alex Saywell (*Accepted by PRL*).

5. *Structural characterisation of molecular conformation and the incorporation of adatoms in an on-surface Ullmann-type reaction*, **Chris J. Judd**, Filipe L.Q. Junqueira, Sarah L. Haddow, Neil R. Champness, David A. Duncan, Robert G. Jones, Alex Saywell, (*Under review at Communications Chemistry*).

Contents

Abstract i

Acknowledgements iii

List of Publications iv

1 Introduction 1

1.1 Probing surface structures 1

1.2 Thesis overview 4

2 Studying 2D Molecular Self-Assembly and On-Surface Synthesis 6

2.1 Molecular self-assembly in two-dimensions 6

2.1.1 Van der Waals mediated structures 8

2.1.2 Hydrogen-bonded supramolecular self-assembly 8

2.1.3 Two dimensional metal-organic structures 9

2.1.4 Comparison of non-covalent interactions 10

2.2 On-surface synthesis 10

2.2.1 Ullmann Coupling 11

2.2.2 Glaser Coupling 12

2.2.3 Other Coupling 14

2.2.4 Summary of on-surface synthesis protocols 14

2.3 Development of on-surface synthesis via Ullmann Coupling 15

2.3.1 Implementations of on-surface Ullmann coupling 17

2.4 Controlling and influencing on-surface reactions 20

2.4.1 Role of Halogen Chemistry 20

2.4.2 Role of Substrate Chemistry 22

2.4.3 Role of Substrate Topography 24

2.4.4 Use of templates to control reactions 25
2.5 Summary 27
3 Theory and Methods **28**
3.1 Scanning Tunnelling Microscopy 28
3.1.1 Tunneling Theory 29
3.1.2 Tersoff-Hamann 30
3.1.3 Current flow 32
3.1.4 Scanning Tunnelling Spectroscopy 34
3.1.5 STM Operation 35
3.2 Ultra-high Vacuum 37
3.3 Surfaces 37
3.3.1 Au(111) 38
3.3.2 Surface Preparation 38
3.4 Molecular deposition 39
3.4.1 Sublimation 40
3.4.2 Electrospray 40
Electrospray Process 40
Electrospray deposition 42
3.5 X-ray Photoelectron Spectroscopy 43
3.6 Normal Incidence X-ray Standing Wave 46
3.6.1 Underlying Principles 46
3.6.2 Measurement Process 48
3.6.3 Theoretical concepts 48
3.6.4 Using Coherent Fraction and Position Values 51
3.6.5 Triangulation 51
3.6.6 Reflecting planes 52
4 Ullmann Coupling Reactions on Ag(111) and Ag(110) **54**
4.1 Introduction 54
4.2 Metal-Organic Intermediate Structures 55

4.2.1 Ag(111) . . . 56
4.2.2 Ag(110) . . . 59
4.3 Covalently Coupled Products . . . 62
4.4 Surface Lattice determination . . . 67
4.5 Conclusions . . . 68
5 X-ray standing wave based structure determination 70
5.1 Introduction . . . 70
5.2 XPS Characterisation . . . 73
5.3 C 1s NIXSW analysis: (111) reflection . . . 74
5.3.1 NIXSW analysis methods . . . 75
5.3.2 Chemically sensitive NIXSW results . . . 76
5.3.3 Twisting model of phenyl end groups . . . 79
5.3.4 The role of metal adatoms within MO structures . . . 81
5.4 I 3d NIXSW Analysis . . . 83
5.5 C 1s NIXSW analysis: (200) reflection . . . 86
5.5.1 Chemically sensitive NIXSW results . . . 86
5.5.2 Structural characterisation via STM . . . 89
5.5.3 Adsorption modelling methods . . . 93
5.5.4 Results of modelling . . . 95
TPB Lateral Adsorption Modelling . . . 95
TP Lateral Adsorption Modelling . . . 97
5.6 Conclusion . . . 99
6 On-Surface Synthesis within a Porphyrin Nanoring Template 101
6.1 Introduction . . . 101
6.2 Characterisation of reactant molecule and molecular template . . . 103
6.2.1 STM characterisation of TIPB . . . 105
6.2.2 STM characterisation of *c*-P40 . . . 106
6.3 Results . . . 108
6.4 Discussion: Use of *c*-P40 as a porous molecular template . . . 111

6.4.1 Thermal stability of *c*-P40 on Au(111) 111
6.4.2 Characterisation of co-deposited species 112
6.4.3 Implications for STM resolution within porous structures . . 113
6.5 Conclusions 118
7 Molecular Quantum Rings 119
7.1 Introduction 119
7.2 Geometric structure of *c*-P40 nanorings 124
7.3 DFT and xTB calculations of electronic states of *c*-P40 126
7.3.1 Experimental characterisation of the electronic states of *c*-P40 128
7.3.2 Spatial Distribution of Molecular States 130
7.4 Conclusions 134
8 Conclusions 135
8.1 Summary of findings 135
Appendices 139
A List of Abbreviations 139
B Structural Characterisation of an On-Surface Reaction 140
B.1 An Idealised Twisting Model 140
B.2 Derivation of the relationship between coherent fraction and twisting angle 142
B.3 Results 143
C Details of Quantum Ring xTB and DFT calculations 145
C.1 Computational Methods 145
C.2 Molecular Orbital calculations 146
Bibliography 146
List of Figures 167
List of Tables 171

Chapter 1

Introduction

This chapter introduces the concept of scanning probe microscopy and its implementation in generating and investigating surface confined structures. Manual assembly, via atomic manipulation, and molecular self-assembly are discussed before covering the topic of on-surface synthesis, and importantly, the characterisation of such reactions on the single molecule level. Finally, a summary of the content covered in each chapter is provided.

1.1 Probing surface structures

The progress of empirical science requires detailed observations of natural phenomena. The development of the observation tools used is therefore coupled to our understanding of the physical systems. An example of this is seen in microscopy, where early optical microscopes allowed the visualisation of cells, a finding which underpins much of modern biology. Optical microscopes however are fundamentally limited in resolution by the wavelength of visible light ($\sim$500 nm), limiting their use in investigating smaller systems. This constraint was reduced with the invention of electron microscopy techniques, for example transmission electron microscopy. Utilising the much smaller wavelengths achievable with electrons, producing images with resolutions of less than 1 nm became possible. However, instead of relying upon wavelength limitations, imaging techniques using measure-

ments of different types of interaction are able to achieve even higher resolving powers. One such technique is scanning probe microscopy, where an atomically sharp tip is scanned across a 2D surface to generate an image. Examples of this include atomic force microscopy (AFM) and scanning tunnelling microscopy (STM), both of which have led to significant advancements in imaging. Using AFM, it has been shown that a tip terminated with a single C-O molecule can achieve achieve submolecular resolution. An early example of this was demonstrated by Gross *et al.* where they were able to resolve individual bonds within a pentacene molecule (figure 1.1a).

In addition to its use as an imaging tool, SPM techniques have also shown promise for use in bottom-up fabrication at the nanoscale. Using the tip of a scanning probe as a tool, one can manipulate atoms and create structures. This was first performed in 1990 to assemble Xe atoms into the IBM logo [1]. This technique was later used to assemble Fe atoms into a quantum corral, providing an image of the 'wavefunction' of confined electrons [2]. More recent work into this technique has looked at its potential as a tool for reading and writing of high density computer memory. Work by Kalff *et al.* demonstrated how a scanning probe may be used to manipulate atoms on a chlorine terminated Cu(100) surface, such that a single vacancy site can be used to encode a bit of information (figure 1.1b (top)) [3]. Through this method, a vacancy site (darker regions) is either in a top or bottom position, to represent a 0 or 1 in binary. Combining eight of these regions together represents a byte of data, which can be interpreted. For example, in the case of figure 1.1b (top), the ASCII code for the letter 'e' is shown. The STM tip can then be used to manipulate these vacancy sites in such a way to write and rewrite information (figure 1.1b (bottom)). This technique was used to store a quote from Richard Feynman's talk 'There's plenty of room at the bottom' [4]. Expanding this has the potential to create memory with three orders of magnitude greater storage density than current technology.

Manual assembly of structures however is very time consuming and can be dif-

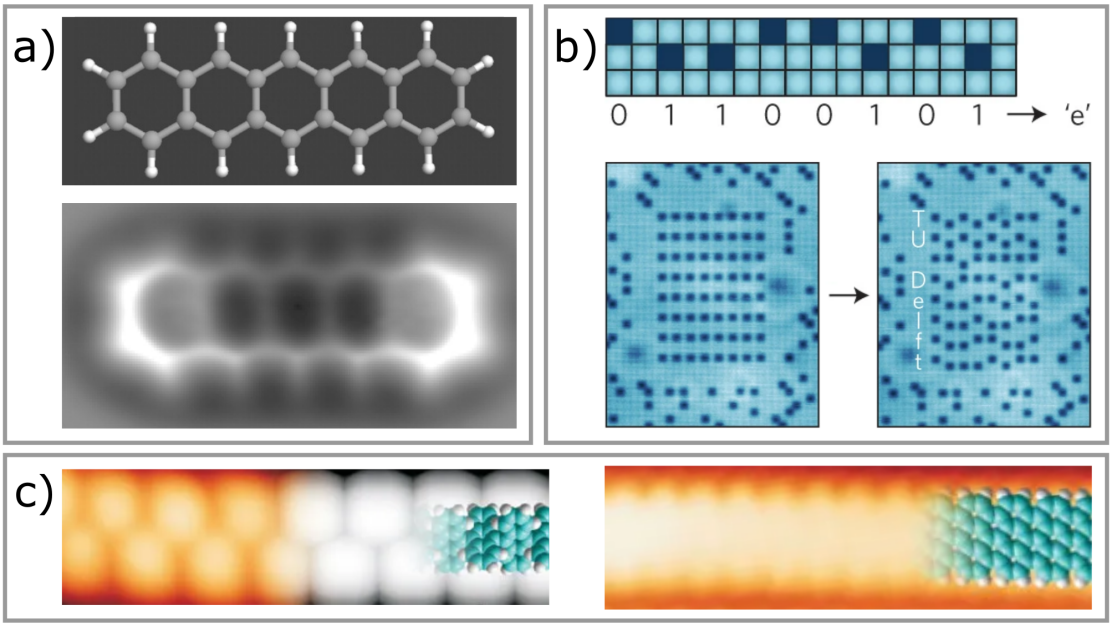


Figure 1.1: (a) Pentacene molecule (top) resolved through AFM imaging (bottom). Adapted from [5]. (b) Use of chlorine vacancies on Cu(100) to encode data. (Top) Example of how vancancies can be used to store a byte of data. (Bottom) transition from ordered set of vacancies to storing several bytes by manipulating atoms using an STM tip. Adapted from [3]. (c) STM images showing on-surface synthesis of graphene nanoribbons. Adapted from [6].

ficult to scale up. An alternative approach is fabrication through self-assembly, where a number of smaller building blocks form more complex structures without external direction. This concept is often found in nature, whereby simple molecular building blocks are combined to form much more complex structures, such as in the assembly and folding of proteins. The concept of on-surface synthesis of molecular structures builds upon these ideas. As with self-assembly, molecular precursors are designed to form arrangements of structures without the need for direction from external sources. However on-surface synthesis generates covalently bonded structures, making products that are more thermally stable and so can be used for a wider variety of applications. One of the first examples of this is the generation of 2D molecular networks using the Ullmann coupling reaction [7]. It has also been used in the synthesis of graphene nanoribbons (GNRs), which have the potential for use in molecular electronics [6]. Molecular precursors deposited onto a surface were found to form linear chains of graphene material after anneal-

ing the sample (figure 1.1c). STM imaging of this system revealed the reaction to produce GNRs occurred through a two-step process; first a coupling step where molecular precursors become covalently bonded, followed by a cyclodehydrogenation step. Characterisation of this system using STM therefore was able to provide a greater understanding for how the reaction progressed. STM characterisation of on-surface reactions allows the initial, intermediate and product structures to be studied. In addition, it provides a methodology for determining a mechanistic understanding of on-surface synthesis reaction pathways.

The work within this thesis builds on these ideas and, by utilising a range of on-surface analysis techniques, aims to further the understanding of on-surface reactions. Specific focus is given to understanding the underlying mechanisms of the Ullmann-like coupling reaction and the factors that influence it.

1.2 Thesis overview

Within this thesis the properties of various molecules adsorbed at metallic surfaces, the mechanisms for how they react and form structures, and how these reactions can be controlled are investigated. Chapter 2 acts as a review of the background literature and begins with a discussion of self-assembly and the various methods of on-surface synthesis. This is followed by a more detailed discussion of the Ullmann-like coupling reaction; looking at the development of its use within on-surface synthesis as well as current research into how to influence and control such reactions.

Chapter 3 explains the theoretical concepts and experimental methods used throughout this thesis. The underlying theory and basic operational details of STM are explained, as well as its use in other techniques such as scanning tunnelling spectroscopy (STS). Surface preparation and molecule deposition techniques of sublimation and electrospray ionisation are then detailed. Finally, the principles of X-ray analysis techniques, such as X-ray photoelectron spectroscopy (XPS) and normal incidence X-ray standing wave (NIXSW), are outlined.

Chapter 4 details the work carried out investigating the effect of surface topography on the structures formed at different stages of the Ullmann-coupling reaction. Molecular structures are formed through reactions of the molecule DITP (4,4"-diiodo-m-terphenyl) on Ag(111) and Ag(110). These structures are analysed using STM measurements and their adsorption geometries are compared. This chapter acts to highlight one of the methods for influencing on-surface reactions.

Chapter 5 develops these ideas by further investigating structures formed using the Ullmann coupling reaction. Two different molecules, DITP and a related molecule, TIPB (1,3,5-tris(4-iodophenyl)benzene), are separately investigated. X-ray techniques (XPS and NIXSW) are used to follow the progress of the Ullmann-coupling reaction and determine the locations of chemical species within each molecule, relative to the bulk surface, at each stage of the reaction. This is used in conjunction with STM measurements to develop 3D structural arrangements of molecules for intermediate and product structures.

A novel method for controlling on-surface reactions is developed in Chapter 6 through the use of molecular templates. Large nanorings, made from cyclic porphyrin polymers, are used to confine the Ullmann coupling reaction of TIPB and limit access to reaction sites such as surface step edges and metal adatoms. STM measurements are used to investigate the reaction products within nanorings, as well as the limitations of nanoring templates.

Chapter 7 contains work investigating the electronic properties of porphyrin nanorings and their potential to act as quantum rings. STS spectra were obtained finding energies of resonant electronic states. Further to this, the localised electron densities within the rings are probed through use of conductance mapping techniques. These results are supported by computational calculations using tight binding and density functional theory.

Finally, Chapter 8 provides a summary of the work within this thesis and the key findings.

Chapter 2

Studying 2D Molecular Self-Assembly and On-Surface Synthesis

This chapter serves as an overview of the literature which provides the foundation for the work presented within this thesis. The concept of molecular self-assembly is introduced, starting with structures driven by non-covalent interactions and is supported by several examples. The focus here is on characterisation by scanning probe microscopy techniques, facilitating molecular and sub-molecular resolution. Building upon studies of molecular assembly, on-surface synthesis reactions are introduced here with examples of some of the unique structures generated by this methodology. Particular focus is given to Ullmann-type coupling, explaining the development and current research into this type of reaction. Finally, the known factors which influence on-surface molecular synthesis and methods to control these reactions are discussed.

2.1 Molecular self-assembly in two-dimensions

Self-assembly is a process where a series of disordered components come together to form an organised structure driven by local interactions between component

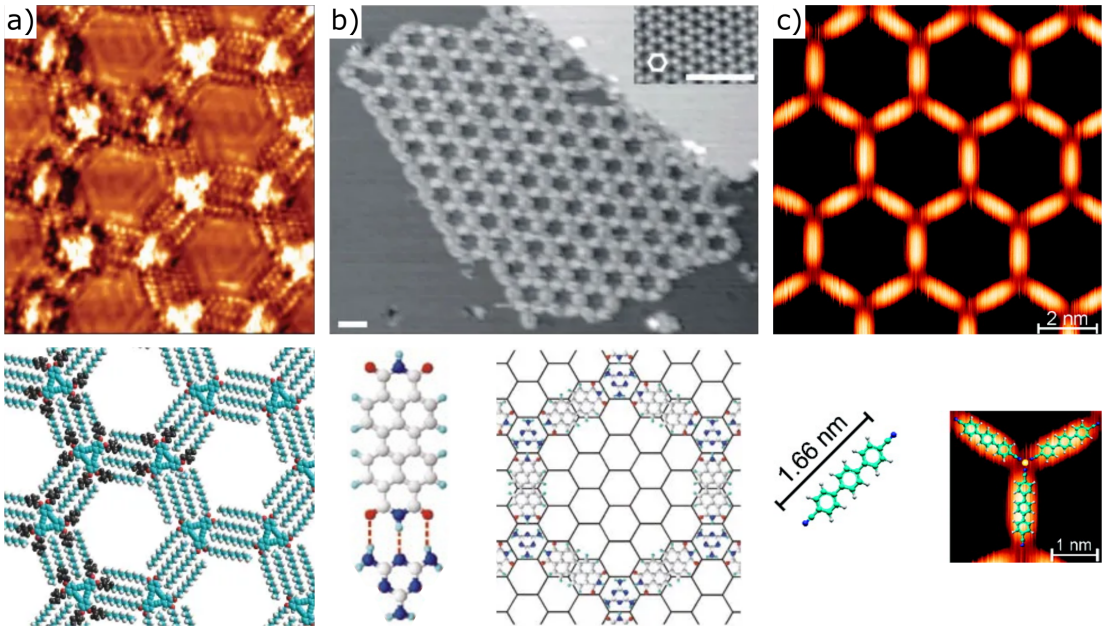


Figure 2.1: Examples of on-surface supramolecular assemblies, driven by various molecule-molecule bonding schemes. These include: (a) van der Waals interactions, (b) hydrogen bonding, and (c) metal-organic bonding. Top figures show STM images of assembled structures and bottom figures show molecular models for these structures. Adapted from [8–10] respectively.

parts. Molecular self-assembly was studied by Lehn in the context of supramolecular chemistry [11], where, through self-assembly, several molecular species can form complex structures held together by non-covalent intermolecular interactions. These processes are commonly observed in nature, for example, proteins self-assembling from amino acid chains into complex folded structures.

These ideas have been applied to surface science, where molecules with tailored geometries and chemical functionality have been used to self-assemble into a diverse range of surface structures. In order to fully understand self-assembly on surfaces, it is necessary to understand the roles of the various intermolecular interactions involved. Because of the on-surface nature of these structures, scanning probe microscopy (SPM) techniques, in particular scanning tunnelling microscopy (STM), has been utilised to offer local spatial information on structures formed. Three examples of structures formed through self-assembly are given in figure 2.1. Each of the examples is driven by a different intermolecular interaction, detailed in the following sections

2.1.1 Van der Waals mediated structures

Van der Waals forces occur between all molecules and arise from a combination of London, Debye and Keesom intermolecular interactions. Each of these correspond to a different type of dipole interaction: instantaneous-induced dipole, permanent-induced dipole and permanent-permanent dipole interactions for London, Debye and Keesom interactions respectively. Most self-assembly of molecules on surfaces into close-packed island structures are driven by these types of interactions. However, van der Waals interactions exhibits very weak interaction energies that decrease rapidly with increasing separation. This can be modelled using the Lennard-Jones potential which shows attractive interaction energy varies with $(1/r)^6$ [12]. Weak interaction strength and lack of directionality limits the use of van der Waals as a driving force for self-assembly. However, this can be overcome using molecules with large surface areas, allowing for 'multiple' van der Waals interactions, in order to maintain a stable structure. One example of this is the use of long hydrocarbon chains, which have been shown to assemble into a series of stable parallel lines [13]. Many groups have utilised this feature by using interweaving hydrocarbon chains to produce various stable structures [8, 14–17]. An example of this is shown in figure 2.1a, where precursor molecules, consisting of six hydrocarbon chains connected to a central core, were found to self-assemble into 2D hexagonal porous structures on the surface.

2.1.2 Hydrogen-bonded supramolecular self-assembly

Hydrogen bonding occurs in molecules where partial positive charges (δ^+) are induced in H atoms due to their proximity to an electronegative chemical species (*e.g.* O or N atoms). The partially charged hydrogen then electrostatically interacts with lone pair electrons of another electronegative atom. This effect produces an interaction that is significantly stronger than van der Waals (see table 2.1). Additionally, unlike van der Waals interactions, hydrogen bonding is directional. This characteristic has been utilised within molecular self-assembly, using specific

molecular geometries with directional hydrogen bonds to produce structures on surfaces [9, 18–26]. One important example of surface structures formed from hydrogen-bonds was by Theobald *et al.* [9]. The group exploited a triple hydrogen bond between PTCDI (3,4,9,10-perylene tetracarboxylic acid diimide) and melamine such that molecules self-assemble into a stable two dimensional porous network (figure 2.1b). The hydrogen bonded template was then used to confine up to seven C_{60} molecules within the pores. This use of surface templating will be explored in further detail in section 2.4.4.

2.1.3 Two dimensional metal-organic structures

An alternative way to stabilise 2D molecular systems is by metal-organic interactions. These types of interactions often occur between metal adatoms and lone pair electrons, in atoms such as O and N, within organic molecules. Similar to hydrogen bonding, metal-organic interactions are highly directional, allowing for their use in the self-assembly of specific structural geometries. For metal organic structures on substrates, the metal atoms involved in the bond can either be obtained by selecting a metal substrate where adatoms are present [27–29] or from co-deposition onto a surface of metal atoms with precursor molecules [30–32]. An example of this is the work by Schlickum *et al.* who deposited Co atoms onto a Ag(111) surface with nitrogen terminated polyphenyl molecules [10]. Nitrogen moieties formed directional metal coordination bonds with Co adatoms, with molecules assembling into an extended porous hexagonal network (figure 2.1c). The pore sizes within the network were found to be scalable by increasing the number of phenyl groups in the precursor molecules, demonstrating the flexibility of this bonding motif. Similarly, through the use of different precursor molecules, it has been shown that various shaped structures can be formed such as square or rectangular lattices [33–36].

Interaction Type	Interaction Strength (eV)
Van der Waals	0.02 - 0.1
Hydrogen bonding	0.05 - 0.4
Metal-Organic bonding	0.5 - 2.0
Covalent bonding	∼3.0

Table 2.1: Typical bond strength energies for common types of on-surface intermolecular interactions. [37]

2.1.4 Comparison of non-covalent interactions

Each of the above bonding types have relatively low interaction strengths when compared to thermal energy available at room temperature (see table 2.1). When the requisite amount of energy is provided (often raising the temperature above room temperature), molecules are able to diffuse on the surface, forming then breaking these lower energy bonds, until self-assembling into a low energy state. This allows islands of molecules to form long range extended structures containing very few defects. The reversible nature of these types of bonds are therefore of great advantage for self-assembly. However, due to their weak interaction strength, structures formed in this way have low thermal stability, making them unsuitable for many applications at elevated temperatures.

2.2 On-surface synthesis

The use of covalently bonded structures offers an alternative route to forming well ordered molecular structures. Covalent bonds typically have a higher interaction strength when compared to the non-covalent interactions discussed above. This means that they are stable over a larger temperature range, making structures formed using covalent bonds better suited to higher than room temperature applications. This higher interaction strength however can lead to structures becoming kinetically trapped in local energy minima, producing structures with a higher defect density when compared to non-covalently assemblies. Additionally, on-surface covalent coupling offers the potential of new reaction pathways when compared to solution-phase chemistry.

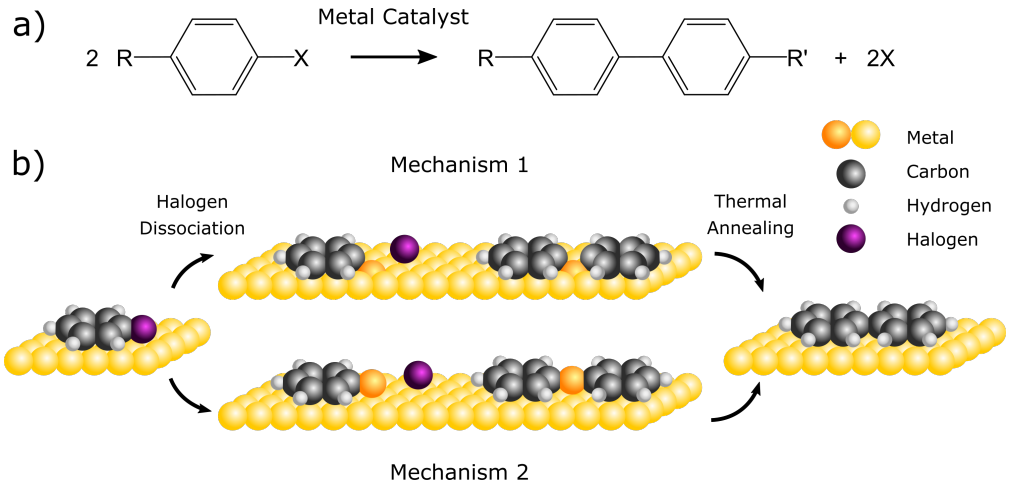


Figure 2.2: (a) Simplified reaction scheme for Ullmann coupling, showing the covalent coupling of two aryl-halides. (b) On-surface Ullmann-like coupling reaction for aryl-halides on a metal substrate, progressing from initial reactant to metal-organic intermediate structure, then to covalently bonded structure after annealing. The metal-organic intermediate forms through one of two different mechanisms: either bonding to an atom in the metal surface (Mechanism 1) or to a surface adatom (Mechanism 2).

2.2.1 Ullmann Coupling

One of the most studied on-surface covalent coupling reactions is the Ullmann-like coupling reaction. The solution based Ullmann reaction, originally discovered in 1901, is a cross-coupling reaction performed with a copper catalyst where aryl-halides are coupled via the removal of halogen groups [38]. A schematic of the on-surface Ullmann reaction is shown in figure 2.2. Here, aryl-halides deposited onto a metal surface undergo dissociation of their halide groups in a reaction catalysed by the metal substrate. This is caused by partial filling of the π^* orbital upon deposition of the molecule. Subsequent charge transfer between π^* and σ^* orbitals destabilises the C-X (carbon-halogen) bond, leading to homolysis. The resulting surface-stabilised radicals are then joined via substrate metal atoms, creating an intermediate metal-organic state. The addition of thermal energy leads to the reductive elimination of the metal atoms, resulting in the formation of covalent bonds between molecular units [39]. The exact process involved in the formation of the metal-organic intermediate is still debated however, with aryl-radicals forming metal-organic bonds to either bulk surface atoms (Mechanism

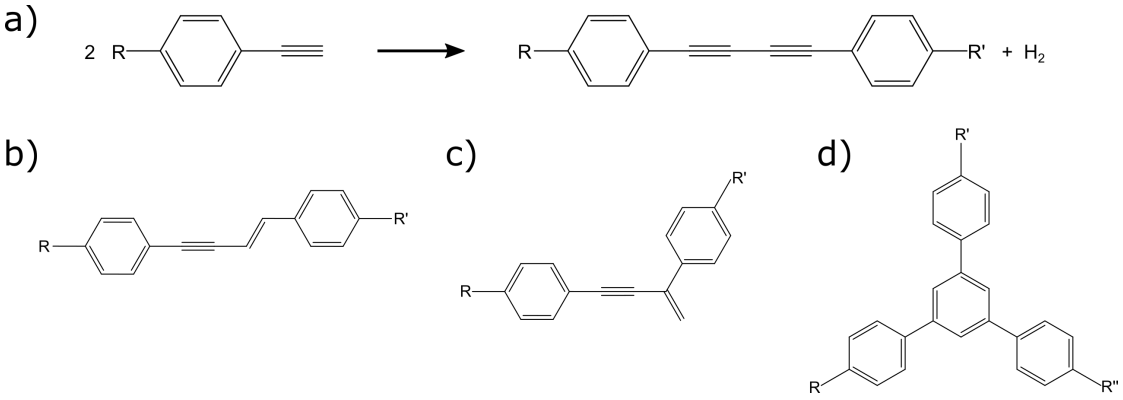


Figure 2.3: (a) Simplified reaction scheme for Glaser coupling of terminal alkynes. (b-d) Example alternative products for the Glaser reaction shown in (a), resulting in defect (b,c) and branching (d) structures.

1) [40] or with diffusing adatoms (Mechanism 2)[41–44]. The mechanism of the Ullmann coupling reaction and the factors that influence structures formed in this way are explored in detail in this thesis.

2.2.2 Glaser Coupling

An alternative but still frequently used on-surface covalent reaction is the homo-coupling of terminal alkynes, or Glaser coupling. Similar to Ullmann coupling, Glaser coupling was originally used in solution chemistry [45]. In this reaction, terminal alkyne groups of precursor molecules are joined through dehydrogenation, resulting in the formation of a covalent bond between initial reactants (see figure 2.3a). In recent years, this reaction has been used for the synthesis of a range of products including linear chains [46–51], 2D extended networks [52, 53] and is progressing towards the synthesis of graphyne structures [54, 55].

One of the main advantages Glaser coupling has over similar reactions is that the only byproduct it produces is H_2. This is likely to desorb from the surface after reacting and so keeps the surface clean from contaminants that could otherwise influence the reaction. A limitation to the Glaser coupling reaction however is its tendency for poor chemo- and regioselectivity. This leads to unwanted side reactions and results in the formation of defects in final products [47, 56]. Figure

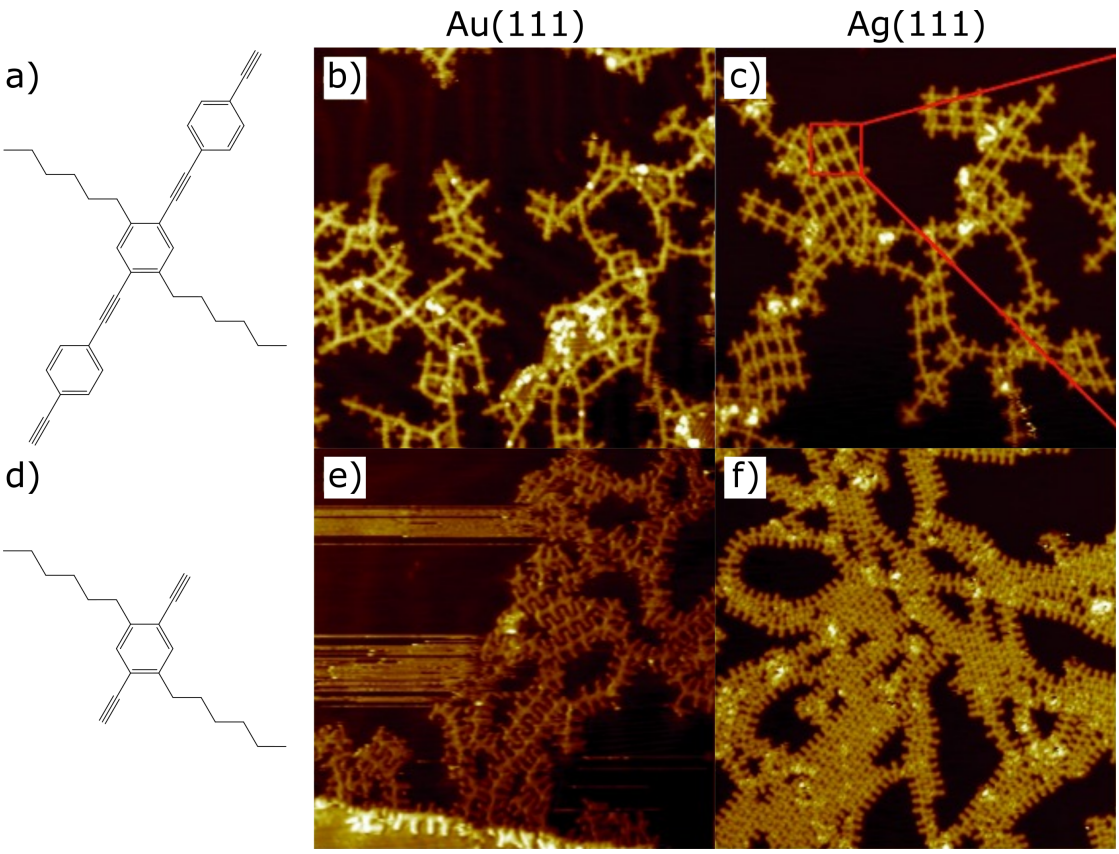


Figure 2.4: (a) Initial precursor for on-surface Glaser coupling, producing highly branched structures on Au(111) (b) with greater order observed for structures of Ag(111) (c). (d) Secondary precursor for Glaser coupling reaction, producing significantly greater ordered chain structures on Au(111) (e) and Ag(111) (f). Adapted from [47].

2.3b-d shows several examples of possible side reactions including kink defects found in chains and the formation of branching structures.

Despite these problems, several methods for controlling the Glaser reaction have been investigated, such as the effect of precursor design and role of surface chemistry. Gao *et al.* [47] investigated the structures formed through Glaser coupling of an initial precursor molecule (2.4a) deposited onto Au(111) (2.4b) and Ag(111) (2.4c) surfaces. They found that structures formed on the Au(111) surface had a significant number of defects and branches, accounting for ∼75% of coupling reactions. Whereas on Ag(111), structures were much more ordered, although defects were still present (∼35% of reactions). A second precursor molecule (2.4d) containing fewer phenyl groups was then investigated. On both surfaces, signifi-

cantly fewer defects were observed than with the initial precursor, with molecules on Ag(111) forming long range chains up to 59 units long. The differences observed between the two precursors was attributed to steric hinderance in the second precursor reducing the formation of defects. Similar results have been achieved through the use of the highly stepped Ag(877) surface to confine the Glaser coupling reaction to step-edges, resulting in the formation of low defect chains [48]. Differing surface topographies have also been investigated and were found to produce different products from the same precursor. Liu *et al.* compared the formation of molecular wires on different surface facets of silver. They found that on Ag(111) the Glaser coupling reaction dominated, resulting in covalently bonded chains, whereas on Ag(110) and Ag(100) the majority of chains were found to be metal-organically linked. This effect was attributed to the dimensions of each product matching better to different substrate lattice constants [51].

2.2.3 Other Coupling

In addition to those previously mentioned, there are a great number of other on-surface covalent reactions being investigated by the surface-science community. Examples of this include dehydration reactions, with particular interest going to reactions involving boronic acid or the schiff-base coupling reaction (figure 2.5a and b respectively) and have been shown to produce a diverse range of product structures [10, 57–62]. In addition to this, dehydrogenation reactions (figure 2.5c) have been shown to be possible on metal surfaces [63–66]. Finally, similar to the Ullmann coupling reaction, general dehalogenation reactions have been explored (figure 2.5d) [67, 68].

2.2.4 Summary of on-surface synthesis protocols

This section has highlighted the vast range of different reaction schemes that have been explored for on-surface synthesis. For each reaction examples have been given that demonstrate the variety of structures that can be produced from these

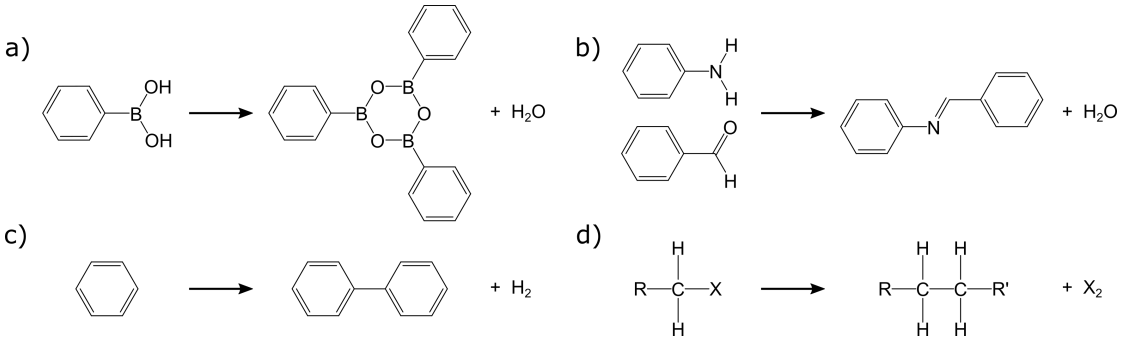


Figure 2.5: Schemes for other common on-surface reactions. (a) Dehydration reaction. (b) Schiff-Base coupling reaction. (c) Dehydrogenation reaction. (d) Dehalogenation reaction.

reactions. The following sections will build on this while focusing primarily on the Ullmann-coupling reaction (due to the scope of this thesis). The development of the Ullmann-coupling reaction will be shown as well as current research into how it can be influenced or controlled.

2.3 Development of on-surface synthesis via Ullmann Coupling

The first investigation into the Ullmann coupling reaction through scanning probe microscopy was performed by Hla *et al.* [69]. Here, iodobenzene is confined to a step-edge on a Cu(111) surface and the tip of an STM is used to induce the Ullmann coupling reaction. First, tunnelling electrons are injected into the molecule to break the C-I bond by applying a 1.5 V bias at a fixed height relative to the surface. This is repeated for a second iodobenzene molecule. The tip is then used to laterally translate one of the resulting benzene radicals next to the other, where further tunnelling electrons are injected using a 0.5 V bias to form a covalent bond between the constituent molecules. This is shown in figure 2.6.

Grill *et al.* were the first to use the Ullmann coupling reaction in the formation of covalently bonded molecular frameworks [70]. Various bromo-tetraphenyl porphyrin (BrTPP) molecules were deposited onto Au(111), where thermal annealing

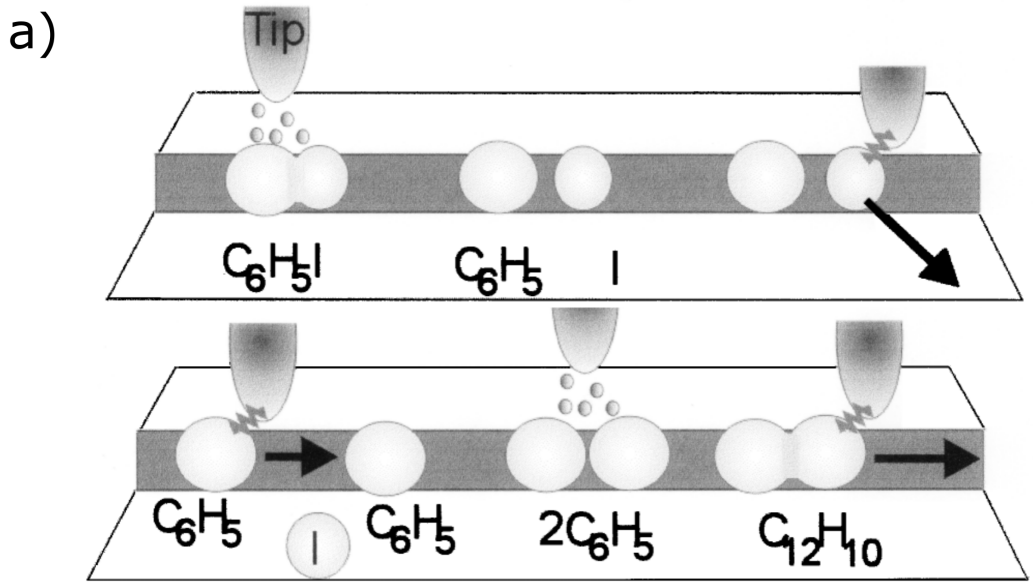


Figure 2.6: Schematic for the process of inducing the Ullmann coupling reaction of iodobenzene to biphenyl using an STM tip. Adapted from [69].

of the surface was found to break the C-Br bond, inducing the Ullmann reaction to create covalently coupled products. The group used various forms of TPP, containing 1, 2 or 4 terminal bromine atoms (2.7a-c). Selection of the precursor in this way allowed for the formation of different structures, with monobromo-TPP forming dimers, dibromo-TPP forming linear chains and tetrabromo-TPP forming disordered 2D networks. This work was expanded on by investigating the possibility of hierarchical growth using TPP with two bromine and two iodine substituents in *trans* positions [71]. Due to the lower bond energy of C-I relative to C-Br, an initial annealing step led to the dissociation of iodine and the formation of linear chains through the Ullmann coupling reaction, while leaving the bromine groups intact. A subsequent annealing step removed the bromine groups, resulting in the formation of 2D networks, with significantly greater order than seen in tetrabromo-TPP (figure 2.7d). This work has also led to the development of coupling of heteromolecules [72], allowing for more complicated structures to be formed on surfaces. Overall, these works demonstrate the importance of careful precursor selection for building structures through on-surface synthesis.

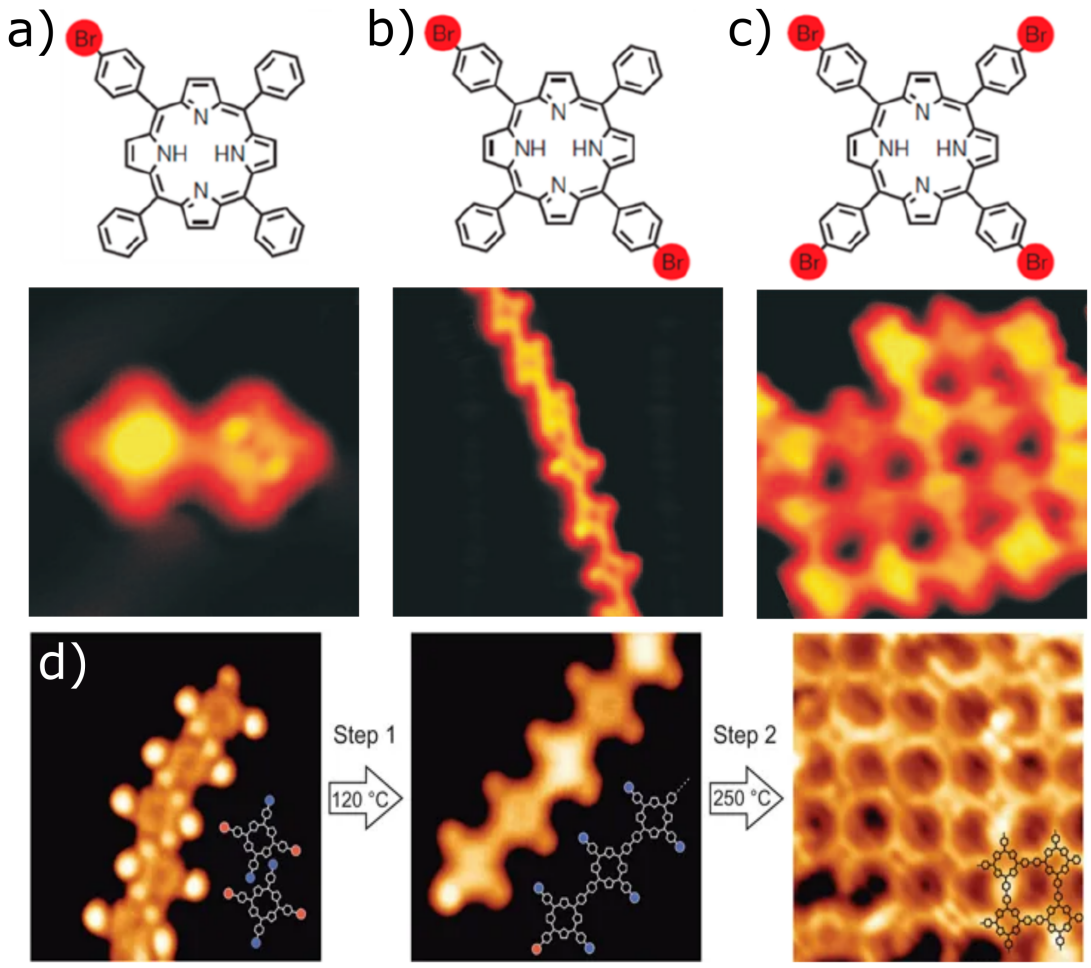


Figure 2.7: (a)-(c) Chemical structures for Br-TPP with 1, 2 and 4 bromine substituents, forming dimers, chains and 2D networks respectively. Adapted from [70]. (d) Two step hierarchical growth of ordered 2D network from Br_2I_2TPP. Chemical structures overlaid on STM images. Initial annealing leads to removal of iodine atoms (orange) and the formation of linear chains. Further annealing removes bromine atoms (blue) and the formation of extended 2D covalent networks. Adapted from [71].

2.3.1 Implementations of on-surface Ullmann coupling

Over the past decade, there has been great progress in the development in the use of Ullmann coupling for on-surface synthesis of 1D and 2D covalently bonded structures. Planar aromatic molecules functionalised with two halide groups have been shown to form linear molecular chains [41, 73–76] as well as zigzag chain structures [42, 77, 78] via the on-surface Ullmann reaction. Further to this, experiments using molecules with three and four-fold symmetries facilitate the synthesis of 2D molecular networks [79–84]. Finally, molecular precursors with more tailored

geometries have led to the on-surface synthesis of more unique structures such as hyperbenzene macrocycles [42, 85].

One developing application of Ullmann coupling is its use in the synthesis of graphene-like materials. Graphene has shown potential as a material for use in electronic devices, due in particular to its carrier transport properties [86]. However, graphene's applications in semiconductor devices are limited, partially due to its zero bandgap. Because of this, other graphene-like materials are being investigated to determine their feasibility as a substitute for graphene. One limiting factor for this is synthesising these materials. Ullmann coupling however has shown potential in this area, so far having been utilised in the fabrication of porous graphene networks of varying size [81, 82], synthesis of individual nanographenes [87] as well as functionalising existing graphene structures with different molecular species [88].

Of particular interest are graphene nanoribbons (GNR), where theory has predicted that introducing boundary conditions to graphene will induce a bandgap within the material [90]. The first synthesis of GNRs through Ullmann coupling was performed by Cai *et al.* [6]. Here they deposited a bromine functionalised bianthryl precursor monomer (figure 2.8a and b) onto a Au(111) surface, where the Ullmann coupling reaction was utilised to form linear polymers on the surface. Further heating of the sample induced intramolecular cyclodehydrogenation of the chains, forming armchair GNRs, 7 atoms wide. Band structure calculations found that these GNRs are expected to exhibit a bandgap of 1.6 eV, with further calculations finding that the bandgap decreased with increasing width of the GNR. Further investigation into using Ullmann coupling to form GNRs has facilitated synthesis of GNRs of varying thickness [91], formation of different GNR structures [6] and study the effects of substrate on the reaction [92].

An additional potential application for GNRs is as molecular wires. The charge transport effects for GNRs have been previously investigated [93], comparing the effects of various GNR lengths and geometries. Two main structural geometries

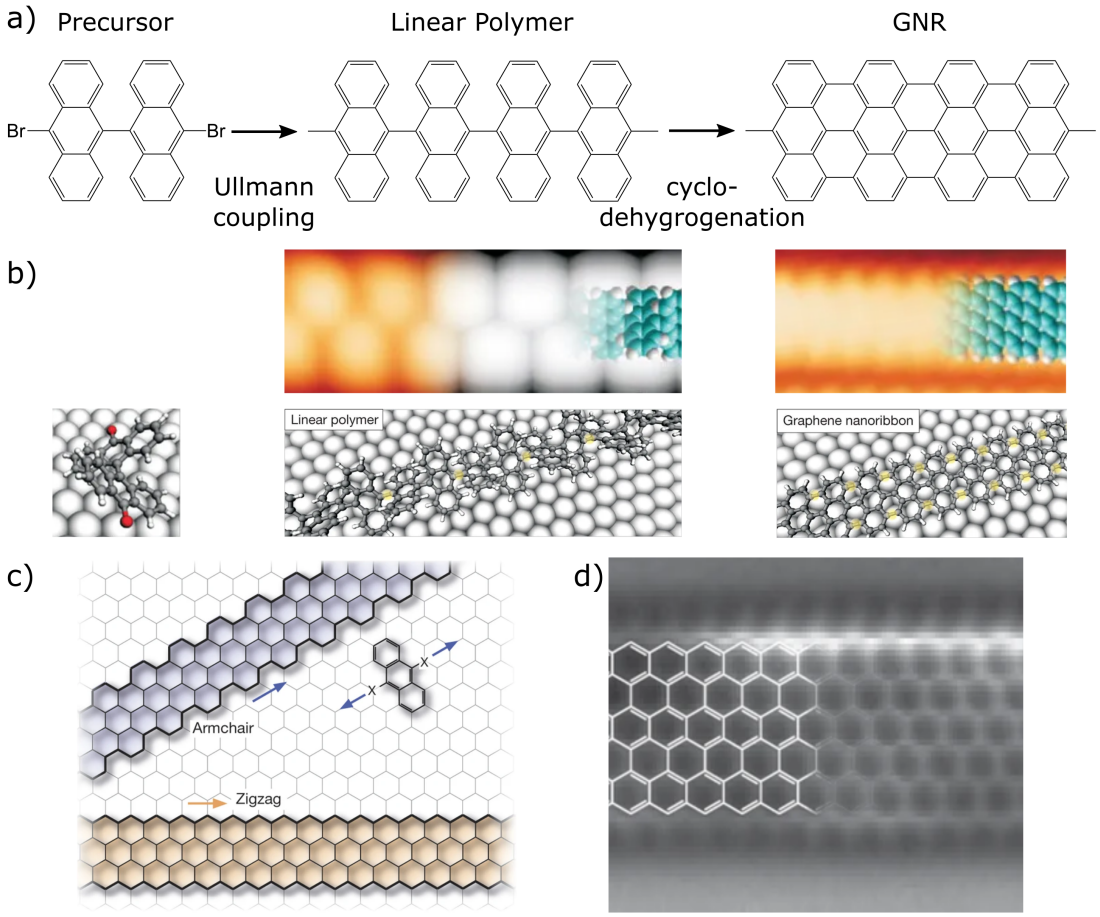


Figure 2.8: (a) Reaction scheme showing the two stage process for synthesis of graphene nanoribbons (GNR). Bianthryl precursors on Au(111) are heated initiating Ullmann coupling reaction to form linear polymers. Further heating leads to intramolecular cylcodehydrogenation of the chain and the formation of GNRs. (b) STM images (top) of synthesised structures with molecules overlaid. Molecular models (bottom) show progress at each reaction step, with new bonds formed at each stage of the reaction highlighted. Adapted from [6]. (c) Model showing structural differences between armchair (blue) and zigzag (orange) GNRs. (d) high resolution AFM image showing surface synthesised zigzag GNR, with molecular model overlaid. Adapted from [89].

were compared: armchair edge and zigzag edge (see figure 2.8c). From these investigations, it was found that conductance in armchair GNRs decayed rapidly with distance at low electron energies whereas zigzag GNRs did not, making zigzag GNRs preferable for use as molecular wires. The synthesis of zigzag GNRs is non-trivial, however this was first demonstrated by Ruffieux *et al.* where, using a novel precursor design, they synthesised atomically precise zigzag GNRs on Au(111) using an Ullmann-coupling reaction (figure 2.8d) [89].

2.4 Controlling and influencing on-surface reactions

In the last few years, research into Ullmann coupling has focused on what factors influence the reaction. This approach has the potential to provide a better understanding into how to control the reaction, allowing for the synthesis of structures displaying characteristics such as high spatial ordering or bespoke geometry. Within this field the emphasis has been on furthering understanding in two main areas: selection of precursor molecules and the influence this has on how structures form (bulding upon the early work of Ullmann coupling) and the choice and effect of substrate.

2.4.1 Role of Halogen Chemistry

It is tempting to consider the halogen atoms left on the surface as part of Ullmann coupling simply as byproducts, however one may expect the presence of an electronegative species on the surface to influence the reaction through charge effects or simply as steric hindrance. Recent research by Galeotti *et al.* into this problem separately investigated the structures formed from five derivatives of 1,4-dihalobenzene, each terminated with a different combination of halogen atoms (see figure 2.9) [94]. Initial deposition of molecules onto Cu(110) held at room temperature resulted in the dissociation of halogens and molecules formed various metal-organic chain structures on the surface. Of note is that molecules containing chlorine did not not have their halogens fully dissociate upon deposition. Instead, for each molecule, one chlorine atom remained bonded with molecules forming metal-organic dimers. Annealing the samples to 150°C then resulted in the full dissociation of all chlorine atoms and molecules formed extended metal-organic structures, similar to other halogen terminated molecules.

The transition of molecules from metal-organic to covalent phase was then examined using fast-XPS spectra, measuring changes in the C 1s core level as a function of temperature (figure 2.9). In these experiments, the activation temperature for transition between organometallic and covalent phase (T_{start}) and the

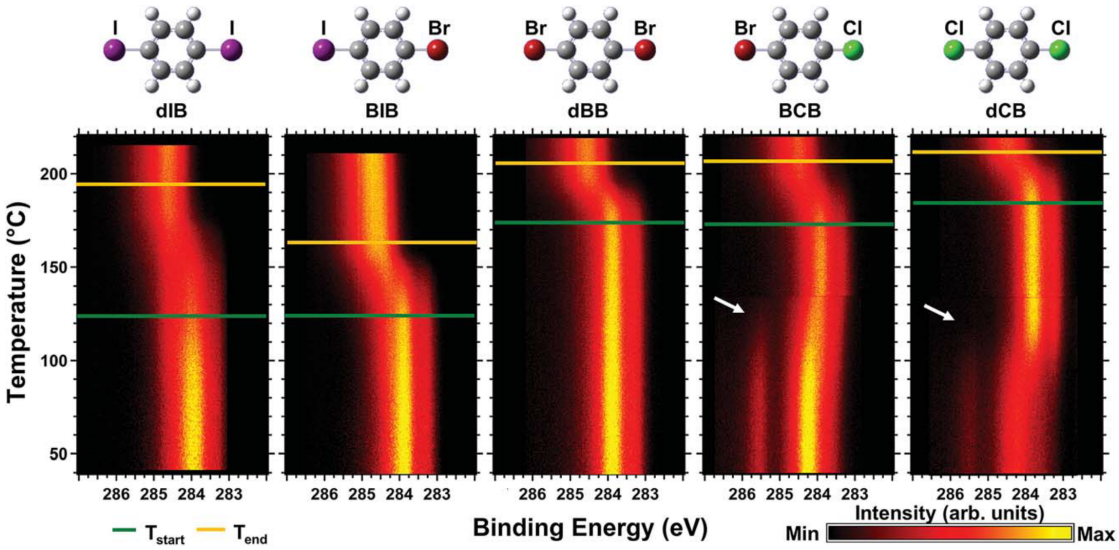


Figure 2.9: Fast XPS measurements of C1s during annealing (0.2°C/s) showing transition from metal-organic to covalent phases for five precursor molecules. T_{start} (green line) and T_{end} (yellow line) represent when 10% and 90% of the covalent coupling reaction has occurred respectively. White arrow indicates temperature C-Cl dissociation occurs. Adapted from [94].

temperature range of transition was found to differ for each halogen type. This is seen in the XPS spectra in figure 2.9 as a shift in the main peak to a higher binding energy. The temperatures in which the transition begins and ends are indicated with green and yellow lines respectively. Iodine containing compounds begin the transition at lower temperatures and have a higher temperature range, whereas the opposite was found to be true for chlorine precursors. Finally, STM measurements highlighted the differences between reaction products on the surface for the different precursors, with halogen type found to influence structural arrangements. Precursors containing halogens with higher bond dissociation energy were found to form longer metal-organic chains. Further to this, the orientation of structures relative to the (110) surface in both organometallic and covalent phases were found to differ between halogen type.

A related study comparing the effects of halogen choice for precursors found that iodine containing molecules produce longer GNRs when compared to similar brominated molecules [95]. This effect was attributed to the lower dissociation temperature for iodine compared to bromine. As iodine dissociates from molecules

at a lower temperature, there is less overlap between the Ullmann coupling and cyclodehydrogenation reaction steps. This allows more time for the formation of long chains before growth is stopped by cyclodehydrogenation.

2.4.2 Role of Substrate Chemistry

The role of the substrate in the Ullmann reaction has been widely studied. Bieri *et al.* investigated this by comparing structures formed by cyclohexa-*m*-phenylene (CHP, see figure 2.10a) on three different surfaces: Cu(111), Au(111) and Ag(111) [82]. This molecular precursor was expected to form extended 2D covalent networks across the surface. Immediately following deposition of CHP at room temperature, it was found that iodine would dissociate from the molecules and form surface stabilised radicals on each of the different substrates. Further annealing was required to initiate covalent bonding in the molecules. Each substrate required a different annealing temperature to induce the covalent coupling: 475 K, 525 K and 575 K for Cu, Au and Ag respectively. Other studies comparing Ullmann reactions on various surfaces have found similar results, with different substrates requiring differing activation energies to initiate both halogen dissociation and covalent coupling [83, 96].

Further to this, Bieri *et al.* found that the polyphenylene networks differed significantly in the density of structures produced depending on the substrate. STM imaging of the structures (figure 2.10b) revealed CHP to form branched, low density structures on Cu(111) surface, whereas on Ag(111) highly ordered, compact islands were observed. A mixture of dense and branching structures were seen on Au(111). To investigate this further, they performed Monte Carlo simulations in an attempt to qualitatively reproduce the structures observed. By varying a coupling probability, P, defined as a ratio of coupling and diffusion rates of molecules, molecular structures resembling those observed in experiments were produced (figure 2.10c). From these results they found that on the Cu surface, coupling rates dominate over diffusion such that molecules react forming irreversible covalent

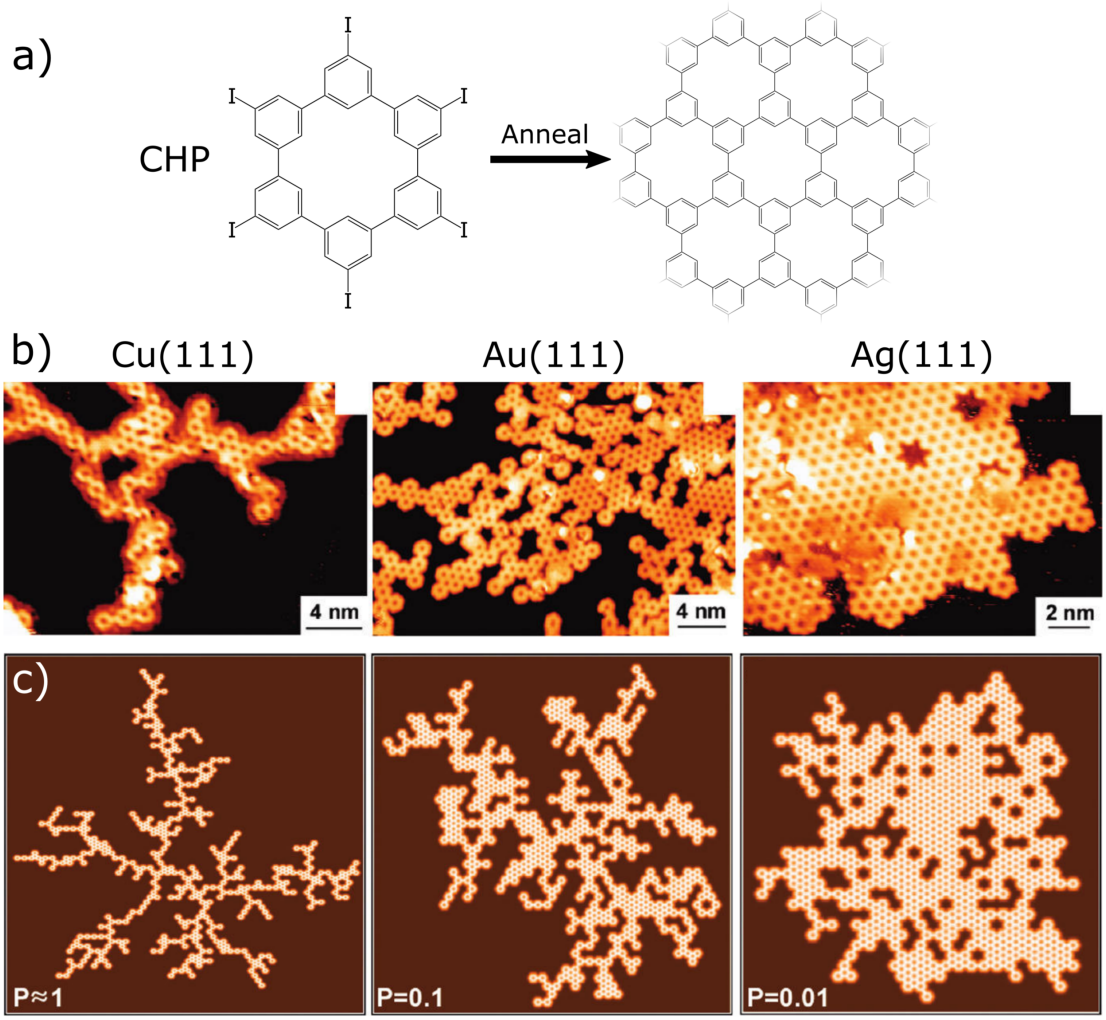


Figure 2.10: (a) Reaction scheme for Ullmann coupling of cyclohexa-*m*-phenylene (CHP) to produce extended polyphenylene networks. (b) Comparison of STM images of CHP after undergoing Ullmann coupling on different coinage metal surfaces. (c) Monte Carlo simulations comparing effects of different coupling probabilities (P) on the structures formed by CHP. Adapted from [82].

bonds before being able to pack efficiently. This is in contrast to the Ag surface where diffusion rates dominate and molecules are able to rearrange to form close packed networks before bonding. This shows control over the coupling and diffusion rates are important in structure formation and can prevent structures becoming kinetically trapped in low density arrangements. Overall, these studies show the importance of substrate choice for Ullmann coupling in both its effect on activation temperature for the reaction but also the type of structures that form as a result.

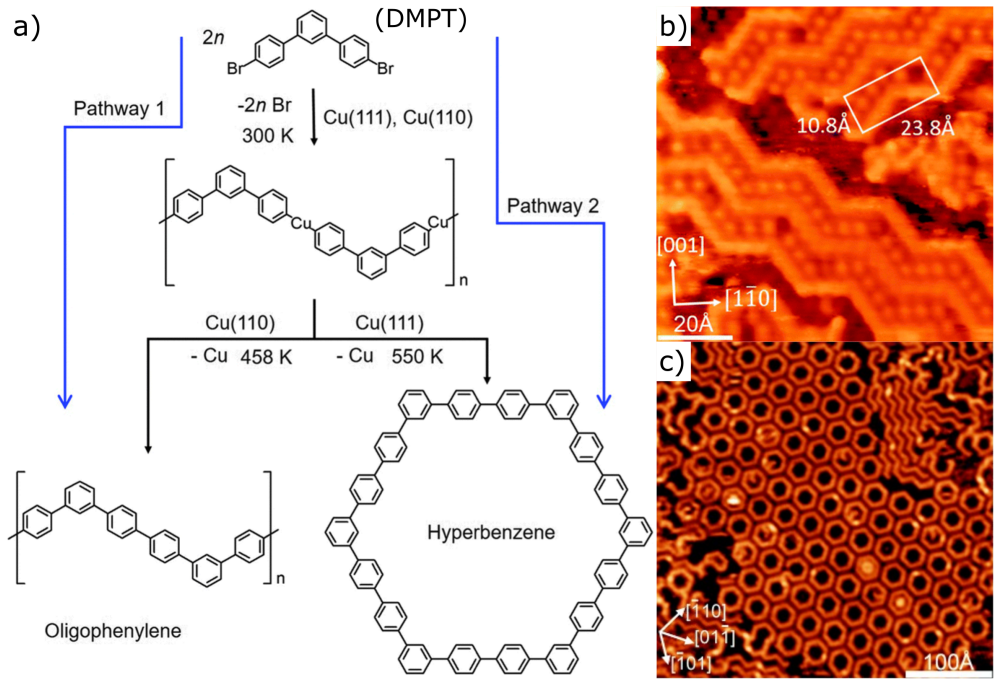


Figure 2.11: (a) Reaction scheme showing two pathways for DMTP on Cu(110) versus Cu(111) resulting in oligophenylene zigzag chains (b) and hyperbenzene (c) structures respectively. Adapted from [78] and [77].

2.4.3 Role of Substrate Topography

In addition to the type of surface, the surface topography can also be used to influence the Ullmann reaction. Dai *et al.* compared the effects of performing Ullmann coupling on two different surface facets of copper. Depositing 4,4"-dibromo-*m*-terphenyl (DMPT) onto Cu(110) [78] and Cu(111) [77] results in the dissociation of bromine and the formation of metal-organic zigzag structures on both surfaces. Annealing then leads to the covalent coupling of molecules on each surface. However, on Cu(110), only short oligophenylene zigzag chains were observed (figure 2.11b), whereas on Cu(111) the majority of structures formed are hyperbenzene macrocycles with a small number of zigzag polyphenylene chains (figure 2.11c). This effect was assigned to the three-fold symmetry of the (111) surface being more energetically favourable to the formation of hexagonal structures, as opposed to the two-fold symmetry of the (110) surface. Additionally, the oligophenylene on Cu(110) was noticeably stretched, with zigzag angle increased to 125° and the lattice constant for the chains increase by 2 Å when compared to chains on Cu(111).

This stretching was assigned to the need for the chains to achieve commensurability with the surface. Further to this, an investigation by Saywell *et al.* on the highly stepped Au(10,7,7) surface showed the importance of kink defect sites on step-edges for initiating the dissociation of halogens from molecules, allowing for the easier formation of polymer chains [97].

2.4.4 Use of templates to control reactions

Disordered and irregular sized structures are commonly produced through on-surface Ullmann-coupling reactions. This presents problems in producing structures of a consistent size and geometry. One solution for controlling reactions is by using a templated surface. Confining reactions within a template can act to limit space available to molecules and with the potential of using this to control the reaction.

This concept has been explored by Fan *et al.* where reactions were confined using a Cu(110)-(2×1)O nanotemplate [98]. Through a controlled oxidation process, surfaces were produced consisting of alternating stripes of bare Cu and Cu-O with varying widths. Within this template, the Ullmann reaction was found only to proceed on areas of bare Cu due to availability of Cu atoms necessary to catalyse the reaction. This acts to confine any reaction processes to within the Cu stripes of the template. Figure 2.12a shows an example STM image of this surface with Cu-O areas (blue arrow) appearing brighter than bare Cu (green) arrow.

The precursor molecule DMPT (see figure 2.11a for details) was deposited onto the surface, and was found to form islands of parallel zigzag chains within templated areas, as observed previously [78]. However, within the template, zigzag chains were found to be of uniform length, with chain growth limited by the width of the stripe. Further to this, within sufficiently narrow stripes (<5.6 nm) DMTP was found to consistently produce macrocycle structures. The size and shape of synthesised macrocycles varied depending on stripe width, with examples of this shown in figure 2.11b. Interestingly, a number of these structures were

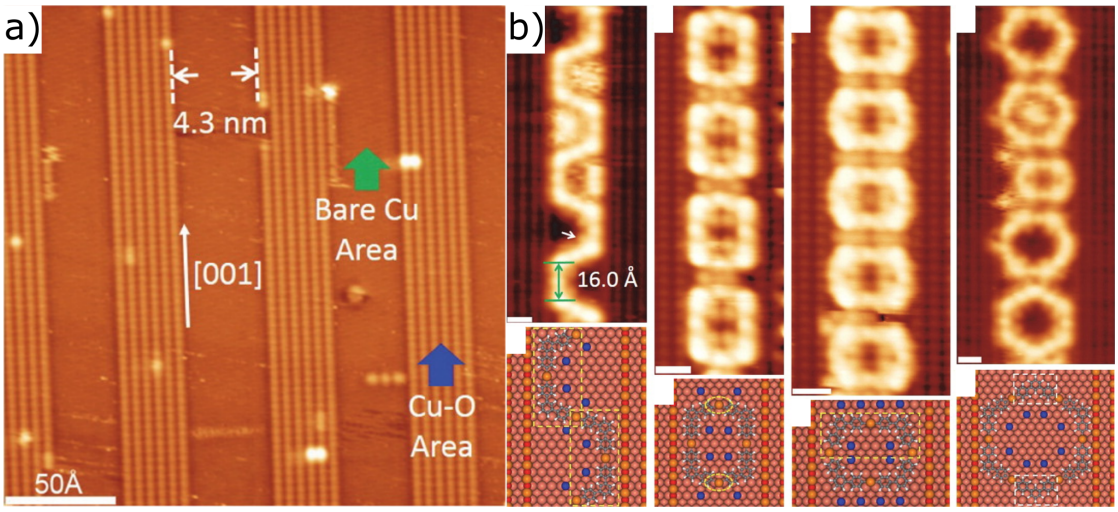


Figure 2.12: (a) STM image of Cu(110) surface templated with Cu-O, Green arrow shows bare Cu surface, blue arrow shows Cu-O template. (b) STM images (top) and molecular models (bottom) showing various structures formed within templated Cu-O stripes of different widths. Adapted from [98].

only observed within the template and had not been produced previously on non-templated surfaces. Overall, this experiment demonstrates the use of templated surfaces in controlling the size and structure of reaction products.

In addition to limiting the space available for reacting molecules, templates can also be used to limit availability of reaction sites, such as surface adatoms and step-edges. This concept has been previously employed, using a PTCDI melamine self assembled network (2.1b) to produce a hexagonal porous molecular template on a Ag(111) surface [44]. An iodine terminated reactant molecule, TIPB (1,3,5-tris(4-iodophenyl)benzene), was deposited onto the templated surface, and molecules within templated areas were compared to molecular islands on clean areas of the surface. Cleavage of iodine from TIPB was observed immediately following deposition. TIPB was found to form metal-organic structures as part of the Ullmann reaction on clean areas of the surface. However, within the templated pores, no metal-organic structures were observed. This offers insight into the reaction pathway of the Ullmann coupling reaction, suggesting the presence of step-edges or metal adatoms is necessary for the formation of metal-organic intermediate structures.

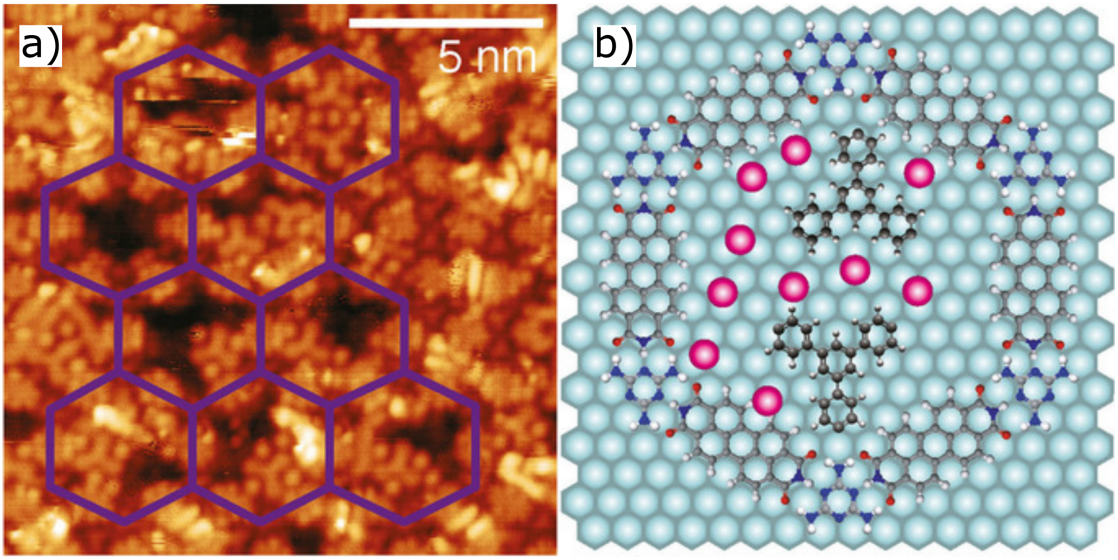


Figure 2.13: (a) STM image showing TIPB confined within porous PTCDI melamine template. Pore regions highlighted with hexagons. (b) Molecular model showing TIPB reactant molecule with iodine (purple) dissociated within a molecular template, without forming a metal-organic intermediate structure. Adapted from [44].

2.5 Summary

In summary, a number of factors influencing on-surface synthesis have been explored within the current literature, with particular focus give to the Ullmann-coupling reaction. Previous works have shown the importance of molecule chemistry and geometry, as well as surface chemistry and topography. These factors have been shown to significantly influence the structures formed on surfaces, affecting the overall size, shape and geometry of structures as well as defect density within them. In the remainder of this thesis, I will expand upon these ideas, investigating the influence of surface topography on an Ullmann-coupling reaction in chapter 4, and then building on this in chapter 5 by exploring the adsorption geometry of molecules throughout the different stages of the Ullmann-coupling reaction. The use of templated surfaces will also be explored in chapter 6, investigating the role the surface plays within the Ullmann reaction.

Chapter 3

Theory and Methods

This chapter details all of the theoretical concepts and experimental methods which underpin the work within this thesis. Initially, the theory of scanning tunnelling microscopy is discussed, as well as the basic operational principles. This is followed by experimental procedures performed throughout experiments such as surface preparation and molecule deposition. Finally the techniques of X-ray photoelectron spectroscopy and normal incidence X-ray standing wave are discussed.

3.1 Scanning Tunnelling Microscopy

Scanning tunnelling microscopy (STM) is a scanning probe technique used to generate images of surface structures. A tip is moved across a surface with a small voltage applied between them. The applied bias results in a flow of electrons between the tip and surface, which can be measured experimentally as a current. These current measurements are then used to create an image of the topography of the surface. Typical STMs have lateral resolution of <1 Å and vertical resolution which can be of the order of picometers, allowing for resolution of individual surface atoms and sub-molecular resolution of molecules. STM has the advantage of being a real space analysis technique. This allows local areas around individual molecules to be imaged, providing site specific information, as opposed to diffraction techniques, such as low-energy electron diffraction (LEED), where an average

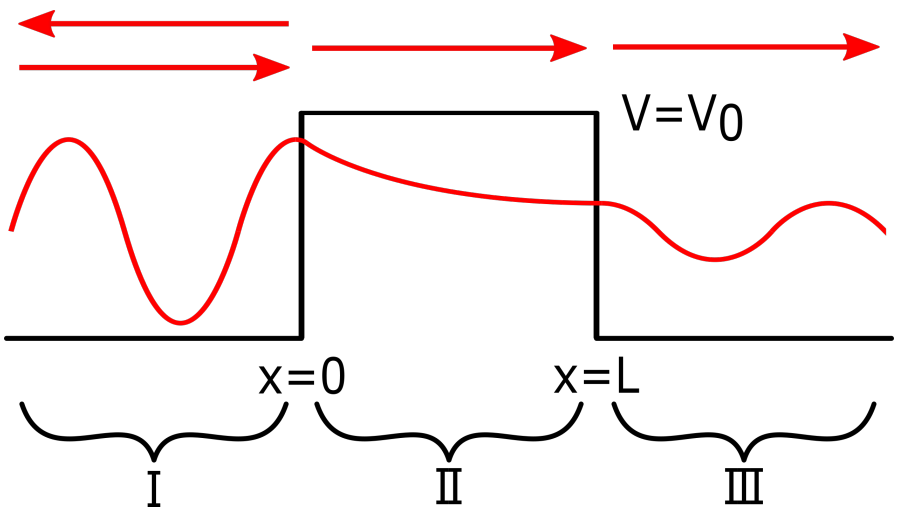


Figure 3.1: Potential barrier model of electrons of energy E tunnelling through a barrier of width L and height $V > E$. The model can be considered in three separate regions: (I) ($x < 0$) The incident electron travelling from the right, meeting the barrier and being partially reflected. (II) ($0 < x < L$) The electron wave function in the classically forbidden barrier region. (III) ($x > L$) The Transmitted electron wave function.

value of an ensemble of molecules is obtained.

This technique provides information on adsorbed features on surfaces such as imaging their adsorption geometries or information about their electronic structures. In this thesis, STM is used to image molecular structures on surfaces. These images are then used to infer details about the formed structures, such as their dimensions and composition. This then allows for the characterisation of molecular adsorption geometries and how they arrange relative to surfaces.

3.1.1 Tunneling Theory

In classical physics, a particle cannot pass through a potential barrier unless it has sufficient energy to overcome it. In quantum mechanics however, particles with less energy than a barrier have a finite probability of passing through, in a process known as quantum mechanical tunnelling. STM exploits this to produce images.

In an STM, tunnelling occurs between a sharp metallic tip and a flat metal sample, separated either by vacuum, air or a liquid. This system can be modelled as a one dimensional rectangular potential barrier, with an electron of mass m and energy E travelling in the x direction, incident on the barrier (figure 3.1).

The barrier has a potential value of $V = V_0$ between $x = 0$ and $x = L$ and is 0 elsewhere. This model can be considered in three separate regions. Region I ($x < 0$), consisting of the incident and reflected waves, region 2 ($0 < x < L$) containing a potential barrier of height V_0 and width L, and region III ($x > L$), containing the transmitted wave. The wave functions for these three regions can then be written as

$$\psi_1 = A_0 e^{ikx} + Ae^{-ikx}, \tag{3.1}$$

$$\psi_2 = Be^{-\alpha x} + Ce^{\alpha x}, \tag{3.2}$$

$$\psi_3 = De^{ikx}, \tag{3.3}$$

where $k = \sqrt{2mE}/\hbar$ and $\alpha = \sqrt{2m(V_0 - E)}/\hbar$. The transmission coefficient, T, represents the ratio of incident and transmitted wave amplitudes and is given by

$$T = \left| \frac{D}{A_0} \right|^2. \tag{3.4}$$

By applying boundary conditions and assuming a thick barrier ($\alpha L \gg 1$), T can be approximated as

$$T \approx 16 \left(\frac{E}{V_0} \right) \left(1 - \frac{E}{V_0} \right) e^{-2\alpha L}. \tag{3.5}$$

In the context of STM, the transmission coefficient is proportional to tunnel current. Equation 3.5 therefore shows measured tunnel current scales exponentially with barrier width and effective barrier height ($V_0 - E$). This can be used to show that a 1Å change in tip surface separation, results in approximately an order of magnitude change in tunnel current. It is this relationship that gives rise to the exceptional vertical resolution of the STM technique [99].

3.1.2 Tersoff-Hamann

The wave function treatment for tunnelling is a very simple model and is difficult to extend to the three-dimensional case of a real STM. Instead, first-order time dependent perturbation theory can be used to formulate a more realistic model.

The more general theory of tunnelling between two metal plates in a vacuum was first developed by Bardeen [100] in 1961. This was then applied to STM by Tersoff and Hamann by considering one plate as the surface and the other as the tip. [101, 102] Using this, the tunnel current becomes

$$I = \frac{2\pi e}{\hbar} \sum_{\mu\nu} f(E_\mu)[1 - f(E_\nu + eV)] \left|M_{\mu\nu}\right|^2 \delta(E_\mu - E_\nu) \tag{3.6}$$

where $f(E)$ is the fermi function, V is the applied bias, $M_{\mu\nu}$ is the tunnelling matrix element between the electronic states ψ_μ of the tip and ψ_ν of the sample surface, and E_μ is the energy of the state ψ_μ in the absence of tunnelling. This equation considers only positive voltages, there is a corresponding equation for reverse tunnelling.

This equation can be considered in three parts. The first, $(f(E_\mu)[1-f(E_\nu+eV)])$ represents the probability of an electron occupying a filled state in the tip (ψ_μ) possessing the same energy as an empty state in the surface (ψ_ν). This ensures tunnelling only occurs from a filled to an empty state. The second part $(\left|M_{\mu\nu}\right|^2)$ represents the probability of these states overlapping. Finally, the delta function ensures conservation of energy in the case of elastic tunnelling, such that $I = 0$ if $E_\mu \neq E_\nu$.

The tunnelling matrix can be evaluated by integrating wave functions of the tip and surface over an arbitrary surface, lying entirely within the vacuum barrier region between the two electrodes,

$$M_{\mu\nu} = \frac{-\hbar^2}{2m} \int (\psi_\mu^* \nabla \psi_\nu - \psi_\nu \nabla \psi_\nu^*). \tag{3.7}$$

To simplify equation 3.6, Tersoff and Hamann considered tunnelling current in the limit of low temperature and small applied bias. This gives

$$I = \frac{2\pi}{\hbar} e^2 V \sum_{\mu\nu} \left|M_{\mu\nu}\right|^2 \delta(E_\mu - E_F)\delta(E_\nu - E_F), \tag{3.8}$$

where E_F is the fermi energy. The wave function for tip in this equation however is usually unknown. To solve this, Tersoff and Hamann assumed a spherical tip with radius R and centre at position $r = r_0$. This removes angular dependence and the tip wave function can be approximated as an S-wave with the tunnel current becoming

$$I \propto \sum_{\nu} |\psi_\nu(r_0)|^2 \, \delta(E_\nu - E_F). \tag{3.9}$$

This is simply the local density of states (LDOS) of the surface, therefore showing that the tunnel current from an STM is a measure of the LDOS at the position of the tip r_0.

This model can be extended to a more realistic description by considering the effects of finite applied voltages to the system. Integrating over all states contributing to the tunnel current (between E_F and $E_F + eV$) gives

$$I \propto \int_{E_F}^{E_F+eV} |\psi(E, r_0)|^2 \, \delta(E - E_F) T(E, eV) dE \tag{3.10}$$

where $T(E, eV)$ is the transmission coefficient defined previously (equation 3.5) which, for small biases, can be approximated as constant.

3.1.3 Current flow

The current flow between an STM tip and a surface, and how this changes with different applied biases, can be described through a simple energy level diagram, shown in figure 3.2. At zero applied bias (3.2a), the Fermi levels (E_{Fermi}) of the tip and surface are in equilibrium and there is no flow of electrons between them. A positive bias applied to the surface raises the Fermi level of the tip. This allows electrons from filled states in the tip to tunnel into empty states in the surface of the same energy (3.2b), providing information on empty surface states. Similarly, a negative bias applied to the surface sample raises the Fermi level of the surface, allowing tunnelling between filled surface states and empty tip states (3.2c), giving information on filled surface states.

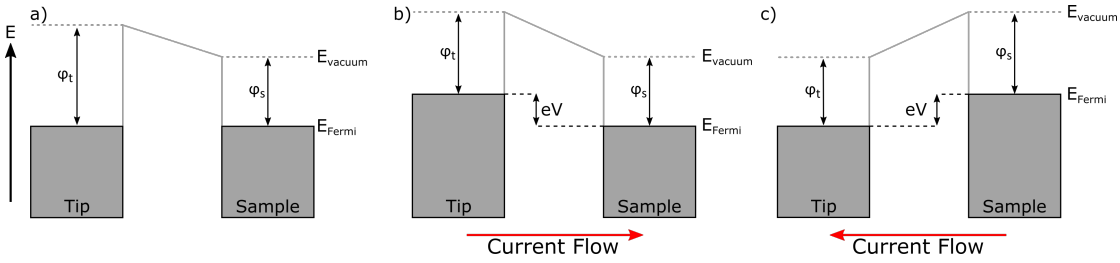


Figure 3.2: Energy level diagrams for STM tip and sample at various biases. (a) Zero applied bias. The Fermi levels for tip and sample are equal so no tunnelling occurs and there is no current flow. (b) Positive sample bias. The Fermi level in the sample is shifted lower relative to the tip and so tunnelling can occur from filled tip states to empty sample states, resulting in current flowing from tip to surface. (c) Negative sample bias. The Fermi level in the sample is shifted higher compared to the Fermi level of the tip, allowing electrons to tunnel from sample to tip, giving a current in that direction.

This model can be extended to include surfaces with adsorbed molecular species and used to demonstrate how information about a molecule's molecular orbitals can be gathered through STM. Adsorbed molecules are in close proximity to the surface and so their molecular orbitals are likely to be strongly coupled, relative to the molecule and the tip. This means that a shift in the Fermi level of the surface will shift the molecular orbitals by the same amount [103]. Figure 3.3 shows the energy states of a tip and a surface with an adsorbed molecular species, at different biases. For positive biases (3.3a), the sample Fermi level is lower relative to the tip, allowing electrons in filled states in the tip to tunnel into the lowest unoccupied molecular orbital (LUMO). At negative applied biases (3.3b), the Fermi level of the sample is raised and electrons can tunnel from filled states in the sample to the empty tip states. Electrons tunnel through the highest occupied molecular orbital (HOMO) in this case. Using these ideas, STM can be used to probe the energy levels of molecules adsorbed to surfaces. Imaging at different applied biases will give information about different molecular orbitals.

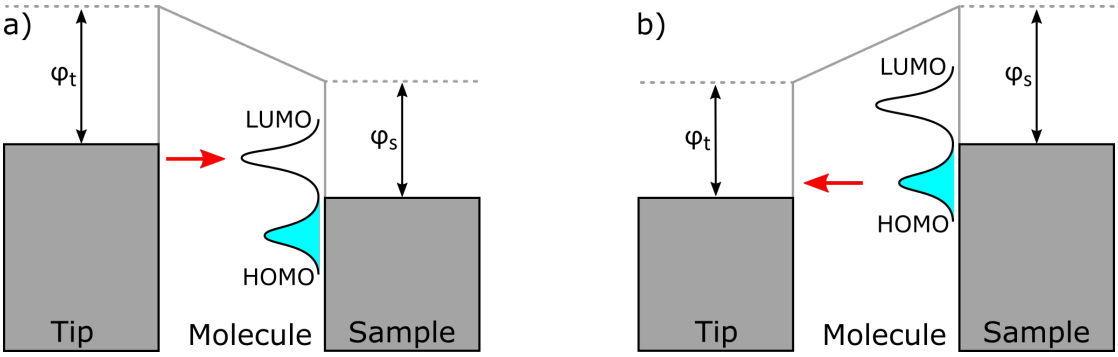


Figure 3.3: Images showing tunnelling between states for a surface with an adsorbed molecular species at different biases. (a) Positive bias applied to the surface. Electrons tunnel from filled states in the tip to empty states in the surface, giving information about the LUMO. (b) Negative bias applied to the surface. Electrons tunnel from filled states in the sample and molecule to empty states in the tip, giving information about the HOMO.

3.1.4 Scanning Tunnelling Spectroscopy

From equation 3.10, by taking the differential with respect to voltage of the tunnel current, it can be shown that

$$\frac{dI(V)}{dV} \propto \rho s(E_F - eV), \tag{3.11}$$

where $\rho s(E)$ is the density of states of the surface. With this, STM can be used to probe the electronic structure of a sample in a process known as scanning tunnelling spectroscopy (STS).

In this technique, the tip is held at a position above the region of interest on the sample at a fixed current set point. Voltage is then swept through a range of values and the current measured. In order to measure dI/dV directly a small sinusoidal oscillation (dV) is applied to the main bias. This results in an oscillating output signal, with amplitude related to the change in current (dI) over the oscillating voltage range. This is shown graphically in figure 3.4a.

In order to extract the values for dI from the measured signal, a lock-in technique is used. The oscillating current signal is fed into a lock-in amplifier, with the applied oscillating bias used as a reference, and a signal proportional to the

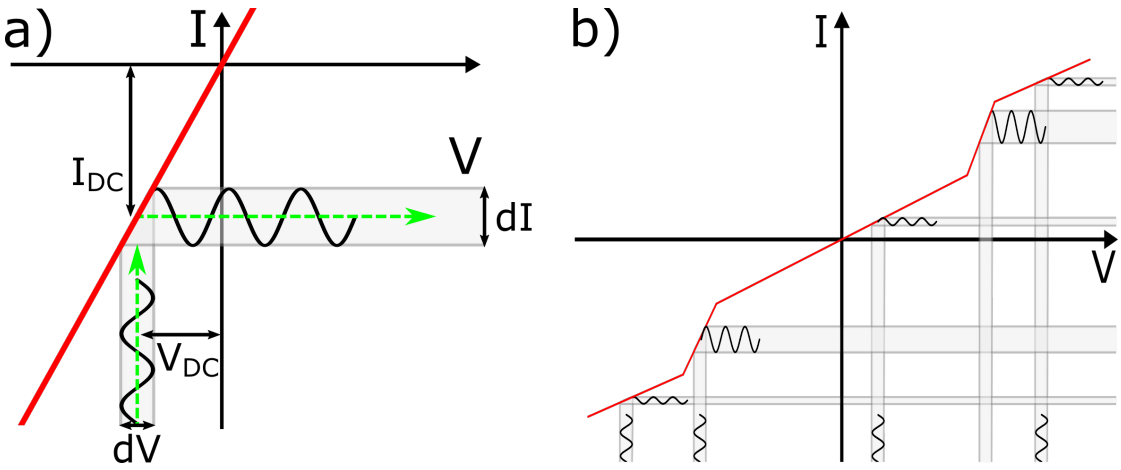


Figure 3.4: (a) Example figure showing how an applied oscillating bias can extract a gradient measurement from a signal. An applied voltage V_{DC}, oscillating with amplitude dV gives a measured signal I_{DC} oscillating with amplitude dI. (b) Applying oscillating signals over a range of voltages can be used to extract dI/dV signal from a system.

amplitude, and hence proportional to dI, is output. This is repeated over a range of voltages of interest and used to build up a dI/dV signal (figure 3.4b). The advantage of using this technique as opposed to taking the differential of the I(V) measurement manually is this results in a significantly more accurate measurement with greatly reduced noise.

A related technique, known as conductance mapping, can also be used for imaging electronic states. Instead of varying tip sample voltage at a fixed point as in STS, the STM probe is scanned across an imaging area with the bias set to a fixed value. From dI/dV measurements, the spatial distribution of the density of states of a sample can be determined.

3.1.5 STM Operation

An STM is able to create an image by raster scanning across a surface, taking a series of discrete measurements on each line. These individual measurements correspond to pixel values in the final image. Measurements are obtained in one of two modes: constant height or constant current.

In constant height mode, the tip is scanned across the surface while held at a constant z position, determined by a set point. The measured tunnel current is

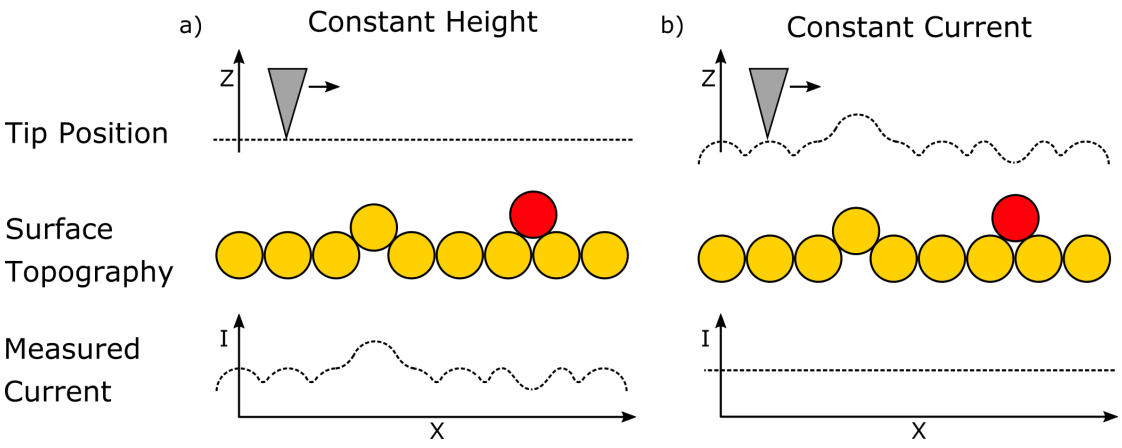


Figure 3.5: The two main operational modes of STM. (a) Constant height mode. The tip is kept at a constant z position and variations in the measured tunnel current are used to image the surface. (b) Constant current mode. Feedback loops are used to adjust tip position above the surface so that the measured tunnel current remains constant. The z position of the tip is used to produce an image the of surface. Yellow and red circles represent surface atoms and contaminants respectively.

recorded at a series of points, with each point corresponding to a pixel value in the STM image. In constant current mode, a feedback control system is used to maintain a constant measured current across the surface. At each image point, the z position of the tip is adjusted via a feedback loop so that the tunnel current is kept at a set value. The tip z position is then recorded for each pixel in the image. A summary of imaging modes is shown in figure 3.5.

In both imaging modes, a larger tunnel current or greater z position (above the surface) typically corresponds to a raised surface feature. Therefore the image is often considered an approximation of the surface topography. However, the exception to this is for features with different conductivity to the surface. Features with a lower conductivity for example will appear as depressions, due to having a lower tunnel current for a given height. This is seen for both imaging modes in figure 3.5 at the red circle.

Constant height mode has the disadvantage that the tip cannot react to large changes in topography or a largely sloped surface and can result in crashing the tip into the surface, potentially damaging the tip. For this reason, STMs are typically operated in constant current mode.

3.2 Ultra-high Vacuum

In order to study the properties of on-surface reactions, it is necessary to ensure the surface is free from any contaminant species that could otherwise influence the reaction. To do this, experiments were performed under ultra-high vacuum (UHV) conditions, where UHV is defined as pressures $< 10^{-9}$ mbar. Under atmospheric conditions, a clean surface will become covered in contaminants in less than a second, whereas in UHV pressures, surfaces can remain clean for several hours [104]. UHV conditions are provided by performing STM experiments in steel chambers, with the vacuum maintained through various pumping methods (ie turbo-molecular pumps or ion pumps)[105].

3.3 Surfaces

The surfaces employed within this thesis are crystalline metals and their orientation is described using Miller indices. This refers to the subset of lattice planes determined by three integer values, h, k and l (written as (hkl)). These values denote a set of planes orthogonal to the vector $h\mathbf{a_1} + k\mathbf{a_2} + l\mathbf{a_3}$, where $\mathbf{a}_n$ are the unit vectors for the crystal unit cell. A surface cut to a specific plane will produce a specific arrangement of atoms at the surface. An example of this is shown in figure 3.6a using a face-centred cubic (fcc) crystal unit cell. This type of crystal structure is common amongst metals and all surfaces within this thesis are of this type. The (111) surface plane is overlaid in red and highlights which atoms in the unit cell make up the top layer of atoms for the (111) surface. The resulting surface structure of a (111) plane is shown in figure 3.6b. This is a close packed arrangement, with each surface atom surrounded by 6 other surface atoms. An example STM image showing the Ag(111) surface structures is shown in figure 3.6c.

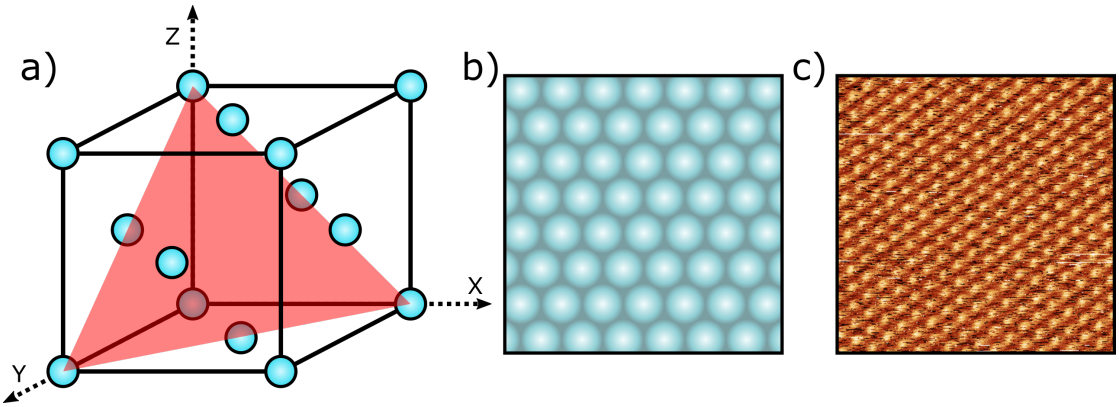


Figure 3.6: (a) Unit cell for a face-centred cubic crystal lattice. (111) crystal plane is overlaid in red. (b) Model for the atomic surface lattice of the (111) crystal plane. (c) STM topograph of Ag(111) surface showing atomic silver. $I_{set} = 2$ nA, $V = -0.1$ V.

3.3.1 Au(111)

Unlike the simple close packed arrangement of the Ag(111) surface shown above, the Au(111) surface differs as it exhibits a $22 \times \sqrt{3}$ surface reconstruction [107]. The reconstruction causes the top layer of surface atoms to compress as 23 surface atoms (along one of the $\langle 110 \rangle$ surface direction) are made to fit in the space of 22 bulk lattice spacings. This effect is shown in figure 3.7a. Strain from the additional atom causes deformation of the surface and produces an alternating topography, resulting in a 'herringbone' pattern on the surface. This has interesting effects as certain sites on the herringbone structure are more catalytically active than others [106]. An example STM image of the Au(111) herringbone pattern is shown in figure 3.7b.

3.3.2 Surface Preparation

The metallic surfaces studied within this thesis were prepared by cycles of argon sputtering followed by annealing to ensure all surfaces are 'atomically flat' and free from contaminants. Argon sputtering is performed by leaking small amounts of argon gas into the UHV system (typically up to pressures of 5×10^{-6} mbar) and passing this through a large electric field ($\sim$0.8 keV). This ionises the gas and

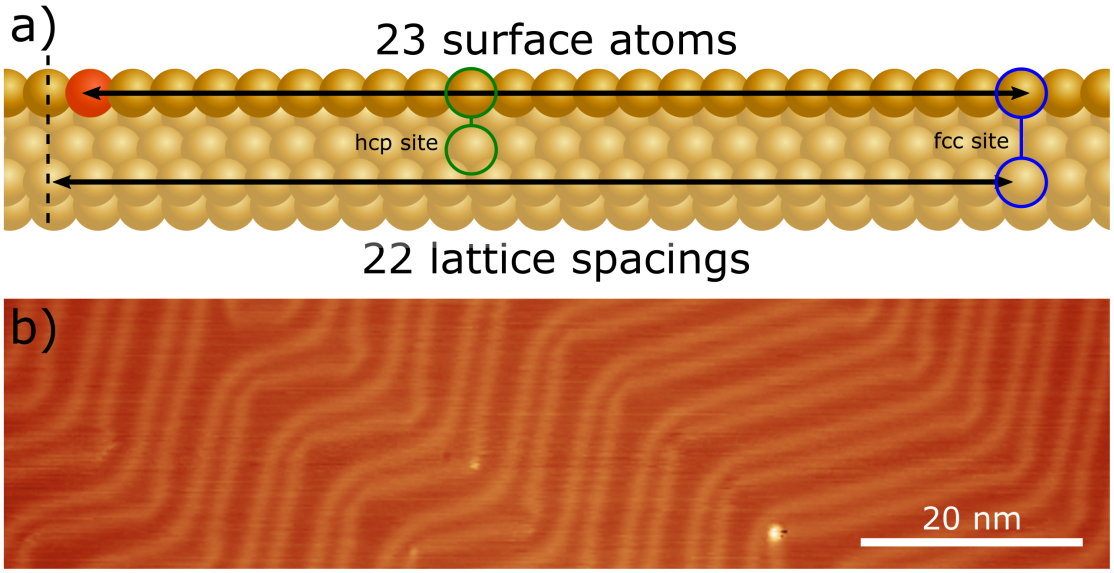


Figure 3.7: (a) Side view of Au(111) crystal lattice, showing surface reconstruction. 23 surface atoms are shifted to fit into the space of 22 lattice sites, with the extra surface atom highlighted in red. Positions where surface atoms align with hcp (hexagonal close-packed and fcc (face-centred cubic lattice sites are indicated. Vertical corrugation of surface layer atoms not shown for clarity. Adapted from [106]. (b) Example STM topograph of Au(111) surface showing herringbone pattern. $I_{set} = 10$ pA, $V = -1.8$ V.

accelerates the Ar^+ ions towards the sample. This is performed for between 10 and 30 minutes and acts to bombard the surface, removing contaminants. This process is followed by an annealing step where the sample is heated for approximately 30 minutes, after which, the current is slowly reduced to ensure the sample cools slowly and forms large areas of the desired surface structure (e.g. the (111) plane).

3.4 Molecular deposition

The aim of this thesis is to investigate the properties of molecules on surfaces. As outlined above, it is necessary to study these molecules under UHV conditions. This presents the problem of how to get molecules onto a surface, as typical methods for doing this, such as solution deposition, are much more difficult in UHV. Instead a range of UHV based deposition techniques are used, the most common of which is thermal sublimation, although other techniques may be necessary depending on the molecule.

3.4.1 Sublimation

Sublimation is a technique used to deposit molecules onto a surface through thermal evaporation, typically using a Knudsen cell in UHV. A Knudsen cell consists of a metal or ceramic crucible, where molecules are placed (normally in a crystalline or powder form), surrounded by a heating coil. A current passed through the coil heats the crucible, causing molecules to enter the gas phase. The 'molecular gas' is then directed at a sample plate for deposition.

3.4.2 Electrospray

Sublimation cannot be used to deposit all molecules. Large or biological molecules may have lower intra-molecular binding energies than the energy required to initiate sublimation. This results in thermal decomposition of the molecule before sublimation can occur. In order to investigate these molecules and their behaviour on surfaces, an alternative technique is required to transfer them into the gas phase intact [108]. Electrospray ionisation was originally developed by Fenn *et al.*. [109] for use in non-destructive ion beam creation for mass spectrometry and has since been successfully employed as a deposition technique, used to get large organic molecules onto surfaces in UHV [110, 111].

Electrospray Process

The process of electrospray ionisation can be split into three steps: production of charged droplets, droplet size reduction by evaporation and disintegration, and production of gas phase ions.

Initially, a solution containing the molecule to be deposited is passed through a metal spray emitter needle of radius r (25-50 μm) using a syringe pump. This is positioned a distance d (1-3 cm) away from a grounded capillary tube, acting as the entrance to the UHV system. A high voltage, V, ($\sim$2 kV) is applied to the

needle creating a large electric field between the needle and the capillary, given by

$$E_c = \frac{2V_c}{r \ln\left(\frac{4d}{r}\right)}. \tag{3.12}$$

In the case of a positive bias, the induced electric field causes positive ions to migrate to the surface of the liquid where they accumulate at the end of the emitter needle. The build-up of charge leads to a repulsion of the ions and a Taylor cone is formed (see fig 3.8) [112].

For a sufficiently high electric field, the repulsion between ions is large enough to overcome the surface tension of the liquid, γ, and a fine jet containing ionised solvent and molecules is emitted from the end of the cone. The critical value of electric field at which this occurs can be calculated by

$$E_{crit} \approx \sqrt{\frac{2\gamma \cos(\theta)}{\epsilon_0 r}}, \tag{3.13}$$

where ϵ_0 is the vacuum permittivity, and θ is half the angle of the Taylor cone [113].

After emission, the jet breaks up into charged droplets. These reduce in size as the solvent evaporates while the charge remains constant. This has the effect of increasing the charge density within the droplet and results in an increased electrostatic repulsion force between ions. As more solvent evaporates, the repulsive force increases until the Rayleigh limit is reached where the electrostatic repulsion equals the cohesive force of the surface tension of the droplet. This limit is calculated by

$$Q_{Ry} = 8\pi\sqrt{\epsilon_0 \gamma R^3}, \tag{3.14}$$

where Q_{Ry} is charge, and R is the radius of the droplet [112].

Once the Rayleigh limit is exceeded the droplets undergo coulomb fission, releasing a jet of smaller droplets, each containing fewer ionised molecules. There are currently two proposed models for how individual charged molecules are released

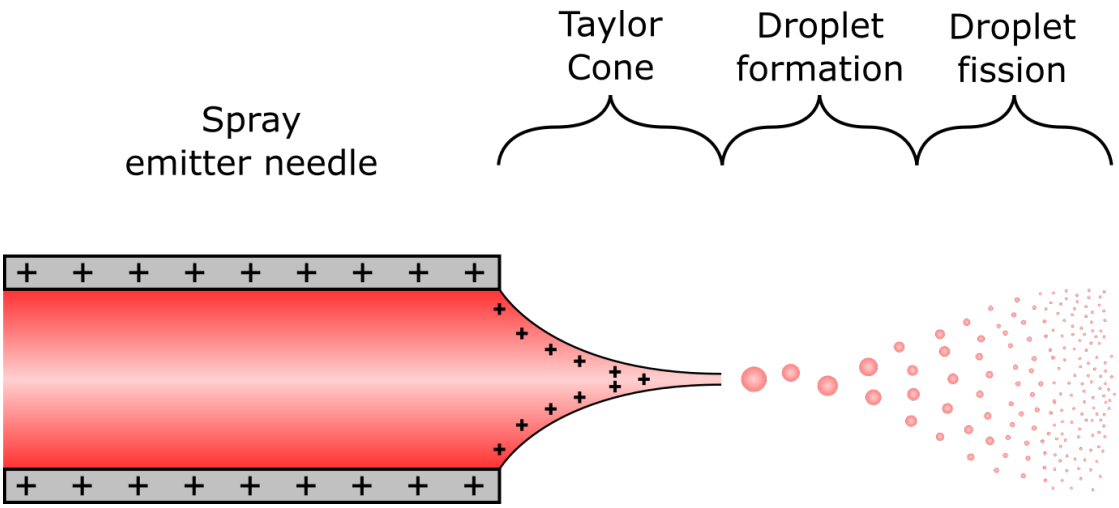


Figure 3.8: Diagram showing the process of electrospray ionisation to produce gas phase molecules. A solution of molecules is passed through an emitter needle. Applying a large positive bias causes positive ions to move to the emitter end and form a Taylor cone, where a fine jet of charged droplets is then emitted. These droplets decrease in size through solvent evaporation and subsequent coulomb fission, eventually leading to to the production of gas phase molecules.

from droplets into the gas phase. The first, proposed by Dole *et al.*[114] suggests that droplets undergo repeated coulomb fission until only a single molecule remains in a droplet. Further solvent evaporation then leads to the molecule entering the gas phase with the residual charge from the droplet. This is known as the charge residual model. The second model [115], known as the ion evaporation model, assumes coulomb fission repeats until the radii of droplets decreases to below a certain size (approximately 10 nm). After this point, ions can be emitted directly from the droplet into the gas phase in a process known as ion evaporation.

Electrospray deposition

The initial emission from the electrospray occurs at atmospheric pressure. However, at higher pressures, scattering of gas-phase molecules will occur, reducing the amount deposited onto the surface. Additionally, sample surfaces that are being deposited onto are kept in UHV conditions. To facilitate this, the ion beam is passed through several chambers that are pumped to successively lower pressures, in a process known as differential pumping. Each chamber is connected via a skim-

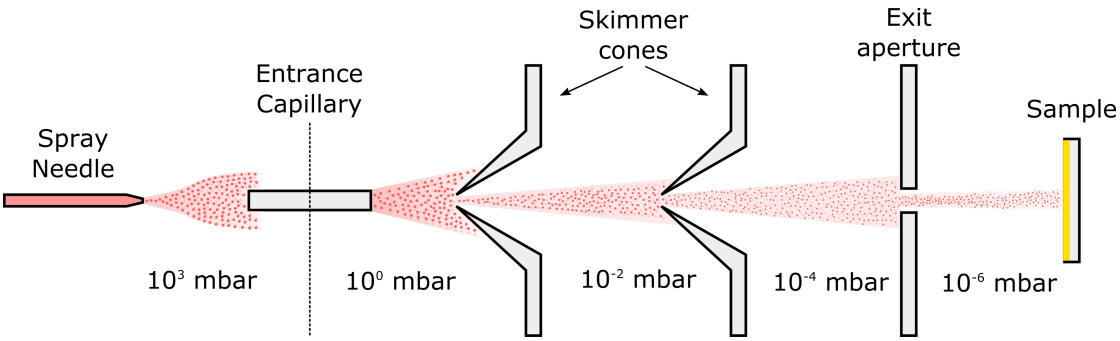


Figure 3.9: Basic apparatus for electrospray deposition system. After emission from capillary needle, the electrospray ion beam is passed through a series of chambers held at progressively lower pressures to reach a surface. The ion beam becomes finer as it passes through each section due to selection of forward travelling ions by skimmer cones. Adapted from [110].

mer cone, consisting of a cone with a small aperture . These allow molecules to pass between each differentially pumped section of the electrospray system, while maintaining the pressures in each. After entering a lower pressure section, the ion beam will expand. The skimmer cone selects only ions travelling through the middle of the chamber, ensuring the beam remains straight. The set up for a basic electrospray system is shown in figure 3.9 [110].

3.5 X-ray Photoelectron Spectroscopy

X-ray photoelectron spectroscopy (XPS) is a surface sensitive analysis technique used to identify elements and gain information about their chemical environment. This is achieved by exploiting the photoelectric effect to generate photoelectrons, from which information on the electronic state the electron originated from can be obtained [116].

In order to initiate the process, a beam of photons of energy $h\nu$ (where ν is photon wavelength and h is Planck's constant) are directed at a sample. Energy is transferred from incident photons to a core electron within an atom, and if the transferred energy is greater than the electron binding energy the electron may leave the surface. The photoelectron produced this way escapes with a kinetic

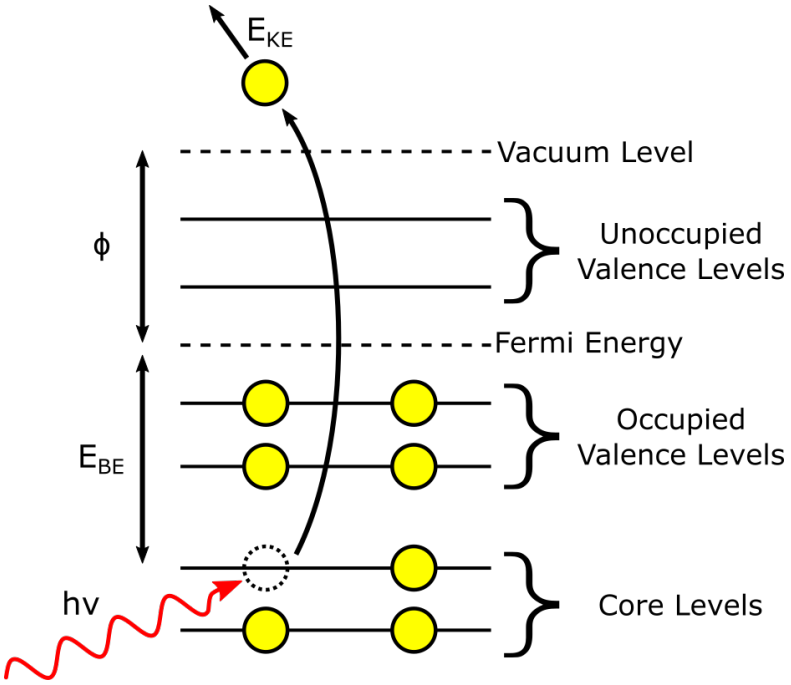


Figure 3.10: Schematic diagram for the generation of photoelectrons as employed within XPS measurements. High energy X-ray photons of energy $h\nu$ excite a core electron so that it is released from the atom with a kinetic energy E_{KE}. Measuring the kinetic energy of the released photoelectron can then be used to calculate the binding energy.

energy E_{KE}. Measuring this kinetic energy can then be used to calculate the binding energy, E_{BE}, of the state the photoelectron escaped from by

$$E_{BE} = h\nu - E_{KE} - \phi, \tag{3.15}$$

where ϕ is the work function for the photoelectron detector. This process is illustrated in figure 3.10. The binding energy of the electronic states are unique to each element. This means that binding energies of core states can be used to identify each element within the sample by comparing measured values to expected values.

Further to this, XPS measurements can be used to identify the specific chemical environment of an element [117]. Core levels of atoms can be perturbed by the presence of neighbouring atoms resulting in a chemical shift in binding energy. The amount of chemical shift is dependent on the properties of the neighbouring atoms. This means that a measured change in binding energy from an expected value for a particular element can be used to identify its chemical environment,

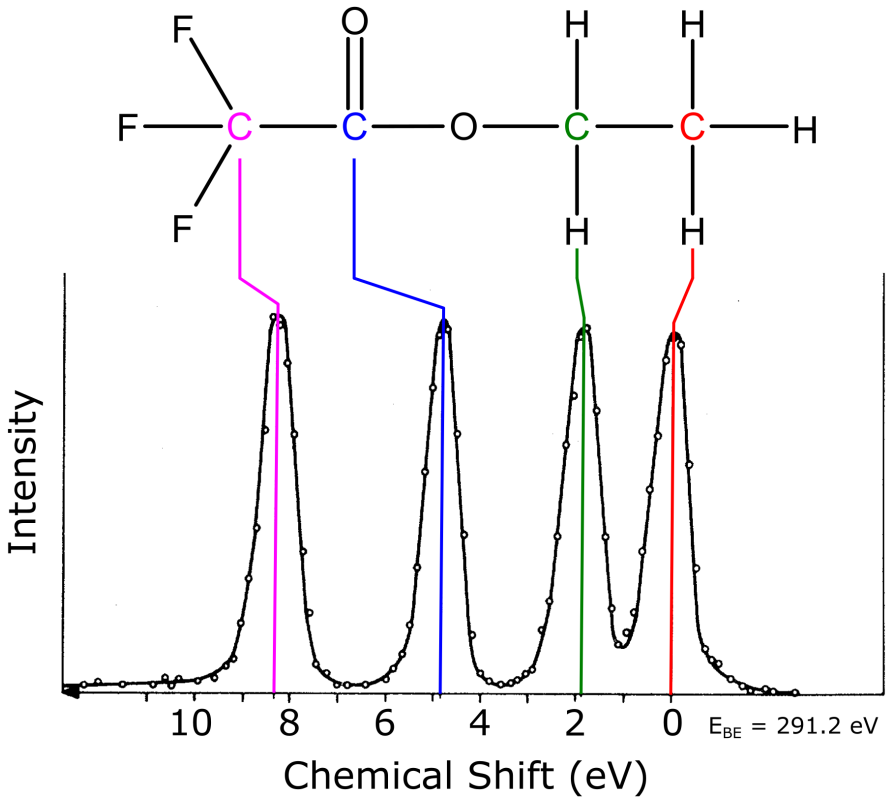


Figure 3.11: Example figure showing chemical shifts in XPS measurements due to different chemical environments of molecules. Ethyl trifluoroacetate (top) produces a C 1s XPS spectrum (bottom) with four distinct peaks at different binding energies, each associated with a different carbon environment in the molecule. Adapted from [117].

and hence determine the functional groups within molecules present on a sample. An example of this is shown in figure 3.11. XPS measurements for the C 1s orbital of ethyl trifluoroacetate (3.11 top) produce four distinct peaks in the spectra at different binding energies. The chemical shift associated with each of these peaks is due to the four distinct carbon environment within the molecule.

The photoelectrons produced during XPS have a low mean free path, meaning only photoelectrons produced near the surface of a sample will escape and be measured. This has the result that the vast majority of XPS signal is produced in the top layers of the sample, hence XPS is a surface sensitive technique. However, the short mean free path of photoelectrons means the signal can become attenuated between sample and detector. To reduce this effect, the majority of XPS measurements are performed in UHV conditions.

3.6 Normal Incidence X-ray Standing Wave

Normal incidence X-ray standing wave (NIXSW) is a chemically specific, surface sensitive analysis technique. NIXSW can be used as a local probe for determining the structure of molecules at a surface. This includes determining adsorbed geometries of atoms or molecules on a surface, which this section focuses on, but can also be used for investigating the epitaxial growth of materials. The process is based upon the chemical sensitivity of XPS and the X-ray diffraction properties of the substrate. Varying the wavelength of incident X-rays on the sample over a specified range produces a unique signal, dependent on both the chemical environment of the atom and location relative to the surface. From this data, information on the adsorption geometries of each chemical species on a sample surface can be determined. These types of measurements require a source of high energy, highly collimated X-rays with wavelengths that can be precisely varied. Because of this, NIXSW experiments can typically only be performed using synchrotron X-ray sources [118, 119].

3.6.1 Underlying Principles

At the heart of NIXSW is the generation of an X-ray standing wave, perpendicular to a set of substrate planes. Incident light with a specific wavelength, λ, is required to meet the Bragg condition,

$$n\lambda = 2d\sin\theta, \tag{3.16}$$

where d is the separation of the reflecting planes, θ is the angle of incidence and n is a positive integer. Due to the small interplanar separations, high energy X-rays are required to meet the Bragg condition and set up a standing wave.

Under this simplistic model a standing wave is only set up when the Bragg condition is exactly met. However this fails to account for multiple scattering events in the crystal where X-ray intensity becomes attenuated which leads to a finite penetration depth into the sample. This has the result that the standing

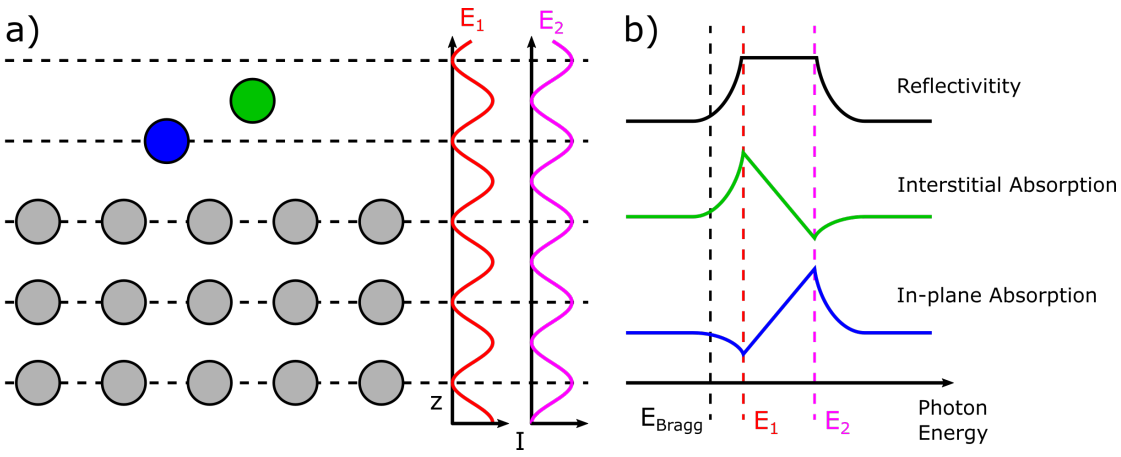


Figure 3.12: Diagrams showing the variation of X-ray absorption with position of atoms. (a) Two atoms are adsorbed at different positions above a bulk surface (grey), one atom in line with a bulk reflection plane (blue) and one interstitial atom (green), halfway between reflecting planes. Reflecting planes positions shown as dashed lines. Two example standing waves are shown, separated by a phase difference of π, with maximum (E_1, red) and minimum (E_2, pink) intensities at the reflection plane positions. (b) Variation of reflectivity (black) and X-ray absorption with intensity of interstitial (green) and in-plane (blue) atoms. Dashed lines show X-ray absorption for example standing waves, E_1 and E_2.

wave occurs over a finite range of incident wavelengths around the Bragg condition. Within this range, the reflectively is at its maximum value of unity. This flat top curve is known as a Darwin reflectivity curve and is shown in figure 3.12b (black). Of note is that over the course of this high reflectivity range, there is a phase change of π to the standing wave.

Consider the system shown in figure 3.12 where two atoms are adsorbed above a surface. Bulk surface atoms (grey) are located on reflecting planes (dashed lines), one adsorbed atom is in line with a bulk reflection plane (blue) and one interstitial atom (green) is halfway between reflecting planes. X-rays with energy E_1, corresponding to the lower energy region of the Darwin reflectivity curve, are incident on the surface. This generates a standing wave with nodes located at the reflection planes of the crystal (shown in (a) in red). Under these conditions, the atom at the bulk reflecting plane (blue) is located in an area with zero X-ray intensity, and therefore X-ray absorption for this atom will be will be zero. Sweeping through photon energies to the higher energy end of the reflectivity curve (E_2) produces a

phase shift of π to the standing wave (pink profile in (a)). This results in antinodes in the standing wave at the reflection planes and therefore maximum X-ray absorption for the blue atom. The opposite is true for the interstitial atom, with maximum X-ray absorption occurring at the lower energy (E_1) and minimum absorption at the higher energy (E_2). The X-ray absorption profiles for these two atoms are shown in figure 3.12b.

From this result, it can be seen that atoms at different distances from reflecting planes produce distinct X-ray absorption profiles. NIXSW absorption profiles can therefore be used to determine distances of atoms from reflecting planes and therefore the adsorption geometries of atoms on surfaces.

3.6.2 Measurement Process

Measuring X-ray absorption directly as part of NIXSW is non-trivial. This issue is often overcome by measuring photoelectrons emitted from core energy levels after absorption. The flux of photoelectrons can then be counted and used as a measure of X-ray absorption. An additional benefit to using photoelectrons is they can easily be used to determine the binding energy of the core level they were emitted from. Measuring the flux of photoelectrons with binding energy associated with different chemical shifts can therefore be used to determine absorption for atoms in specific chemical environments (as with to XPS measurements, see section 3.5). Alternatively, absorption can also be measured from signals associated with core hole decay after absorption has occurred by measuring Auger electrons.

3.6.3 Theoretical concepts

In order to use the X-ray absorption measurements to quantitatively determine the locations of atoms relative to the surface, the underlying theory needs to be understood. To do this, first assume the amplitude of incident X-ray flux to be 1. The intensity I of the Bragg standing wave at position z above the surface can be

then defined as modulus squared sum of incident and reflected waves,

$$I = \left| 1 + \frac{E_r}{E_0} \exp\left(-\frac{2\pi i z}{d} \right) \right|^2, \tag{3.17}$$

where E_r and E_0 are the incident and reflected wave amplitudes and d is the layer spacing of the sample. The wave amplitudes can then be used to define reflectivity R such that

$$\frac{E_r}{E_0} = \sqrt{R} e^{i\phi} \tag{3.18}$$

where ϕ is a phase factor. From this, equation 3.17 becomes

$$I = \left| 1 + \sqrt{R} \exp\left(i\phi - \frac{2\pi i z}{d} \right) \right|^2, \tag{3.19}$$

or equivalently

$$I = 1 + R + 2\sqrt{R} \cos\left(\phi - \frac{2\pi z}{d} \right). \tag{3.20}$$

This assumes a single position z for all absorbing atoms, whereas in reality atoms could be adsorbed in multiple different z locations. Additionally, thermal vibrations will lead to a small distribution of atomic positions, rather than a single location. Because of this, equation 3.20 needs to be generalised such that it can account for multiple adsorption sites. To do this, a function $f(z)$is assigned which describes the fraction of atoms at a position z over a range dz, such that

$$\int_0^d f(z) dz = 1. \tag{3.21}$$

From this, the standing wave intensity is given by

$$I = 1 + R + 2\sqrt{R} \int_0^d f(z) \cos\left(\phi - \frac{2\pi z}{d} \right) dz. \tag{3.22}$$

Resolving this integral gives the final description for standing wave intensity,

$$I = 1 + R + 2C_f \sqrt{R} \cos\left(\phi - 2\pi C_p \right), \tag{3.23}$$

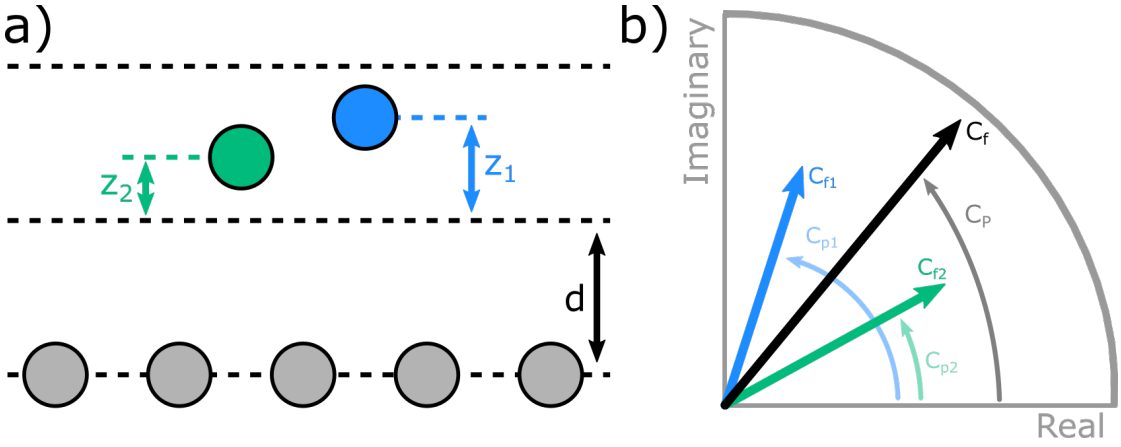


Figure 3.13: (a) Example system showing two atoms adsorbed at different heights z_1 and z_2 above a reflection plane (dashed lines). (b) Argand diagram showing coherent fraction (C_f) and position (C_p) values for the system shown in (a). Green and blue vectors represent coherent fraction and position of the two atoms. Resultant vector is shown in black. Vectors not to scale.

where C_f and C_p are the coherent fraction and coherent position respectively. These are two structural fitting parameters, representing a measure of the fraction of atoms at a particular position. In the special case of a single adsorption geometry, the coherent fraction is found to be 1 and the coherent position is simply the location of the atoms z divided by the layer spacing. More generally, These values are defined such that

$$C_f \exp\left(2\pi i C_p\right) = \int_0^d f(z) \exp\left(\frac{2\pi i z}{d}\right) dz. \tag{3.24}$$

The variation of absorption signal for each specific chemical environment with incident X-ray energy can be plotted, and equation 3.23 used to fit an absorption profile to the data. From this fitting, coherent fraction and position values can be extracted. Models of various absorption geometries can then be tested using equation 3.24 to determine which agree with measured C_f and C_p values. Repeating this for all chemical environments, a model of the adsorption geometry can be determined [119].

3.6.4 Using Coherent Fraction and Position Values

Figure 3.13a shows an example system of two different atom positions (z_1 and z_2) above a reflecting plane, separated by the layer spacing d. The fraction of the total number of atoms in the system at each position is given by C_{f_1} and C_{f_2}. The coherent fraction and position values for these two atoms are shown in 3.13b (green and blue) as vectors on an Argand diagram. This is a graph in complex space where C_f and C_p respectively correspond to r and θ values of the vectors in polar coordinates.

The total coherent fraction and position for the system can be calculated using equation 3.24, such that

$$\begin{aligned} C_f \exp\left(2\pi i C_p\right) &= C_{f_1} \exp\left(\frac{2\pi i z_1}{d}\right) + C_{f_2} \exp\left(\frac{2\pi i z_2}{d}\right) \\ &= C_{f_1} \exp\left(2\pi i C_{p_1}\right) + C_{f_2} \exp\left(2\pi i C_{p_2}\right). \end{aligned} \tag{3.25}$$

In figure 3.13b, this equates to vector addition of the component vectors of the system, giving a resultant vector (black).

3.6.5 Triangulation

Initial NIXSW measurements are typically performed using the same reflecting plane as the orientation of the surface. This can give information on the height of adsorbed molecules above the surface (although care must be taken to recall the heights are given relative to the projected planes of the bulk, not the surface atoms). However, in order to obtain information on the lateral adsorption of molecules, additional NIXSW measurements from different reflecting planes are required. Obtaining the distances of molecules from additional reflecting planes can then be used to determine a more exact adsorption geometry through a triangulation process.

Figure 3.14 shows an example of triangulation. In this example, several atoms (grey) are adsorbed above a (111) surface. Initial NIXSW measurements from the

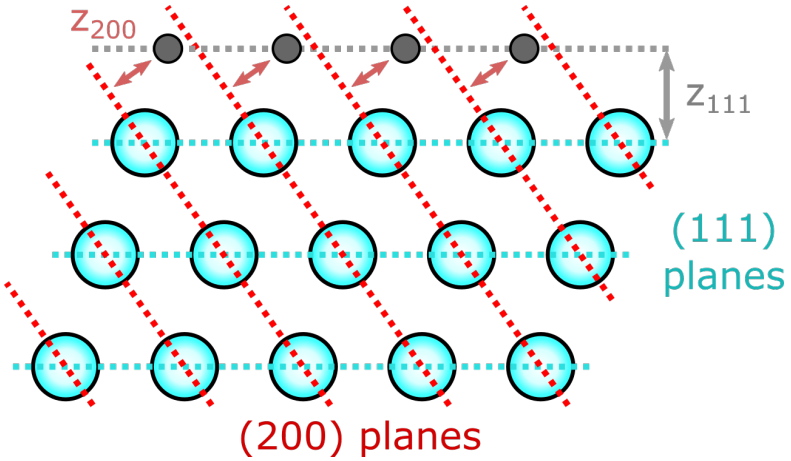


Figure 3.14: Diagram showing the the principles of triangulation for NIXSW analysis. NIXSW measurements are used to determine the distance of adsorbed atoms from two (or more) surface reflecting planes. Combining these distances can be used to develop a more complete model of adsorption geometries.

(111) reflection can be used to obtain the height (z_{111}) molecules are adsorbed above the surface. Further NIXSW measurements obtained from the (200) reflecting plane gives the separation of that plane and the molecules (z_{200}). This has a horizontal component that when combined with the adsorption height gives lateral information on the adsorption geometry of atomic species in a specific chemical environment.

3.6.6 Reflecting planes

Section 3.3 previously explained the use of miller indices to describe surface planes. Miller indices are similarly used here to describe the orientation of crystal plane used for reflection in NIXSW. Figure 3.15 shows the two reflecting planes used in experiments within this thesis: (111) and (200) planes. The plane orientations relative to a crystal unit cell and a (111) surface are shown. NIXSW measurements are used to measure the distance of atoms perpendicular to the reflecting plane. From these diagrams, it can be seen that the (111) reflecting plane will produce measurements of the heights of atoms above the surface, and the (200) plane can be used to gain information on the lateral positioning of atoms, as discussed previously.

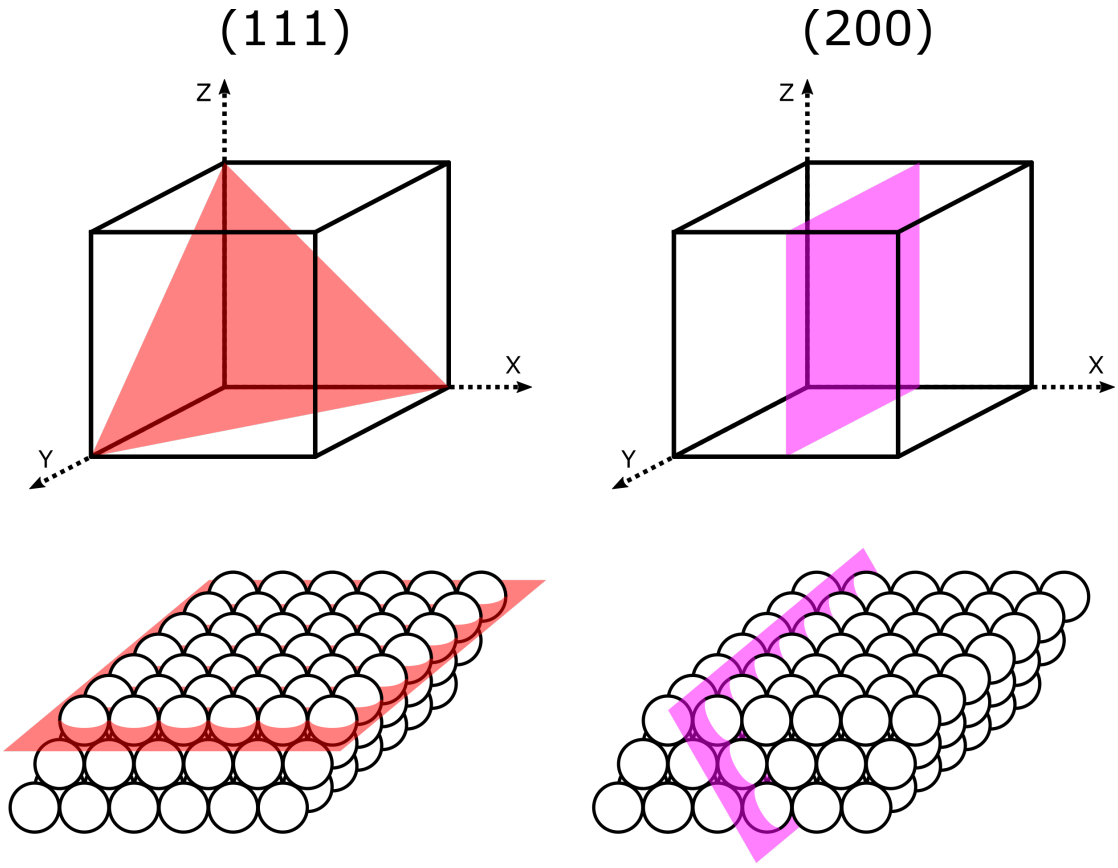


Figure 3.15: Diagram comparing the orientations of the (111) and (200) reflecting planes. Top figure shows the arrangements of different reflecting planes for a cubic unit cell. Bottom figure shows the relative arrangements of reflecting planes for a face centred cubic (111) surface.

Chapter 4

Ullmann Coupling Reactions on Ag(111) and Ag(110)

In this chapter experimental results are presented for the characterisation of structures formed at different stages of an Ullmann-coupling reaction using an iodine functionalised precursor molecule. This is compared for two surfaces, Ag(111) and Ag(110), with the substrate-molecule system investigated via STM. The precise geometries of overlayer structures formed on each substrate are found to differ, with differences driven by the registry of the structures with the underlying surface.

4.1 Introduction

As stated in chapter 2, on-surface synthesis based on the Ullmann coupling reaction is of interest due to its versatility. For example, a broad range of molecular species can be functionalised with halogen groups to facilitate on-surface reactions. However, the mechanistic process by which the metal-organic intermediate state is formed and converted to the covalent product is still debated. Several studies have attempted to address the problem, investigating the role of both the bulk chemistry [82] and topography of the surface [97]. Other factors, such as the influence of the co-adsorbed halogen species [43, 94] and reaction kinetics [120], on structure formation have also been studied. Here, investigations into the role of atomic

corrugation of the substrate with an on-surface coupling reaction are performed. Specifically, the relationship between the alignment of the intermediate and final structures with respect to the atomic lattice of the substrate is investigated.

Recent studies of 4,4"-dibromo-*m*-terphenyl on Cu(111) [42, 77] and Cu(110) [78] have shown the formation of intermediate metal-organic structures at room temperature. After heating the substrates, covalently bonded structures were observed. These structures included zigzag chains and closed hexagonal rings, both before and after annealing. Here, a related iodine terminated molecule (figure 4.1) is studied on silver substrates, investigating how the structure of the surface affects the formation of intermediate and final products; with emphasis on the templating effect of the surface.

4.2 Metal-Organic Intermediate Structures

This investigation focuses on the molecule 4,4"-diiodo-*m*-terphenyl (DITP), shown in figure 4.1. The molecule consists of three phenylene rings, with the outer aryl groups bonded at the *meta* positions of the central ring and functionalised with iodine. Following deposition of DITP onto silver substrates, iodine dissociates from the molecule (cleavage of the C-I bond), leading to the formation of C-Ag-C coordination bonds between molecules. This creates a metal-organic (MO) intermediate structure. Annealing at 460 K then leads to the removal of linking silver atoms and the formation of a covalently bonded structure. Dehalogenated units within MO and covalently bonded structures are denoted as *m*-terphenyl (TP). The following sections detail an STM based characterisation of the molecular overlayer at various stages of the on-surface reaction. Comparisons between metal-organic structures formed on the Ag(111) and Ag(110) surfaces are made before moving on to comparing covalent products on both surfaces.

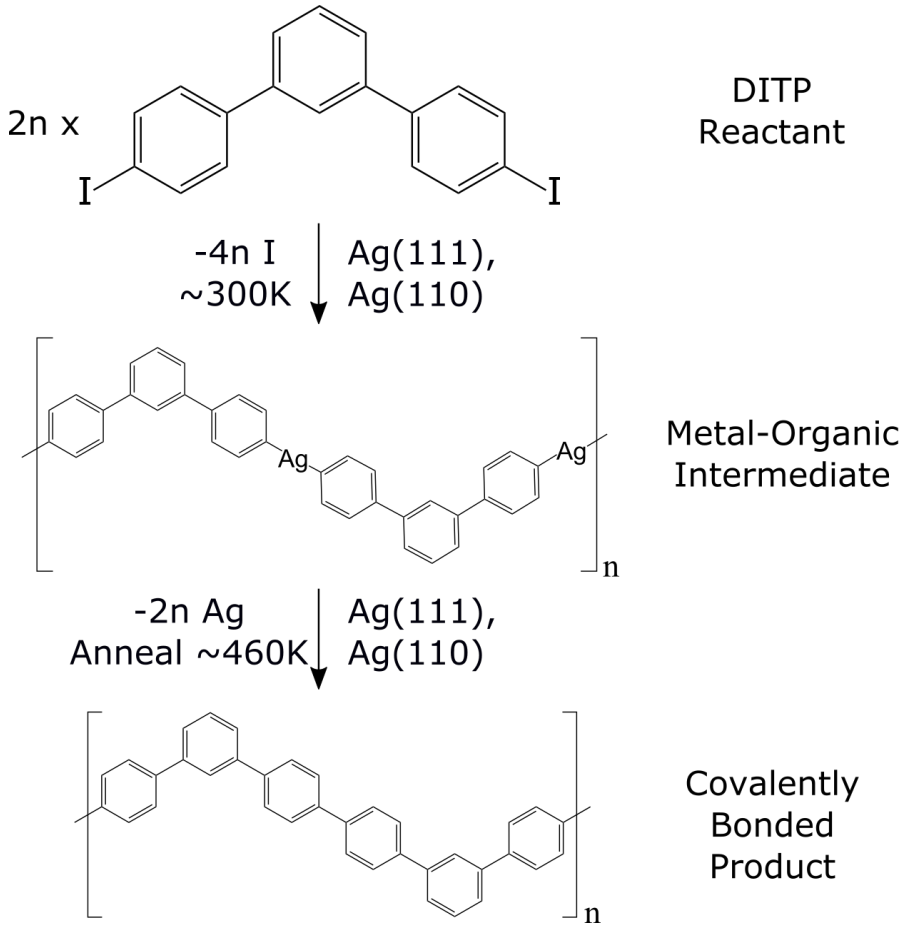


Figure 4.1: Reaction pathway for 4,4"-diiodo-*m*-terphenyl (DITP). Deposition onto Ag(111) or Ag(110) surfaces at 300K, results in iodine dissociation and formation of a metal-organic intermediate structure. After annealing the surfaces at 460 K Ag atoms are eliminated from the intermediate, creating covalent bonds between molecular subunits.

4.2.1 Ag(111)

Initially, DITP was deposited onto a clean Ag(111) surface by exposing it for 5 minutes to the flux from a knudsen cell, heated to 130°C, resulting in sub-monolayer coverage. Previous studies have shown that similar molecules undergo dissociation of their halide groups upon deposition onto metal surfaces [42] and it is expected that DITP will behave similarly on silver.

Small islands of molecules were observed to form on the surface, as shown in figure 4.2a. Islands appear as arrays of periodic circular bright features, with each feature attributed to three phenylene rings (DITP after dissociation of iodine, or TP), similar to previously observed results [77]. The blurred edges of the island, seen in the top left of figure 4.2a, suggest that molecules are readily diffusing across

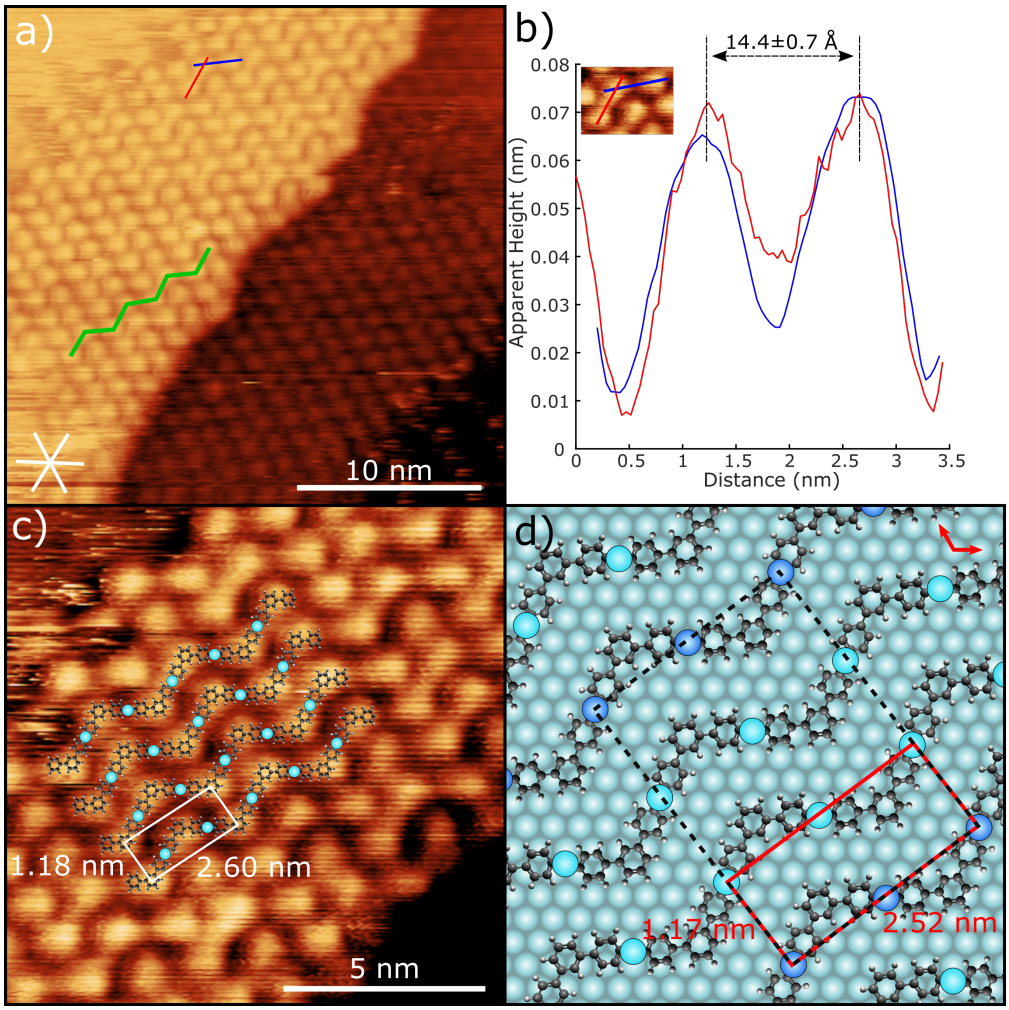


Figure 4.2: a) STM image of Ag(111) surface after deposition of DITP, including approximate crystallographic directions of the surface lattice. Zigzag structure shown in green ($V_{sample-bias}$ = -1.5 V, $I_{set-point}$ = 5.0 pA). (b) Average of 10 line profiles taken along the different directions of the zigzag (red and blue lines shown in (a) and inset). Intermolecular separation is consistent with a metal-organic structure. (c) Close-up of the TP island in (a) with adsorption model and dimensions overlaid ($V_{sample-bias}$ = 1.0 V $I_{set-point}$ = 5.0 pA). (d) Adsorption model for TP on Ag(110) with overlaid molecular lattice (red), commensurate overlayer structure (black dashed) and surface lattice vectors (top right). Light blue silver adatoms rest in three-fold hollow sites, dark blue in atop sites.

the surface, with continuous attachment/detachment at the island periphery. A series of images were taken of this area over a 20 minute period and showed the edge of the island growing and shrinking as molecules detached then rejoined. Furthermore, it was observed that STM images acquired at higher current set points (>10 pA) could disrupt island structures. This is indicative that the molecules are only weakly bound to the surface and can easily move due to diffusion and tip

interactions.

Based on the symmetry of the molecule, the formation of zigzag patterns is expected, highlighted in green in figure 4.2a. To investigate this, several line profiles were acquired over the expected zigzag directions, indicated by red and blue lines in figure 4.2a. The averages of these line profiles are shown in figure 4.2b. Both profiles appear to have the same form, showing two clearly distinguishable peaks separated by 1.44 ± 0.07 nm. This is much greater than the separation of 1.29 nm for four covalently linked phenylene rings that is anticipated for the linear component of a covalently coupled structure [80]. This suggests that iodine has dissociated from the DITP molecules, with molecules now forming extended metal-organic structures, linked together through C-Ag-C bonds. The STM data does not exhibit topographic features at the expected location of the Ag atoms. However, this occurrence has been observed for similar metal-organic systems [83], and due to the known convolution of topographic and electronic structure in STM measurements, cannot be used to characterise the height of the Ag atoms relative to the surface.

Islands of molecules were found to consist of a series of parallel zigzag chains, with the long axis length of the chain oriented at approximately 35° to the $[0\bar{1}1]$ high symmetry direction of the surface, as shown in figure 4.2a. The zigzag pattern is also measured to have a period of 2.60 ± 0.07 nm, with the separation of neighbouring chains found to be 1.18 ± 0.07 nm (figure 4.2c); defining the dimensions of the molecular lattice.

The spatial arrangement of the zigzag pattern and its angle relative to the crystallographic directions of the surface lattice have been used to form an adsorption model for TP on Ag(111). This is shown in figure 4.2c, overlaid on a close-up of the molecule island seen in figure 4.2a. The proposed molecular arrangement agrees well with the STM images, with circular bright features corresponding to TP and the regions between them to silver adatoms. Figure 4.2d shows the adsorption model of TP on the Ag(111) surface, which is in agreement with estimated lattice

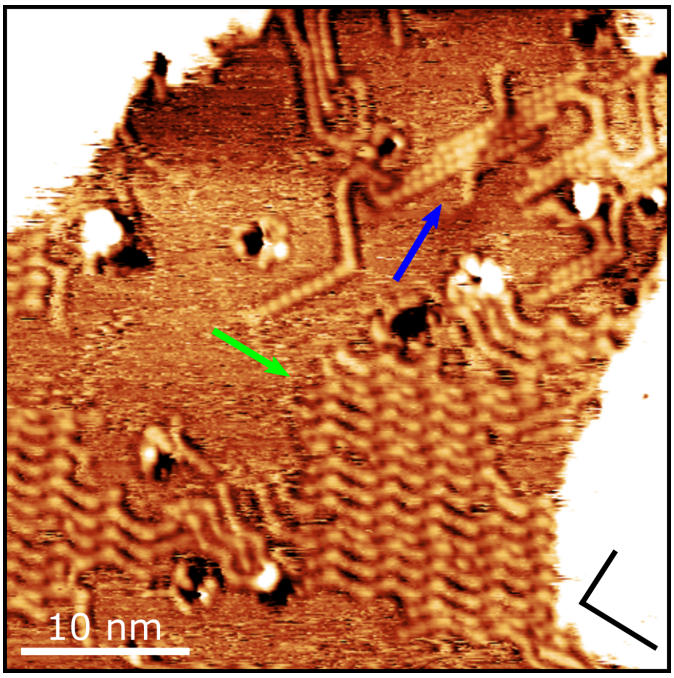


Figure 4.3: (a) STM image of the Ag(110) surface after deposition of DITP. Islands of TP in a zigzag structure (green arrow) as well as islands of iodine (blue arrow) are present. Lattice directions are shown in the bottom right ($V_{sample-bias}$ = 1.8V, $I_{set-point}$ = 100 pA).

directions, with the molecule structure commensurate with the surface. The experimentally measured period and separation of the zigzag pattern (2.60 ± 0.07 nm $\times$ 1.18 ± 0.07 nm) also agrees with the molecular lattice predicted by the adsorption model (based on ideal Ag(111) dimensions and molecular mechanics calculated structure for DITP). However, silver adatoms in different chains are predicted to rest alternately in atop and three-fold hollow sites. Thus, the unit cell for the molecular lattice is different to that of the commensurate overlayer structure.

4.2.2 Ag(110)

In order to investigate the effect of substrate topography on molecular arrangement, the deposition of DITP was repeated onto a Ag(110) surface. This surface possesses two-fold rotational symmetry, as opposed to the three-fold symmetry of the Ag(111) surface and it is therefore expected that alternative structures will be stabilised.

Figure 4.3 shows an STM image of the Ag(110) surface after DITP deposition.

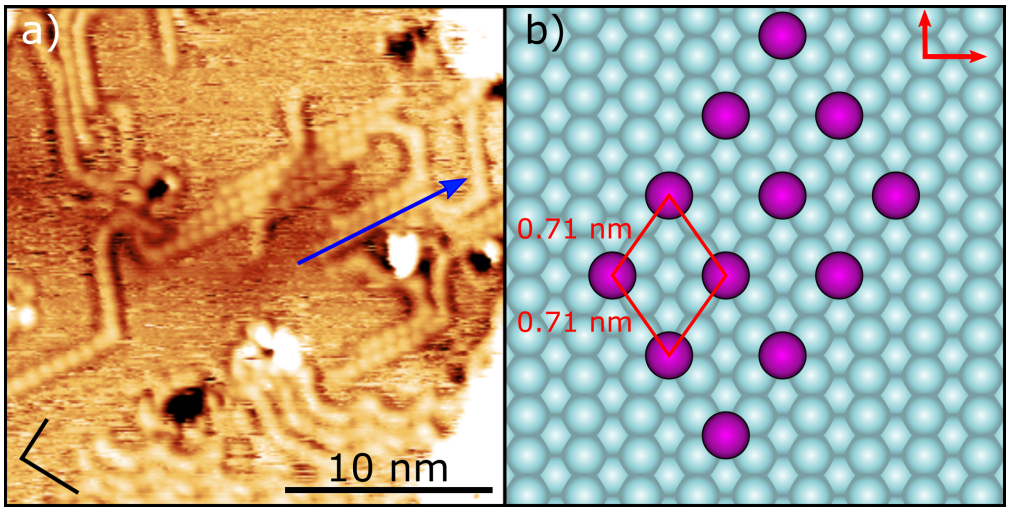


Figure 4.4: (a) STM image of an island of iodine on the Ag(110) surface before annealing, indicated by the blue arrow. Surface lattice directions are overlaid ($V_{sample-bias}$ = 1.8 V $I_{set-point}$ = 100 pA). (b) Proposed adsorption model for iodine on Ag(110) surface lattice, based on observed separation of features and their orientation relative to underlying surface lattice.

Bright circular features were observed, connected by dimmer areas to form islands of parallel zigzag chains, similar to those observed on the Ag(111) surface. Two different domains of the zigzag are present, with the direction of the chains approximately ±20° to the [001] lattice direction. This is expected due to the mirror symmetry about the [001] direction and similar results have been observed for molecular domains on Cu(110) substrates [78].

An additional structure is present on the surface following deposition of DITP (indicated in figure 4.3 with a blue arrow). This consists of close-packed rows of circular features separated by 0.72 ± 0.08 nm. Rows are oriented at approximately 30° to the $[1\bar{1}0]$ lattice direction. A close-up of the structure is shown in figure 4.4a. These features were observed to be highly mobile, with the diffusion of mobile species leading to rearrangement of the structure over several STM image cycles. These features are assigned to iodine adsorbed to the surface; in agreement with the assertion that iodine has dissociated from the DITP molecules after deposition onto the Ag(110) surface. The dimensions of these structures are consistent with iodine adsorbed at alternate four-fold hollow sites on the Ag(110) lattice and figure 4.4b shows a suggested adsorption model for this.

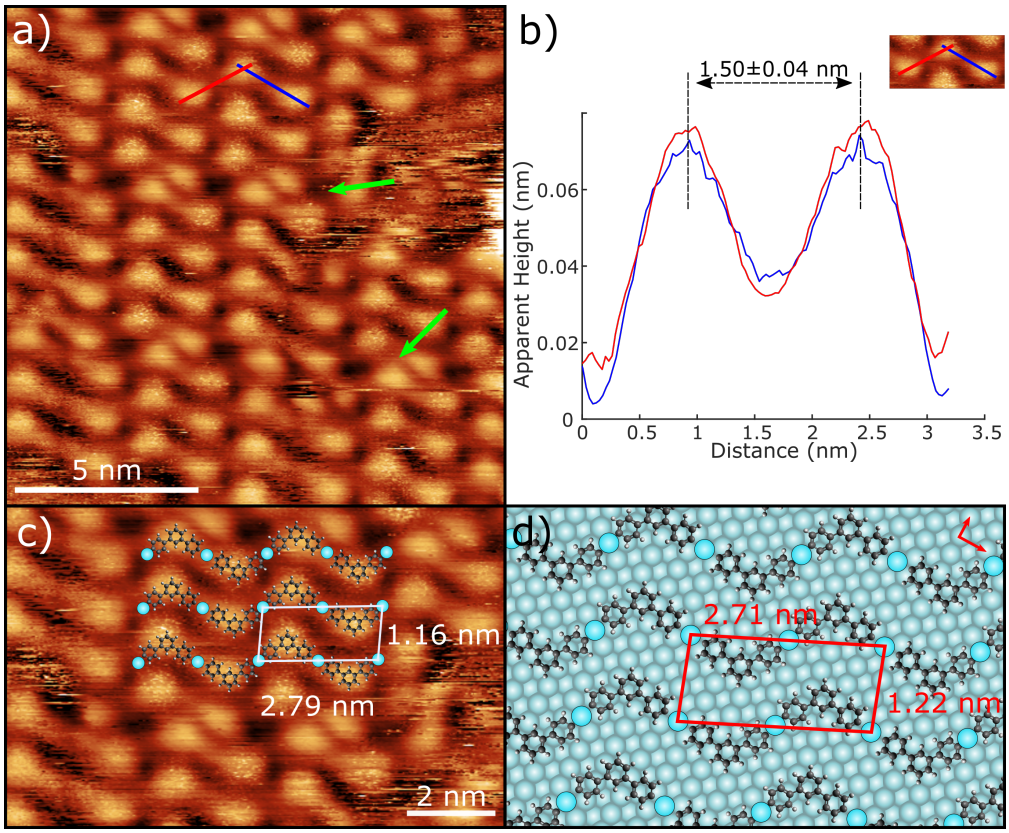


Figure 4.5: (a) Close-up of TP island shown in 4.3. Green arrows show areas of disorder in the island ($V_{sample-bias} = 1.0$ V $I_{set-point} = 50$ pA). (b) Average of 10 line profiles taken along the different zigzag line sections (red and blue lines in (a) and inset). Molecule-molecule separation is consistent with proposed metal-organic structure. (c) Close-up of metal-organic structure with overlay of proposed model and measured dimensions ($V_{sample-bias} = 1.0$ V $I_{set-point} = 50$ pA). (d) Adsorption model for TP on Ag(110) with overlaid molecular lattice (red) and surface lattice vectors (top right).

Figure 4.5a shows a close-up of the island of molecules in figure 4.3, indicated by the green arrow. The island consists of several domains of zigzag chains, slightly displaced relative to each other, leading to the formation of domain boundaries and causing disorder within the island (indicated with green arrows). Bright circular features at the vertices of the zigzags appear to be TP units. These features are separated by 1.50 ± 0.04 nm. Similar values (1.57 ± 0.06 nm [83]) have been observed previously for metal-organic structures on Ag(110), suggesting metal-organic structures containing a single Ag adatom are observed here. Several line profiles were taken of the zigzag pattern and their averages are shown in figure 4.5b. The overall shape of the line profiles and the peak separation are very similar to that seen on Ag(111), suggesting that TP units are forming metal-organic bonds

with silver adatoms.

An adsorption model for this arrangement of molecules is proposed based on measurements of feature dimensions and angles relative to the silver surface (figure 4.5c). The model agrees well with the STM data, with TP and silver adatoms corresponding to circular bright features and the areas linking them respectively. The period of the zigzag chain was measured to be 2.79 ± 0.04 nm and the separation of chains 1.16 ± 0.04 nm (figure 4.5c). The separation of zigzag chains is consistent with observations on the Ag(111) surface (1.18 ± 0.07 nm), whereas the zigzag period is noticeably larger, by approximately 0.2 nm. The differences in size of the molecular lattices on each surface can most likely be attributed to elongation of the C-Ag bonds between molecules, facilitating a better registry with the different surface lattices. The differences between the dimensions seen in the molecular lattice is also greater than that observed for the zigzag structures formed from similar molecules on Cu(111) [77] and Cu(110) [78], where the difference was found to be ~ 0.15 nm. This highlights the effects of different surfaces on structure formation.

Figure 4.5d shows the proposed adsorption model for TP on the Ag(110) surface. It can be seen that the model is commensurate with the surface, with the silver adatoms resting in four-fold hollow sites and TP units spaced evenly between them. The measured separation and period for the zigzag arrangement also agrees well with the predicted dimensions of the molecular lattice.

4.3 Covalently Coupled Products

Following previous methodologies [41, 78], the covalently coupled products were obtained by an additional thermal annealing step, heating samples to 460 K. Examples of the resulting structures for the Ag(111) and Ag(110) surfaces are shown in figure 4.6a and c, respectively. In both cases, islands of molecules consisting of parallel chains in a clear zigzag pattern were observed. The zigzag structures exhibit a constant apparent height along their length, with no individually resolved features (as opposed to the clearly distinguishable circular features of the metal-

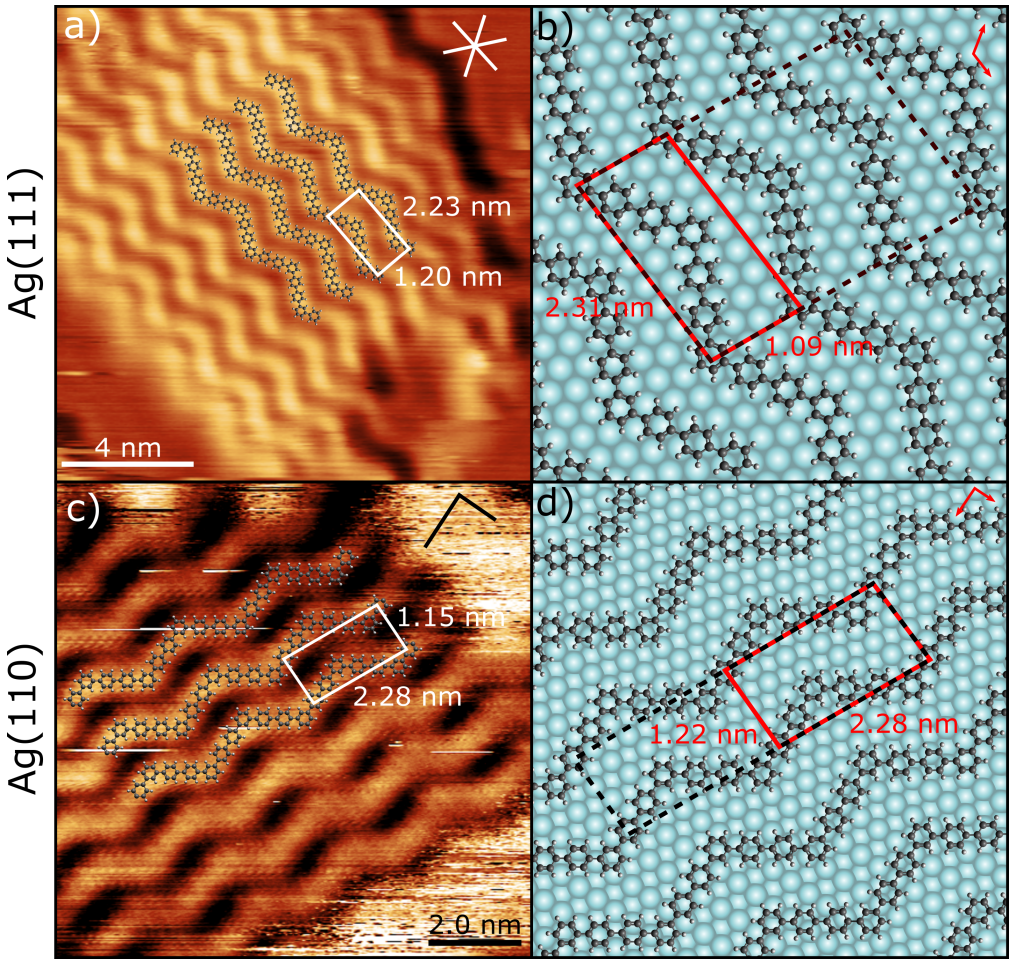


Figure 4.6: (a) STM image of the annealed Ag(111) surface seen in figure 4.3. Overlaid are the TP adsorption model, structure dimensions and lattice vectors of the surface. ($V_{sample-bias}$ = -1.0 V $I_{set-point}$ = 5.0 pA). (b) Adsorption model for TP on Ag(111) after annealing at 460 K with overlaid molecular lattice (red), commensurate overlayer structure (black dashed) and surface lattice vectors (top right). (c) STM image of annealed Ag(110) surface seen in (a) with overlaid adsorption model, structure dimensions and surface lattice vectors ($V_{sample-bias}$ = 1.5 V $I_{set-point}$ = 5.0 pA). (d) Adsorption model for TP on Ag(110) after annealing at 460 K with overlaid molecular lattice (red), commensurate overlayer structure (black dashed) and surface lattice vectors (top right).

organic structure observed prior to heating). Similar to the structures observed prior to annealing, two different zigzag domains were present on the Ag(110) surface, oriented at ±20° to the [001] surface lattice direction. The period of the zigzag was found to be 2.23 ± 0.05 nm for the Ag(111) surface and 2.28 ± 0.05 nm for Ag(110), smaller than the that observed for the metal-organic structures (2.60 ± 0.07 nm on Ag(111) and 2.79 ± 0.04 nm on Ag(110)). The separations between the chains were found to be 1.20 ± 0.05 nm and 1.15 ± 0.05 nm for Ag(111)

and Ag(110) respectively, which are consistent with chain separation measurements before annealing.

The very similar values for the repeat unit along the zigzag domain on both annealed substrates suggests the same structure has formed on both surfaces. Additionally, both repeat units are significantly smaller than those observed for each structure prior to annealing. Due to the lack of resolvable features, and the apparent shortening of chains, it is suggested that silver atoms have been eliminated from the TP monomer units, leading to the formation of covalent bonds. Adsorption models for the annealed samples are proposed and are shown overlaid on examples of the zigzag islands in figure 4.6a and 4.6c. In both cases, the modelled molecular chains agree well with STM images of the structures.

Figure 4.6b shows the proposed adsorption model on the Ag(111) lattice. As for the sample prior to annealing, the vertices of the zigzag on different chains alternate between atop and three-fold hollow sites. The model agrees well with the measured period and separation of the zigzag.

It is interesting to note that for the commensurate overlayer structure, zigzag chains are oriented differently before and after annealing the surface. Prior to annealing, the chain is $\sim$30° to the $[0\bar{1}1]$ direction, whereas after annealing, it runs parallel to this crystallographic axis. This shows that the zigzag structures have undergone a significant rearrangement, indicating that the mechanism for covalent coupling is not simply removal of Ag atoms but significant molecular displacement is also involved. This structural alteration is likely to be driven by the reduction in surface free energy associated with maintaining a commensurate structure in both the metal organic intermediate and covalently bonded states. However, this is in contrast to previous measurements of zigzag structures on Cu(111) [77], where no significant reorientation is observed, showing the influence of surface chemistry on structure formation.

The adsorption model for TP chains on the Ag(110) surface is shown in figure 4.6d. Molecules are aligned to the lattice such that one arm of the zigzag is almost

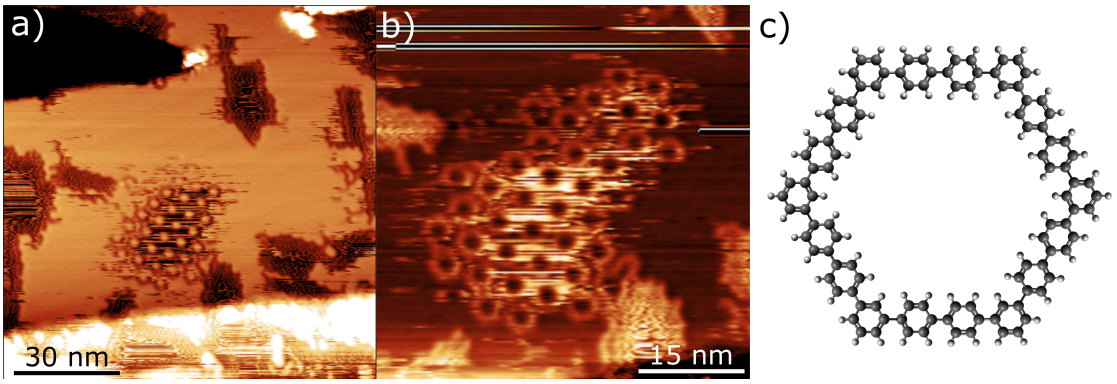


Figure 4.7: (a) STM image showing the hexagonal structures observed on the Ag(111) surface after annealing. ($V_{sample-bias}$ = -1.0 V $I_{set-point}$ = 5.0 pA). (b) Close-up of island of hexagonal structures. Image colouring is inverted for clarity ($V_{sample-bias}$ = -1.0 V $I_{set-point}$ = 5.0 pA). (c) Predicted molecular model for hexagonal macrocycles.

parallel (<5°) to the [001] direction. This is a similar arrangement to the model before annealing, and shows molecules have not needed to reorientate significantly after heating to be commensurate with the surface, in contrast to the large change in orientation observed for the Ag(111) surface. Similar results have been observed previously for Cu(110) annealed zigzag structures [78]. The two centre rings on the parallel arms of the zigzag rest alternately in four-fold hollow and long bridge sites on the lattice.

It should be noted that a small number of additional structures were also seen on the Ag(111) surface after annealing. Figure 4.7a shows an island consisting of an array of bright circular features, separated by 3.2 ± 0.2 nm with rows at an angle of ∼60° relative to each other. These features are attributed to an island of close packed hexagonal structures imaged in an inverted contrast mode, with circular bright features corresponding to the centres of each hexagon. Figure 4.7b shows a close-up of the same area, with the image colouring inverted. Hexagonal structures can clearly be seen at the edges of the island. These highly mobile features are difficult to image and were only observed once on the Ag(111) surface after annealing. A predicted molecular model for these structures is shown in Figure 4.7c. Similar structures have been observed previously on (111) metal surfaces [77, 85]. The study on a silver surface however was performed at 78 K or

	Experimental data [a]		Adsorption model [b]	
	Zigzag period (nm)	Inter-row separation (nm)	Zigzag period (nm)	Inter-row separation (nm)
Ag(111)	2.60 ± 0.07	1.18 ± 0.07	2.52	1.17
Ag(110)	2.79 ± 0.04	1.16 ± 0.04	2.71	1.22
Annealed Ag(111)	2.23 ± 0.05	1.20 ± 0.05	2.31	1.09
Annealed Ag(110)	2.28 ± 0.05	1.15 ± 0.05	2.28	1.22

Table 4.1: Comparison of STM Image Measurements and Adsorption Model Unit Cells.
[a] Values for zigzag dimensions are based on repetitions seen in structures in the STM images.
[b] Adsorption model distances are calculated based on the unit cells of the silver lattice and molecular overlayer.

lower, suggesting that there may be more hexagonal structures on the surface, but they are diffusing too rapidly to be observed at room temperature.

Table 4.1 shows a comparison of the measured directions for the observed structures. For both substrates, before and after annealing, the separations between zigzag chains (inter-row separations) are the same within error. This is possibly due to iodine atoms resting between the chains, causing them to maintain a constant separation. Similar observations were made on both Cu(111) [42] and Cu(110) [78] where it was proposed that assembly of islands from the zigzag chains was assisted by bromine adatoms forming hydrogen bonds with the chains, helping to stabilise the structure. Additionally, both the Ag(111) and Ag(110) annealed samples have very similar periods, whereas prior to annealing significant variation between zigzag period for Ag(111) and Ag(110) was observed. This is likely due to the limited variation in lengths achievable by the C-C bonds in the covalently bonded structures formed after annealing, in contrast to the greater degree of flexibility between TP molecules, facilitated by metal-organic bonds. This variation in bond length allows molecules to adopt energetically favourable positions, potentially allowing a greater diversity of structures, dependent on the surface chosen.

4.4 Surface Lattice determination

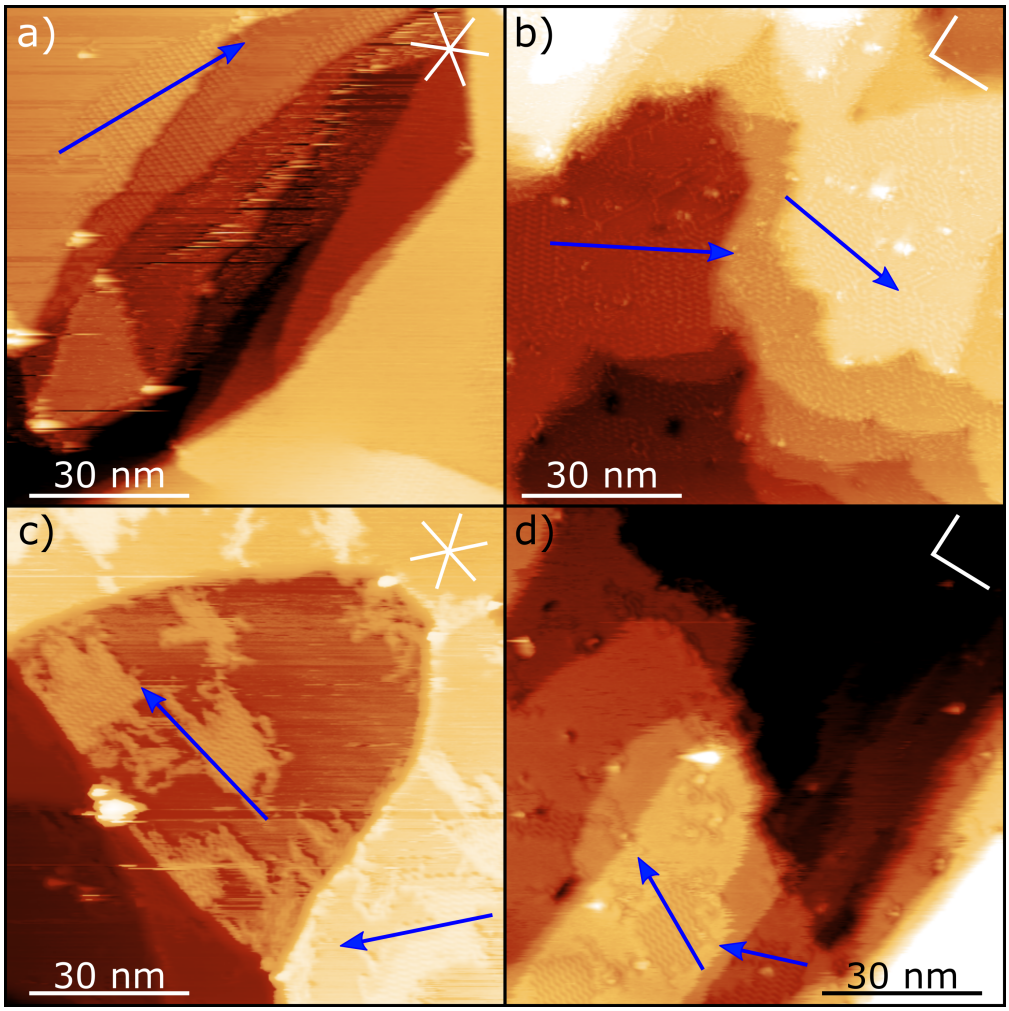


Figure 4.8: STM images showing directions of zigzag chains (blue arrows) relative to surface lattice vectors. In each case, surface lattice directions were obtained from the directions of flat step-edges and are shown in white. (a) Ag(111) surface before annealing ($V_{sample-bias}$ = -1.5 V $I_{set-point}$ = 5.0 pA). (b) Ag(110) surface before annealing. Two differently oriented domains are observed at ± 20° to the [001] lattice direction ($V_{sample-bias}$ = 1.8 V $I_{set-point}$ = 100 pA). (c) Ag(111) surface after annealing. Two different island domains are observed with chains parallel to one surface lattice direction ($V_{sample-bias}$ = -1.0 V $I_{set-point}$ = 5.0 pA). (d) Ag(110) surface after annealing. Two differently oriented domains are observe at ± 20° to the [001] lattice direction ($V_{sample-bias}$ = 1.5 V $I_{set-point}$ = 5.0 pA).

Within this experiment, in order to develop adsorption models for TP, the angles that structures adsorbed relative to the surface needed to be determined. Large overview images of the surface containing several islands of molecules were used to determine the direction of the surface lattice. From these overviews, the directions of step-edges were assumed to be aligned along the high-symmetry crystallographic

directions of the surface (in the same direction as the underlying surface atoms). The orientation of zigzag chains relative to the surface was then determined by measuring their angles relative to the surface step-edges.

Figure 4.8 shows example overview images for the Ag(111) and Ag(110) surfaces before and after annealing. Blue arrows indicate the direction of zigzag chains in islands of TP. These images were used to determine the directions of the underlying surface lattice. For Ag(111), there are typically three step-edges, oriented at 60° to each other, which were assumed to follow the directions of the surface lattice. Similarly, for the Ag(110) surface, the majority of straight step-edges follow the [110] direction, and this was used to determine the lattice directions.

4.5 Conclusions

The on-surface Ullmann-type coupling reaction has been demonstrated for 4,4"-diiodo-*m*-terphenyl (DITP) on Ag(111) and Ag(110) surfaces. Deposition onto these surfaces at room temperature causes dissociation of iodine, followed by the formation of metal-organic structures, via bonding with Ag adatoms on the surface. In both cases, islands of parallel zigzag chains are formed. Adsorption models for molecules on each substrate were proposed and showed C-Ag-C bonds stretch to allow the formation of commensurate structures on Ag(111) and Ag(110), producing different sized structures on each surface.

Annealing of the surfaces at 460 K results in removal of Ag adatoms from the structures and the formation of covalently-bonded continuous zigzag chains. It was found that on Ag(111) the resulting poly(*m*-phenylene) chains undergo a rotation of approximately 30° relative to the surface lattice, in order to achieve commensurability with the surface. This is in contrast to the Ag(110) surface where no rotation was observed, or required, to achieve commensurability. These results clearly demonstrate the influence of substrates on the formation of covalently-coupled structures on surfaces, and that the relationship between orientation of the intermediate and final state may assist transit along the reaction pathway.

The adsorption models presented for the structures in this experiment rely on inferring crystallographic directions from surface features. However, it is worthwhile to note that there is an inherent degree of ambiguity involved in developing molecular adsorption models based upon STM data where molecules and atomic lattices were not observed simultaneously. These ideas are therefore expanded on in chapter 5 where measurements from additional techniques (XPS and NIXSW) are used in conjunction with STM data to develop more detailed adsorption models.

Chapter 5

X-ray standing wave based structure determination

In this chapter, a combination of NIXSW and STM characterisation is used to determine the three-dimensional adsorption geometries for two molecular precursors on Ag(111) at different stages of the Ullmann-coupling reaction. The adsorption heights of molecules are initially determined utilising the (111) reflection for NIXSW measurements. This is used to demonstrate the important role of Ag adatoms within the Ullmann-type reaction. Subsequent NIXSW measurements from the (200) surface reflection, combined with high-resolution STM measurements, are then used to determine lateral adsorption geometries for both molecules.

5.1 Introduction

A consequence of confining reactions to a substrate is the transition from the 'three-dimensional' reaction volume of solution phase synthesis to a quasi-two-dimensional platform. This new environment has the potential to facilitate alternative reaction pathways to those available in solution. To fully utilise this alternative environment, a detailed understanding of the underlying mechanistic processes underpinning these reactions is required.

STM has been the predominant characterisation technique for such systems.

The sub-angstrom lateral resolution and real-space imaging abilities has facilitated study of the initial, intermediate, and final states of on-surface reactions, even down to the level of individual bond formation in the case of the related non-contact atomic force microscopy technique [121, 122]. However, the family of SPM techniques lack detailed chemical specificity, compared to X-ray photoelectron spectroscopy (XPS) based techniques, and do not facilitate accurate characterisation in terms of molecular adsorption heights [123]. Specifically, accurate structural characterisation of adsorption geometry and molecular conformations is required to provide information on details of the underlying reaction mechanism.

Studies of Ullmann-type coupling utilising XPS have provided information on the chemistry of the molecular structures at various stages of the reaction [79], and time-resolved XPS studies have allowed the reaction kinetics of an on-surface process to be probed [43, 120]. These studies provide useful information, but questions remain as to the role of surface adatoms within the reaction as well as the evolution of the conformation of the molecular species during the reaction.

In this chapter it is demonstrated that, by combining the exceptional lateral resolution of STM with the chemical sensitivity of X-ray standing wave (XSW) structure determination using photoelectron detection [118, 119], it is possible to characterise molecular conformations and adsorption geometries within an on-surface covalent coupling reaction. In addition, the role of metal adatoms within the reaction mechanism is determined, evidenced by the structure of the intermediate state of the Ullmann coupling reaction of two molecular species on Ag(111).

This study presents the characterisation of two molecules, DITP (discussed in chapter 4 and 1,3,5-tris(4-iodophenyl)benzene (TIPB), both of which possess aryl rings functionalised at the periphery with C-I groups to facilitate Ullmann coupling reactions when deposited upon a Ag(111) substrate (chemical structures shown in figure 5.1a and b). As stated in the previous chapter studying DITP on Ag(111) (chapter 4), it is expected that covalent coupling progresses via a metal-organic intermediate; figure 5.1c shows the reaction scheme for DITP on the

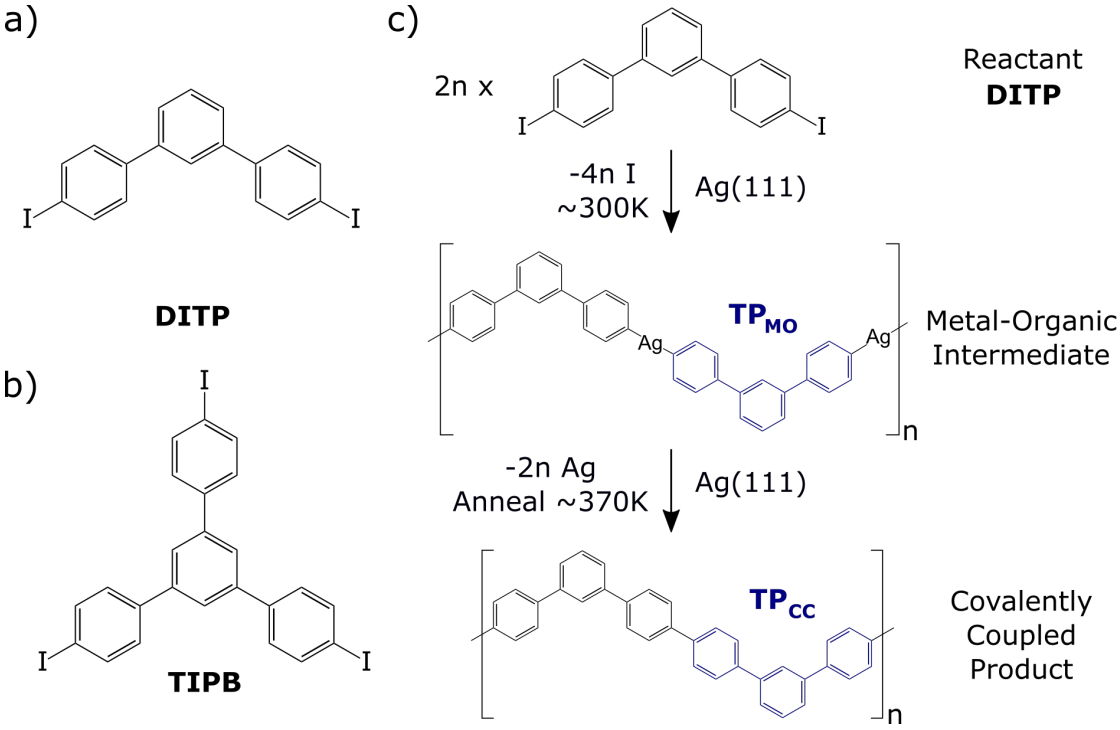


Figure 5.1: Chemical structures of (a) 4,4"-diiodo-*m*-terphenyl (DITP) and (b) 1,3,5-tris(4-iodophenyl)benzene (TIPB). (c) Reaction scheme for DITP on Ag(111), as shown in chapter 4. Cleavage of the C-I bond and formation of an extended metal-organic intermediate, TP_{MO}, occurs at ~300 K. Annealing at ~ 370 K results in the formation of a covalently coupled product, TP_{CC}. Molecular precursor components of MO and covalently coupled structures highlighted for clarity.

Ag(111) surface. A similar reaction progression is expected for TIPB. Adsorption of DITP and TIPB onto a Ag(111) substrate held at room temperature results in the cleavage of the C-I bond and the formation of a metal-organic (MO) structure. The dehalogenated molecular species are connected via organometallic (C-Ag-C bonds) within the MO structure. The sub-units within these structures are denoted as *m*-terphenyl (TP_{MO}) and 1,3,5-triphenylbenzene (TPB_{MO}) – indicating the relationship to the reactant molecules DITP and TIPB respectively. Following the formation of the MO structure the provision of additional thermal energy gives rise to formation of the covalently coupled (CC) product (370 K and 400 K to produce TP_{CC} and TPB_{CC}, respectively).

5.2 XPS Characterisation

Initial characterisation of the on-surface reaction was conducted using XPS measurements to identify the distinct chemical species present within the MO and covalently-coupled structures. I 3d and C 1s core level XP spectra were obtained, each using photon energies of 770 eV and 435 eV respectively. Figure 5.2a shows the C 1s photoelectron spectra obtained on Ag(111) for TP_{MO} (i.e. in the MO phase; pre-anneal) and TP_{CC} (covalent phase; post-anneal). For the MO phase two features are identified. In agreement with previous work, the major peak (284.1 eV) was assigned to aromatic carbon species within the backbone of TP_{MO}, with the shoulder at lower binding energy (283.2 eV) attributed to organometallic C-Ag-C species within the MO phase. The absence of features at higher binding energies is assigned to the lack of intact aryl-halides species (i.e. non-dissociated C-I bonds) [43, 124].

Following annealing the surface to 370 K, a temperature at which initiation of the on-surface covalent coupling is expected, the main peak (284.3 eV) is still present and a substantial attenuation in the signal from the shoulder feature is observed. These findings are consistent with conversion of the majority of the molecular species present to extended covalent structures (i.e. reductive elimination of the Ag from the organometallic C-Ag-C bond to give rise to a new C-C bond, resulting in reduction in intensity of the shoulder peak). The slight shift, by 0.2 eV, of the main peak towards higher binding energy is in agreement with several similar results for covalent coupling on surfaces [120, 125]; attributed to differences in charge transfer between the surface and metal-organic and covalent phases.

The I 3d photoelectron spectra for TP within MO and covalent phases on Ag(111), shown in figure 5.2b, support the reaction model where cleavage of the C-I bond, and formation of Ag-I with the substrate, occurs following deposition onto the surface at ∼300 K. Two peaks are present in the spectra, assigned to I $3d_{3/2}$ (630.5 eV) and I $3d_{5/2}$ (619.0 eV). Both prior to, and after, annealing to

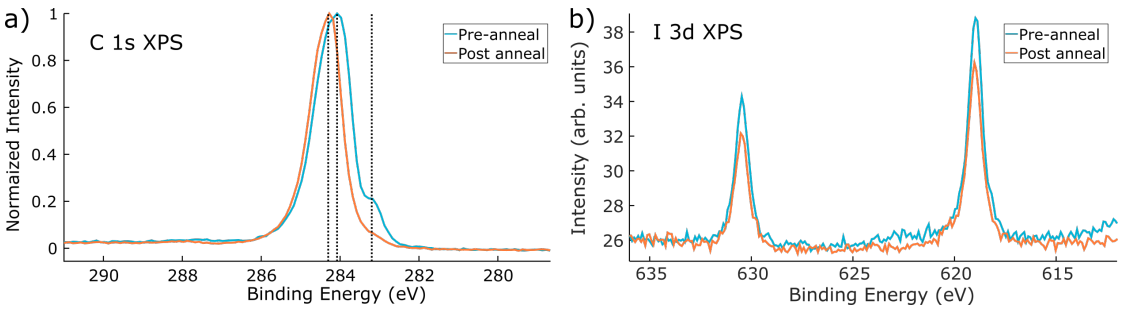


Figure 5.2: C 1s and I 3d photoelectron spectra acquired following the deposition of TIPB on Ag(111), before (blue) and after (orange) annealing. The metal-organic phase (TP_{MO}) is present on the surface following deposition, and the covalent phase (TP_{CC}) is formed following annealing at 370 K. (a) C 1s photoelectron spectra, obtained using photon energies of 435 eV. Spectra are normalised for clarity. (b) I 3d photoelectron spectra, obtained using photon energies of 770 eV.

370 K a single chemical environment for iodine is observed, as evidenced by the constant binding energy. The I $3d_{5/2}$ peak is at a binding energy consistent with chemisorbed iodine bonded to Ag [126], in agreement with the assertion that the C-I bond within DITP has dissociated following deposition. Similar results were observed for TIPB.

5.3 C 1s NIXSW analysis: (111) reflection

The identification of specific chemical states via XPS characterisation of the intermediate and final structures of the on-surface reaction facilitated the use of chemically sensitive normal incidence X-ray standing wave (NIXSW) studies to perform structural characterisation [118, 119]. NIXSW analysis provides two structural parameters; a coherent fraction (C_f) and a coherent position (C_p), approximately relating to the fraction of a chemical species in a given position, as discussed in chapter 3.6. Here focus was given to the C 1s signatures for the aromatic and organometallic carbon species (as characterised above) to determine the coherent fraction and position of the species relative to the (111) crystal plane of the bulk Ag substrate.

NIXSW measurements were acquired from the (111) reflection plane, using a

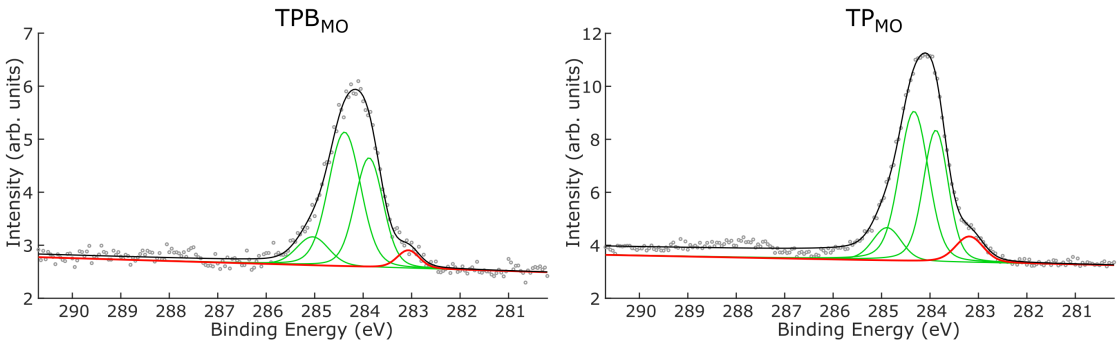


Figure 5.3: Examples of methods used to fit curves to pre-anneal (MO phase) C 1s data for TPB$_{MO}$ (left) and TP$_{MO}$ (right). Four peaks are used to create the shape of the curve observed in the data. The areas of the three peaks at higher binding energies (green) are summed to extract data for the main peak. The peak at lower binding energy (red) is used to gain information on the shoulder feature. The black line shows the overall fit, summed from all four peaks, to the data, shown in grey.

nominal energy of $E_{Bragg} = 2629$ eV, for both I 3d and C 1s. Each NIXSW measurement was repeated at least three times, with each new measurement performed at a different sample location to avoid beam damage. Before and after each measurement, core level spectra for both the I 3d and C 1s were obtained in order to monitor possible beam damage, with no significant changes observed (no observable chemical shift and less than noise level, ∼10%, change in peak intensities). Prior to the acquisition of the NIXSW measurement, a reflectivity curve of the respective reflection was acquired in order to judge the quality of that region of the surface, and to ensure that each NIXSW measurement was acquired across the same energy range with respect to the Bragg energy.

5.3.1 NIXSW analysis methods

In order to extract C_f and C_p values from the NIXSW data, it is necessary to extract the intensities of each chemical species at each acquired photon energy. This was done by fitting a convolution of a Doniach-ŝunjiċ line shape [127] and a Gaussian to spectral data averaged over at least three repeats. Examples of this fitting are shown in figure 5.3 for both TPB$_{MO}$ and TP$_{MO}$. The single peak shown in red (centred on 283.1 for both TPB$_{MO}$ and TP$_{MO}$) was used to extract information from the shoulder feature and was attributed to the organometallic

C 1s (111)	Phase / Carbon Type	C_f	C_p	Twist Angle Θ (°)
TP	MO / Organometallic	0.79 ± 0.14	0.05 ± 0.06	
	MO / Aromatic	0.49 ± 0.03	0.28 ± 0.02	29 ± 1
	Covalent / Aromatic	0.56 ± 0.03	0.32 ± 0.02	28 ± 1
TPB	MO / Organometallic	0.94 ± 0.11	0.03 ± 0.05	
	MO / Aromatic	0.50 ± 0.02	0.28 ± 0.01	26 ± 1
	Covalent / Aromatic	0.43 ± 0.06	0.30 ± 0.04	31 ± 3

Table 5.1: C 1s (111) XSW data. Data for Coherent fraction (C_f) and position (C_p) values obtained from C 1s (111) reflection NIXSW data and end phenyl group twist angle Θ for TP and TPB.

carbon species. The three peaks shown in green at higher binding energies (centred on, from left to right, 285.1 eV, 284.4 eV, 283.9 eV for TPB_{MO} and 284.8 eV, 284.3 eV, 283.8 eV for TP_{MO}) were summed to obtain the fitting for the main peak, and were attributed to aromatic carbon atoms. Three components were necessary to reproduce the shape of the main peak, and allow the intensity of the shoulder peak due to C-Ag-C to be evaluated. The three main peak components are not considered to be sufficiently unique or attributable to specific chemical environments within the molecule to allow them to be used to determine adsorption sites individually.

5.3.2 Chemically sensitive NIXSW results

Using these methods, C_f and C_p values were extracted by fitting absorption profiles to the intensity data. This is shown in figure 5.4 for both TP and TPB. A full comparison of C_f and C_p values is given in table 5.1.

Focusing initially on the organometallic carbon atoms forming a bond with a silver species (C-Ag-C), the profiles obtained from the XSW measurements (figure 5.4 - top) show a similar form for both TPB_{MO} and TP_{MO}. The TPB_{MO} measurements yield a coherent fraction of $C_{f(111)-C1s} = 0.94 \pm 0.11$. This high coherent fraction suggests a high degree of order and most likely indicates a single adsorption site on the Ag(111) surface for all organometallic carbon species within TPB_{MO}. A slightly lower level of order is found for TP_{MO}, $C_{f(111)-C1s} = 0.79 \pm 0.14$, however this still indicates a single adsorption position. Argand diagrams

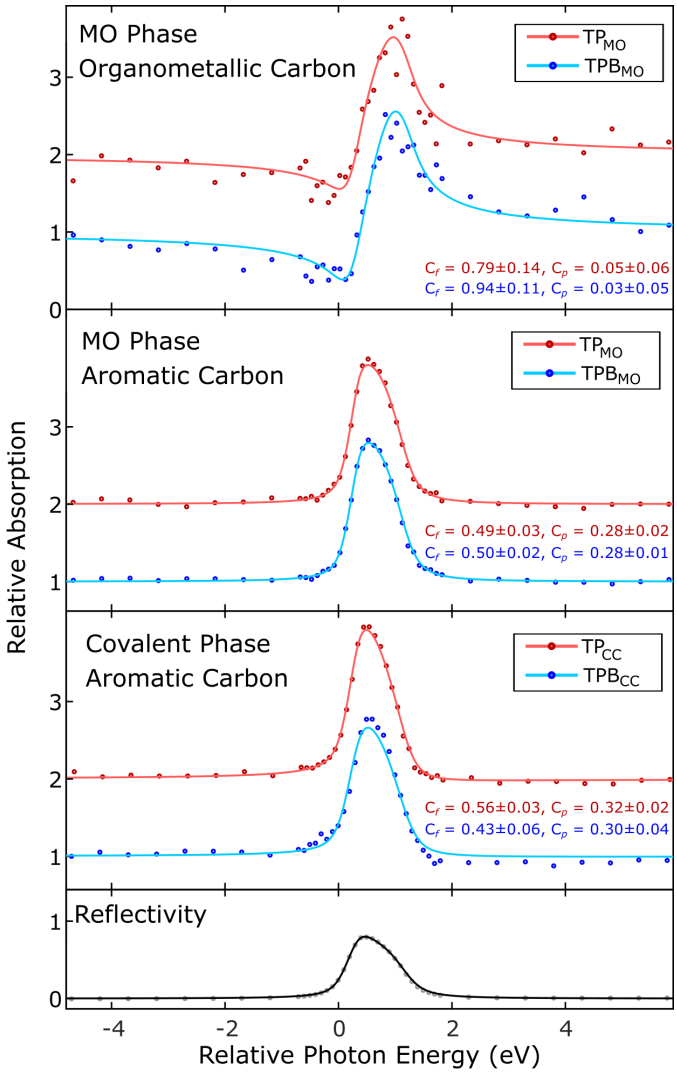


Figure 5.4: Chemically sensitive NIXSW measurements of the C1s region of TP and TPB within the MO and covalently coupled phases. NIXSW photoelectron yields obtained using the (111) reflection of the Ag(111) substrate for the C 1s core level, comparing MO and covalent phases of TP (red) and TPB (blue). Each profile is normalised to 1 away from the Bragg condition, with TP results offset by 1 unit for clarity. The obtained C_f and C_p values are shown for each fit. The reflectivity curve for TPB is shown (bottom), with similar results obtained for TP.

in figure 5.5, present C_f and C_p values in polar co-ordinates and show a model of organometallic carbon atoms (black arrow). This model agrees well with experimental results (red error bars). The coherent position values, which are given as fractions of the (111) layer spacing, for the organometallic carbons of both molecules agree within error ($C_{p(111)-C1s} = 0.05 \pm 0.06$ and $C_{p(111)-C1s} = 0.03 \pm 0.05$ for TP_{MO} and TPB_{MO} respectively). This indicates that the carbon species forming the C-Ag-C bond in both molecules are adsorbed at similar heights above

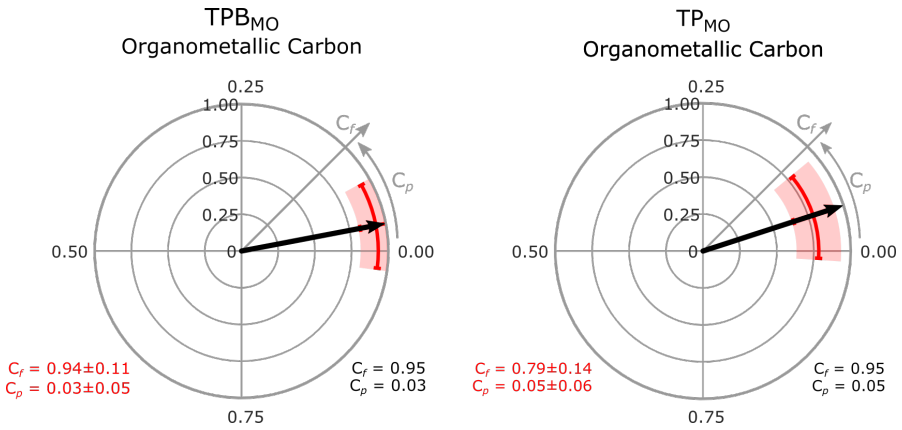


Figure 5.5: Argand diagrams showing C_f and C_p values obtained from XSW measurements from the (111) reflection. Shown are the measurements of organometallic carbons for TPB (left) and TP (Right). Experimental values are shown as red error bars, with the estimated uncertainty range highlighted by the light red area. Each arrow is a vector showing C_f and C_p values in polar co-ordinates. The solid black arrow shows the predicted C_f and C_p values for models applied to each data set. The organometallic carbon data is modelled such that each carbon atom is at a single height above the surface.

the surface (0.25 ± 0.01 nm and 0.24 ± 0.01 nm for TP$_{MO}$ and TPB$_{MO}$ respectively). The agreement in adsorption height for these two related but structurally different species show that the observations offer insight into a more general feature of molecule-surface interactions for the intermediates of Ullmann-type on-surface coupling.

It should be noted that all obtained XSW distances are relative to the extended crystallographic planes of the bulk Ag crystal. Therefore the adsorption 'heights' relative to the surface of the Ag(111) crystal are distances from the outermost (111) plane. This analysis is based on the assumption that the surface Ag atoms reside on this plane, with little to no reconstruction, thereby allowing the construction of adsorption models.

XSW profiles obtained from analysis of the aromatic carbon species in both MO and covalent structures are shown in figure 5.4 - middle. These profiles show a high degree of similarity, with fits to all profiles resulting in similar coherent fraction and position values. Notably, the coherent fraction values for the aromatic carbon species are significantly smaller than 1 (∼0.5 for TP and TPB in both the MO and covalent phases), indicating that the aromatic carbon atoms within the molecules are adsorbed at multiple heights.

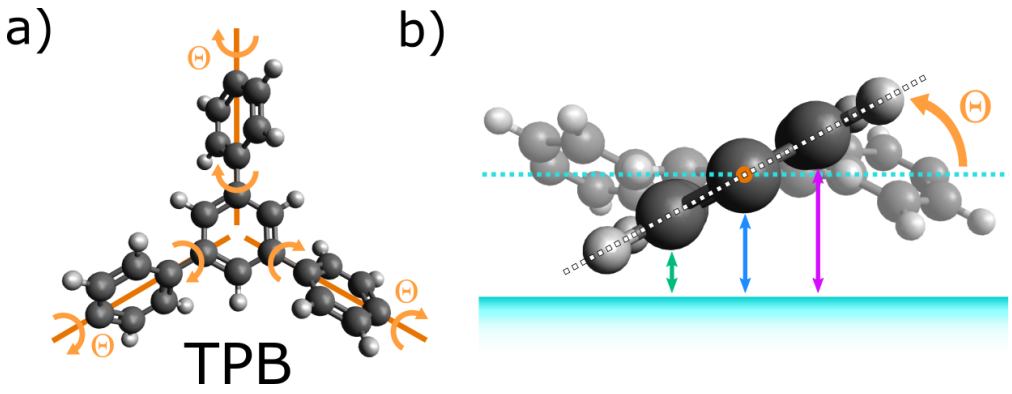


Figure 5.6: Structural model for the conformation of TPB_{CC} on Ag(111). (a) Model showing twisting of TPB_{CC} phenyl end groups around axes of rotation (orange) level with the plane of the molecule, with Θ showing the dihedral angle. (b) Side view of twisted TPB_{CC} model. Arrows show three different heights of carbon atoms above the surface: above (purple), below (green) and level with (blue) the molecular plane (dashed cyan line).

5.3.3 Twisting model of phenyl end groups

Although both the MO intermediate phase and covalently coupled final reaction products are extended structures it is possible to analyse the structure of the monomer units within the 2D networks. A model was developed where the outer phenyl groups (i.e. those with *para* connections) of each molecule are twisted relative to the central ring, i.e. those with *meta* connections (see figure 5.6a). The central phenyl groups are locked in place (due to the *meta* connections) and are expected to be parallel to the substrate surface. The *para* groups can twist, and this twisting results in the aromatic carbon atoms within the molecule being orientated at several different heights above the surface.

To model the structure, it was assumed that the central phenyl ring, and carbon atoms on the rotational axes of the terminal phenyl rings, remain flat relative to the surface in a single plane (i.e. the molecular plane is parallel to the (111) plane of the surface), and that all terminal phenyl groups are rotated by the same dihedral angle, Θ. An example for TPB_{CC} is shown in figure 5.6b. From this model, experimental C_f and C_p values were used to determine a value for Θ for both TPB and TP in MO and covalent phases. These values are given in table 5.1), with full details of calculations provided in appendix B.

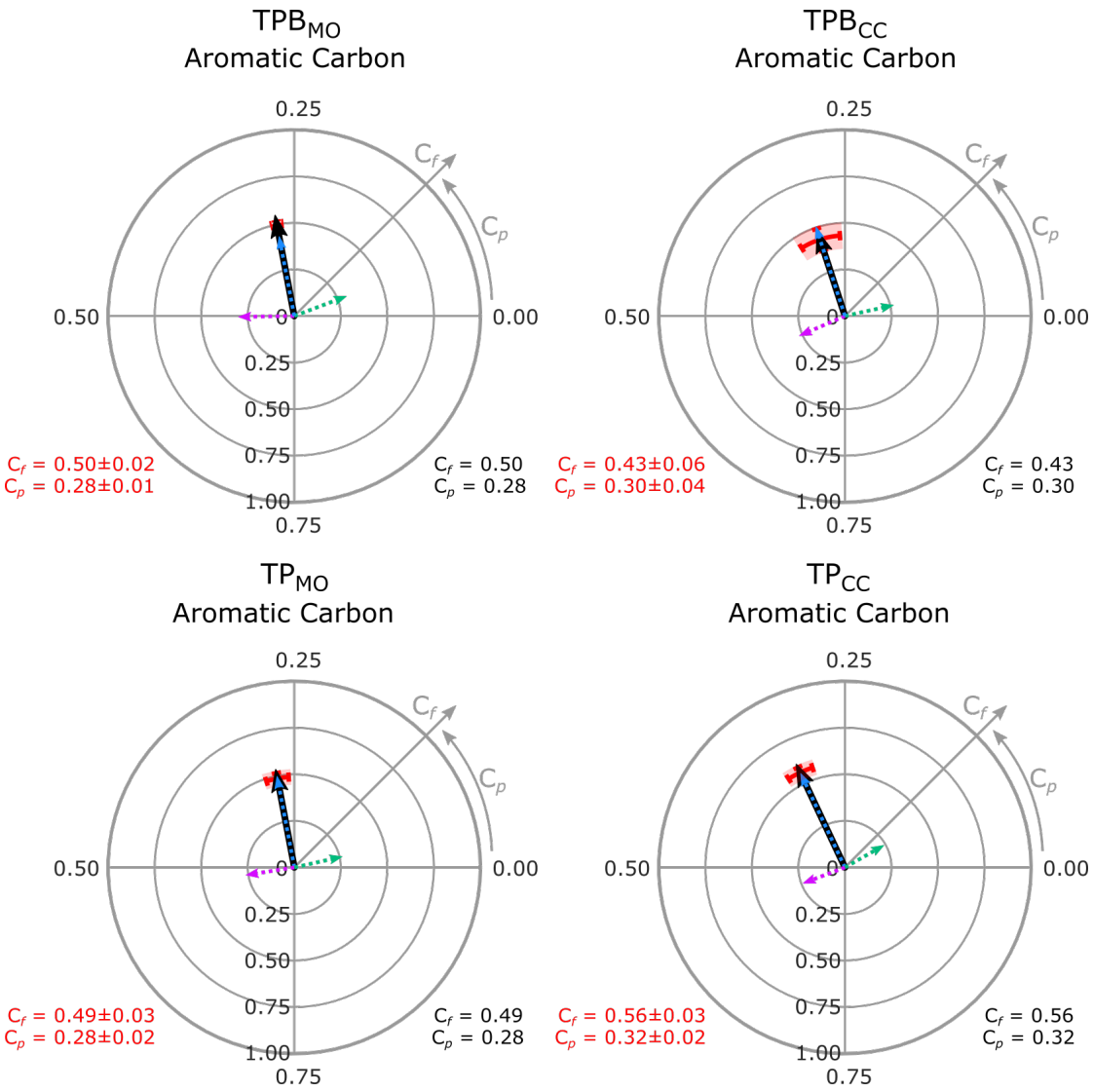


Figure 5.7: Argand diagrams showing C_f and C_p values obtained from XSW measurements from the (111) reflection. Shown are the measurements of aromatic carbons in the MO phase (left) and covalent coupling phase (right), for TPB (top) and TP (bottom). Experimental values shown as red error bars, with estimated uncertainty range highlighted by the light red area. Each arrow is a vector showing C_f and C_p values in polar co-ordinates. The solid black arrow shows the predicted C_f and C_p values for models applied to each data set. Aromatic carbon data is predicted using the twisted phenyl rings model, with Θ for each given in table 5.1. Within this model dashed arrows represent aromatic carbon atoms higher (purple), lower (green) and level with the molecular plane (blue), as described in figure 5.6b. Experimental and predicted C_f and C_p values are given respectively in red and black, in the bottom left and right of each diagram.

Calculated values for C_f and C_p based upon this model are presented using Argand diagrams in figure 5.7. Each arrow is a vector showing C_f and C_p values in polar co-ordinates. Dashed arrows represent aromatic carbon atoms higher

(purple), lower (green), and level with the molecular plane (blue), as represented in figure 5.6. The solid black arrow shows the predicted C_f and C_p values for the model and is in excellent agreement with experimental values (red error bars).

These results show the side phenyl groups in all cases are twisted by approximately 30°. For comparison, biphenyl molecules in free space have a twist angle of 44° (due to steric hindrance between the hydrogens on adjacent phenyl groups [128]). The observation that the dihedral angle is reduced for the surface-confined molecule compared to a molecule in free space can be understood due to the interaction with the surface; flattening of the molecule maximises the molecule-surface interaction with the π orbitals of the terminal phenyl rings. The findings here support the previously suggested conformation flexibility of intermediates with Ullmann-type on-surface reactions [6, 129].

It should be noted that in the following section (5.3.4) molecules in the MO phase are found to not be fully planar to the surface, with organometallic carbons bending towards the surface. This is not considered in these models for simplicity.

5.3.4 The role of metal adatoms within MO structures

The location of the organometallic carbon species within the MO phase show distinct differences to the aromatic carbon atoms. Organometallic carbon atoms are found to be 0.25 ± 0.01 nm and 0.24 ± 0.01 nm above the surface; for TP_{MO} and TPB_{MO} respectively. This can be compared to the average heights of the aromatic carbons within the MO phase; both TPB_{MO} and TP_{MO} are found to be ∼0.30 nm relative to the height of the topmost Ag(111) plane (0.302 ± 0.005 nm and 0.302 ± 0.002 nm above the surface; for TP_{MO} and TPB_{MO} respectively). This is in agreement with results for relative heights above surfaces for large π–conjugated molecules on Ag(111) (0.29 nm for diindenoperylene adsorbs on Ag(111) [130]). The value of the adsorption height is therefore significantly lower for organometallic carbon species than the purely aromatic, resulting in a curved structure for the adsorbed molecular species (see figure 5.8a). This indicates that the end phenyl

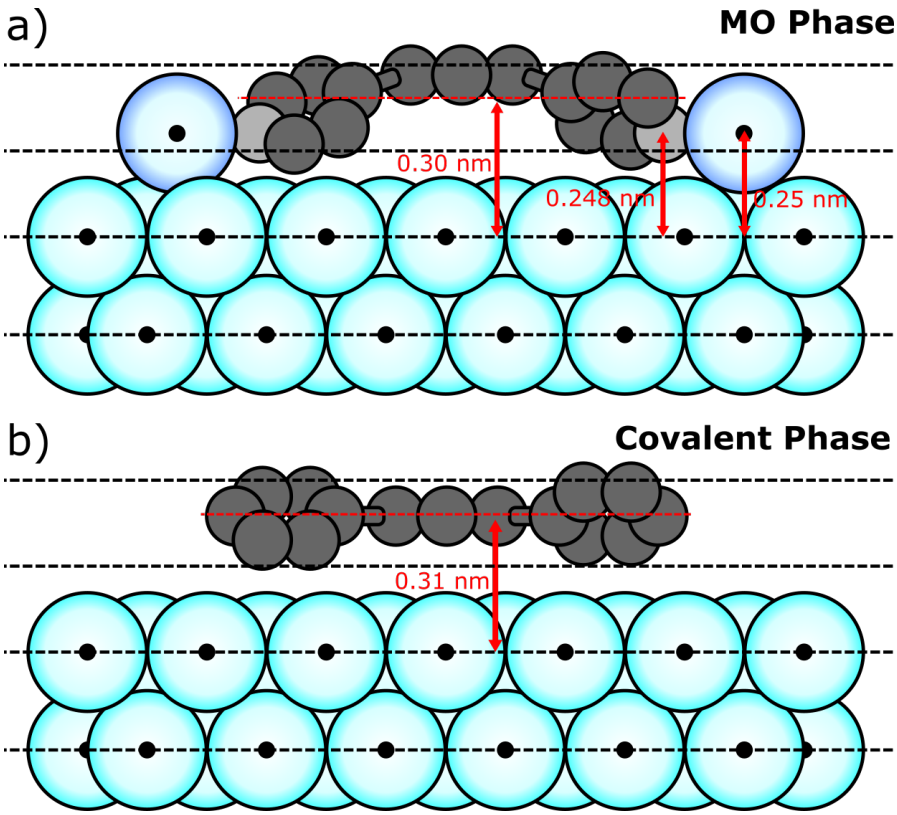


Figure 5.8: Models for the vertical positioning of molecules above the Ag(111) surface. (a) Metal-organic intermediate phase of the Ullmann-type coupling reaction, with molecules bonded to silver adatoms (dark blue) adsorbed in bridge sites. Average heights of the molecule (red dashed line), C-Ag-C bonded carbon (light grey) and Ag adatoms are shown. (b) Covalent phase of Ullmann coupling reaction, with average height of the molecule shown.

groups are likely to bend down towards the surface when forming the organometallic C-Ag-C bond.

Previous computational studies of Ullmann-type on-surface coupling reactions, employing density functional theory (DFT), have suggested that MO structures are bound to substrate lattice atoms [40]. This is in contrast to experimental findings where structures are characterised as incorporating surface adatoms [41, 43, 79, 129]. The NIXSW analysis presented here indicates that the organometallic carbon atoms are significantly higher above the surface (∼0.25 nm) than a single C-Ag bond length (approximately 0.21 nm [131]), implying that the Ag species involved in the metal-organic bond is unlikely to be in the surface silver layer. The metal-organic bond must therefore be made with either a surface adatom or a silver atom that has been significantly raised out of the surface. STM data for the same

molecule-substrate systems do not provide evidence for removal of Ag atoms from surface layer, which would likely result in the presence of etch pits and were not observed in this study. It is therefore suggested that Ag adatoms diffusing from low-coordinated step-edge sites play a significant role. The proposed model for TP in the metal-organic phase of the Ullmann-coupling reaction (TP_{MO}), including the labelled heights of the organometallic carbon atoms, is shown in figure 5.8a. The adsorption height or the organometallic carbons are compatible with Ag adatoms located at bridge or 3-fold hollow sites (further details of the adsorption geometry are given below).

Following completion of the reaction, the covalent phases of TP and TPB (now consisting exclusively of aromatic carbon species) were both found to be adsorbed at an average of 0.31 ± 0.01 nm above the surface, with the end phenyl groups twisted around a central axis (as discussed above). A model for a single TPB_{CC} molecule in the covalent phase is shown in figure 5.8b.

5.4 I 3d NIXSW Analysis

As with the C 1s orbital, the NIXSW measurements for the I $3d_{5/2}$ orbital can be used to determine adsorption locations for iodine atoms on the surface after dissociating. XSW profiles for I 3d orbital for the (111) reflection are shown in figure 5.9a. Profiles for TPB and TP show very similar form, with C_f and C_p values (given in table 5.2) agreeing within error. Similarly, NIXSW measurements obtained from the (200) reflection show very similar profiles. This suggests iodine remains in the same adsorption site for each phase of the Ullmann reaction after dissociation, in agreement with the XPS measurements shown previously.

The C_f and C_p values from the iodine species are the same within error and do not vary significantly with respect to precursor molecule type and annealing. An average of these values is therefore used in the following discussion. The average of TP and TPB measurements, before and after anneal give a coherent fraction value of $C_{f(111)-I3d} = 0.94 \pm 0.02$. This high coherent fraction value

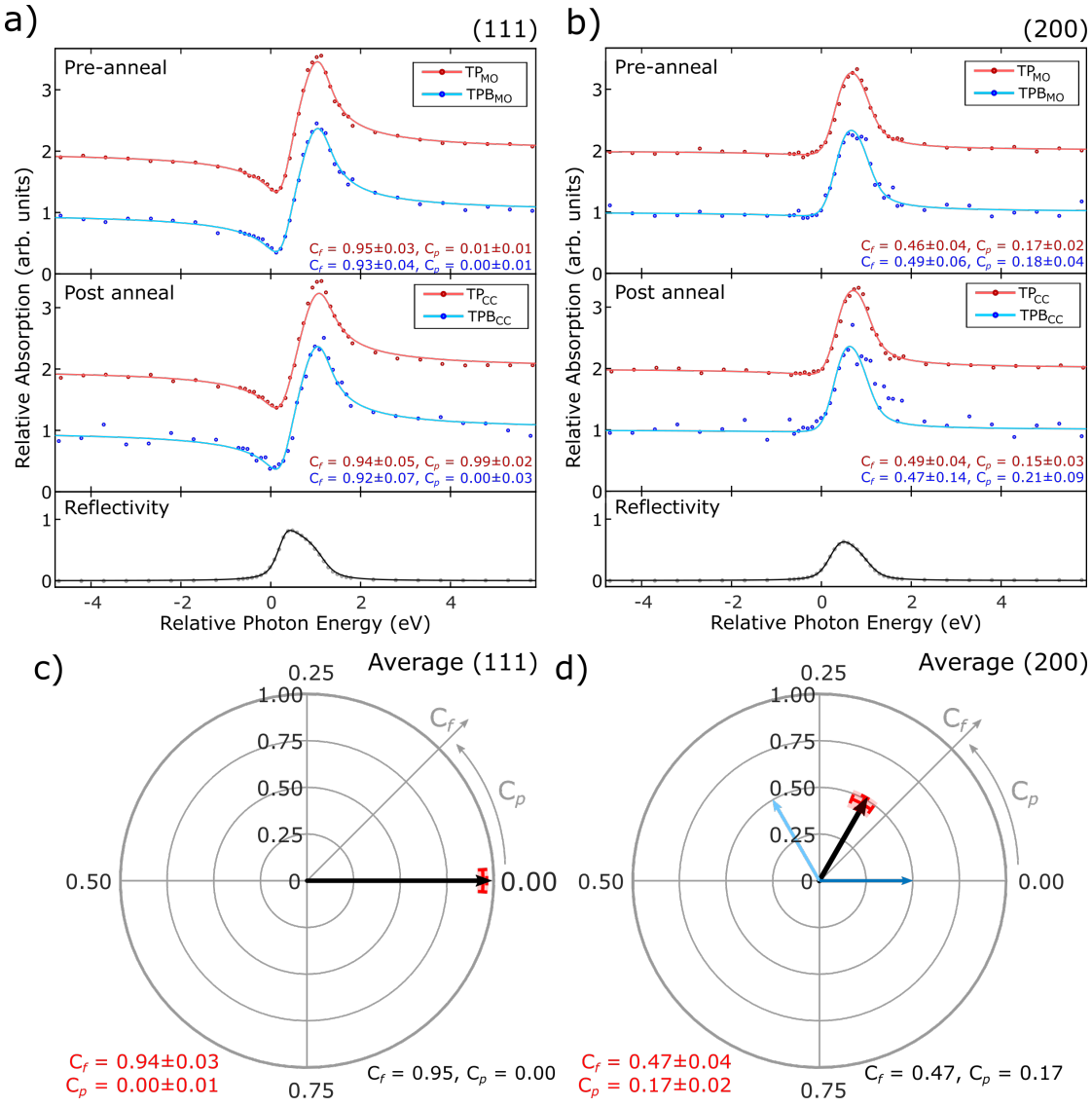


Figure 5.9: NIXSW characterisation of the iodine species (I 3d core level) present as part of TP and TPB assemblies on Ag(111) in the metal-organic structure (pre-anneal) and the covalently bonded structure (post-anneal). (a) and (b) NIXSW photoemission yields obtained using the (111) and (200) reflections, respectively, comparing TP (red) and TPB (blue) before and after annealing. Each profile is normalised to a value of 1 away from the Bragg condition, with TP results offset by 1 unit for clarity. The obtained coherent fraction (C_f) and position (C_p) values are shown for each profile. (c) and (d) Argand diagrams showing average coherent fraction, C_f, and, C_p, values for the (111) and (200) reflections. (c) Shows a model consisting of iodine atoms at a position of 0.236 nm (C_p=0.00) above the silver surface (111) plane. This is measurement is used in (d) to show iodine adsorbed in a 1:1 ratio at fcc:hcp hollow sites. Dark blue arrow is the fcc site and the light blue the hcp site. Black arrow shows resultant vector for proposed models for iodine, and red error bars show average of all experimental measurements, with C_f and C_p values shown.

I 3d	Phase	(111)		(200)	
		C_f	C_p	C_f	C_p
TP	Pre-Anneal	0.95 ± 0.03	0.01 ± 0.01	0.46 ± 0.04	0.17 ± 0.02
	Post Anneal	0.94 ± 0.05	0.99 ± 0.02*	0.49 ± 0.04	0.15 ± 0.03
TPB	Pre Anneal	0.93 ± 0.04	0.00 ± 0.01	0.49 ± 0.06	0.18 ± 0.04
	Post Anneal	0.92 ± 0.07	0.00 ± 0.03	0.47 ± 0.14	0.21 ± 0.09
Average		0.94 ± 0.02	0.00 ± 0.01	0.47 ± 0.04	0.17 ± 0.02

Table 5.2: I 3d XSW measurments Coherent fraction (C_f) and position (C_p) values for NIXSW measurements acquired for the I 3d level of TP and TPB on the Ag(111) surface. Acquired for the (111) and (200) reflections. *C_p values are cyclic such that 0 and 1 are equivalent.

suggests that all iodine atoms are in similar adsorption sites relative to the (111) Bragg reflection, meaning a single height above the Ag(111) surface. From this and averaged coherent position, $C_{p(111)-I3d} = 0.00 \pm 0.01$, all iodine atoms are expected to rest in plane with the (111) layer spacing, most likely at the first Ag(111) layer spacing above the surface, at 0.236 nm. This adsorption model is presented as an Argand diagram in figure 5.9c (black arrow), with the NIXSW measured coherent fraction and position values (red error bars).

The precise adsorption site (in 3D) of iodine on the surface can then be determined using NIXSW measurements from the (200) reflection for triangulation (see chapter 3.6.5). Averaging all measurements from the (200) reflection gives a coherent fraction of $C_{f(200)-I3d} = 0.47 \pm 0.04$ and position of $C_{p(200)-I3d} = 0.17 \pm 0.02$ (similar for both molecules before and after annealing). The coherent fraction value of ∼0.5 suggests multiple iodine adsorption sites on the surface, at least two distinct sites. Using the height of iodine above the surface determined from the (111) reflection, a model of iodine adsorbed in hexagonally close-packed (hcp) and face-centred cubic (fcc) three-fold hollow sites in a 1:1 ratio is proposed in figure 5.9d. The $C_{f(200)-I3d}$ and $C_{p(200)-I3d}$ values for hollow sites are shown as blue arrows with the resultant vector shown in black. This model gives coherent fraction and position values of $C_{f(200)-I3d} = 0.47$ and $C_{p(200)-I3d} = 0.17$, in excellent agreement with measured values. This also agrees well with previous STM measured adsorption structures for related iodine containing molecules [129].

5.5 C 1s NIXSW analysis: (200) reflection

Similarly to iodine, NIXSW measurements from the (111) and (200) reflection planes of the Ag(111) can be used to provide information on the lateral adsorption positions of carbon atoms within TPB and TP. NIXSW measurements for the (200) reflection were acquired using a nominal energy E_{Bragg} = 3035 eV, with at least three repeat measurements for each molecule and reaction phase. Results were analysed in a similar manner as described above (section 5.3.1) to extract absorption profile data and obtain coherent fraction and position values.

5.5.1 Chemically sensitive NIXSW results

Figure 5.10 shows fitted XSW profiles for C 1s 200 reflection for both TPB (blue) and TP (red) in both MO and covalent phases of the Ullmann reaction. C_f and C_p values obtained from the fitted curve are shown below each curve, with all values summarised in table 5.3. XSW absorption measurements for aromatic carbons, within TPB and TP, show very similar profiles, in a similar manner to the (111) reflection measurements. This perhaps would suggest that aromatic carbons occupy similar adsorption sites between molecules. However, the measured coherent fraction value for the aromatic carbon measurements is low (<0.2). This suggests that aromatic carbon atoms, within TPB and TP, are adsorbed at a large number of positions, relative to the (200) reflecting plane. Therefore, the measured coherent position values are inherently unreliable and so could not be used in the determination of adsorption sites.

C 1s (200)	Phase/ Carbon Type	C_f	C_p
TP	MO / Organometallic	0.39 ± 0.16	0.77 ± 0.11
	MO / Aromatic	0.18 ± 0.02	0.85 ± 0.02
	Covalent / Aromatic	0.16 ± 0.02	0.82 ± 0.02
TPB	MO / Organometallic	0.26 ± 0.17	0.81 ± 0.14
	MO / Aromatic	0.17 ± 0.02	0.79 ± 0.02
	Covalent / Aromatic	0.17 ± 0.03	0.85 ± 0.03

Table 5.3: Data for Coherent fraction (C_f) and position (C_p) values obtained from C 1s (200) reflection NIXSW data

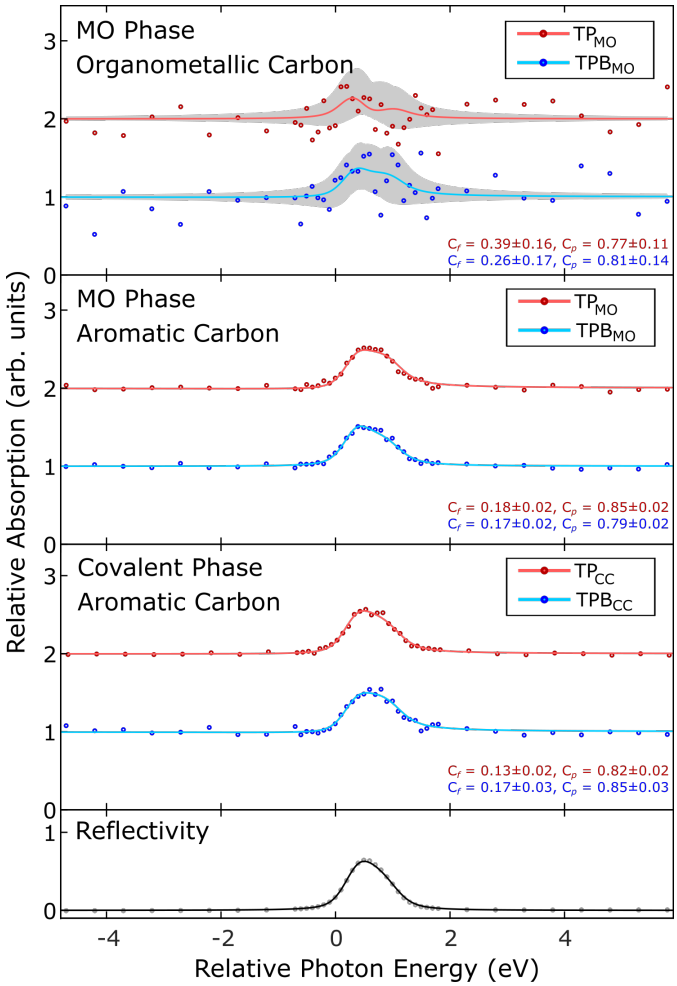


Figure 5.10: (a) NIXSW photoelectron yields obtained using the (200) reflection for the C 1s core level, comparing TP_{MO} (red) and TPB_{MO} (blue). Grey shading shows curves fitted using values of C_f and C_p within quoted uncertainty range. Each profile is normalised to 1, away from the Bragg condition, with TP_{MO} results offset by 1 unit for clarity. The obtained C_f and C_f values are shown for each profile.

XSW profiles obtained using the (200) reflection of the Ag(111) surface (figure 5.10 - top) provide information on the organometallic carbon atoms within the TP_{MO} and TPB_{MO} structures. The data for the organometallic species results in low values for the coherent fractions ($C_{f(200)-C1s} = 0.39 \pm 0.16$ and $C_{f(200)-C1s} = 0.26 \pm 0.17$ for TP_{MO} and TPB_{MO} respectively) from which it may be inferred that the organometallic carbon atoms are adsorbed at multiple positions relative to the (200) reflection. The resulting C_f and C_p values have a large uncertainty range. This is due to the low measured intensity in the shoulder feature, compared to the main peak, making consistently fitting the feature difficult. This uncertainty range

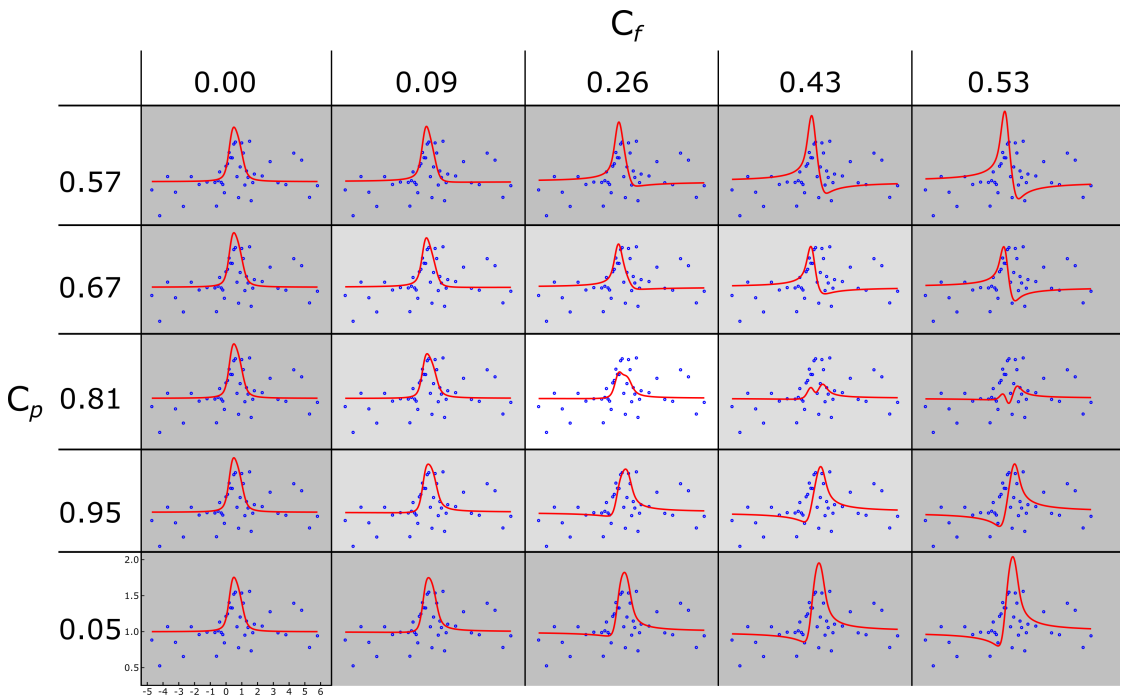


Figure 5.11: Table of comparisons of different XSW profiles (red) with varied coherent fraction (C_f) and position (C_p) values. Data points (blue) are for TPB measurements of the organometallic carbon atoms from the (200) reflection. Each XSW profile is generated from C_f and C_p values either at the quoted values (white, centre), within the quoted uncertainty (light grey) or 0.1 outside the uncertainty range (dark grey, outer). Profiles with C_f and C_p values within the uncertainty range are found to acceptably fit the data whereas profiles with values outside this range do not. All figures have the same scaling, with axes shown in the bottom left figure. X axes show relative photon energy (eV) and Y axes show relative absorption (in arbitrary units).

is demonstrated by the grey region in figure 5.10 - top. The region highlights the area enclosed by all possible NIXSW profiles for C_f and C_p values within the quoted uncertainty range. This area visually fits the data well, suggesting accuracy in the large uncertainty range. Additionally, the experimentally obtained XSW curves cover a very large range of adsorption versus photon energy. This means that although the data for the organometallic species presented here have a less than ideal signal-to-noise ratio, a very large proportion of C_f and C_p combinations are completely excluded as fits to them.

Examples of this are shown in figure 5.11, where the range of possible NIXSW profiles are displayed in a table comparing the effects of fitting using various coherent fraction and position combinations. Blue dots show the data points for

organometallic carbons in TPB_{MO} and red curves show simulated absorption profiles for the corresponding C_f and C_p. The central (white) square shows the calculated fitting for the data, with surrounding (light grey) squares showing profiles for the extreme values of the quoted uncertainty range of C_f and C_p values. Finally, outer (dark grey) squares show profiles for C_f and C_p 0.1 outside the quoted uncertainty range. From this figure, it can be seen that absorption profiles within the range of uncertainties fit well to the data, with the quoted C_f and C_p values producing the most representative fit. This is in contrast to profiles using values outside the uncertainty range, which are not consistent with the data. This highlights the small range of possible absorption conformations obtained from these results

5.5.2 Structural characterisation via STM

In order to facilitate an interpretation of the XSW measurements and to produce an adsorption model of the MO and covalently bonded TPB and TP structures, the molecular species were separately characterised on the Ag(111) surface using room temperature STM. Figure 5.12b shows the edge of a MO structure formed from the as-deposited TIPB adsorbed on a Ag(111) surface. A model showing the position of TPB_{MO} molecules and Ag adatoms is overlaid. Individual TPB_{MO} units can be seen, connected by circular bright features, similar to features previously observed for MO structures [41, 79]. These bright features were therefore attributed to silver adatoms. The molecular units exist as part of an extended porous structure (figure 5.12a), comprising mostly of hexagonal pores with some disordered regions of other polygonal arrangements (as previously observed for structures formed from the brominated analogue of TIPB [81]). Additionally, further bright features were observed adjacent to the molecules (examples indicated by white arrows in figure 5.12b) and are attributed to iodine atoms adsorbed to the surface after dissociating from the molecules (similar to that observed for studies on other iodinated species [129]).

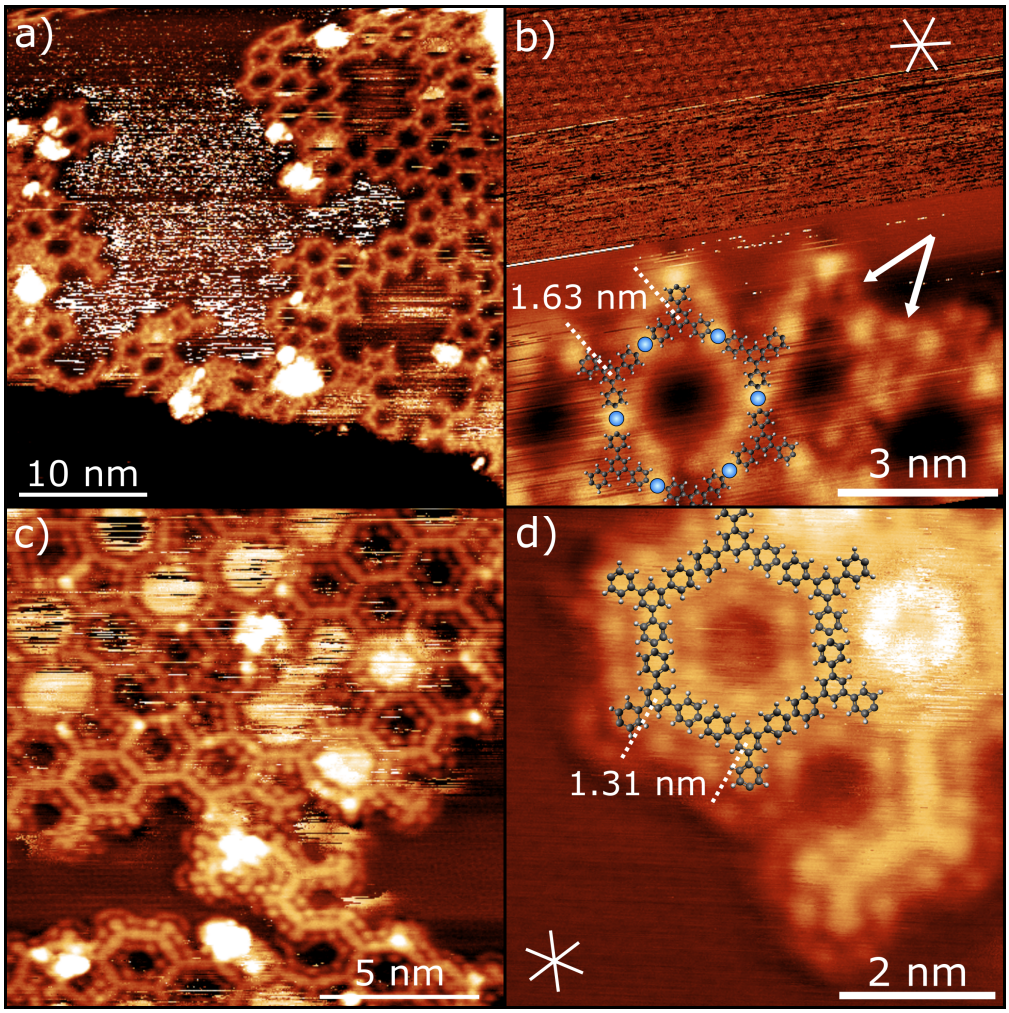


Figure 5.12: STM images for TPB on Ag(111) in MO and covalent bonding phases. (a) Overview of MO phase of TPB (TPB_{MO}). Image parameters: V_{bias} = -1.8 V I_{set} = 20 pA. (b) Close up image of TPB_{MO} structures. Top section shows a region of atomic contrast, used to calibrate image. Molecular model, intermolecular separations and lattice vector directions are overlaid. White arrows indicate example locations of iodine atoms. Imaging parameters: V_{bias} = -80 mV, I_{set} = 2 nA for the top section, V_{bias} = -1.8 V, I_{set} = 20 pA for bottom section. (c) Overview of covalent phase of TPB (TPB_{CC}). Image parameters: V_{bias} = -1.8 V I_{set} = 20 pA. (d) close up image of TPB_{CC}. Molecular model, intermolecular separations and lattice vector directions are overlaid. Image parameters: V_{bias} = -1.8V, I_{set} = 20 pA.

Details of registry with the underlying surface can be obtained by imaging the underlying Ag(111) substrate (top region of figure 5.12b shows atomic resolution). Combined imaging of the substrate and molecular overlayer was obtained by pausing image acquisition at the edge of the island (following imaging of the molecular structure) and altering the bias voltage and current set-point. The region of atomic resolution was then used to calibrate the image in order to determine accurate dis-

tances and angles of molecules relative to the surface crystallographic directions. Combining this with measurements from additional images of the same surface, the centre-centre separation for TPB units within the MO structure is found to be 1.63 ± 0.1 nm. This is consistent with the expected dimensions for two TPB molecules bridged by a C-Ag-C link, 1.61 ± 0.2 nm for a similar molecule [79]). The axis of this bond is misaligned to the $\langle\bar{1}10\rangle$ set of crystal directions by 25 ± 2°.

STM experiments were also performed on annealed surfaces for TPB_{CC} to gain insights into its adsorption geometry. Figure 5.12c shows an overview area of TPB_{CC} forming covalent hexagonal structures on the surface following anneal. A close-up region is shown in figure 5.12d. Unlike the pre-anneal surface, molecules appear to have a constant apparent height along their structures with no features associated with Ag adatoms, indicating that the molecules are covalently bonded. Bright circular features were also seen surrounding TPB units and within hexagonal pores, attributed to iodine. A model showing the molecular structure is overlaid. As with the TPB_{MO} phase, images were calibrated to obtain accurate measurements of surface structures using regions of atomic contrast. TPB units were found to be separated by 1.31 ± 0.03 nm, again in good agreement with previous work [81]. Covalent between TPB_{CC} were aligned at an angle of 3 ± 2° to the surface $\langle\bar{1}10\rangle$ crystallographic directions.

Similar STM investigations were performed for TP on Ag(111). Example STM images of the metal-organic phase are shown in figure 5.13a and b. TP_{MO} units appear as periodic circular bright features, arranged in islands of parallel zigzag chains. Islands were observed in three different rotations, matching the symmetries of the surface. Topographic features associated with Ag adatoms are not seen in STM images (noted previously [83]). Instead, their positions are inferred from the arrangement of TP_{MO} units and a model is overlaid to show this (figure 5.13b). Measurements from STM images were calibrated using regions of atomic contrast and show the zigzag chains to have a period of 2.63 ± 0.05 nm, and are oriented

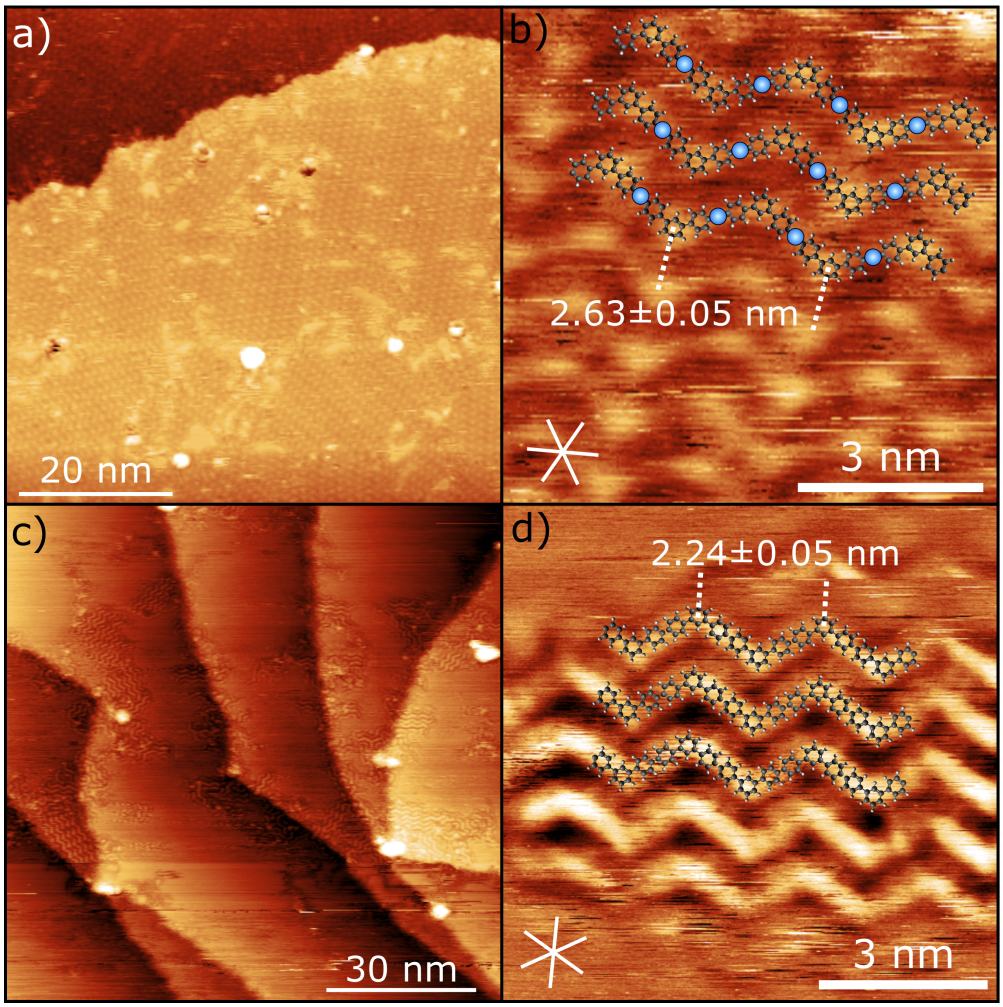


Figure 5.13: STM images for TP on Ag(111) in MO and covalent bonding phases. (a) Overview of MO phase of TP (TP_{MO}). Image parameters: V_{bias} = 1.5 V I_{set} = 5.0 pA. (b) Close up image of TP_{MO} structures. TP units and silver adatoms are overlaid, with molecule-molecule separation and surface lattice directions indicated (white - bottom left). Image parameters: V_{bias} = 1.8 V I_{set} = 20.0 pA. (c) Overview of covalent phase of TP (TP_{CC}). Image parameters: V_{bias} = -1.0 V I_{set} = 5.0 pA. (d) Close up image of TP_{CC}, with molecule-molecule separation and surface lattice (white - bottom left) shown. Image parameters: V_{bias} = -1.8 V I_{set} = 10.0 pA.

at approximately -5° relative to the $\langle\bar{1}10\rangle$ set of crystal directions. Zigzag chains were found to be separated by 1.14 ± 0.05 nm. The dimensions of these structures show clear agreement with the measurements of TP presented in chapter 4.

STM experiments were also performed for the covalent phase of TP (TP_{CC}) and an example STM image of an island of molecules is shown in figure 5.13d. Zigzag chains have constant apparent height along their lengths, indicating that molecules are covalently bonded. A molecular structure for the zigzag chains is

overlaid. TP_{CC} molecular chains were found to have a period of 2.24 ± 0.05 nm at an angle of 31° to the underlying surface. Chains were found to be separated by 1.19 ± 0.05 nm. These results similarly agree with measured dimensions of the covalent TP structures obtained in chapter 4.

5.5.3 Adsorption modelling methods

Utilising a combination of the XSW measurement from the (111) and (200) planes in concert with the STM measurements described above, it is possible to locate the molecular adlayer relative to the surface substrate layer for both TPB_{MO} and TP_{MO} structures. This was done by constructing a simple molecular model of the adsorbed molecules, and adjusting its parameters to match experimental C_f and C_p values. The low coherent fraction values obtained from (200) NIXSW measurements for aromatic carbons suggested a large number of adsorption sites, with low information gained from coherent position values. Additionally, the large number of aromatic carbon atoms would introduce significantly more variables, making modelling very complex. Models were therefore developed using only NIXSW measurements from organometallic carbon atoms. From these atoms, the lateral position of the rest of the molecule can be inferred. Because of this, these methods were only used for the MO phase and not for covalently coupled structures.

The method used for building a model of molecules is described in figure 5.14. Firstly, (a) shows the simplified TPB unit used for the model. Only organometallic carbon atoms (black circles) were considered as only these atoms contribute to the organometallic carbon features seen in XSW measurements. The distance, D, between the carbon atoms and the centre of the molecule (blue cross) can be varied by small amounts to account for stretching of the molecule and the end phenyl groups bending down towards the surface (from (111) XSW results, section 5.3.4). Next, an additional molecule is added (rotated by 180°) to create the molecular overlayer structure observed in STM images. The separation of molecule centres, s, as well as the unit cells rotation, α (relative to one of the high symmetry

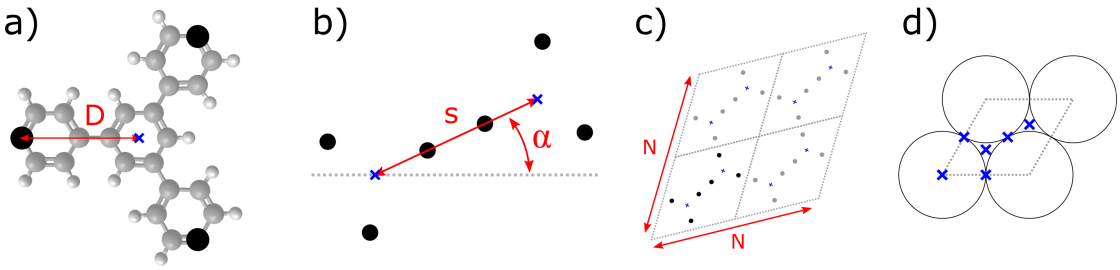


Figure 5.14: Figures showing methods used to model lateral adsorption of molecules from NIXSW measurements of organometallic carbon atoms. (a) Only organometallic carbon atoms are used within the model, with the aromatic carbon atoms adsorption sites inferred from these positions. The distance, D, of these atoms to the centre of the molecule (blue cross) is varied to account for variations in bending of molecule arms down towards the surface. (b) An additional molecule is added, rotated 180°, to form a molecular unit cell and the separation of the two molecules, s, and their angle relative to the x axis ($[1\bar{1}0]$ direction), α, is allowed to vary. (c) The unit cell is copied N times in two directions to account for extended structures on the surface. (d) Positions of molecules were allowed to vary laterally relative to the surface. Only models where all molecules have their centres in a high symmetry (atop, bridge or three-fold hollow – shown as blue crosses) site are considered for simplicity.

$\langle\bar{1}10\rangle$ surface directions), can be varied to account for different positioning of molecules on the surface (figure 5.14b). Then, the unit cell is repeated $N = 6$ times to create an extended structure (figure 5.14c). This accounts for the fact that the molecular adlayer has a regular periodicity but is not necessarily coincident with the underlying Ag(111) unit mesh. Finally, the model is placed over a Ag(111) surface model, at a height above the surface determined from (111) XSW measurements of organometallic carbons. The model assumes the central phenyl ring of all molecules will be adsorbed at a high symmetry site (atop, bridge or three-fold hollow) on the surface (figure 5.14d). This was done to simplify calculations as otherwise there would be a near infinite number of sites that would satisfy C_f and C_p values. In addition to this, the model was extended to include ±120° rotations and the reflection over the $[1\bar{1}0]$ direction to account for additional domains that form due to the symmetry of the (111) crystal surface.

Using this model and adjusting its variables (D, s, α, height and molecule centre lateral position relative to the surface), the distances of all organometallic carbon atoms from the (200) reflecting plane can be calculated and used to determine an

expected overall C_f and C_p value for the model. D was taken to be 0.56 ± 0.02 nm (based upon dimensions of the gas phase molecule determined via a molecular mechanics-based model), the other variables were based upon the STM measured dimensions and those acquired from the (111) reflection NIXSW data. This was then compared to the measured C_f and C_p values to determine which models produced values that were within the range of uncertainties. This methodology was used to model both TPB and TP structures, based on XSW and STM data. In the case of TP, an additional variable was added to account for the separation of zigzag chains.

5.5.4 Results of modelling

STM measurements of molecular separation and angle relative to the surface were used as starting values for variables in the model and allowed to vary within a small range. Additionally, the height of molecules above the surface was varied within a range of values determined from XSW measurements from the (111) reflection. Finally, the lateral position of molecules was varied with molecule positions limited such that the central phenyl ring of all molecules was adsorbed in a high symmetry site. Coherent fraction and position values calculated for each model were compared to XSW measurements with the assumption that Ag adatoms were adsorbed in high symmetry sites as well. For both TPB_{MO} and TP_{MO}, a single high symmetry structural arrangement was found in agreement with experiments. These potential adsorption models are presented below.

TPB Lateral Adsorption Modelling

The adsorption model for metal-organic TPB_{MO} (figure 5.15b) shows all molecular centres in three-fold hollow adsorption sites (either all hcp or all fcc sites), with Ag adatoms predicted to rest in the same three-fold hollow sites as the molecular centres. Lateral translation of the molecular overlayer, such that molecule centres are adsorbed at bridge sites (with adatoms positioned in bridging sites as well),

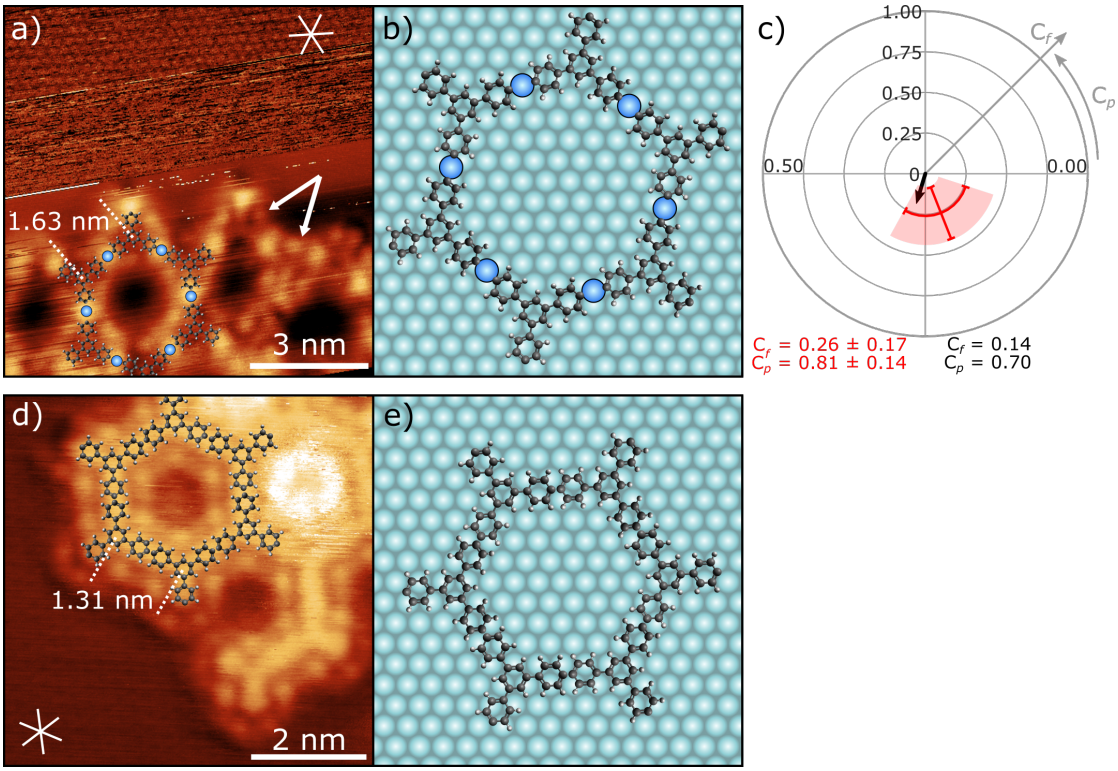


Figure 5.15: (a) STM image showing the metal-organic phase of TPB, as shown in figure 5.12b. Molecular model, intermolecular separations and lattice vector directions are overlaid. (b) Proposed adsorption models for metal-organic phases of TPB on Ag(111) based on XSW modelling. (c) Argand diagram for TPB_{MO} of proposed adsorption model for organometallic carbon atom locations relative to the (200) plane. Black arrows represent vectors based on proposed adsorption models. Measured coherent fraction and position values are shown in red and the model C_f and C_f values are given in the bottom right. (d) STM image of covalently bonded TPB on Ag(111) after annealing the surface, as shown in figure 5.12d. Molecular model, intermolecular separations and lattice vector directions are overlaid. (e) Proposed adsorption model for covalent phase of TPB. Models based on measurements obtained from STM images.

also results in a model that agrees well with the STM and XSW results. Of note is that adsorption models with molecular centres adsorbed above atop sites, and hence Ag adatoms in atop sites, gave calculated values for C_f and C_p incompatible with the experimental values. This may be rationalised by considering the lower stability of Ag adatoms adsorbed in atop sites for this model.

The proposed adsorption model has a molecular centre to centre separation of 1.53 nm, in agreement with STM measurements (1.63 ± 0.1 nm). Additionally, the adsorption model predicts molecules are aligned to the high symmetry directions of the surface at an angle of 19°, in rough agreement with the measured angle of

$25 \pm 2°$.

An Argand diagram showing the resultant C_f and C_p values for this model is shown in figure 5.15c. Based upon the model of the metal-organic phase of TPB values of $C_{f(200)-C1s} = 0.14 \pm 0.04$ and $C_{p(200)-C1s} = 0.70 \pm 0.03$ are obtained. These values are in agreement with the experimentally determined XSW values ($C_{f(200)-C1s} = 0.26 \pm 0.17$, $C_{p(200)-C1s} = 0.81 \pm 0.14$). It is important to note that the 'ranges' quoted on modelled C_f and C_p values account for variation in molecular flexibility. These variations give rise to several models which would fit with the experimental data due to minor changes in height and separation (D) of the organometallic carbon atoms, altering $C_{f(200)-C1s}$ and $C_{p(200)-C1s}$, while keeping the same high-symmetry adsorption site of the Ag adatoms and molecular centres.

As stated previously, these modelling methods could not be applied to develop adsorption models of covalent TP_{CC}, due to the complexity of molecules and the number of possible variables within the system. Adsorption models were instead produced using STM measurements of dimensions and angles relative to the surface. Structures were positioned relative to the underlying surface by attempting to align molecule centres to high symmetry sites. A tentative adsorption model developed using these methods is shown in figure 5.15e. TPB unit centres were found to be separated by 1.30 nm, at an angle of 4° to the surface $\langle\bar{1}10\rangle$ crystallographic directions. This agrees well with STM measurements (see above, section 5.5.2) of 1.31 ± 0.03 nm unit separation at an angle of $3 \pm 2°$ to the surface.

TP Lateral Adsorption Modelling

Using a similar method to that used for TPB, the lateral adsorption geometry of TP on Ag(111) was investigated by combining NIXSW and STM measurements. For TP_{MO}, only a single physically reasonable structural arrangement (with all Ag adatoms positioned above high symmetry sites) was found that agreed with both STM and XSW measurements. An example model is shown in figure 5.16b.

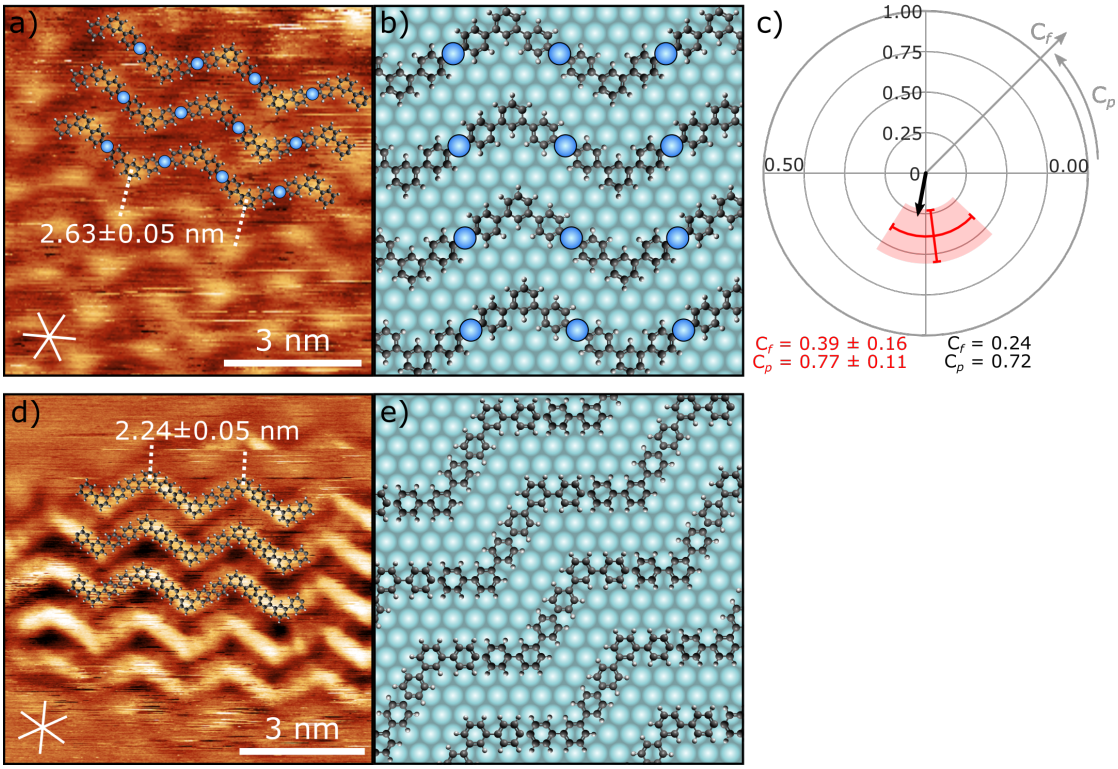


Figure 5.16: (a) STM image of TP in the metal-organic phase (TP_{MO}), as shown in figure 5.13b. TP units and silver adatoms are overlaid to show structures formed with molecule-molecule separation and surface lattice directions indicated (white - bottom left). (b) Proposed adsorption model for metal-organic phase of TP_{MO} on Ag(111) based on XSW modelling. (c) Argand diagram for TP_{MO} of proposed adsorption model for organometallic carbon atom locations relative to the (200) plane. Black arrows represent vectors based on proposed adsorption models. Measured coherent fraction and position values are shown in red and the model C_f and C_f values are given in the bottom right. (d) STM image of covalently coupled TP (TP_{CC}), as shown in figure 5.12d. Molecular model, intermolecular separations and lattice vector directions are overlaid. (e) Proposed adsorption model for covalent phase of TP (TP_{CC}). Model based on measurements obtained from STM images.

Molecule centres are adsorbed at similar bridge sites, with molecules in adjacent chains adsorbed at a different bridge site. Ag adatoms are found to alternate between adsorbing at bridge and atop sites and only bridge sites for adjacent chains.

The adsorption model shows zigzag chains to have a period 2.60 nm, at an angle of 0° relative to the $\langle\bar{1}10\rangle$ set of crystal directions, in agreement with STM measurements (2.63 ± 0.05 nm and -5° respectively). Additionally, the adsorption model has molecular chains separated by 1.13 nm which is in good agreement with

the measured value of 1.14 ± 0.05 nm.

An Argand diagram showing the resultant C_f and C_p values for this model is shown in figure 5.16b. For metal-organic TP, all valid models gave values of $C_{f(200)-C1s} = 0.24 \pm 0.01$ and $C_{p(200)-C1s} = 0.72 \pm 0.03$. Similar to models of TPB_{MO}, both C_f and C_p values are lower than expected from measurements ($C_{f(200)-C1s} = 0.39 \pm 0.16$, $C_{p(200)-C1s} = 0.77 \pm 0.11$) but still agree within the experimental uncertainty.

As with TPB_{CC}, simulations using NIXSW measurements of C_f and C_p values were not used to develop adsorption models of covalent TP_{CC}. Instead, adsorption models were developed based on measured dimensions and angles relative to the surface, attempting to align molecule centres to high symmetry sites. A tentative adsorption model developed using these methods is shown in figure 5.16e. Chains in this model have a period of 2.25 nm, are oriented at 30° to the underlying surface and are separated by 1.15 nm. These results are in good agreement with STM measurements of these structures, which were found to have a period of 2.24 ± 0.05 nm at an angle of 31° to the underlying surface, with chains separated by 1.19 ± 0.05 nm.

5.6 Conclusion

A combination of XPS, STM, and chemically sensitive NIXSW measurements were employed to characterise an on-surface Ullmann-type reaction. Through these techniques, the molecular conformation, adsorption geometries and role of substrate adatoms within the intermediate (MO) and final (covalently bonded) phases of the reaction were determined. Structural characterisation of the adsorption geometries for organometallic carbons, within the MO intermediate phase, indicates that it is metal adatoms that play an important role within the intermediate complex (and not atoms within the surface layer). It is therefore likely that strategies seeking to control on-surface reactions based upon limiting the availability of such species are a promising route towards bespoke functional materials.

This approach of utilising the exceptionally high-lateral resolution of STM alongside the chemical sensitivity and vertical resolution (relative to the plane of the substrate) of NIXSW underpins a methodology for accurately determining the 3D structure (specifically molecular conformations) at various stages of on-surface reactions. Such information is not easily obtained by scanning probe techniques in the absence of complementary experimental and/or theoretical approaches. Importantly, these findings demonstrate a universality for this type of on-surface reaction, specifically with regards to molecular conformations and the role of metal adatoms as indicated by the observed similarities for two structurally different aryl-halide functionalised molecules.

Chapter 6

On-Surface Synthesis within a Porphyrin Nanoring Template

Within previous chapters, the factors influencing on-surface Ullmann-coupling have been investigated. So far the focus has been on the role of surface topography on the geometry of reaction products, as well as determining the presence of surface adatoms in metal-organic intermediate molecular structures. This chapter builds on these results by exploring the use of molecular templates as a method to confine the Ullmann reaction. The use of a surface template in this way aimed to limit the access of reaction molecules to reaction sites such as metal adatoms and surface step-edges. Cyclic porphyrin polymer molecules were selected for use as a molecular template. Porphyrin nanorings were initially deposited onto a clean Au(111) surface, followed by the deposition of a reactant molecule. The sample was then annealed in order to initiate the Ullmann reaction. The resulting surface was then characterised by STM to determine the effectiveness of the porphyrin template.

6.1 Introduction

As discussed in chapters 2,4 and 5, the on-surface synthesis of 1D and 2D covalently bonded structures, performed on metal substrates under UHV conditions, has been achieved through a variety of different strategies [27, 39, 132–134]: facilitating the

synthesis of molecular chains [46, 47, 66, 97, 135, 136], graphene nanoribbons [6, 89], and 2D molecular frameworks[70, 71, 79].

Many studies have focused on the transfer of classical solution-phase reactions (for example, Ullmann coupling and Glaser coupling [133]) onto supporting substrates held under UHV conditions. Such reactions are often initiated via the interaction between the vacuum deposited monomer species and the catalytic surface, resulting in the breaking of covalent bonds (carbon-halogen bonds in the case of Ullmann coupling). This produces a reactive intermediate species that may then participate in the on-surface formation of a covalently bonded product. Confining molecules to two dimensions in this way can lead to stereo- and regioselective reaction pathways not seen in solution synthesis, due to confinement to the quasi-2D plane provided by the supporting substrate. This can in turn lead to the selective formation of low dimensional molecular structures.

Covalently bonded structures produced by implementing current on-surface synthesis protocols often exhibit a high degree of disorder, particularly over length scales greater than a few nanometers [79, 81]. A promising approach is to influence, and direct, the on-surface reaction by utilising the structure of the catalytically active surface. Previous studies have focused on two main areas. Firstly, native surface structures, such as step-edges [66, 97] or the topography of anisotropic crystallographic planes [74], have been used to align reactant molecules in a specific geometry, assisting the formation of more ordered structures. The results presented in chapter 4 demonstrate the importance of alignment of intermediate and product structures with the atomic corrugation of the substrate. Secondly, surface reconstructions such as Cu(110)-(2x1)O, have been produced for use as templates; spatially confining molecules in order to influence the structure of the covalently coupled products formed via an on-surface reaction [98].

More recently, the use of molecular structures as templates has been demonstrated by employing a self-assembled extended porous network to confine molecules, facilitating an investigation of reactions within the pores [44]. As discussed in chap-

ter 2, in this study a porous hydrogen-bonded supramolecular network was formed on a Ag(111) surface. Reactant species confined within these pores were then found to undergo breaking of intramolecular carbon-halogen bonds, with the substrate acting as a catalyst. This approach has the potential to allow catalytic surfaces to be templated by molecular systems, leading to surfaces with well-defined reactive regions. However, the internal dimensions of such networks can be similar to those of the precursor molecules and hence alternative templates for the formation of extended structures are required.

Some of the largest macromolecular systems synthesised to-date are porphyrin nanorings [111, 137] (cyclic structures consisting of 10s of covalently bonded porphyrin units) which offer an ideal porous material with which to template a catalytic surface. In this chapter, the use of porphyrin nanorings as a molecular template to constrain an on-surface Ullmann coupling reaction is investigated via room temperature STM under UHV conditions.

6.2 Characterisation of reactant molecule and molecular template

The reactant molecule used in this experiment was 1,3,5-tris(4-iodophenyl)benzene (TIPB), and is shown in Figure 6.1a. TIPB consists of a central phenyl ring with three outer iodobenzene groups and is known to react through an Ullmann-type coupling mechanism [80, 81, 138]. As part of the reaction the dissociation of the C-I bond within the TIPB molecule leads to the formation of a 1,3,5-triphenylbenzene (TPB) monomer unit, from which the extended polymers are formed (as discussed previously in chapter 5).

The molecule used to template the surface was a cyclic porphyrin structure [137, 139] - *c*-P40, shown in figure 6.1b. The ring consists of 40 Zn-centred porphyrin units, each with two 1,3-bis(octyloxy)benzene side groups, covalently bonded to form a cyclic polymer. *c*-P40 nanoring is synthesised using a method

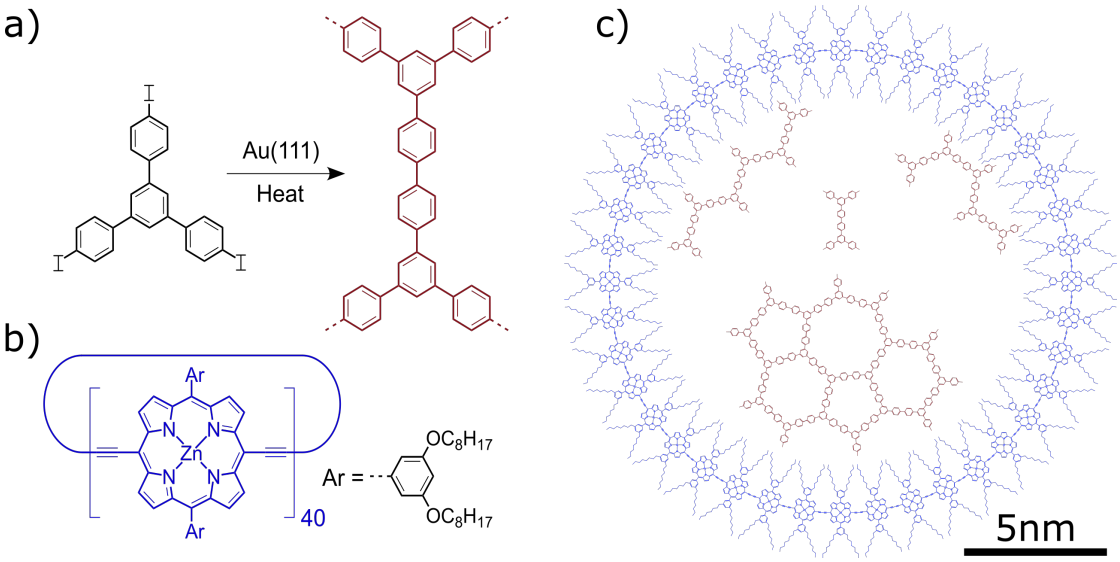


Figure 6.1: Chemical structures of TIPB and *c*-P40 molecular species. (a) Schematic diagram of the TIPB Ullmann-type coupling reaction forming covalently bonded structures. (b) Chemical structure of the *c*-P40 nanoring. (c) Schematic showing a *c*-P40 ring with examples of covalently bonded structures which may be formed via Ullmann-type coupling of TIPB inside the ring.

based upon Vernier templating described here [111, 137]. The geometry of the rings allows molecular species to be confined within a well defined area. This has been demonstrated previously using smaller nanorings (c-P24) to confine islands of C_{60} [140]. In this experiment, C_{60} was found to form close-packed islands of up to 37 units within the nanorings. In this work it is demonstrated that the pores are of sufficient size to allow extended covalent structures to form inside of them.

In order to visualise the relative dimensions of TIPB and the nanoring template, a structural model for a *c*-P40 ring and several potential reaction products (1D, 2D, and dimer) are shown in figure 6.1c. A single *c*-P40 (shown in blue) is used to contain several covalently bonded TIPB structures (red). These may consist of various linear chains and 2D networks, formed through Ullmann-type coupling of TIPB monomer units deposited inside the ring. Preliminary experiments to characterise TIPB and *c*-P40 individually on Au(111) via STM, were performed. Images of both molecules and the structures they form are shown in figure 6.2.

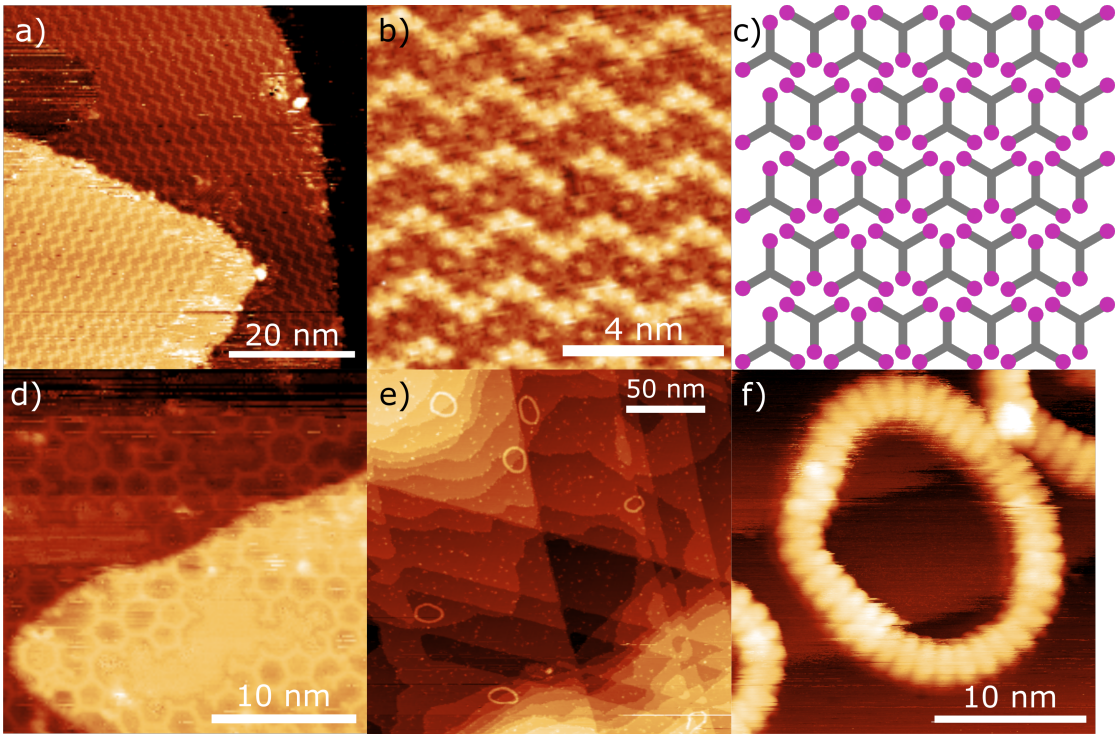


Figure 6.2: (a) STM image of the self-assembled TIPB zigzag structures formed on the Au(111) surface; demonstrating that iodine has not dissociated from the molecules (I_{set} = 30 pA, V = −1.8 V). (b) Close up of TIPB structures observed on Au(111), prior to annealing. (c) Structural model showing the regular zigzag arrangement formed by TIPB when deposited onto a Au(111) surface, prior to annealing. Purple circles represent iodine groups and grey lines the carbon backbone of the molecule. This structure has previously been reported [80]. (d) STM image showing a region of the two-dimensional extended network of covalently bonded TPB formed on Au(111) following activation of the on-surface reaction (I_{set} = 50 pA, V = 1.8 V). (e) Example overview STM image showing several stacks of *c*-P40 nanorings on Au(111) (I_{set} = 30 pA, V = −1.8 V). (f) Close-up STM image of a stack of *c*-P40 nanorings on Ag(111) showing clear resolution of individual porphyrin units (I_{set} = 10 pA, V = −1.8 V).

6.2.1 STM characterisation of TIPB

TIPB was deposited via sublimation from a Knudsen cell evaporator, heated to 180°C, for 5 minutes onto a Au(111) sample held at room temperature (Figure 6.2a and b). This was found to form a 'zigzag' phase, as observed previously [80], indicating that iodine had not dissociated from the molecule immediately following deposition. A model of this phase is shown in figure 6.2c, where grey trefoils represent the aromatic backbone of the molecule, with the position of iodine species indicated by purple circles. Annealing the surface to ∼110°C induced

catalytic cleaving of the C-I bonds within TIPB, leading to the formation of TPB as part of the Ullmann-type coupling reaction. TPB molecules were then observed to form two-dimensional networks, shown in figure 6.2d. The structures formed exhibit a non-regular arrangement, with cells of square, pentagonal, hexagonal, and higher-order polygonal symmetries [81, 83].

6.2.2 STM characterisation of *c*-P40

The large size of the *c*-P40 nanorings rings prohibits deposition via traditional UHV techniques, such as thermal sublimation, therefore an electrospray ionisation deposition technique was employed (see section 3.4.2 for details). This has been previously used for similar porphyrin based systems [137, 141]) and allows the molecules in solution to be transferred to a surface held under UHV. Similar approaches have been applied to investigate a range of molecules including proteins [142], single molecule magnets [141, 143], and a variety of other species [144, 145].

c-P40 was deposited from a solution of toluene and methanol (3:1 mixture) onto a clean Au(111) surface held at 10^{-6} mbar. A syringe pump was used to supply a constant flow of solution at a rate of 4 μL/hour to the spray emitter needle. Depositions were performed for a period of 30 minutes, with the electrospray event initiated by applying a potential difference of $\sim$1.8 kV between the emitter needle and entrance capillary to the UHV system.

When deposited onto a separate, clean Au(111) surface the *c*-P40 rings were observed to form stacks on the surface (figure 6.1e), typically 2-4 units high (between 0.4 and 1.0 nm). This is similar to that observed in previous experiments ($\sim$ 0.4 nm for double stacks, $\sim$ 0.7 nm for triple stacks, and $\sim$ 0.1 nm for single height rings [137]), where the number of rings in a stack can be affected by the composition of the solvent used for electrospray deposition [146].

No diffusion of the rings was observed during the STM measurements, with the adsorbed rings mainly present at step-edges. Sub-molecular resolution STM images of rings (performed of Ag(111)) allows features corresponding to individual

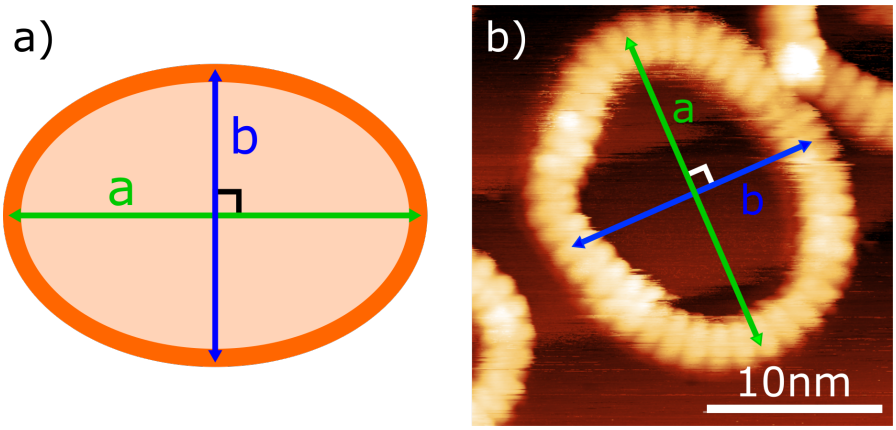


Figure 6.3: (a) Diagram showing major (a) and minor (b) axes of an ellipse. (b) Example image showing how measurements were made to calculate values for major and minor axes for nanorings. Image parameters: $I_{set} = 10$ pA, $V = -1.8$ V.

porphyrin units to be resolved (figure 6.1f), providing confirmation that each ring contained 40 units. The separation between each unit was found to be 1.31 ± 0.09 nm, in agreement with previous results (1.33 ± 0.07 nm [46]). Rings were found to have an average internal diameter of 13.0 ± 0.2 nm.

Additionally, *c*-P40 is known to be flexible and very few circular rings were observed, with most arranged in stacks of ovals. This was quantified by determining the average flattening factor, a measure of compression of a circle, for all observed rings on the surface. The flattening factor, f, of an ellipse is defined such that

$$f = \frac{a - b}{a}, \tag{6.1}$$

where a and b are the lengths of the major and minor axes of the ellipse respectively (figure 6.3a). A flattening factor of $f = 0$ corresponds to a perfect circle and a value of $f = 1$ to a flat line. Within this experiment, the flattening factor for nanorings was determined by measuring the lengths of the major and minor axes of each ring, and was found to be $f = 0.31 \pm 0.03$, from 61 measurements. An example of this is shown in figure 6.3b.

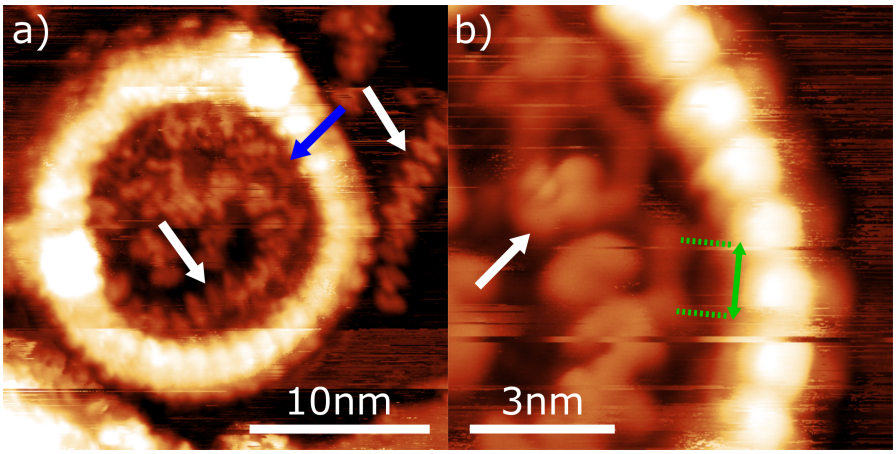


Figure 6.4: STM images acquired following the deposition of TIPB onto a Au(111) surface pre-patterned with *c*-P40 nanorings, followed by annealing the surface to ∼110°C. Images acquired with I_{set} = 20 pA, V = −1.8 V. (a) Image showing TPB covalently bonded structure inside *c*-P40 ring (blue arrow) and broken chains of porphyrins (white arrows). (b) Close up of (a) showing clear TPB covalent structure. Porphyrin chain covering structure indicated with white arrow. The size and direction of the average line profile of this TPB structure (shown in figure 6.6) is indicated in green.

6.3 Results

Following the studies of the homomolecular systems, a templated Au(111) surface was prepared by first depositing *c*-P40, obtaining a surface coverage of approximately 1.1 ± 0.3 *c*-P40 stacks per 100 nm^2. TIPB was subsequently deposited using the methodology described above. Heating the surface to ∼110°C initiated the Ullmann coupling reaction between the TIPB molecules and resulted in the formation of extended TPB structures. These were observed at several locations on the surface, both inside and outside of the stacked *c*-P40 rings. An example STM image of a *c*-P40 ring on the Au(111) surface is shown in figure 6.4a. Sections of porphyrin polymers, which are not part of the cyclic *c*-P40 rings, are observed on the surface, both inside and outside of the rings (indicated by white arrows in Figure 6.4a) and are attributed to *c*-P40 species in which a covalent bond connecting neighbouring porphyrin units has been broken. It is evident from these structures that the elevated temperatures required to initiate the on-surface coupling of TIPB also led to disruption of the *c*-P40 ring structures (via the breaking of covalent bonds within the nanoring).

Characterisation of the surface following annealing reveals that TPB structures

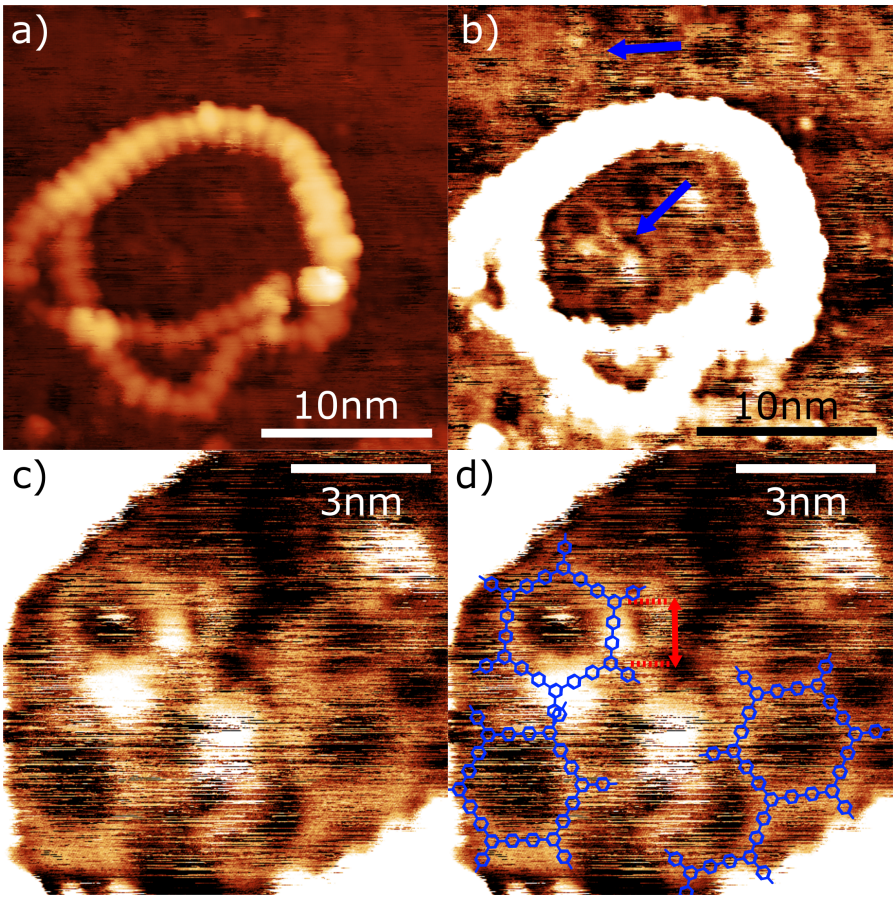


Figure 6.5: (a) STM image showing TPB structures seen inside and outside of a broken *c*-P40 ring. (b) STM image shown in (a) with adjusted contrast. TPB are structures seen inside and outside of *c*-P40 ring indicated with blue arrows. (c) Close up STM image of of TPB structures shown in (a) and (b). (d) Proposed molecular structures of TPB overlaid on (c). The size and direction of the average line profile for this TPB structure (shown in figure 6.6) is indicated in red. Images acquired with I_{set} = 20 pA, $V = -1.8$ V.

are present inside the *c*-P40 rings (figure 6.4a - blue arrow). A close-up image acquired within this ring is shown in figure 6.4b. The structures here are attributed to a chain of covalently bonded TPB units, potentially incorporating a TPB macrocycle (partially obscured by the broken *c*-P40 ring - white arrow).

An additional set of structures is shown in figure 6.5 where a distorted stack of nanorings is observed, with several cyclic network features present both inside and outside of the ring (the contrast in 6.5b has been 'enhanced' from (a) to show details of structures within the ring, leading to a corresponding reduction in the definition of the *c*-P40 ring). Figures 6.5c and d show a close up view of the TPB structures inside this ring.

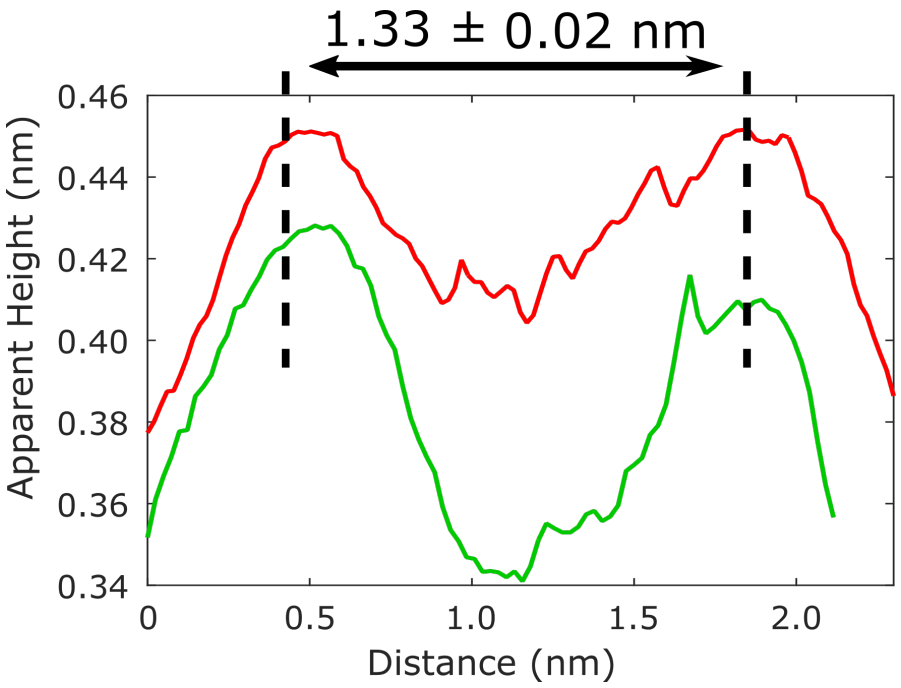


Figure 6.6: Average of 5 line profiles showing separation of TPB covalent structures in figures 6.4b (green) and 6.5d (red).

The separation of TPB units within the observed structures was then compared. Line profiles were taken between vertices of observed structures, from positions indicated in figures 6.4b and 6.5d in red and green respectively. These measurements are shown in figure 6.6. The separation of TPB units in both structures was found to be 1.33 ± 0.02 nm. These measurement agree with the expected value of 1.31 nm for four covalently bonded aryl units [81] and suggests that the observed structures are formed from covalently bonded TPB. Based on the covalent nature of the bonding between molecules, a model is proposed for the structures observed in figure 6.5. This is shown overlaid on an STM image in figure 6.5d and reveals a number of covalently bonded, cyclic TPB structures within the *c*-P40 ring.

Due to the mobility of material on the surface (e.g. motion of the porphyrin chain forming part of the broken ring) achieving stable imaging conditions within the stacked rings is challenging. However, it is evident from these measurements that the molecular structures observed within the *c*-P40 rings have the expected dimensions and geometry for the coupled product formed from TIPB species reacted within the porphyrin nanorings.

6.4 Discussion: Use of *c*-P40 as a porous molecular template

The methodology described above provides a promising route towards the application of macromolecular structures as templates for on-surface synthesis. It is, however, evident that there are also several technical limitations encountered as part of the current methodology which affect the formation and characterisation of extended TPB structures within the *c*-P40 rings. These limitations are outlined below

6.4.1 Thermal stability of *c*-P40 on Au(111)

Experiments conducted to determine the thermal stability of the rings in the presence of TIPB revealed that *c*-P40 thermally degrades at similar temperatures to those required to initiate the Ullmann-type coupling reaction (∼110°C). Heating samples to ∼105°C resulted in sections of the rings breaking (figure 6.7a). Further heating to ∼115°C produced similar results, with a slightly greater numbers of broken rings observed (figure 6.7b). Finally, after heating to ∼120°C almost no rings were observed on the surface, likely due to the majority of rings decomposing (6.7c).

Looking at these results in more detail, figure 6.7a shows two stacks of rings which have been affected by the anneal. The topmost ring of the left stack exhibits discontinuities in the observed contrast around the circumference of the ring (indicative of a break in the ring), and a section of the detached polymer material is observed within the pore of the ring. Similarly, the topmost porphyrin rings of the right stack exhibit discontinuities in contrast, but also appear to have been laterally displaced, with the upper layers of rings not resting upon the lower ones. Also commonly observed are linear chains of porphyrins, assigned to broken rings, seen both inside and outside intact rings. Examples of these are highlighted by white arrows in figure 6.7b.

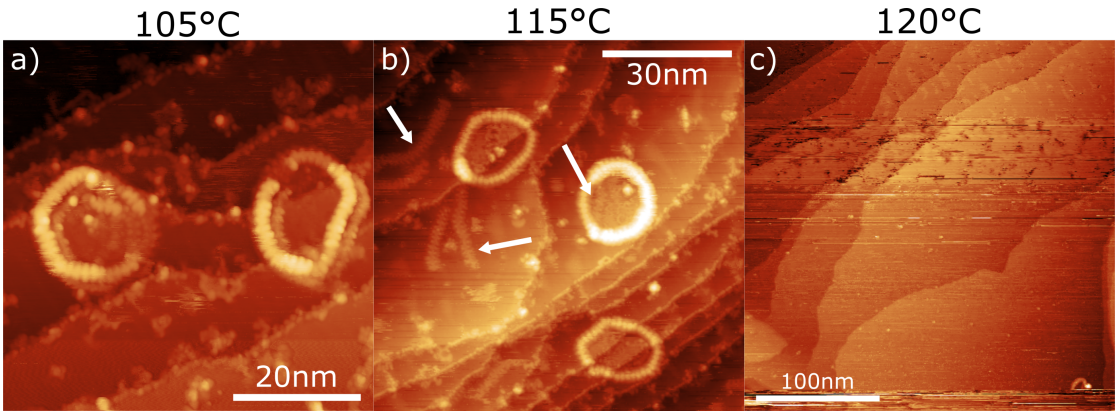


Figure 6.7: Details of the effect of elevated temperatures on the *c*-P40 rings in the presence of co-deposited TIPB. (a) STM image showing *c*-P40 rings after annealing the Au(111) surface to ∼105 °C for 30 mins. Rings are broken in several places and rings within stacks have been laterally displaced (I_{set} = 30 pA, V = −1.8 V). (b) STM image of *c*-P40 rings on Au(111) after annealing to ∼115°C for 20 mins. Broken porphyrin chains inside and outside rings are indicated (white arrows), (I_{set} = 20 pA, V = −1.8 V). (c) STM image acquired after an anneal of the surface at ∼120°C for 30 mins. The majority of rings on the surface are observed to break, with very little evidence for the presence of intact nanorings (I_{set} = 30 pA, V = −1.8 V).

These thermally decomposed structures create difficulties in both finding and imaging TPB structures on the surface. The weak intermolecular binding between the stacked rings (most likely mediated by π-π stacking) means that under standard tunnelling parameters (I_{set} = 20 pA, V = −1.8 V) it was observed that a spontaneous tip-sample interaction could result in the displacement or distortion of a stack of rings, preventing further imaging of that area.

6.4.2 Characterisation of co-deposited species

STM characterisation of the surface following electrospray deposition of *c*-P40 revealed that a contaminant species had been co-deposited. This was found to be present over the majority of the surface, as shown in Figure 6.8a, with such domains observed both inside and outside of the rings. A higher resolution image of this area (Figure 6.8b) shows several domains of the contaminant arranged in rows oriented at 120° relative to each other; likely to be aligned to the major crystallographic directions of the surface lattice. The separation of these rows

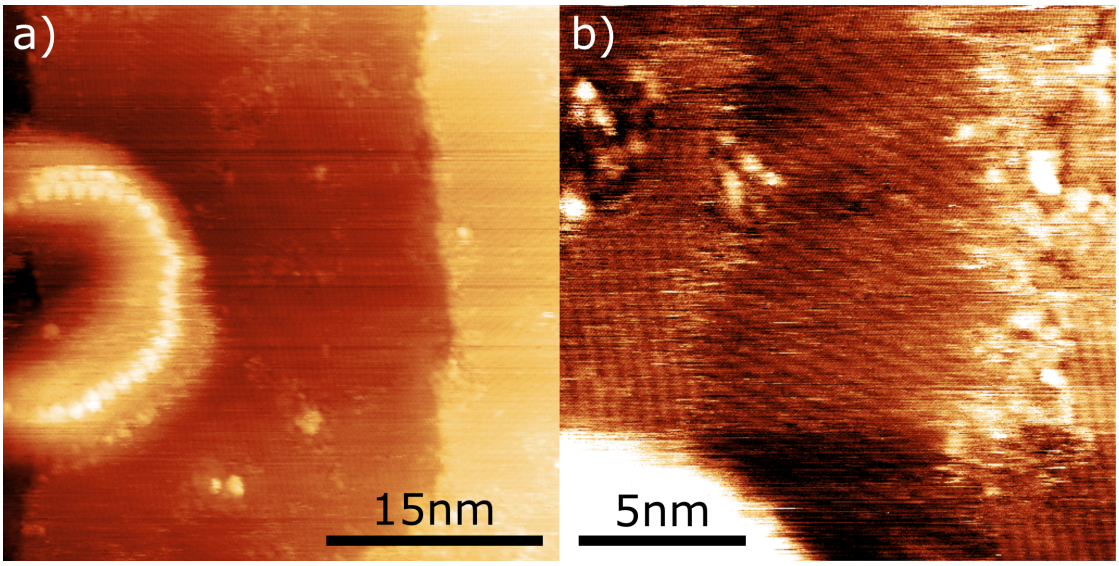


Figure 6.8: (a) STM overview image showing several large domains of co-deposited contaminant material the on surface (I_{set} = 20 pA, V = −1.8 V). (b) Close up of area in a) showing various domains of contaminant material (I_{set} = 20 pA, V = −1.8 V).

was found to be 0.51 ± 0.03 nm. Linear alkane chains are known to adsorb and form ordered domains similar to those observed here [13, 147]. It is therefore proposed that the contaminant consists of alkane chains either originating from the electrospray solvent, or potentially via decomposition of the *c*-P40 side groups. The observed contaminant is likely to have prevented TIPB adsorption on the surface in many areas (via a reduction in the sticking coefficient for TIPB incident upon the surface). In particular, the presence of the contaminant may have acted to passivate the surface, reducing the effectiveness of the surface as a catalyst. Overall, the co-deposition of the contaminant has the potential to limit the initial step of the Ullmann-type coupling process (C-I bond cleavage) required to form covalent bonds, reducing the efficiency of the on-surface reaction.

6.4.3 Implications for STM resolution within porous structures

It is also worth noting a more general point with regards to obtaining STM images within the pore of the cyclic porphyrin rings; in such cases the sharpness of the

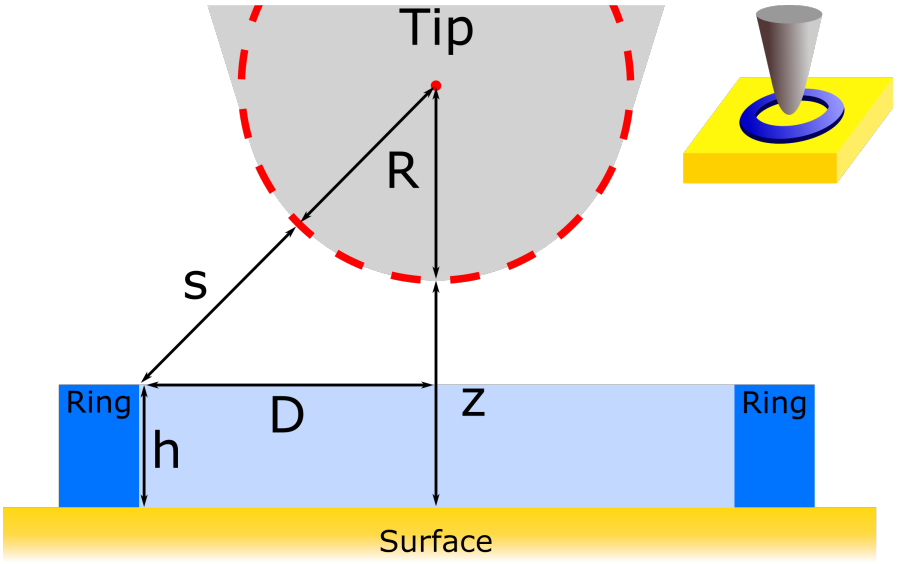


Figure 6.9: Schematic of tip-surface structure within a circular pore. Inset shows three dimensional perspective of the model.

STM probe (which can be qualified by the radius of curvature) may be comparable to the dimensions of the pore. Therefore, when imaging near the inside edge of *c*-P40 rings, the probe-surface separation and the separation between probe and the topmost ring within the stack may be of a similar magnitude - resulting in the measured tunnel current signal containing contributions, of similar magnitudes, from both the probe-surface and the probe- *c*-P40 ring interactions. Images produced this way will then be a convolution of both ring and surface states, resulting in the 'blurring' of the areas near the edges of rings. This effect is exacerbated for stacks containing several *c*-P40 rings, making the acquisition of images from an area inside a ring difficult. This issue can, in principle, be mitigated by preparing a high aspect-ratio STM probe. However, maintaining such a probe at room temperature (where diffusion of atoms at the apex of the probe is likely to be an important consideration) with a multi-component surface preparation (where diffusing molecular species may adsorb upon the probe) is particularly challenging.

The effect of imaging within a pore, with appreciable vertical height, upon the resolution obtainable can be seen through a simple model, shown in figure 6.9 as a cross section of the surface. The stack of rings is modelled as a hollow cylinder of height h. The STM tip can be considered a sphere of radius R, positioned a

distance horizontal D away from the ring stack and a height z above the surface. The distance s is the shortest separation between the edge of the ring stack and any part of the tip. Using this model, it can be shown that

$$(s + R)^2 = D^2 + (z + R - h)^2, \tag{6.2}$$

and this can be rearranged to give

$$s - z = \sqrt{D^2 + (z + R - h)^2} - R - z. \tag{6.3}$$

When the tunnel current originating from the ring stack (tunnelling through distance s) becomes comparable to the main tunnel current between tip and surface, the ring stack will have an effect on images produced. Due to the sensitivity to distance of STM measurements, with tunnel currents changing by an order of magnitude for a 1 Å change in separation, effects will be seen in images when $s \approx z$. The closest horizontal distance ($D = D_{min}$) the tip can get to the ring stack before tip-ring interactions are noticeable in the tunnel current signal therefore occurs when $s - z = 0$. Using this, equation 6.3 can be rewritten

$$D_{min} = \sqrt{h(2R + 2Z - h)}. \tag{6.4}$$

Figure 6.10a is a graph showing the variation of D_{min} with tip radius R at various ring heights and tip-surface separations. In this graph h was chosen to be 0.4, 0.7, and 1.0 nm, corresponding to the heights of 2, 3 or 4 nanorings respectively [137] and and z was chosen to be 0.1, 0.5, and 1.0 nm above the surface. From this graph several factors can be noticed. Firstly, variation in tip height has very little effect on tip ring interactions compared to other factors. An increase in tip radius however results in a large increase in D_{min}. This is as expected as a blunter tip (larger radius of curvature) will produce less clear images with lower resolution. The height of rings also has a significant impact on D_{min}, such that tip

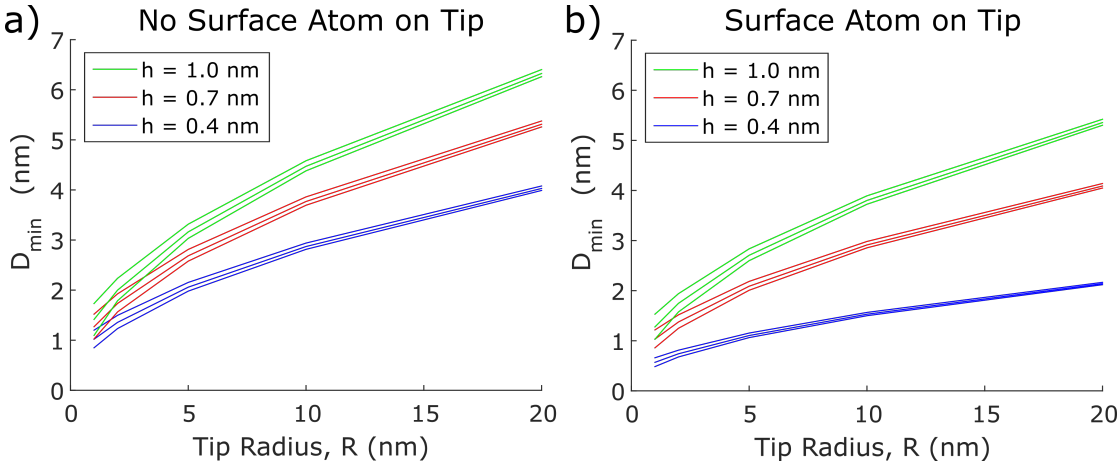


Figure 6.10: Graphs showing variation in the closest distance (D_{min}) the tip can approach a ring of height h before tip-ring interactions become comparable to tip surface interactions. (a) shows variation for a regular metallic tip of radius R and (b) shows variation for a tip of radius R, terminated in a Au atom of radius $r = 0.144$ nm. In each graph, variation is shown for ring heights of 0.4, 0.7 and 1.0 nm, corresponding to stacks of two, three and four nanorings respectively. Tip heights, z, above the surface of 0.1, 0.5 and 1.0 nm are also shown for each h value, with lower z values producing lower values of D_{min}.

ring interactions occur at shorter distances for shorter ring stacks meaning that the STM tip can image closer to the ring for small heights and will need to be further away from the ring for taller stacks of rings. Overall it can be seen that for all tip sizes and ring heights, images of areas taken within at least 1 nm of a ring will be affected by tip ring interactions and this distance is significantly increased for higher ring stacks and blunter tips.

This can be explored further by considering a tip terminated with a single Au atom of radius $r = 0.144$ nm, shown in figure 6.11. Following the derivation steps above, it is found that

$$s - z = \sqrt{D^2 + (z + R + 2r - h)^2} - R - z, \tag{6.5}$$

and under the conditions of $s - z = 0$ at $D = D_{min}$

$$D_{min} = \sqrt{h(2R + 2Z - h) - 4r(Z + R + r - h)}. \tag{6.6}$$

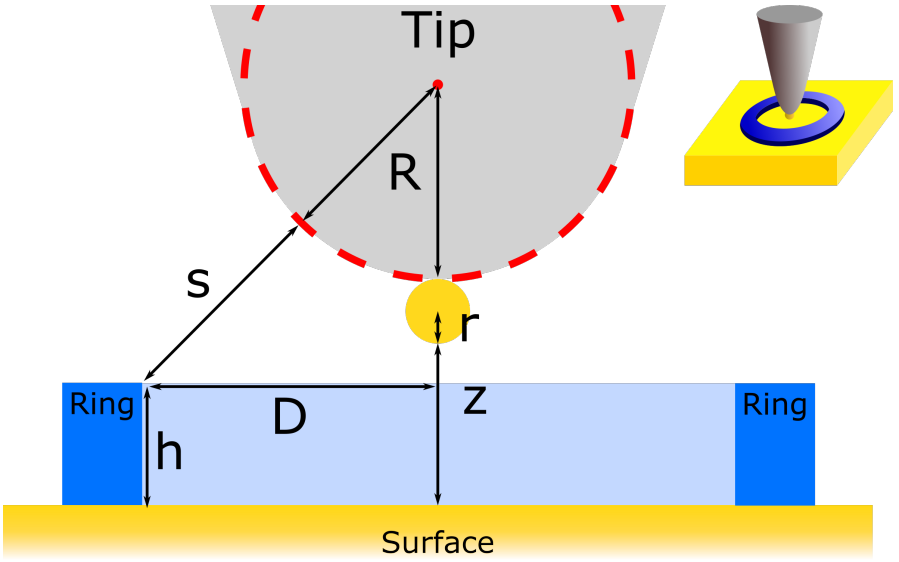


Figure 6.11: Extension of the model in figure 6.11 to include a tip terminated with a single Au atom.

This is similar equation 6.4 but with an additional factor in the square root. This factor results in a reduction in D_{min} for all h, R and z values. A graph of equation 6.6 (figure 6.10b) shows a similar trend to the case with no atom on the tip (figure 6.10a) but with all values of D_{min} reduced. This is as expected as tips terminated with surface atoms often produce images with better resolution. The result is significant however as it shows that images can be taken from 0.5 nm of the ring edge without significant contributions from tip-nanoring interactions. However, this requires very sharp tips, which can be difficult to prepare under room temperature conditions. This further increase the difficulty seen of imaging structures within rings, as seen in experiments. For these reasons it is possible that for "blunt" tips with $R \approx 15$ nm, the area inside three or four unit high stacks of rings will be convolved and have poor resolution.

Overall, from this geometric model, it is found that for stacks of rings consisting of three rings, combined with spherical probes of radius 15 nm or greater, it is expected that imaging inside a ring would lead to a considerable contribution to the measured tunnelling current from the interaction between the tip and the stack of rings, and hence STM images acquired in these regions will exhibit reduced resolution. This prediction supports the experimental observation that imaging

molecular structures within the rings is non-trivial, and potentially explains the low contrast variation between the TPB networks and the surface, (see figure 6.5b) as the STM current signal is influenced by the probe-ring interaction.

6.5 Conclusions

In conclusion, it has been demonstrated that *c*-P40 porphyrin nanorings can be used as a macromolecular template for the confinement of a reactant species, which can subsequently participate in an Ullmann-type on-surface coupling reaction. Covalently bonded reaction products were observed both inside and outside of rings and these products were characterised by room temperature UHV-STM. The use of *c*-P40 as a template for confinement however is limited by a number of technical issues; most notably the low thermal stability of the rings, and the requirement for deposition of *c*-P40 via electrospray (introducing contaminant species to the surface), both of which limit the probability for the on-surface reactions to proceed. Issues with characterising any structures within *c*-P40 have also been demonstrated, primarily due to the difficulty of preparing and maintaining a suitable sharp STM tip at room temperature on a multi-component surface. However, the results presented here demonstrate that large macromolecular structures can be used to template catalytically active surfaces, that on-surface reactions can be initiated within the pores of this templating structure, and that the reaction products can be observed within these templates.

Chapter 7

Molecular Quantum Rings

Following on from the use of c-P40 as a molecular template for on-surface synthesis, this chapter focuses on characterising the electronic structure of these nanorings. The effects of quantum confinement upon electrons within molecular nanorings is investigated, and through this their potential to act as quantum rings is explored. A combination of STM and STS measurements were used to experimentally probe the electronic states of c-P40 rings. These findings are supported through computational tight binding and density functional theory calculations. It was found that c-P40 molecules possess quantised energy states and localisation of electron densities, consistent with expected properties for quantum rings.

7.1 Introduction

Quantum rings are nanoscale ring structures that have been previously shown to exhibit interesting quantum phenomena due to the confinement of electronic states within a cyclic geometry. A notable example of such phenonema is persistent ring currents. Typically, electric currents induced in a circuit will dissipate energy without an applied voltage, with the current rapidly decaying to zero. However, quantum mechanics predicts that electrons may be able to flow through a resistive circuit, without dissipating. This effect has been demonstrated experimentally within quantum rings [148]. In addition to this, quantum rings have been shown

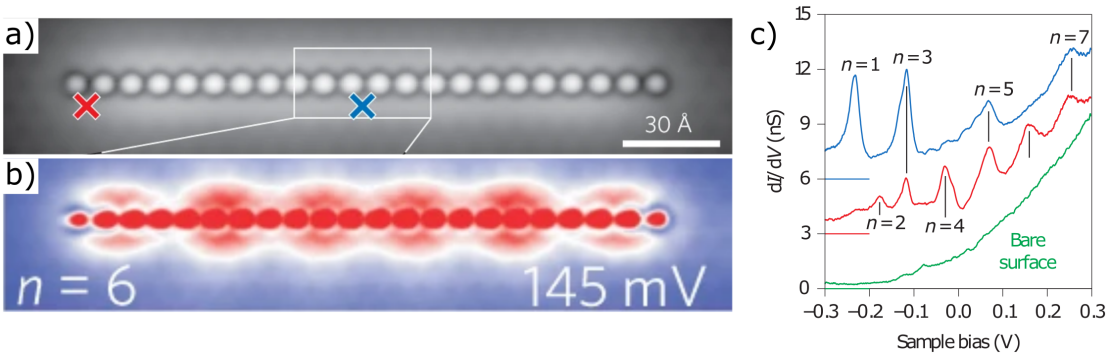


Figure 7.1: (a) STM image showing a chain of 22 In adatoms on InAs(111)A. Blue and red X's indicate positions of STS spectra acquisition. (b) A conductance map showing the localisation of energy states along the chain. Image obtained at a bias of 145mV and shows the n=6 quantum state. (c) STS spectra for different sections of the chain (blue and red, positions indicated in (a)) as well as a background spectra (green) of the pristine InAs(111)A surface for reference. Adapted from [150].

to exhibit the Aharonov-Bohm effect, where charged particles are found to be influenced by an electromagnetic potential, even in a region of zero electric or magnetic field [149]. Demonstrations of both of these effects act as verification for unique aspects of quantum mechanics.

Experiments have previously been performed to investigate the electronic structural properties of quantum rings and linear chains (acting as 1D potential wells), as well as detailing the quantum effects associated with them. One experimental approach is to use an STM tip to manipulate (see ref [1]) In adatoms into a linear chain, as shown in figure 7.1a where 22 In adatoms were aligned. The In adatoms within the chain are positively charged, creating an electrostatic potential which acts to confine electrons from the InAs surface. Electrons trapped in this way lead to quantisation of energy states within the chain. These can be modelled by considering confined electrons as a 'particle in a box', such that, for a chain of length L, the quantised energy states of the electron are given by

$$E_n = \frac{\hbar^2 k_n^2}{2m^*} = \frac{\hbar^2}{2m^*}\left(\frac{\pi}{L}\right)^2 n^2, \qquad n = 1, 2, 3..., \tag{7.1}$$

where k_n is the wave vector for the nth state, L is the length of the chain and

m^* is the effective electron mass. This behaviour was investigated by acquiring conductance maps in order to image the density of states around the chain for different energies. Imaging the nth state of the chain revealed n lobes and n-1 nodes along the chain, as expected by the wavefunction for a particle in a box. An example of this is shown in figure 7.1b where the $n = 6$ quantised state is imaged by scanning at an applied bias of 145 mV. Here, 6 clear lobes of high electron density can be seen. Additionally, STS spectra were acquired at different sections of the chain, indicated in 7.1a by blue and red X's. The spectra, shown in 7.1c, reveal clear resonant energy states when compared to a background spectra, taken above the clean InAs surface (green). Each of these states were assigned a quantum number n, and were found to agree well with predicted theory, with energy states E_n scaling approximately by n^2.

This idea was extended further to create a ring structure in order to examine quantum ring properties. As previously, an STM tip was used to manipulate 78 In adatoms into a hexagon structure on the surface [150]. This is shown in figure 7.2a. Using a similar model as described above and approximating the hexagon structure as a ring of radius R, the quantised energy states are given by

$$E_l = \frac{\hbar^2}{2m^*}\frac{l^2}{R^2} = \frac{\hbar^2}{2m^*}\left(\frac{\pi}{L}\right)^2 (2l)^2, \qquad l = 0, \pm1, \pm2, \pm3..., \tag{7.2}$$

where L is the ring circumference and l is the quantum number of angular momentum. As with the chain, conductance maps similarly showed localisation of the density of states around the ring. Imaging at increasingly higher energy states revealed $2l$ lobes of high electron density around the ring (figure 7.2b). Further to this, STS measurements acquired at different locations around the ring (indicated in 7.2a) demonstrated the quantisation of energy levels, with resonant peaks observed up to quantum numbers $l = \pm9$ (figure 7.2c). These results show qualitative agreement with electrons confined to a closed loop and act to demonstrate the energy structures within quantum rings.

The use of atomic manipulation to assemble quantum rings demonstrates that

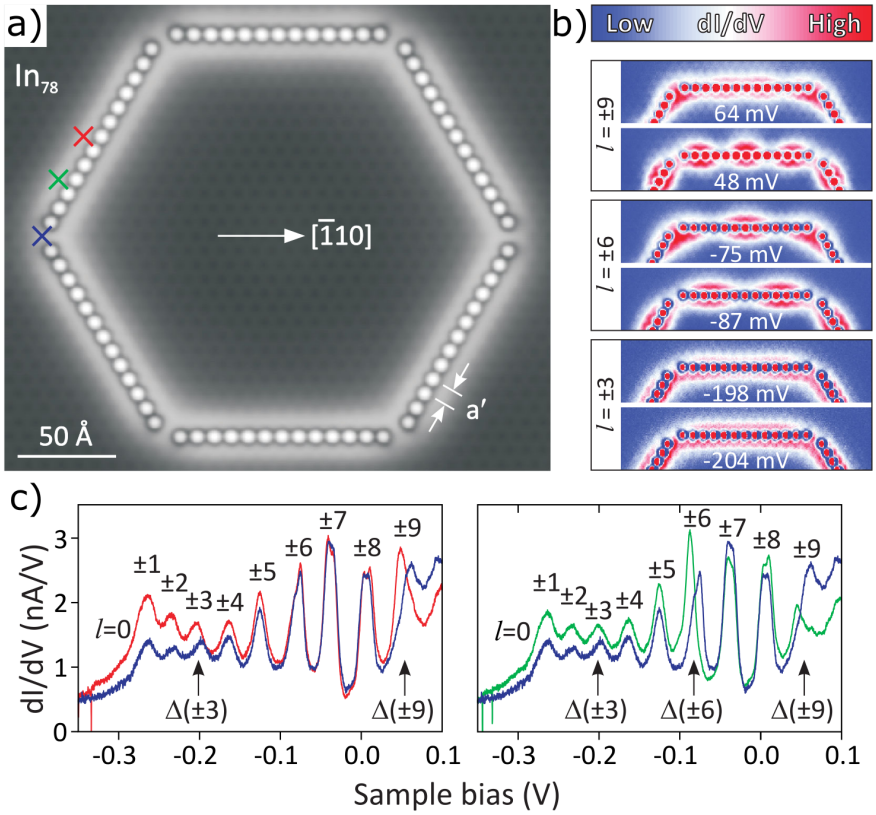


Figure 7.2: (a) STM image showing 78 In adatoms assembled into a hexagonal quantum ring. (b) Conductance maps showing formation of localised density of states for different imaging biases. (c) Comparisons of STS measurements taken at different positions around the ring (see crosses in (b)) showing quantisation of energy levels. Adapted from [151].

quantum confinement effects can be visualised within an idealised ring structure. However, assembling structures in this manner is labour intensive and time consuming, relying entirely on manual manipulation of atoms, making this technique difficult to scale up.

Efficient fabrication of quantum rings however can currently be achieved through growth on semiconductor samples (for example GaAs), using molecular beam epitaxy. In this technique, self-assembled quantum dots are capped with a semiconductor layer, thinner than the dot height. Subsequent annealing of the sample leads to redistribution of the quantum dot material and the formation of elongated ring shaped islands with a central crater. An example AFM image of the rings formed this way is shown in figure 7.3a. Using this method, a large number of quantum rings can be fabricated on a sample, reaching area densities of

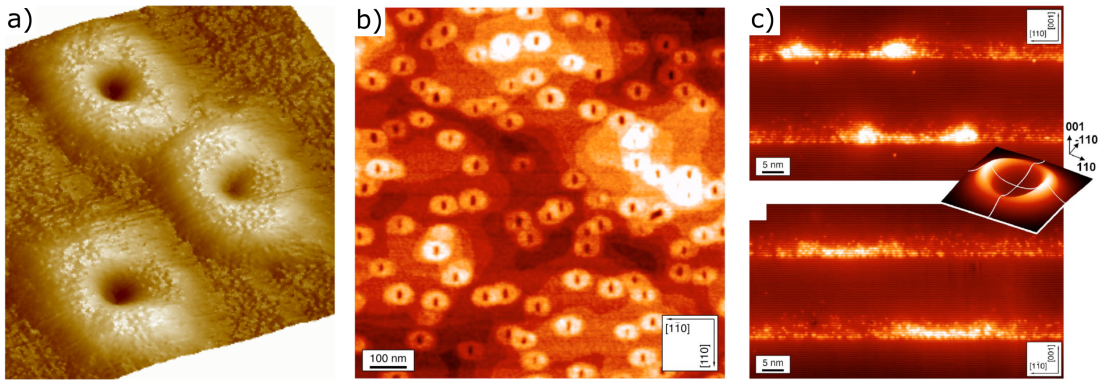


Figure 7.3: (a) AFM image showing semiconductor quantum rings. Taken from [152]. (b) Overview AFM image of large area (1×1 μm^2) showing the distribution of quantum rings over a sample. (c) Cross-sectional STM image showing example cross sections of quantum rings from two perpendicular directions. Inset shows modelled quantum ring based on these measurements. Adapted from [153].

$\sim$100 rings/μm^2 [153] (see figure 7.3b). However, rings produced in this way exhibit a large variation in size, with outer diameter varying between 60 and 140 nm [152]. Additionally, it has previously been shown that these rings exhibit uneven morphology. Figure 7.3c shows example cross sections of semiconductor quantum rings, acquired from orthogonal cleavage planes using a cross-sectional STM technique [153]. Here it was found that higher sections within rings were preferentially produced along the [110] direction (7.3c top) compared to the [1$\bar{1}$1] direction (7.3c bottom). This produces an asymmetric ring shape, with two higher lobes on opposite sides of the ring (7.3c inset). Computational studies have shown that variations in geometry such as these are likely to give rise to inhomogeneous broadening and shifting of the energy levels with quantum rings. [154, 155].

The methods for producing quantum rings outlined above show two extremes, between complete control of the structural properties of rings (adatom manipulation) and the ability to mass produce them (semiconductor rings). Each of these methods have a number of problems, as discussed above. A potential alternative is the use of molecular systems, for example cyclic porphyrin polymers, as molecular quantum rings. These cyclic polymers possess a delocalised π-conjugated electronic structure and have previously been shown to exhibit ring currents for

systems containing up to 12 porphyrin sub-units [156, 157]. The molecules are relatively simple to produce using a Vernier templating method [111] and porphyrin rings can be synthesised with a range of sizes, varying between 5-50 porphyrin units [137, 139, 158]. These can be preferentially selected through purification after synthesis to ensure a consistent geometry for all rings. Additionally, molecular rings are highly customisable, offering the option to functionalise the rings with different molecular groups or to substitute metal atoms at the centre of porphyrins.

In this chapter, the potential of cyclic porphyrin polymers as molecular quantum rings is explored. A combination of STM and STS techniques are employed to access the energy, and spatial position, of the electronic states of a 40 unit cyclic porphyrin polymer within stacks of 2-3 rings supported on a Ag(111) substrate. Additionally, computational calculations of the electronic structure of *c*-P40 rings were performed to support the experimentally obtained results. These calculations were preformed by Anton Nizovtsev in the group of Elena Besley (University of Nottingham, School of Chemistry). Experimental results were compared with density function theory (DFT) and extended tight-binding (GFN1-xTB method [159]) based calculations. Together, these indicated that the electronic states of the porphyrin rings within the stacks are similar to those of an isolated ring, and that the spatial distribution of the observed states is a consequence of coherent quantum confinement within the molecular quantum ring.

7.2 Geometric structure of *c*-P40 nanorings

The structure of the cyclic porphyrin nanoring (*c*-P40) studied here is shown in figure 7.4a. *c*-P40 rings were synthesised using a vernier templating method [111, 139]. Nanorings used in experiments consisted of 40 Zn-porphyrin units, functionalised with two 3,5-bis(octyloxy)phenyl side groups (Ar_1), covalently bonded via butadiyne linkers to form a cycic polymer.

c-P40 was deposited onto clean Ag(111) via electrospray ionisation (see chapter 6 for details). The sample was then transferred to an Omicron Low Tem-

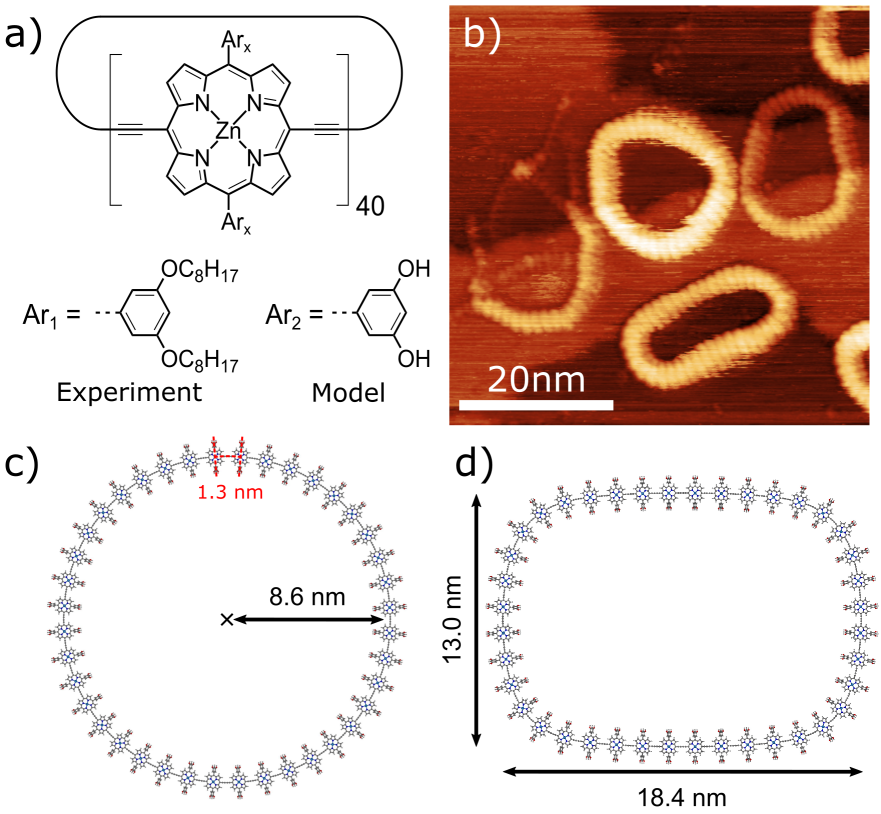


Figure 7.4: (a) Chemical structure of *c*-P40; side groups used in experiment (AR_1) and calculations (AR_2) are shown. (b) STM image of several *c*-P40 nanoring stacks on Ag(111) in different conformations, showing resolution of individual porphyrin units (I_{set} = 10pA, $V = -1.8$ V). (c) and (d) Energy minimised structure of *c*-P40 model (c) and structure of *c*-P40 constrained to average dimensions observed in experiment (d), calculated using an extended tight-binding approach (xTB).

perature STM system using a "vacuum suitcase" where resulting structures were characterised by STM with the substrate held under ultra-high vacuum (UHV) conditions at cryogenic temperatures (∼78 K).

The STM image presented in figure 7.4b shows stacks of between one and three *c*-P40 rings on Ag(111). The stacked nanorings are observed in a variety of non-circular geometries (due to the flexibility of the rings [137]) and the change in the observed contrast indicates variation in the number of rings within the stack [146] (a broken *c*-P40 ring to the upper left of the image exhibits image contrast comparable to that of an un-stacked polymer on the Ag(111) surface).

In order to facilitate computational analysis of these molecules, a geometry optimised structure of a single circular *c*-P40 molecule was calculated using a

xTB approach (details provided in Appendix C). This is shown in figure 7.4c, with the calculated diameter of the ring and separation between porphyrin units indicated, which are in good agreement with previous experimental observations (1.33 ± 0.07 nm [46]). In order to reduce computational time, the porphyrin side groups are substituted for truncated alkyl chains (Ar_2, figure 7.4a). In addition, an optimised structure using starting conditions based on the average dimensions of experimentally observed rings is shown in figure 7.4d. The small difference in energy between the two structures ($\Delta E = 0.15$ eV, structure shown in figure 7.4c is more favourable) accounts for the range of ring conformations observed in the STM data.

7.3 DFT and xTB calculations of electronic states of *c*-P40

The discussion of the electronic properties of the rings is underpinned by calculations of the energy levels of unoccupied/occupied orbitals and the spatial distribution of these states. The computational expense to calculate energy levels and molecular orbitals using DFT for the *c*-P40 structure is prohibitive due to its large size. Therefore a semi-empirical approach based on the GFN1-xTB method [159] was employed for the complete ring. The validity of the computational approach is first demonstrated by comparing short linear chains of porphyrins investigated by xTB and DFT levels of theory (see Appendix C for details). The highest/lowest lying occupied/unoccupied electronic orbitals were calculated for linear porphyrin chains consisting of N monomer units (l-PN, N = 1-7) using both xTB and DFT methods (figure 7.5a). Investigations were also performed into the use of the Δ self-consistent field (ΔSCF) technique to calculate the ionisation potential (IP) and electron affinity (EA) of the compounds under study, as these values have previously been shown to be comparable with experimentally measured quantities (see ref [160]).

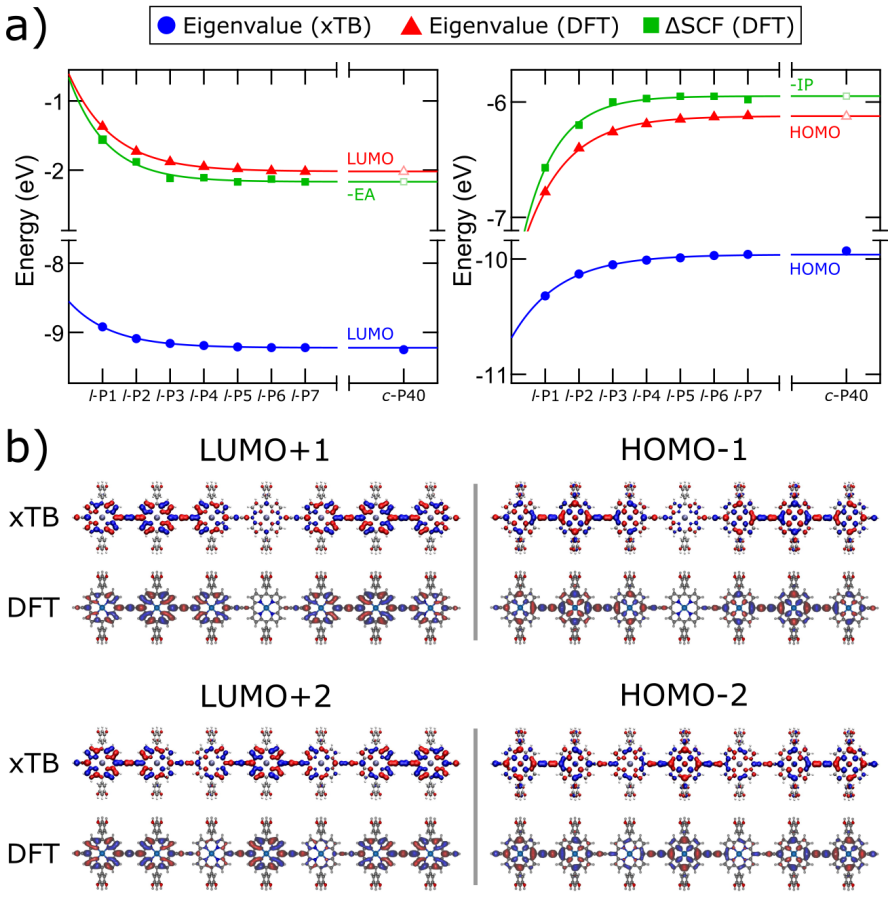


Figure 7.5: (a) Calculated energies of occupied and unoccupied states for linear porphyrin chains (l-PN, N=1–7) and *c*-P40 calculated with xTB and DFT methods (eigenvalue and ΔSCF techniques used to calculate the HOMO/LUMO and -IP/-EA values, respectively). Exponential curves are fitted using l-PN N = 1-7 and extrapolated values for *c*-P40 based upon DFT are shown (hollow markers). Break in x axis after l-P7 included for clarity. (b) Molecular orbital structures calculated for l-P7, (LUMO = lowest unoccupied molecular orbital, HOMO = highest occupied molecular orbital); calculated using xTB and DFT methods.

From figure 7.5a it can be seen that irrespective of the level of theory applied, the energy for all states converges as the length of the polymer chain is increased (l-P1 to l-P7). This convergence was modelled as an exponential dependence which shows good agreement with data. In the case of the xTB approach, direct comparisons between the extrapolated value for an l-P40 chain to that calculated for the *c*-P40 ring could be made. Energies for the lowest unoccupied molecular orbital (LUMO) were found to be -9.93 eV for the calculated xTB method and –9.96 eV for the extrapolated value from exponential model. The high level of agreement between these values allowed for a similar extrapolation, based upon

the DFT calculations for the chains l-P1 to l-P7, to obtain values for the *c*-P40 ring (hollow markers in figure 7.5a).

Comparisons were also made between the spatial distribution of molecular orbitals for l-PN (N = 1-7) as calculated by xTB and DFT methods (details of the l-P7 chain are shown in figure 7.5b). It is evident that there is good agreement with respect to the spatial position of the two orbitals immediately above the LUMO and below the highest occupied molecular orbital (HOMO). Both theoretical protocols predict a similar shape to the molecular orbitals, showing the same spatial distribution of localised clusters of higher electron density which match qualitatively with the expected solutions to electron confinement within a 1D potential well. The equivalence of these results indicates that xTB is a suitable method for the qualitative analysis of the electronic structure of large *c*-P40 nanorings.

7.3.1 Experimental characterisation of the electronic states of *c*-P40

Scanning tunnelling spectroscopy (STS) was subsequently used to gain insight into the electronic structure and molecular orbitals of the stacked *c*-P40 rings. In this technique the differential conductance (dI/dV) is measured as a function of applied sample-bias, with the tip held fixed at a specific point above the surface [99] (see chapter 3.1.4). Conductance spectra were acquired using a lock-in technique with a RMS bias modulation of 10 mV, with three repeat measurements averaged to produce one spectra. The acquired differential conductance is proportional to the density of states at that location and hence provides information on the energies at which resonant tunnelling occurs (attributed to electronic states present at that location).

STS spectra were obtained for a number of locations above stacks of *c*-P40. An example spectrum is shown in figure 7.6a, acquired on a nanoring at the position indicated in figure 7.6c (blue). A background spectra (figure 7.6b) taken above a clean area of the Ag(111) surface (green dot, figure 7.6c) shows no significant res-

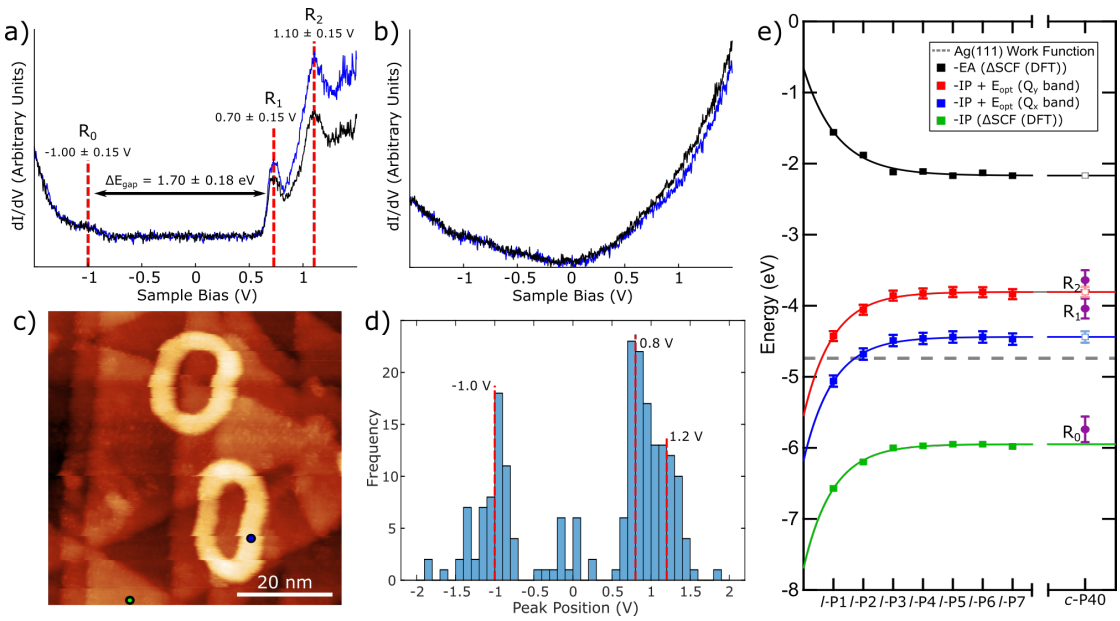


Figure 7.6: (a) Example forward (blue) and reverse (black) STS spectrum showing differential conductance as a function of applied sample bias. Peak positions indicated by dashed red lines and band gap energy (ΔE_{gap}) shown. (b) Background dI/dV spectra taken above the Ag(111) surface. (c) STM image showing locations where spectra were acquired. The blue dot shows the spectra acquired above the nanoring (a) and the green dot above the surface (b). Discontinuities in image occur due to small amounts of thermal drift between spectra measurements. (I_{set} = 40 pA, V = 1.5V). (d) Histogram showing the position of peaks observed in dI/dV spectra. 203 peaks were measured from spectra taken over 8 different rings. Red dashed lines indicate the estimated positions of resonances. (e) Energy levels of various electronic states as a function of polymer length. The experimentally determined values for electronic resonances R_0, R_1, and R_2 are shown.

onances, suggesting the STS measurements taken above *c*-P40 are not influenced by potential contaminants on the tip.

Three distinct electronic resonances are observed in the *c*-P40 spectrum. Those at approximately -1.00 V and 0.70 V, are labelled R_0 and R_1 respectively, with the additional higher energy resonance at 1.10 V being labelled R_2. The following interpretation of the observed resonances is based upon a comparison with the DFT calculated ionisation potentials, discussed above, and previously reported optical transitions of linear and cyclic porphyrin polymers, acquired by UV-vis absorption spectroscopy [161–163].

In figure 7.6e, the DFT-based ionisation potentials and electron affinities for l-P1 to l-P7 and *c*-P40 are presented. Also included are two data sets showing the

predicted excited state energies of the *c*-P40 structure based upon the calculated IP and literature values for the optical transitions (E_{opt}): i.e. Q_x (∼820 nm, 1.51 ± 0.08 eV) and Q_y (∼580 nm, 2.14 ± 0.07 eV) bands for *c*-P40 [163, 164]. A similar approach has been implemented for the STS-based analysis of oligoacenes [160]. Finally, the positions of the experimentally determined tunnelling resonances (R_0, R_1, and R_2) are referenced to the work function of Ag(111) (4.74 eV [165]).

Good agreement is found when comparing the expected separation between the Q_x and Q_y bands (0.63 ± 0.11 eV) and the measured gap between the R_1 and R_2 resonance (equivalent to 0.40 ± 0.14 eV). In addition, the measured separation between R_0 and R_1 (1.70 ± 0.18 eV) matches to the Q_x transition (1.51 ± 0.08 eV). From the data presented in 7.6e it is apparent that there is alignment between the DFT-calculated ionisation potential of the *c*-P40 ring and the experimentally observed electronic tunnelling resonance R_0; indicating that R_0 is associated with the electronic ground state of the molecular rings. The observation that the R_1 resonance does not agree with the calculated EA has been previously observed, for related systems [160], and may be attributed to the transient population of an excited state during tunnelling resonance as opposed to the creation of a negative charged species in the case of EA. However, one may interpret the resonances labelled R_1 and R_2 by considering -IP+E_{opt}; with R_2 corresponding to the Q_y transition (c.f. R_2 = -3.64 ± 0.14 eV and -IP + E_{opt} (Q_y)= -3.81 ± 0.07 eV) and R_1 assigned to the Q_x transition. It should be noted however that intrinsic flexibility of *c*-P40 will introduce variation in Q_x and Q_y [161], which may account for the discrepancy between R_1 and the Q_x transition.

7.3.2 Spatial Distribution of Molecular States

To study the spatial distribution of the molecular states at various energies (including resonant features R_0, R_1 and R_2) differential conductance maps, recorded over a range of sample biases, were acquired for several stacks of *c*-P40 nanorings. Figure 7.7 shows conductance maps of a single stack of rings on a flat area

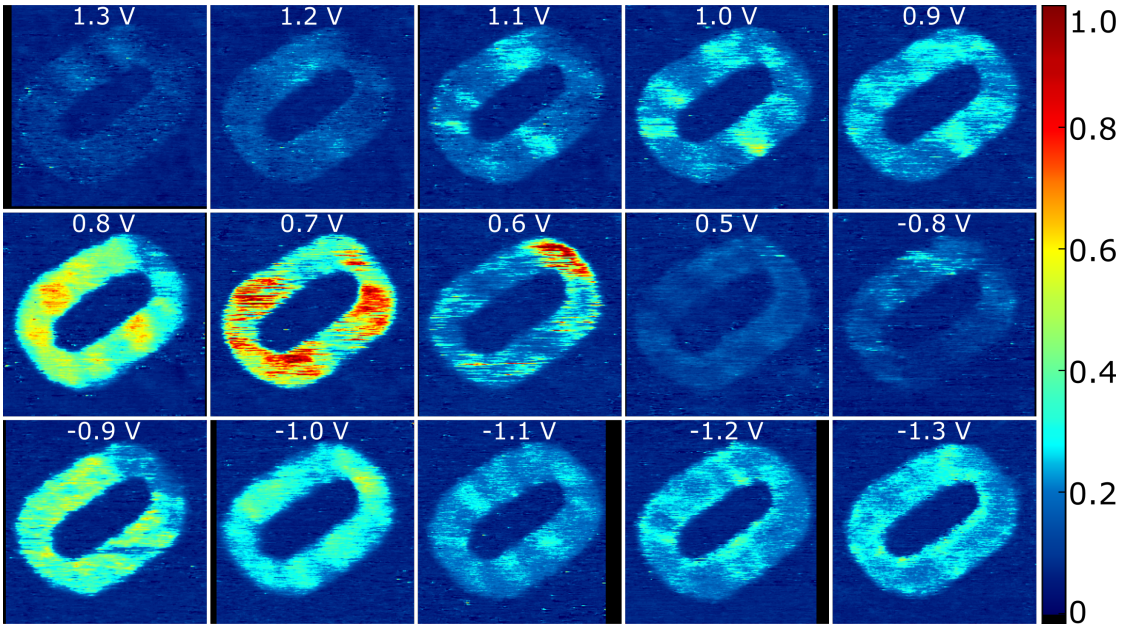


Figure 7.7: Differential conductance maps for a single *c*-P40 nanoring stack acquired for sample bias values +1.3 V to -1.3 V (intensity is normalised to maximum measured dI/dV across all images). Colour scale shows normalised differential tunnelling conductance (I_{set} = 40pA, image dimensions 28.4 x 28.4 nm). Bright contrast features occur at bias values matching observed peaks, R_0, R_1, and R_2, in dI/dV spectra. Bright "stripe" features visible for several biases.

(acquired at +1.3 V to - 1.3 V). In general, greater intensity is seen in images with biases in the ranges of -0.9 to -1.0V and 0.7 to 0.9 V (corresponding to the positions of the electronic resonances, R_0 and R_1, observed in STS spectra - figure 7.6a). For conductance maps acquired with an applied bias of -0.9 V and -1.0 V (corresponding to $\sim R_0$) the distribution of electronic structure is delocalised and although a variation in intensity is observed there is no obvious periodic structure. This is therefore likely due to a dominant contribution from the orbital structure of the *c*-P40 HOMO, where no spatial variation in orbital density was found. Increasing the sample bias to -1.1 V, allowing access to additional occupied states, results in the observation of a regular arrangement of 'stripe' features around the rings (qualitatively similar to that expected for coherent electronic states confined within a conducting quantum ring).

Focusing on the conductance maps acquired at the resonances R_1 and R_2 (+0.7 V and +1.1 V, respectively); the images show regions of higher and lower intensity

around the rings producing aperiodic bands. As the xTB calculations predict a very small difference in energy between molecular orbitals (e.g. <10 meV - see table C.1 in Appendix C), and as the energy resolution of the dI/dV maps is limited to ± 14 mV, the acquired conductance maps are likely to be a convolution of several molecular orbitals within this energy range. As such, the features observed will be a convolution of several structures and may exhibit a majority contribution from a particular state, depending on relative strengths of the tunnelling probabilities. The conductance map associated to R_1 is relatively diffuse, likely indicating a contribution from the LUMO and some higher lying unoccupied molecular orbitals. For the R_2 resonance the conductance maps show the appearance of banded structures; potentially indicating a contribution from a range of LUMO $+N$ states.

Returning to the spatial distribution of the bright 'stripe' features observed at -1.1 V, figure 7.8a shows a differential conductance map of the same ring as shown in figure 7.7 with the location and separation of each bright stripe feature indicated in figure 7.8b. At this energy nine stripes are observed, with an average separation of 5.8 ± 0.2 nm. Figure 7.8c shows how these separations were measured. The variation in differential conductance around the ring was visualised using the Straighten Path tool, from image processing software Gwyddion [166]. By defining a path around the ring, beginning at the red line shown in 7.8b and following the dashed blue line around the edge of the ring, a linear presentation of the contrast variation is produced (7.8c, right). From this, an averaged line profile (7.8c, left) was then taken of the distorted ring, and the separation of peaks measured.

These features can be compared to the xTB model of a nanoring with similar dimensions (figure 7.8d), where a spatially varying electron density is also observed. The periodic features observed in the experimental data will contain a contribution from several occupied states (the dI/dV image at -1.1 V is acquired at 100 mV below the experimentally determined HOMO which, based on the xTB calculations, would result in contributions from occupied states around the HOMO-8; see table C.1). Therefore, it is expected that the spatial distribution of the electron density

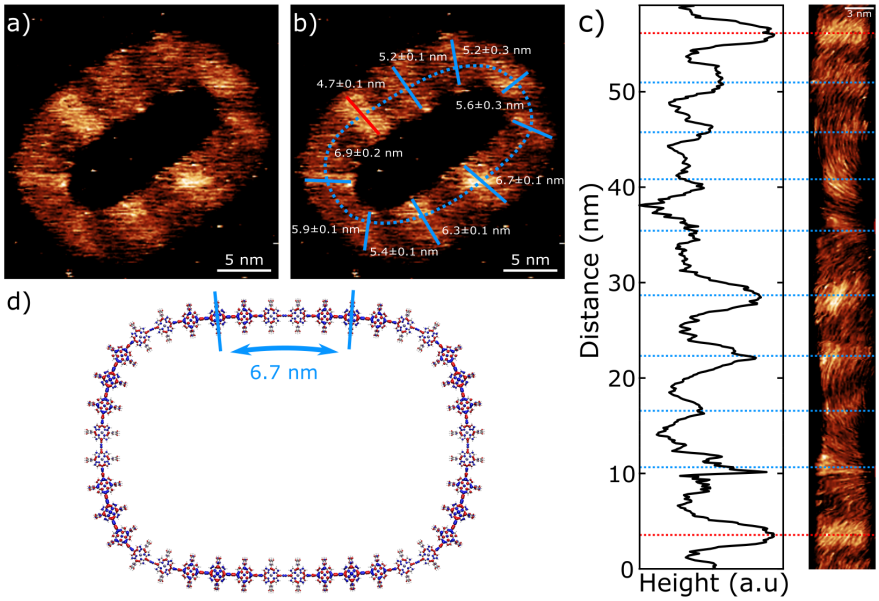


Figure 7.8: Comparisons of stripe features observed in computational models and experiment. (a) Conductance map measurement acquired at -1.1 V showing bright stripe features. (b) Conductance map shown in (a) with blue lines highlighting the position of stripe features. The average separation of bright features (measured approximately along dashed blue line) is shown for each feature. (I_{set} = 40 pA). (c) Example showing how stripe feature separations were measured. Beginning at the red line (shown in (b)), a distorted image (right) of the ring was produced. An averaged line profile (left) was then taken of the distorted ring, and the separation of peaks measured. (d) Model of *c*-P40 HOMO-8 energy level (xTB), showing alternating areas of high electron density separated by 6.7 nm.

related to all accessible energy levels should be visible, with the intensity observed in the image weighted due to the electron-tunnelling transition probability.

Based upon the separation between the 'stripes' in the dI/dV image in figure 7.8b, qualitative agreement is found with the calculated structure of the HOMO-8, where eight regions of higher electron density are observed with a separation of 6.7 nm between them. Such a finding indicates that there is a contribution from the HOMO-8 state. However, it should be noted that the intensity of the 'bands' is not uniform, denoted by the variation in contrast within 7.8a, and in agreement with the assertion that a convolution of electronic states is observed in conduction maps. The relative contributions from different states will be dependent upon both the local density of states at a given energy and the tunnel barrier (which will increase for states further away from the Fermi level). It is important to note

that such features (irrespective of the electronic state they originate from) are a characteristic of coherent electron state which is delocalised around the *c*-P40 nanoring.

7.4 Conclusions

In summary, it has been experimentally shown by a combination of STM and STS that stacks of conjugated porphyrin polymers supported on a Ag(111) surface possess quantised states and that these states are coherent around the ring with well-defined spatial distributions. These findings are supported by DFT and xTB calculations in combination with literature values of optical band gaps for these systems. This is the first demonstration of the characterisation of the spatial and energetic electronic structure of such porphyrin rings which have the potential to act as molecular quantum rings. Tuning the properties of these rings may be facilitated in future work by altering their chemical composition, for example by varying the metallic species within the macrocycle, or changing their size/structure in order to provide customisable quantum molecular rings.

Chapter 8

Conclusions

This chapter summarises the work performed within this thesis and outlines the important findings.

8.1 Summary of findings

The work within this thesis has focused on understanding the progression of on-surface reactions and how such reactions can be influenced. A detailed understanding of these concepts offers the potential to better control on-surface reactions, which in turn can lead to methods to produce more organised surface structures or discover unique reaction pathways for synthesis.

Investigations were performed in chapter 4 into the effects of surface topography on the formation of molecular surface structures as part of the Ullmann coupling reaction. The precursor molecule, DITP, was deposited onto two different surface facets of silver, Ag(111) and Ag(110), producing islands of zigzag structures, with molecular units linked via Ag adatoms, through metal-organic bonds. For each surface, the structural dimensions were characterised via STM imaging, through which adsorption models for each system were proposed. It was found that C-Ag-C bonds stretch to allow the formation of commensurate structures, producing different sized structures on each surface. Annealing the samples then led to the removal of metal adatoms and the formation of covalently coupled zigzag structures.

Comparisons of metal-organic and covalently coupled products revealed structures on Ag(111) underwent a 30° rotation in order to achieve commensurability with the surface, whereas this was not observed for the Ag(110) surface. These results clearly demonstrate the influence of substrate on formation of surface structures within on-surface synthesis. In particular, the alignment of both the intermediate and product along the same crystallographic direction on Ag(110) may provide a route to more efficient synthesis.

This work was then built upon in chapter 5 by using a combination of NIXSW and STM measurements to generate 3D adsorption models for DITP and TIPB molecules on Ag(111). Initial characterisation through XPS found dissociation of iodine from molecules upon deposition, and the presence of two carbon environments, assigned to aromatic and organometallic carbon atoms, with subsequent annealing showing only aromatic carbon atoms present on the surface. NIXSW measurements were then used to characterise the vertical adsorption of molecules through use of (111) surface reflection. From these results, it was determined that end phenyl groups within molecules were twisted by $\sim$30° relative to the central phenyl group. Additionally, organometallic carbons were found to adsorb significantly closer to the surface than aromatic carbons within each molecule, however, not close enough to form metal organic bonds with bulk surface atoms. This was used to determine molecules most likely form metal-organic bonds with surface adatoms.

Additional NIXSW measurements were then acquired from the (200) reflection for use in triangulation calculations. These were combined with STM imaging measurements of structure dimensions and their alignment relative to the surface. Utilising these results, models were developed to determine lateral adsorption locations for organometallic carbon atoms in both molecules, from which the adsorption locations of the rest of the molecule could be inferred. Overall these experiments provide a greater understanding of the process of the Ullmann coupling reaction.

Methods to control on-surface coupling reactions were then explored in chapter 6. Large cyclic porphyrin polymers, c-P40, were utilised as molecular template to confine the Ullmann coupling reaction of TIPB, in an attempt to limit the reaction sites accessible by molecules, such as surface step edges and diffusing metal adatoms. Both molecules were successfully deposited onto a Au(111) surface utilising a combination of sublimation and electrospray deposition techniques. After annealing the surface to initiate the Ullmann coupling reaction, covalently bonded structures within the nanoring template were observed through STM imaging. Limitations in the thermal stability of c-P40 nanorings however reduced its effectiveness as a template. Additionally, the co-deposition of a contaminant species was observed, which likely acted to reduce the catalytic effect of the surface, hindering the reaction. Overall however, these results demonstrated that macromolecular structures can be used to template a surface and on-surface reactions can be initiated within them to produce covalent products.

Finally, chapter 7 further investigated c-P40 nanorings, focusing on their electronic properties as well as their potential to act as molecular quantum rings. These nanorings offer advantages over current methods to produce quantum rings, such as their relative simplicity to mass manufacture (compared to other techniques) as well as being highly customisable through altering their size and structure or their chemical composition. STS spectra were obtained for stacks of c-P40 rings on Ag(111), revealing three quantised energy resonances. These measurements were supported by computational xTB and DFT calculations of molecular orbital energies which showed good agreement with experiment. Further to this, conductance maps revealed localisation of electron densities around the ring which varied with applied bias. This was compared to computational calculations of the distribution of molecular orbitals and revealed quantum confinement effects. Combined, these ideas demonstrate the quantum effects seen within c-P40 and suggest the possibility for porphyrin nanorings to act as quantum rings.

This work provides a greater understanding of on-surface reactions and the fac-

tors that influence them. Going forward, this offers the potential to better control on-surface reactions, leading to improved order in extended surface structures and enhanced selectivity of reactions.

Appendix A

List of Abbreviations

AFM	Atomic force microscopy
BrTPP	Bromo-tetraphenyl porphyrin
CC	covalently coupled
CHP	cyclohexa-*m*-phenylene
c-P40	40 unit cyclic porphyrin
DFT	Density functional theory
DITP	4,4”-diiodo-*m*-terphenyl
DMPT	4,4"-dibromo-*m*-terphenyl
ΔSCF	Δ self-consistent field
EA	Electron affinity
fcc	Face-centred cubic
GNR	Graphene nanoribbon
hcp	Hexagonal close-packed
HOMO	Highest occupied molecular orbital
IP	Ionisation potential
LDOS	Local density of states
LEED	Low-energy electron diffraction
LUMO	Lowest unoccupied molecular orbital
MO	Metal-organic
NIXSW	Normal incidence X-ray standing wave
PTCDI	3,4,9,10-perylene tetracarboxylic acid diimide
SPM	Scanning probe microscopy
STM	Scanning tunnelling microscopy
STS	Scanning tunnelling spectroscopy
TIPB	1,3,5-tris(4-iodophenyl)benzene
TP	*m*-terphenyl
TPB	1,3,5-triphenylbenzene
TPP	tetraphenyl porphyrin
UHV	Ultra high vacuum
XPS	X-ray photoelectron spectroscopy
XSW	X-ray standing wave
xTB	Extended tight-binding

Appendix B

Structural Characterisation of an On-Surface Reaction

This chapter provides additional information on the 'twisting model' employed within chapter 5 as part of the structural characterisation. The model is used to determine the angle of rotation of outer phenyl groups in deposited molecules. The mathematical model is presented in greater detail and the equation used to determine twist angle is shown. The values used for calculations and results of the model are tabulated.

B.1 An Idealised Twisting Model

In order to determine the twisting of side groups in DITP and TIPB from NIXSW data, a simplified model was developed (as employed within chapter 5). This is shown in figure B.1. Within this model, the central phenyl group for all molecules is flat and planar relative to the surface and rests at a single distance, d, from the closest reflecting plane. This position is defined as the molecular plane. Side phenyl groups are twisted around a central axis on the molecular plane (orange dot) by an angle Θ. This results in carbon atoms towards the edge of the phenyl

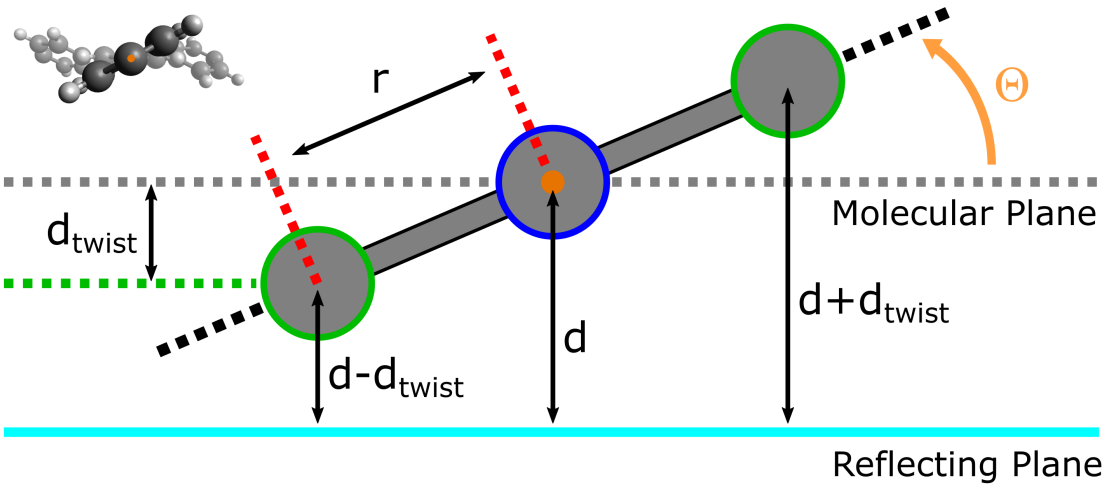


Figure B.1: Model for calculating twisting angle for TP and TPB using NIXSW measurements. Average molecule height is shown as the molecular plane a distance d above the closest reflecting plane. Grey circles represent carbon atoms as part of the phenyl side groups of TP/TPB, with blue highlighted atoms in line with the molecular plane and green highlighted atoms twisted by angle Θ such that they are offset from the molecular plane by distance d_{twist}. Green carbon atoms are a distance r from the axis of rotation (orange dot). Inset (top right) shows an example TPB unit with twisted side phenyl groups as in this model.

group being displaced from the molecular plane by a distance d_{twist} such that

$$d_{twist} = r \sin \Theta, \tag{B.1}$$

where r is the separation of an atom and the axis of rotation.

Due to the rotation, one side of the phenyl group is brought closer to the reflecting plane ($-d_{twist}$) and the other further away ($+d_{twist}$). This has the result that the average height of the molecule is still on the molecular plane. From this, the total coherent position (C_p) of all molecules in the model can be defined such that

$$C_p = \frac{d}{D} \tag{B.2}$$

where D is the separation of the reflecting planes.

Using this model the coherent fractions (C_f) of different atoms can be defined such that

$$C_{f_{fixed}} + C_{f_{twist}} = 1, \tag{B.3}$$

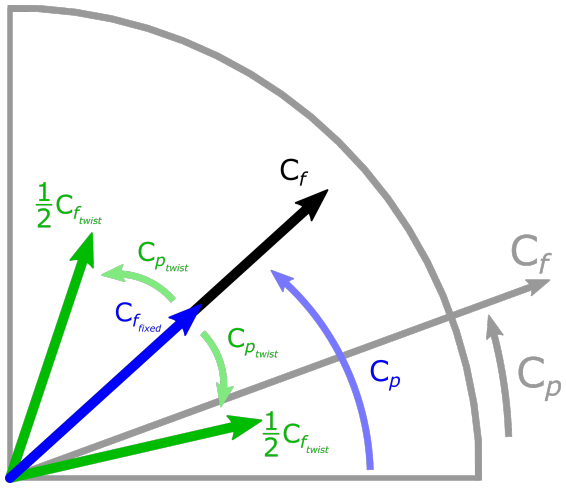


Figure B.2: Example Argand diagram showing for coherent fraction (C_f) and position (C_p) values for the ideal twisting model. Blue vector represents fixed atoms (in line with molecular plane) and green vectors represent twisted atoms (above or below molecular plane). Black vector represents the total coherent fraction and position vector for the model.

where $C_{f_{fixed}}$ is the fraction of atoms on the molecular plane and $C_{f_{twist}}$ is the fraction located above or below due to twisting. The coherent position values for fixed atoms can be seen to be equivalent to the total coherent position ($C_{p_{fixed}} = C_p$) and the coherent position for twisted atoms are $C_p \pm C_{p_{twist}}$. This is shown as an Argand diagram in figure B.2.

B.2 Derivation of the relationship between coherent fraction and twisting angle

For a discrete number of atomic positions, n, equation 3.24 becomes

$$C_f e^{2\pi i C_p} = \sum_n C_{f_n} e^{2\pi i C_{p_n}}. \tag{B.4}$$

Applying this to the ideal twisting model above, C_f and C_p values can be calculated such that

$$\begin{aligned} C_f e^{2\pi i C_p} = & C_{f_{fixed}} e^{2\pi i C_{p_{fixed}}} \\ & + \frac{1}{2} C_{f_{twist}} e^{2\pi i (C_{p_{fixed}} + C_{p_{twist}})} \\ & + \frac{1}{2} C_{f_{twist}} e^{2\pi i (C_{p_{fixed}} - C_{p_{twist}})}, \end{aligned} \tag{B.5}$$

where the first term describes fixed carbon atoms and the second and third terms describe twisted up and twisted down carbon atoms respectively.

As discussed above, $C_{p_{fixed}}$ is equivalent to the coherent position of the molecule, C_p, so equation B.5 simplifies to

$$C_f e^{2\pi i C_p} = e^{2\pi i C_p} \left(C_{f_{fixed}} + \frac{1}{2} C_{f_{twist}} \left(e^{2\pi i C_{p_{twist}}} + e^{-2\pi i C_{p_{twist}}} \right) \right), \tag{B.6}$$

and

$$C_f = C_{f_{fixed}} + \frac{1}{2} C_{f_{twist}} \left(2 \cos \left(2\pi C_{p_{twist}} \right) \right). \tag{B.7}$$

From equation B.3, this can be expressed in terms of $C_{f_{fixed}}$

$$C_f = C_{f_{fixed}} + \left(1 - C_{f_{fixed}} \right) \cos \left(2\pi C_{p_{twist}} \right). \tag{B.8}$$

Finally, using equations B.1 and B.2 this becomes

$$C_f = C_{f_{fixed}} + \left(1 - C_{f_{fixed}} \right) \cos \left(\frac{2\pi r \sin \Theta}{D} \right). \tag{B.9}$$

All of these, except Θ, are known quantities and so can be used to calculate a value of twisting angle for each system used in experiments.

B.3 Results

Using equation B.9, values for Θ were determined for both TP and TPB in MO and covalent phases of the Ullmann reaction. r was determined to be 0.1205 nm, based on molecular mechanics simulations of TPB and TP [167]. $C_{f_{fixed}}$ values

Molecule		C_f	$C_{f_{fixed}}$	Θ
TP	MO / Aromatic	0.49 ± 0.03	$1/2$	$28.7 \pm 1.1°$
	Covalent / Aromatic	0.56 ± 0.03	$5/9$	$27.9 \pm 1.2°$
TPB	MO / Aromatic	0.50 ± 0.02	$9/21$	$26.1 \pm 0.6°$
	Covalent / Aromatic	0.43 ± 0.06	$1/2$	$31.0 \pm 2.6°$

Table B.1: Values used and results of end phenyl twisting calculations

were determined from the number of carbon atoms at each position. For example TPB_{CC} has 12 carbon atoms level with molecular plane (6 for the central phenyl group and 2 in each of the outer phenyls) out of a total 24 carbons, giving $C_{f_{fixed}} = 1/2$. It should be noted that organometallic carbon atoms are excluded from calculations of $C_{f_{fixed}}$ for MO phase structures, as only the C_f values for aromatic carbons are used here. $C_{f_{fixed}}$ values were multiplied by 0.95 to account for small fluctuations in atomic positions caused by effects such as thermal vibration. Finally, C_f values were obtained from NIXSW measurements of molecules relative to the (111) reflection (see section 5.3).

Results of all calculations are given in table B.1. Uncertainty values associated with Θ are calculated from propagation of uncertainty of experimental C_f values, from equation B.9. From these results, it can be seen that all twist angles have similar values of $\sim 30°$. It should be noted that in section (5.3.4) molecules in the MO phase were found to not be fully planar to the surface, with organometallic carbons bending towards the surface. This is not considered in these models for simplicity and the effect on calculated twist angle, $\Theta \approx 30°$, is not included here.

Appendix C

Details of Quantum Ring xTB and DFT calculations

This chapter outlines in more detail the computational calculations used throughout chapter 7. Initially, the computational methods used for xTB and DFT calculations are described. This is followed by full details of results for the calculation of molecular orbital energies and structure. All computational calculations were performed by Anton Nizovtsev and Elena Besley of the Theoretical and Computational Chemistry group, School of chemistry, University of Nottingham.

C.1 Computational Methods

Atomic positions of compounds under study were fully optimized using recently developed tight binding GFN1-xTB method [159], which was subsequently used for analysing molecular orbitals. Molecular orbitals of l-PN (N=1-7) systems were also calculated within density functional theory (DFT) using ωB97X-D3/def2-SVP computational protocol [168–172]. The total energies of l-Pn (n=1-7) cations and anions were computed using quasi-restricted orbitals [173] generated from the unrestricted DFT solutions. The RI-COSX resolution of identity approximation [174, 175] was employed in DFT computations to accelerate convergence and the integration grid was controlled by grid6 and gridx6 keywords. GFN1-xTB and DFT calculations were performed with the xTB and ORCA 4.1 [176] software packages, respectively.

C.2 Molecular Orbital calculations

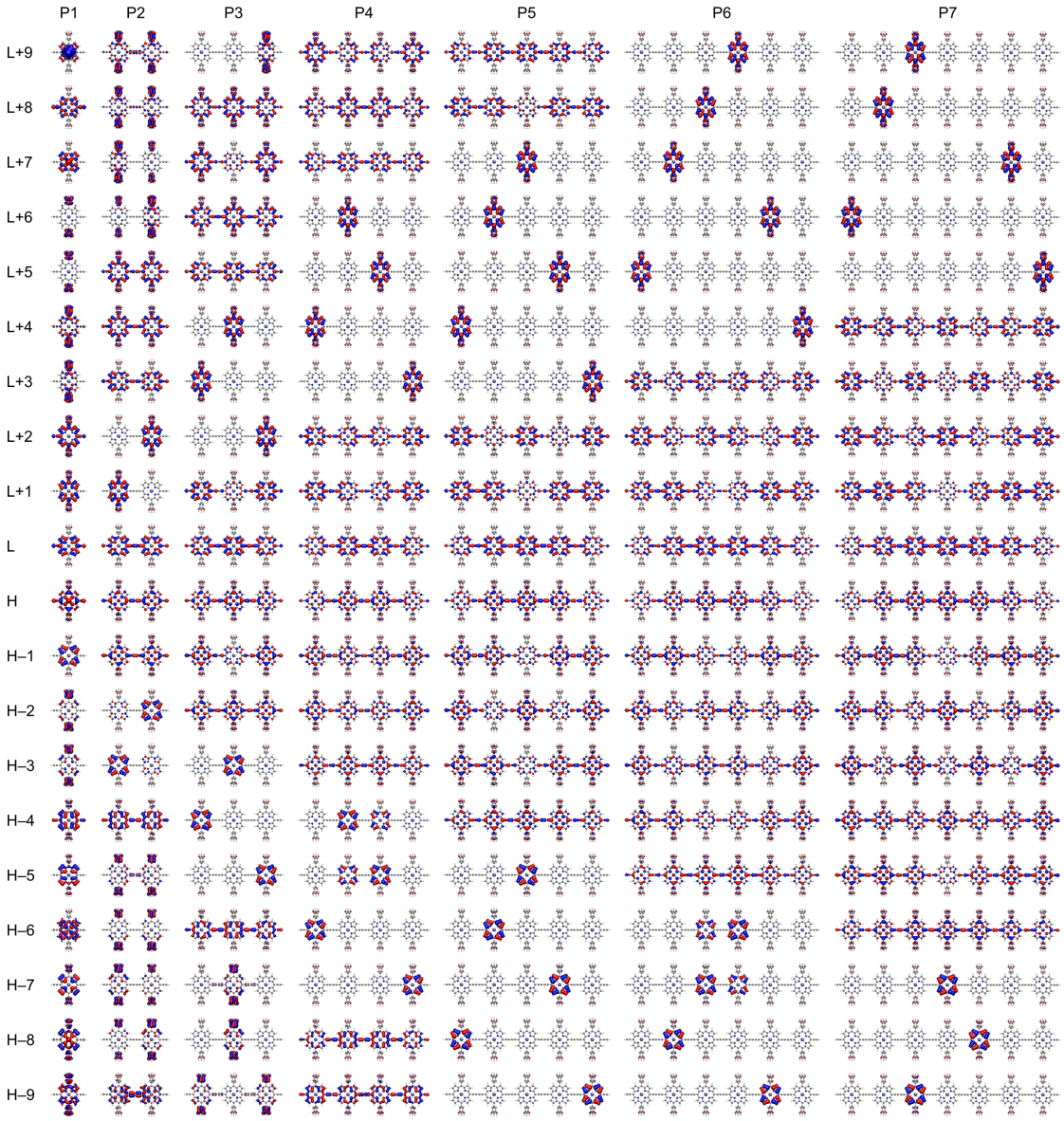


Figure C.1: Highest occupied molecular orbitals (H) and lowest unoccupied molecular orbitals (L) of l-Pn (n=1–7) model compounds calculated at the GFN1-xTB level of theory.

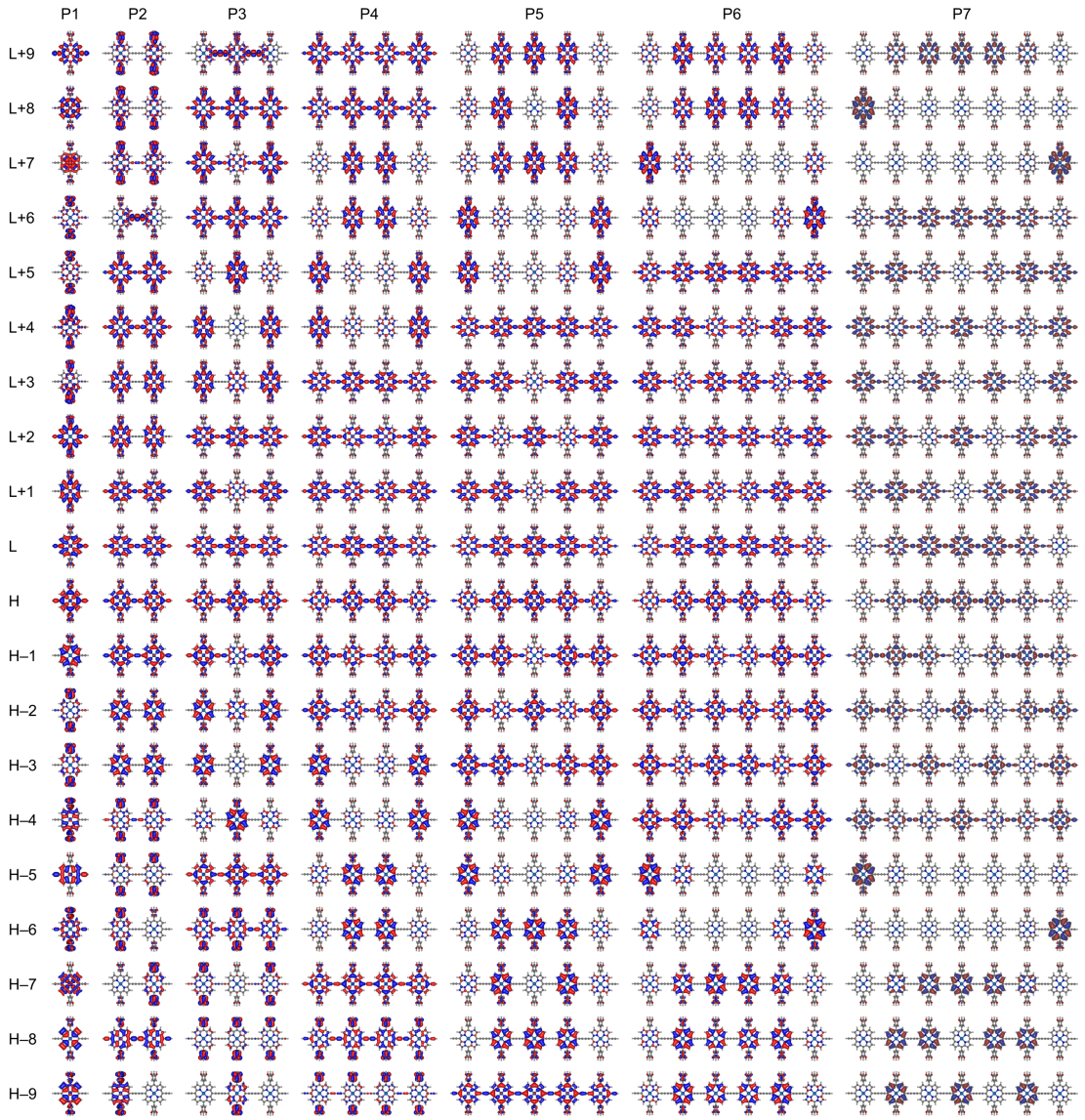


Figure C.2: Highest occupied molecular orbitals (H) and lowest unoccupied molecular orbitals (L) of l-Pn (n=1–7) model compounds calculated at the ωB97X D3/def2-SVP level of theory.

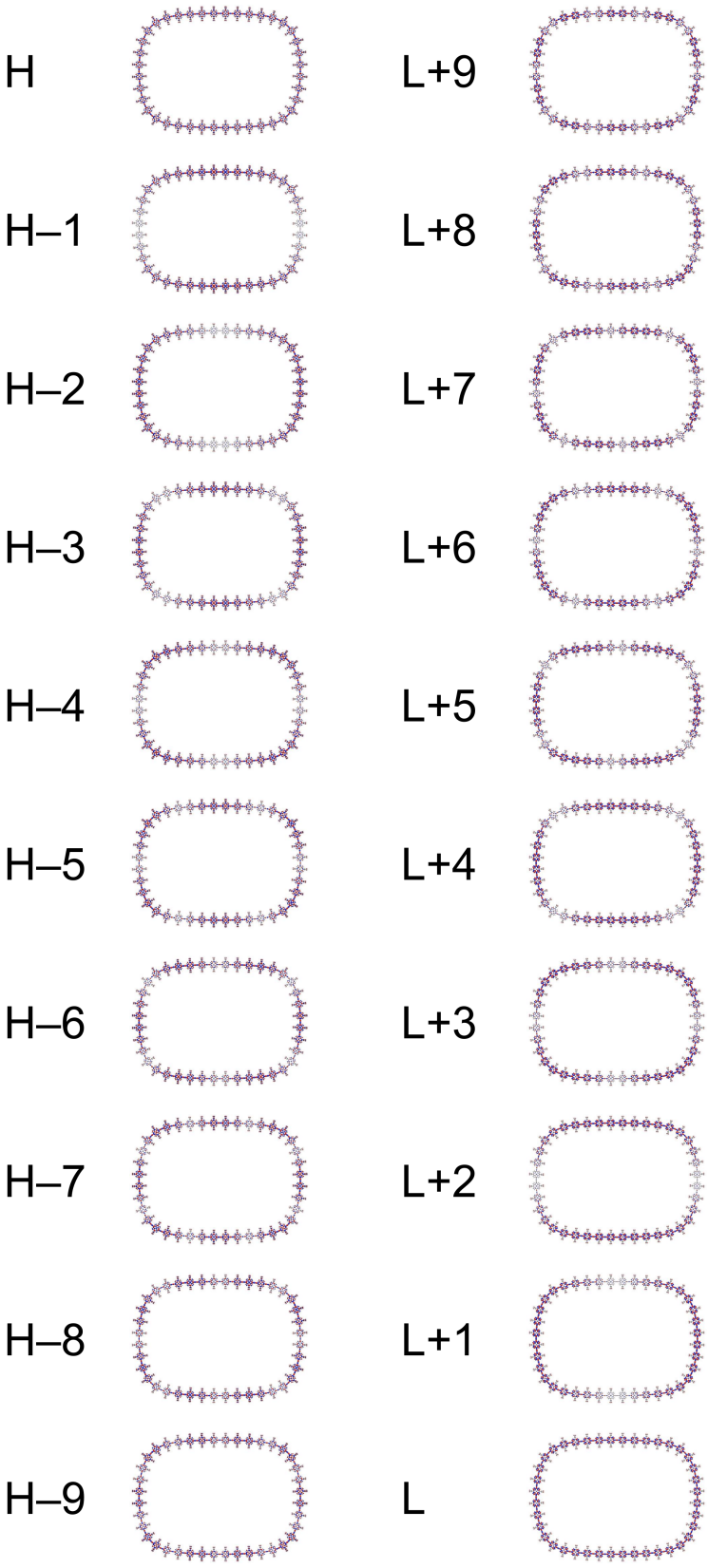


Figure C.3: Highest occupied molecular orbitals (H) and lowest unoccupied molecular orbitals (L) of *c*-P40 model compound calculated at the GFN1-xTB level of theory.

	l-P1	l-P2	l-P3	l-P4	l-P5	l-P6	l-P7	*c*-P40
ϵ(LUMO+9)	-5.49	-6.99	-7.01	-7.97	-8.62	-8.75	-8.75	-9.14
ϵ(LUMO+8)	-5.65	-7.01	-7.76	-8.12	-8.75	-8.75	-8.75	-9.18
ϵ(LUMO+7)	-6.01	-7.02	-7.90	-8.64	-8.75	-8.75	-8.75	-9.18
ϵ(LUMO+6)	-6.70	-7.02	-8.09	-8.76	-8.76	-8.75	-8.76	-9.21
ϵ(LUMO+5)	-6.70	-7.81	-8.67	-8.76	-8.76	-8.77	-8.76	-9.21
ϵ(LUMO+4)	-7.01	-8.04	-8.76	-8.77	-8.77	-8.77	-8.79	-9.23
ϵ(LUMO+3)	-7.03	-8.74	-8.77	-8.77	-8.77	-8.85	-8.92	-9.23
ϵ(LUMO+2)	-7.93	-8.78	-8.77	-8.82	-8.92	-8.99	-9.04	-9.24
ϵ(LUMO+1)	-8.79	-8.78	-8.92	-9.02	-9.08	-9.12	-9.15	-9.24
ϵ(LUMO)	-8.92	-9.09	-9.16	-9.19	-9.21	-9.22	-9.22	-9.25
ϵ(HOMO)	-10.32	-10.13	-10.05	-10.01	-9.99	-9.97	-9.96	-9.93
ϵ(HOMO-1)	-10.63	-10.44	-10.28	-10.17	-10.11	-10.07	-10.04	-9.94
ϵ(HOMO-2)	-11.30	-10.61	-10.49	-10.36	-10.26	-10.19	-10.14	-9.94
ϵ(HOMO-3)	-11.30	-10.61	-10.60	-10.51	-10.41	-10.32	-10.25	-9.95
ϵ(HOMO-4)	-11.34	-11.23	-10.60	-10.59	-10.52	-10.44	-10.37	-9.95
ϵ(HOMO-5)	-11.37	-11.29	-10.60	-10.59	-10.59	-10.53	-10.47	-9.97
ϵ(HOMO-6)	-11.38	-11.29	-11.16	-10.60	-10.59	-10.59	-10.53	-9.97
ϵ(HOMO-7)	-11.40	-11.29	-11.28	-10.60	-10.59	-10.59	-10.58	-10.00
ϵ(HOMO-8)	-11.65	-11.29	-11.28	-11.12	-10.60	-10.59	-10.59	-10.00
ϵ(HOMO-9)	-11.65	-11.32	-11.29	-11.24	-10.60	-10.59	-10.59	-10.03

Table C.1: Molecular orbital energies (eV) of l-Pn (n=1-7) and *c*-P40 model compounds calculated at the GFN1-xTB level of theory.

	l-P1	l-P2	l-P3	l-P4	l-P5	l-P6	l-P7	*c*-P40
Eigenvalues								
ϵ(LUMO)	-8.92	-9.09	-9.16	-9.19	-9.21	-9.22	-9.22	-9.25
ϵ(HOMO)	-10.32	-10.13	-10.05	-10.01	-9.99	-9.97	-9.96	-9.93
ΔE_{H-Lgap}	1.40	1.03	0.89	0.82	0.78	0.76	0.74	0.68
ΔSCF								
ϵ(LUMO)	-7.35	-8.02	-8.31	-8.48	-8.6	-8.68	-8.75	-9.16
ϵ(HOMO)	-11.88	-11.19	-10.89	-10.71	-10.59	-10.5	-10.44	-10.01
ΔE_{H-Lgap}	4.53	3.17	2.57	2.23	1.99	1.82	1.69	0.85

Table C.2: Energies (eV) of the highest occupied molecular orbitals (HOMO), lowest unoccupied molecular orbitals (LUMO) and HOMO-LUMO gaps of l-Pn (n=1-7) and *c*-P40. Model compounds calculated at the GFN1-xTB level of theory by using corresponding eigenvalues and ΔSCF technique.[a]

a - ϵ(HOMO) = -IP; ϵ(LUMO) = -EA; ΔE_{H-Lgap} = IP-EA;
IP - ionization potential, EA - electron affinity.

	l-P1	l-P2	l-P3	l-P4	l-P5	l-P6	l-P7
ϵ(LUMO+9)	3.41	1.81	1.49	0.71	-0.98	-0.98	-0.98
ϵ(LUMO+8)	3.41	1.81	1.06	0.47	-0.98	-0.98	-0.99
ϵ(LUMO+7)	2.99	1.80	0.85	-0.98	-0.98	-0.99	-0.99
ϵ(LUMO+6)	2.37	1.50	0.53	-0.98	-0.99	-0.99	-1.02
ϵ(LUMO+5)	2.35	1.02	-0.98	-0.99	-0.99	-1.03	-1.13
ϵ(LUMO+4)	1.80	0.65	-0.99	-0.99	-1.05	-1.17	-1.31
ϵ(LUMO+3)	1.80	-0.99	-0.99	-1.07	-1.23	-1.39	-1.51
ϵ(LUMO+2)	0.92	-0.99	-1.11	-1.32	-1.50	-1.62	-1.72
ϵ(LUMO+1)	-1.00	-1.18	-1.47	-1.66	-1.77	-1.85	-1.90
ϵ(LUMO)	-1.37	-1.73	-1.88	-1.95	-1.98	-2.01	-2.02
ϵ(HOMO)	-6.78	-6.40	-6.26	-6.19	-6.15	-6.13	-6.12
ϵ(HOMO-1)	-7.03	-7.02	-6.68	-6.48	-6.37	-6.29	-6.24
ϵ(HOMO-2)	-8.31	-7.04	-7.04	-6.85	-6.65	-6.52	-6.42
ϵ(HOMO-3)	-8.33	-7.04	-7.04	-7.04	-6.95	-6.78	-6.64
ϵ(HOMO-4)	-8.95	-8.29	-7.05	-7.04	-7.04	-7.02	-6.86
ϵ(HOMO-5)	-8.97	-8.31	-7.11	-7.05	-7.04	-7.04	-7.03
ϵ(HOMO-6)	-9.07	-8.33	-8.26	-7.05	-7.04	-7.04	-7.03
ϵ(HOMO-7)	-9.13	-8.33	-8.30	-7.15	-7.05	-7.04	-7.04
ϵ(HOMO-8)	-9.19	-8.54	-8.30	-8.23	-7.05	-7.05	-7.04
ϵ(HOMO-9)	-9.23	-8.95	-8.32	-8.29	-7.18	-7.05	-7.05

Table C.3: Molecular orbital energies (eV) of l-Pn (n=1-7) and *c*-P40 model compounds calculated at the ωB97X D3/def2-SVP level of theory.

	l-P1	l-P2	l-P3	l-P4	l-P5	l-P6	l-P7	*c*-P40
Eigenvalues								
ϵ(LUMO)	-1.37	-1.73	-1.88	-1.95	-1.98	-2.01	-2.02	-2.02
ϵ(HOMO)	-6.78	-6.40	-6.26	-6.19	-6.15	-6.13	-6.12	-6.12
ΔE_{H-Lgap}	5.41	4.67	4.38	4.24	4.17	4.12	4.10	4.10
ΔSCF								
ϵ(LUMO)	-1.56	-1.88	-2.12	-2.11	-2.17	-2.13	-2.17	-2.17[b]
ϵ(HOMO)	-6.57	-6.20	-6.00	-5.97	-5.95	-5.95	-5.98	-5.95[b]
ΔE_{H-Lgap}	5.01	4.32	3.88	3.86	3.78	3.81	3.81	3.78[b]

Table C.4: Energies (eV) of the highest occupied molecular orbitals (HOMO), lowest unoccupied molecular orbitals (LUMO) and HOMO-LUMO gaps of l-Pn (n=1-7) and *c*-P40. Model compounds calculated at the ωB97X D3/def2-SVP levels of theory by using corresponding eigenvalues and ΔSCF technique.[a]

a - ϵ(HOMO) = -IP; ϵ(LUMO) = -EA; ΔE_{H-Lgap} = IP-EA;
IP - ionization potential, EA - electron affinity.
b - Exponential fit.

Bibliography

[1] D. M. Eigler and E. K. Schweizer. Positioning single atoms with a scanning tunnelling microscope. *Nature*, 344(6266):524–526, April 1990.

[2] M. F. Crommie, C. P. Lutz, and D. M. Eigler. Confinement of Electrons to Quantum Corrals on a Metal Surface. *Science*, 262(5131):218–220, October 1993.

[3] F. E. Kalff, M. P. Rebergen, E. Fahrenfort, J. Girovsky, R. Toskovic, J. L. Lado, J. Fernández-Rossier, and A. F. Otte. A kilobyte rewritable atomic memory. *Nature Nanotech*, 11(11):926–929, November 2016.

[4] Richard P. Feynman. There's Plenty of Room at the Bottom. *Engineering and Science*, 23(5):22–36, February 1960.

[5] Leo Gross, Fabian Mohn, Nikolaj Moll, Peter Liljeroth, and Gerhard Meyer. The Chemical Structure of a Molecule Resolved by Atomic Force Microscopy. *Science*, 325(5944):1110–1114, August 2009.

[6] Jinming Cai, Pascal Ruffieux, Rached Jaafar, Marco Bieri, Thomas Braun, Stephan Blankenburg, Matthias Muoth, Ari P. Seitsonen, Moussa Saleh, Xinliang Feng, Klaus Müllen, and Roman Fasel. Atomically precise bottom-up fabrication of graphene nanoribbons. *Nature*, 466(7305):470–473, July 2010.

[7] Leonhard Grill and Stefan Hecht. Covalent on-surface polymerization. *Nat. Chem.*, 12(2):115–130, February 2020.

[8] Steven De Feyter, Atsushi Miura, Sheng Yao, Zhijian Chen, Frank Würthner, Pascal Jonkheijm, Albertus P. H. J. Schenning, E. W. Meijer, and Frans C. De Schryver. Two-Dimensional Self-Assembly into Multicomponent Hydrogen-Bonded Nanostructures. *Nano Lett.*, 5(1):77–81, January 2005.

[9] James A. Theobald, Neil S. Oxtoby, Michael A. Phillips, Neil R. Champness, and Peter H. Beton. Controlling molecular deposition and layer structure with supramolecular surface assemblies. *Nature*, 424(6952):1029–1031, August 2003.

[10] U. Schlickum, R. Decker, F. Klappenberger, G. Zoppellaro, S. Klyatskaya, M. Ruben, I. Silanes, A. Arnau, K. Kern, H. Brune, and J. V. Barth. Metal-Organic Honeycomb Nanomeshes with Tunable Cavity Size. *Nano Lett.*, 7(12):3813–3817, December 2007.

[11] Jean-Marie Lehn. Supramolecular Chemistry—Scope and Perspectives Molecules, Supermolecules, and Molecular Devices (Nobel Lecture). *Angewandte Chemie International Edition in English*, 27(1):89–112, 1988.

[12] Jacob N. Israelachvili, editor. *Intermolecular and Surface Forces*. Academic Press, Boston, third edition edition, 2011.

[13] Qing Chen, Hui-Juan Yan, Cun-Ji Yan, Ge-Bo Pan, Li-Jun Wan, Guo-Yong Wen, and De-Qing Zhang. STM investigation of the dependence of alkane and alkane (C18h38, C19h40) derivatives self-assembly on molecular chemical structure on HOPG surface. *Surface Science*, 602(6):1256–1266, March 2008.

[14] Gangamallaiah Velpula, Takashi Takeda, Jinne Adisoejoso, Koji Inukai, Kazukuni Tahara, Kunal S. Mali, Yoshito Tobe, and Steven De Feyter. On the formation of concentric 2D multicomponent assemblies at the solution–solid interface. *Chem. Commun.*, 53(6):1108–1111, January 2017.

[15] Yuan Fang, Elke Ghijsens, Oleksandr Ivasenko, Hai Cao, Aya Noguchi, Kunal S. Mali, Kazukuni Tahara, Yoshito Tobe, and Steven De Feyter. Dynamic control over supramolecular handedness by selecting chiral induction pathways at the solution–solid interface. *Nature Chem*, 8(7):711–717, July 2016.

[16] Shuhei Furukawa, Hiroshi Uji-i, Kazukuni Tahara, Tomoyuki Ichikawa, Motohiro Sonoda, Frans C. De Schryver, Yoshito Tobe, and Steven De Feyter. Molecular Geometry Directed Kagomé and Honeycomb Networks: Toward Two-Dimensional Crystal Engineering. *J. Am. Chem. Soc.*, 128(11):3502–3503, March 2006.

[17] Kazukuni Tahara, Shuhei Furukawa, Hiroshi Uji-i, Tsutomu Uchino, Tomoyuki Ichikawa, Jian Zhang, Wael Mamdouh, Motohiro Sonoda, Frans C. De Schryver, Steven De Feyter, and Yoshito Tobe. Two-Dimensional Porous Molecular Networks of Dehydrobenzo[12]annulene Derivatives via Alkyl Chain Interdigitation. *J. Am. Chem. Soc.*, 128(51):16613–16625, December 2006.

[18] Johannes V. Barth, Jens Weckesser, Giancarlo Trimarchi, Masha Vladimirova, Alessandro De Vita, Chengzhi Cai, Harald Brune, Peter Günter, and Klaus Kern. Stereochemical Effects in Supramolecular Self-Assembly at Surfaces: 1-D versus 2-D Enantiomorphic Ordering for PVBA and PEBA on Ag(111). *J. Am. Chem. Soc.*, 124(27):7991–8000, July 2002.

[19] Marta E. Cañas-Ventura, Wende Xiao, Daniel Wasserfallen, Klaus Müllen, Harald Brune, Johannes V. Barth, and Roman Fasel. Self-Assembly of Periodic Bicomponent Wires and Ribbons. *Angewandte Chemie International Edition*, 46(11):1814–1818, 2007.

[20] Kyung-Hoon Chung, Jihun Park, Kye Yeop Kim, Jong Keon Yoon, Howon Kim, Seungwu Han, and Se-Jong Kahng. Polymorphic porous supramolecular networks mediated by halogen bonds on Ag(111). *Chem. Commun.*, 47(41):11492–11494, October 2011.

[21] Tobias Kaposi, Sushobhan Joshi, Tobias Hoh, Alissa Wiengarten, Knud Seufert, Matheusz Paszkiewicz, Florian Klappenberger, David Ecija, Luka Dordević, Tomas Marangoni, Davide Bonifazi, Johannes V. Barth, and Willi Auwärter. Supramolecular Spangling, Crocheting, and Knitting of Functionalized Pyrene Molecules on a Silver Surface. *ACS Nano*, 10(8):7665–7674, August 2016.

[22] Justus Krüger, Frank Eisenhut, Thomas Lehmann, José M. Alonso, Jörg Meyer, Dmitry Skidin, Robin Ohmann, Dmitry A. Ryndyk, Dolores Pérez, Enrique Guitián, Diego Peña, Francesca Moresco, and Gianaurelio Cuniberti. Molecular Self-Assembly Driven by On-Surface Reduction: Anthracene and Tetracene on Au(111). *J. Phys. Chem. C*, 121(37):20353–20358, September 2017.

[23] Jennifer M. MacLeod, Oleksandr Ivasenko, Chaoying Fu, Tyler Taerum, Federico Rosei, and Dmitrii F. Perepichka. Supramolecular Ordering in Oligothiophene-Fullerene Monolayers. *J. Am. Chem. Soc.*, 131(46):16844–16850, November 2009.

[24] Krishna G. Nath, Oleksandr Ivasenko, Jennifer M. MacLeod, Jill A. Miwa, James D. Wuest, Antonio Nanci, Dmitrii F. Perepichka, and Federico Rosei. Crystal Engineering in Two Dimensions: An Approach to Molecular Nanopatterning. *J. Phys. Chem. C*, 111(45):16996–17007, November 2007.

[25] Matthew O. Blunt, James C. Russell, María del Carmen Giménez-López, Juan P. Garrahan, Xiang Lin, Martin Schröder, Neil R. Champness, and Peter H. Beton. Random Tiling and Topological Defects in a Two-Dimensional Molecular Network. *Science*, 322(5904):1077–1081, November 2008.

[26] Markus Lackinger, Stefan Griessl, Wolfgang M. Heckl, Michael Hietschold, and George W. Flynn. Self-Assembly of Trimesic Acid at the Liquid-Solid Interfacea Study of Solvent-Induced Polymorphism. *Langmuir*, 21(11):4984–4988, May 2005.

[27] Qitang Fan, J. Michael Gottfried, and Junfa Zhu. Surface-Catalyzed C–C Covalent Coupling Strategies toward the Synthesis of Low-Dimensional Carbon-Based Nanostructures. *Acc. Chem. Res.*, 48(8):2484–2494, August 2015.

[28] D. Ecija, M. Marschall, J. Reichert, A. Kasperski, D. Nieckarz, P. Szabelski, W. Auwärter, and J. V. Barth. Dynamics and thermal stability of surface-confined metal–organic chains. *Surface Science*, 643:91–97, January 2016.

[29] Junhai Ren, De-Liang Bao, Li Dong, Lei Gao, Rongting Wu, Linghao Yan, Aiwei Wang, Jiahao Yan, Yeliang Wang, Qing Huan, Jia-Tao Sun, Shixuan Du, and Hong-Jun Gao. Lattice-Directed Construction of Metal–Organic Molecular Wires of Pentacene on the Au(110) Surface. *J. Phys. Chem. C*, 121(39):21650–21657, October 2017.

[30] Matthias Marschall, Joachim Reichert, Alexander Weber-Bargioni, Knud Seufert, Willi Auwärter, Svetlana Klyatskaya, Giorgio Zoppellaro, Mario

Ruben, and Johannes V. Barth. Random two-dimensional string networks based on divergent coordination assembly. *Nature Chem*, 2(2):131–137, February 2010.

[31] Dirk Kühne, Florian Klappenberger, Régis Decker, Uta Schlickum, Harald Brune, Svetlana Klyatskaya, Mario Ruben, and Johannes V. Barth. High-Quality 2D Metal-Organic Coordination Network Providing Giant Cavities within Mesoscale Domains. *J. Am. Chem. Soc.*, 131(11):3881–3883, March 2009.

[32] R. Decker, U. Schlickum, F. Klappenberger, G. Zoppellaro, S. Klyatskaya, M. Ruben, J. V. Barth, and H. Brune. Using metal-organic templates to steer the growth of Fe and Co nanoclusters. *Appl. Phys. Lett.*, 93(24):243102, December 2008.

[33] José I. Urgel, Martin Schwarz, Manuela Garnica, Daphné Stassen, Davide Bonifazi, David Ecija, Johannes V. Barth, and Willi Auwärter. Controlling Coordination Reactions and Assembly on a Cu(111) Supported Boron Nitride Monolayer. *J. Am. Chem. Soc.*, 137(7):2420–2423, February 2015.

[34] Sebastian Stepanow, Nian Lin, Johannes V. Barth, and Klaus Kern. Surface-Template Assembly of Two-Dimensional Metal-Organic Coordination Networks. *J. Phys. Chem. B*, 110(46):23472–23477, November 2006.

[35] Sebastian Stepanow, Robin Ohmann, Frederic Leroy, Nian Lin, Thomas Strunskus, Christof Wöll, and Klaus Kern. Rational Design of Two-Dimensional Nanoscale Networks by Electrostatic Interactions at Surfaces. *ACS Nano*, 4(4):1813–1820, April 2010.

[36] Alexander Langner, Steven L. Tait, Nian Lin, Chandrasekar Rajadurai, Mario Ruben, and Klaus Kern. Self-recognition and self-selection in multicomponent supramolecular coordination networks on surfaces. *PNAS*, 104(46):17927–17930, November 2007.

[37] Ludwig Bartels. Tailoring molecular layers at metal surfaces. *Nat Chem*, 2(2):87–95, February 2010.

[38] F. Ullmann and Jean Bielecki. Ueber Synthesen in der Biphenylreihe. *Ber. Dtsch. Chem. Ges.*, 34(2):2174–2185, May 1901.

[39] Lei Dong, Pei Nian Liu, and Nian Lin. Surface-Activated Coupling Reactions Confined on a Surface. *Acc. Chem. Res.*, 48(10):2765–2774, October 2015.

[40] J. Björk. Reaction mechanisms for on-surface synthesis of covalent nanostructures. *J. Phys.: Condens. Matter*, 28(8):083002, February 2016.

[41] Weihua Wang, Xingqiang Shi, Shiyong Wang, Michel A. Van Hove, and Nian Lin. Single-Molecule Resolution of an Organometallic Intermediate in a Surface-Supported Ullmann Coupling Reaction. *J. Am. Chem. Soc.*, 133(34):13264–13267, August 2011.

[42] Qitang Fan, Cici Wang, Yong Han, Junfa Zhu, Julian Kuttner, Gerhard Hilt, and J. Michael Gottfried. Surface-Assisted Formation, Assembly, and Dynamics of Planar Organometallic Macrocycles and Zigzag Shaped Polymer Chains with C–Cu–C Bonds. *ACS Nano*, 8(1):709–718, January 2014.

[43] Marco Di Giovannantonio, Mohamed El Garah, Josh Lipton-Duffin, Vincent Meunier, Luis Cardenas, Yannick Fagot Revurat, Albano Cossaro, Alberto Verdini, Dmitrii F. Perepichka, Federico Rosei, and Giorgio Contini. Insight into Organometallic Intermediate and Its Evolution to Covalent Bonding in Surface-Confined Ullmann Polymerization. *ACS Nano*, 7(9):8190–8198, September 2013.

[44] Chris J. Judd, Neil R. Champness, and Alex Saywell. An On-Surface Reaction Confined within a Porous Molecular Template. *Chemistry - A European Journal*, 24(1):56–61, January 2018.

[45] C. Glaser. Beiträge zur Kenntniss des Acetenylbenzols. *Berichte der deutschen chemischen Gesellschaft*, 2(1):422–424, 1869.

[46] Alex Saywell, Abigail S. Browning, Philipp Rahe, Harry L. Anderson, and Peter H. Beton. Organisation and ordering of 1d porphyrin polymers synthesised by on-surface Glaser coupling. *Chem. Commun.*, 52(68):10342–10345, August 2016.

[47] Hong-Ying Gao, Hendrik Wagner, Dingyong Zhong, Jörn-Holger Franke, Armido Studer, and Harald Fuchs. Glaser Coupling at Metal Surfaces. *Angewandte Chemie International Edition*, 52(14):4024–4028, April 2013.

[48] Borja Cirera, Yi-Qi Zhang, Jonas Björk, Svetlana Klyatskaya, Zhi Chen, Mario Ruben, Johannes V. Barth, and Florian Klappenberger. Synthesis of Extended Graphdiyne Wires by Vicinal Surface Templating. *Nano Lett.*, 14(4):1891–1897, April 2014.

[49] Hong-Ying Gao, Jörn-Holger Franke, Hendrik Wagner, Dingyong Zhong, Philipp-Alexander Held, Armido Studer, and Harald Fuchs. Effect of Metal Surfaces in On-Surface Glaser Coupling. *J. Phys. Chem. C*, 117(36):18595–18602, September 2013.

[50] Philipp Alexander Held, Hong-Ying Gao, Lacheng Liu, Christian Mück-Lichtenfeld, Alexander Timmer, Harry Mönig, Dennis Barton, Johannes Neugebauer, Harald Fuchs, and Armido Studer. On-Surface Domino Reactions: Glaser Coupling and Dehydrogenative Coupling of a Biscarboxylic Acid To Form Polymeric Bisacylperoxides. *Angewandte Chemie International Edition*, 55(33):9777–9782, 2016.

[51] Jing Liu, Qiwei Chen, Lianghong Xiao, Jian Shang, Xiong Zhou, Yajie Zhang, Yongfeng Wang, Xiang Shao, Jianlong Li, Wei Chen, Guo Qin Xu, Hao Tang, Dahui Zhao, and Kai Wu. Lattice-Directed Formation of Covalent and Organometallic Molecular Wires by Terminal Alkynes on Ag Surfaces. *ACS Nano*, 9(6):6305–6314, June 2015.

[52] Yi-Qi Zhang, Nenad Kepčija, Martin Kleinschrodt, Katharina Diller, Sybille Fischer, Anthoula C. Papageorgiou, Francesco Allegretti, Jonas Björk, Svetlana Klyatskaya, Florian Klappenberger, Mario Ruben, and Johannes V. Barth. Homo-coupling of terminal alkynes on a noble metal surface. *Nat Commun*, 3(1):1–8, December 2012.

[53] Borja Cirera, Yi-Qi Zhang, Svetlana Klyatskaya, Mario Ruben, Florian Klappenberger, and Johannes V. Barth. 2 D Self-Assembly and Catalytic Homocoupling of the Terminal Alkyne 1,4-Bis(3,5-diethynyl-phenyl)butadiyne-1,3 on Ag(111). *ChemCatChem*, 5(11):3281–3288, 2013.

[54] Xin Gao, Huibiao Liu, Dan Wang, and Jin Zhang. Graphdiyne: synthesis, properties, and applications. *Chem. Soc. Rev.*, 48(3):908–936, February 2019.

[55] Florian Klappenberger, Yi-Qi Zhang, Jonas Björk, Svetlana Klyatskaya, Mario Ruben, and Johannes V. Barth. On-Surface Synthesis of Carbon-Based Scaffolds and Nanomaterials Using Terminal Alkynes. *Acc. Chem. Res.*, 48(7):2140–2150, July 2015.

[56] Johanna Eichhorn, Wolfgang M. Heckl, and Markus Lackinger. On-surface polymerization of 1,4-diethynylbenzene on Cu(111). *Chem. Commun.*, 49(28):2900–2902, March 2013.

[57] Chunhua Liu, Wei Zhang, Qingdao Zeng, and Shengbin Lei. A Photoresponsive Surface Covalent Organic Framework: Surface-Confined Synthesis, Isomerization, and Controlled Guest Capture and Release. *Chem. Eur. J.*, 22(20):6768–6773, May 2016.

[58] Sylvain Clair, Mathieu Abel, and Louis Porte. Growth of boronic acid based two-dimensional covalent networks on a metal surface under ultrahigh vacuum. *Chem. Commun.*, 50(68):9627–9635, July 2014.

[59] Nikolas A. A. Zwaneveld, Rémy Pawlak, Mathieu Abel, Daniel Catalin, Didier Gigmes, Denis Bertin, and Louis Porte. Organized Formation of 2d Extended Covalent Organic Frameworks at Surfaces. *J. Am. Chem. Soc.*, 130(21):6678–6679, May 2008.

[60] Zhongmiao Gong, Biao Yang, Haiping Lin, Yunyu Tang, Zeyuan Tang, Junjie Zhang, Haiming Zhang, Youyong Li, Yongshu Xie, Qing Li, and Lifeng Chi. Structural Variation in Surface-Supported Synthesis by Adjusting the Stoichiometric Ratio of the Reactants. *ACS Nano*, 10(4):4228–4235, April 2016.

[61] Li Jiang, Anthoula C. Papageorgiou, Seung Cheol Oh, Özge Sağlam, Joachim Reichert, David A. Duncan, Yi-Qi Zhang, Florian Klappenberger, Yuanyuan Guo, Francesco Allegretti, Sandeep More, Rajesh Bhosale, Aurelio Mateo-Alonso, and Johannes V. Barth. Synthesis of Pyrene-Fused Pyrazaacenes on Metal Surfaces: Toward One-Dimensional Conjugated Nanostructures. *ACS Nano*, 10(1):1033–1041, January 2016.

[62] Lirong Xu, Xin Zhou, Yanxia Yu, Wei Quan Tian, Jun Ma, and Shengbin Lei. Surface-Confined Crystalline Two-Dimensional Covalent Organic Frameworks via on-Surface Schiff-Base Coupling. *ACS Nano*, 7(9):8066–8073, September 2013.

[63] Qiang Sun, Bay V. Tran, Liangliang Cai, Honghong Ma, Xin Yu, Chunxue Yuan, Meike Stöhr, and Wei Xu. On-Surface Formation of Cumulene by Dehalogenative Homocoupling of Alkenyl gem-Dibromides. *Angewandte Chemie International Edition*, 56(40):12165–12169, 2017.

[64] Qiang Sun, Chi Zhang, Huihui Kong, Qinggang Tan, and Wei Xu. On-surface aryl–aryl coupling via selective C–H activation. *Chemical Communications*, 50(80):11825–11828, 2014.

[65] Sam Haq, Felix Hanke, John Sharp, Mats Persson, David B. Amabilino, and Rasmita Raval. Versatile Bottom-Up Construction of Diverse Macromolecules on a Surface Observed by Scanning Tunneling Microscopy. *ACS Nano*, 8(9):8856–8870, September 2014.

[66] Dingyong Zhong, Jörn-Holger Franke, Santhosh Kumar Podiyanachari, Tobias Blömker, Haiming Zhang, Gerald Kehr, Gerhard Erker, Harald Fuchs, and Lifeng Chi. Linear Alkane Polymerization on a Gold Surface. *Science*, 334(6053):213–216, October 2011.

[67] Qiang Sun, Liangliang Cai, Yuanqi Ding, Honghong Ma, Chunxue Yuan, and Wei Xu. Single-molecule insight into Wurtz reactions on metal surfaces. *Phys. Chem. Chem. Phys.*, 18(4):2730–2735, January 2016.

[68] Qiang Sun, Liangliang Cai, Honghong Ma, Chunxue Yuan, and Wei Xu. Dehalogenative Homocoupling of Terminal Alkynyl Bromides on Au(111): Incorporation of Acetylenic Scaffolding into Surface Nanostructures. *ACS Nano*, 10(7):7023–7030, July 2016.

[69] Saw-Wai Hla, Ludwig Bartels, Gerhard Meyer, and Karl-Heinz Rieder. Inducing All Steps of a Chemical Reaction with the Scanning Tunneling Microscope Tip: Towards Single Molecule Engineering. *Phys. Rev. Lett.*, 85(13):2777–2780, September 2000.

[70] Leonhard Grill, Matthew Dyer, Leif Lafferentz, Mats Persson, Maike V. Peters, and Stefan Hecht. Nano-architectures by covalent assembly of molecular building blocks. *Nat Nano*, 2(11):687–691, November 2007.

[71] L. Lafferentz, V. Eberhardt, C. Dri, C. Africh, G. Comelli, F. Esch, S. Hecht, and L. Grill. Controlling on-surface polymerization by hierarchical and substrate-directed growth. *Nature Chemistry*, 4(3):215–220, March 2012.

[72] Christophe Nacci, Andreas Viertel, Stefan Hecht, and Leonhard Grill. Covalent Assembly and Characterization of Nonsymmetrical Single-Molecule Nodes. *Angewandte Chemie*, 128(44):13928–13932, 2016.

[73] J. A. Lipton-Duffin, O. Ivasenko, D. F. Perepichka, and F. Rosei. Synthesis of Polyphenylene Molecular Wires by Surface-Confined Polymerization. *Small*, 5(5):592–597, March 2009.

[74] Zeying Cai, Limin She, Liqin Wu, and Dingyong Zhong. On-Surface Synthesis of Linear Polyphenyl Wires Guided by Surface Steric Effect. *J. Phys. Chem. C*, 120(12):6619–6624, March 2016.

[75] Igor Píš, Lara Ferrighi, Thanh Hai Nguyen, Silvia Nappini, Luca Vaghi, Andrea Basagni, Elena Magnano, Antonio Papagni, Francesco Sedona, Cristiana Di Valentin, Stefano Agnoli, and Federica Bondino. Surface-Confined Polymerization of Halogenated Polyacenes: The Case of Dibromotetracene on Ag(110). *J. Phys. Chem. C*, 120(9):4909–4918, March 2016.

[76] Ke Ji Shi, Ding Wang Yuan, Cheng Xin Wang, Chen Hui Shu, Deng Yuan Li, Zi Liang Shi, Xin Yan Wu, and Pei Nian Liu. Ullmann Reaction of Aryl Chlorides on Various Surfaces and the Application in Stepwise Growth of 2d Covalent Organic Frameworks. *Org. Lett.*, 18(6):1282–1285, March 2016.

[77] Qitang Fan, Cici Wang, Yong Han, Junfa Zhu, Wolfgang Hieringer, Julian Kuttner, Gerhard Hilt, and J. Michael Gottfried. Surface-Assisted Organic Synthesis of Hyperbenzene Nanotroughs. *Angew. Chem. Int. Ed.*, 52(17):4668–4672, April 2013.

[78] Jingya Dai, Qitang Fan, Tao Wang, Julian Kuttner, Gerhard Hilt, J. Michael Gottfried, and Junfa Zhu. The role of the substrate structure in the on-surface synthesis of organometallic and covalent oligophenylene chains. *Phys. Chem. Chem. Phys.*, 18(30):20627–20634, July 2016.

[79] Johanna Eichhorn, Thomas Strunskus, Atena Rastgoo-Lahrood, Debabrata Samanta, Michael Schmittel, and Markus Lackinger. On-surface Ullmann polymerization via intermediate organometallic networks on Ag(111). *Chem. Commun.*, 50(57):7680–7682, June 2014.

[80] David Peyrot and Fabien Silly. On-Surface Synthesis of Two-Dimensional Covalent Organic Structures versus Halogen-Bonded Self-Assembly: Competing Formation of Organic Nanoarchitectures. *ACS Nano*, 10(5):5490–5498, May 2016.

[81] Matthew O. Blunt, James C. Russell, Neil R. Champness, and Peter H. Beton. Templating molecular adsorption using a covalent organic framework. *Chem. Commun.*, 46(38):7157–7159, September 2010.

[82] Marco Bieri, Manh-Thuong Nguyen, Oliver Gröning, Jinming Cai, Matthias Treier, Kamel Aït-Mansour, Pascal Ruffieux, Carlo A. Pignedoli, Daniele Passerone, Marcel Kastler, Klaus Müllen, and Roman Fasel. Two-Dimensional Polymer Formation on Surfaces: Insight into the Roles of Precursor Mobility and Reactivity. *J. Am. Chem. Soc.*, 132(46):16669–16676, November 2010.

[83] Rico Gutzler, Hermann Walch, Georg Eder, Stephan Kloft, Wolfgang M. Heckl, and Markus Lackinger. Surface mediated synthesis of 2d covalent organic frameworks: 1,3,5-tris(4-bromophenyl)benzene on graphite(001), Cu(111), and Ag(110). *Chem. Commun.*, 0(29):4456–4458, July 2009.

[84] Rico Gutzler, Luis Cardenas, Josh Lipton-Duffin, Mohamed El Garah, Laurentiu E. Dinca, Csaba E. Szakacs, Chaoying Fu, Mark Gallagher, Martin Vondráček, Maksym Rybachuk, Dmitrii F. Perepichka, and Federico Rosei. Ullmann-type coupling of brominated tetrathienoanthracene on copper and silver. *Nanoscale*, 6(5):2660–2668, 2014.

[85] Min Chen, Jian Shang, Yongfeng Wang, Kai Wu, Julian Kuttner, Gerhard Hilt, Wolfgang Hieringer, and J. Michael Gottfried. On-Surface Synthesis and Characterization of Honeycombene Oligophenylene Macrocycles. *ACS Nano*, 11(1):134–143, January 2017.

[86] K. S. Novoselov, A. K. Geim, S. V. Morozov, D. Jiang, M. I. Katsnelson, I. V. Grigorieva, S. V. Dubonos, and A. A. Firsov. Two-dimensional gas of massless Dirac fermions in graphene. *Nature*, 438(7065):197–200, November 2005.

[87] K. A. Simonov, A. V. Generalov, A. S. Vinogradov, G. I. Svirskiy, A. A. Cafolla, C. McGuinness, T. Taketsugu, A. Lyalin, N. Mårtensson, and A. B. Preobrajenski. Synthesis of armchair graphene nanoribbons from the 10,10'-dibromo-9,9'-bianthracene molecules on Ag(111): the role of organometallic intermediates. *Sci Rep*, 8(1):1–12, February 2018.

[88] Yuanqin He, Manuela Garnica, Felix Bischoff, Jacob Ducke, Marie-Laure Bocquet, Matthias Batzill, Willi Auwärter, and Johannes V. Barth. Fusing tetrapyrroles to graphene edges by surface-assisted covalent coupling. *Nature Chem*, 9(1):33–38, January 2017.

[89] Pascal Ruffieux, Shiyong Wang, Bo Yang, Carlos Sánchez-Sánchez, Jia Liu, Thomas Dienel, Leopold Talirz, Prashant Shinde, Carlo A. Pignedoli, Daniele Passerone, Tim Dumslaff, Xinliang Feng, Klaus Müllen, and Roman Fasel. On-surface synthesis of graphene nanoribbons with zigzag edge topology. *Nature*, 531(7595):489–492, March 2016.

[90] Leopold Talirz, Pascal Ruffieux, and Roman Fasel. On-Surface Synthesis of Atomically Precise Graphene Nanoribbons. *Advanced Materials*, 28(29):6222–6231, 2016.

[91] Haiming Zhang, Haiping Lin, Kewei Sun, Long Chen, Yulian Zagranyarski, Nabi Aghdassi, Steffen Duhm, Qing Li, Dingyong Zhong, Youyong Li, Klaus Müllen, Harald Fuchs, and Lifeng Chi. On-Surface Synthesis of Rylene-Type Graphene Nanoribbons. *J. Am. Chem. Soc.*, 137(12):4022–4025, April 2015.

[92] Konstantin A. Simonov, Nikolay A. Vinogradov, Alexander S. Vinogradov, Alexander V. Generalov, Elena M. Zagrebina, Nils M\aartensson, Attilio A. Cafolla, Tomas Carpy, John P. Cunniffe, and Alexei B. Preobrajenski. Effect of Substrate Chemistry on the Bottom-Up Fabrication of Graphene Nanoribbons: Combined Core-Level Spectroscopy and STM Study. *J. Phys. Chem. C*, 118(23):12532–12540, June 2014.

[93] Matthias Koch, Francisco Ample, Christian Joachim, and Leonhard Grill. Voltage-dependent conductance of a single graphene nanoribbon. *Nature Nanotech*, 7(11):713–717, November 2012.

[94] Gianluca Galeotti, Marco Di Giovannantonio, Josh Lipton-Duffin, Maryam Ebrahimi, Stefano Tebi, Alberto Verdini, Luca Floreano, Yannick Fagot-Revurat, Dmitrii Perepichka, Federico Rosei, and Giorgio Contini. The role of halogens in on-surface Ullmann polymerization. *Faraday Discuss.*, 204(0), April 2017.

[95] Marco Di Giovannantonio, Okan Deniz, José I. Urgel, Roland Widmer, Thomas Dienel, Samuel Stolz, Carlos Sánchez-Sánchez, Matthias Muntwiler, Tim Dumslaff, Reinhard Berger, Akimitsu Narita, Xinliang Feng, Klaus Müllen, Pascal Ruffieux, and Roman Fasel. On-Surface Growth Dynamics of Graphene Nanoribbons: The Role of Halogen Functionalization. *ACS Nano*, 12(1):74–81, January 2018.

[96] Matthias Koch, Marie Gille, Andreas Viertel, Stefan Hecht, and Leonhard Grill. Substrate-controlled linking of molecular building blocks: Au(111) vs. Cu(111). *Surface Science*, 627:70–74, September 2014.

[97] Alex Saywell, Jutta Schwarz, Stefan Hecht, and Leonhard Grill. Polymerization on Stepped Surfaces: Alignment of Polymers and Identification of Catalytic Sites. *Angewandte Chemie International Edition*, 51(21):5096–5100, May 2012.

[98] Qitang Fan, Jingya Dai, Tao Wang, Julian Kuttner, Gerhard Hilt, J. Michael Gottfried, and Junfa Zhu. Confined Synthesis of Organometallic Chains and Macrocycles by Cu–O Surface Templating. *ACS Nano*, 10(3):3747–3754, March 2016.

[99] Roland Wiesendanger. *Scanning Probe Microscopy and Spectroscopy: Methods and Applications*. Cambridge University Press, 1994.

[100] J. Bardeen. Tunnelling from a Many-Particle Point of View. *Physical Review Letters*, 6(2):57–59, January 1961.

[101] J. Tersoff and D. R. Hamann. Theory and Application for the Scanning Tunneling Microscope. *Physical Review Letters*, 50(25):1998–2001, June 1983.

[102] J. Tersoff and D. R. Hamann. Theory of the scanning tunneling microscope. *Phys. Rev. B*, 31(2):805–813, January 1985.

[103] Sense Jan van der Molen and Peter Liljeroth. Charge transport through molecular switches. *J. Phys.: Condens. Matter*, 22(13):133001, 2010.

[104] D. Phil Woodruff. *Modern Techniques of Surface Science*. Cambridge University Press, Cambridge, 3 edition, 2016.

[105] Dorothy Hoffman, Bawa Singh, and John H. Thomas III. *Handbook of Vacuum Science and Technology*. Elsevier, October 1997.

[106] Felix Hanke and Jonas Björk. Structure and local reactivity of the Au(111) surface reconstruction. *Phys. Rev. B*, 87(23):235422, June 2013.

[107] J. V. Barth, H. Brune, G. Ertl, and R. J. Behm. Scanning tunneling microscopy observations on the reconstructed Au(111) surface: Atomic structure, long-range superstructure, rotational domains, and surface defects. *Phys. Rev. B*, 42(15):9307–9318, November 1990.

[108] Stephan Rauschenbach, Frank L. Stadler, Eugenio Lunedei, Nicola Malinowski, Sergej Koltsov, Giovanni Costantini, and Klaus Kern. Electrospray Ion Beam Deposition of Clusters and Biomolecules. *Small*, 2(4):540–547, April 2006.

[109] J. B. Fenn, M. Mann, C. K. Meng, S. F. Wong, and C. M. Whitehouse. Electrospray ionization for mass spectrometry of large biomolecules. *Science*, 246(4926):64–71, October 1989.

[110] Enzo Fornari, Clive J. Roberts, Robert H. Temperton, and James N. O'Shea. Electrospray deposition in vacuum as method to create functionally active protein immobilization on polymeric substrates. *Journal of Colloid and Interface Science*, 453:252–259, September 2015.

[111] Melanie C. O'Sullivan, Johannes K. Sprafke, Dmitry V. Kondratuk, Corentin Rinfray, Timothy D. W. Claridge, Alex Saywell, Matthew O. Blunt, James N. O'Shea, Peter H. Beton, Marc Malfois, and Harry L. Anderson. Vernier templating and synthesis of a 12-porphyrin nano-ring. *Nature*, 469(7328):72–75, January 2011.

[112] Paul Kebarle and Udo H. Verkerk. On the Mechanism of Electrospray Ionization Mass Spectrometry (ESIMS). In *Electrospray and MALDI Mass Spectrometry*, pages 1–48. John Wiley & Sons, Inc., 2010.

[113] D. P. H. Smith. The Electrohydrodynamic Atomization of Liquids. *IEEE Transactions on Industry Applications*, IA-22(3):527–535, May 1986.

[114] Malcolm Dole, L. L. Mack, R. L. Hines, R. C. Mobley, L. D. Ferguson, and M. B. Alice. Molecular Beams of Macroions. *The Journal of Chemical Physics*, 49(5):2240–2249, September 1968.

[115] B. A. Thomson and J. V. Iribarne. Field induced ion evaporation from liquid surfaces at atmospheric pressure. *The Journal of Chemical Physics*, 71(11):4451–4463, December 1979.

[116] Gianangelo Bracco and Bodil Holst, editors. *Surface Science Techniques*. Springer Series in Surface Sciences. Springer-Verlag, Berlin Heidelberg, 2013.

[117] Kai Siegbahn. Electron spectroscopy for atoms, molecules, and condensed matter. *Rev. Mod. Phys.*, 54(3):709–728, July 1982.

[118] Robert G. Jones, A. S. Y. Chan, M. G. Roper, M. P. Skegg, I. G. Shuttleworth, C. J. Fisher, G. J. Jackson, J. J. Lee, D. P. Woodruff, N. K. Singh, and B. C. C. Cowie. X-ray standing waves at surfaces. *J. Phys.: Condens. Matter*, 14(16):4059–4074, April 2002.

[119] D. P. Woodruff. Surface structure determination using x-ray standing waves. *Rep. Prog. Phys.*, 68(4):743–798, March 2005.

[120] Marco Di Giovannantonio, Massimo Tomellini, Josh Lipton-Duffin, Gianluca Galeotti, Maryam Ebrahimi, Albano Cossaro, Alberto Verdini, Neerav Kharche, Vincent Meunier, Guillaume Vasseur, Yannick Fagot-Revurat, Dmitrii F. Perepichka, Federico Rosei, and Giorgio Contini. Mechanistic Picture and Kinetic Analysis of Surface-Confined Ullmann Polymerization. *J. Am. Chem. Soc.*, 138(51):16696–16702, December 2016.

[121] Dimas G. de Oteyza, Patrick Gorman, Yen-Chia Chen, Sebastian Wickenburg, Alexander Riss, Duncan J. Mowbray, Grisha Etkin, Zahra Pedramrazi, Hsin-Zon Tsai, Angel Rubio, Michael F. Crommie, and Felix R. Fischer. Direct Imaging of Covalent Bond Structure in Single-Molecule Chemical Reactions. *Science*, 340(6139):1434–1437, June 2013.

[122] Bruno Schuler, Shadi Fatayer, Fabian Mohn, Nikolaj Moll, Niko Pavliček, Gerhard Meyer, Diego Peña, and Leo Gross. Reversible Bergman cyclization by atomic manipulation. *Nature Chem*, 8(3):220–224, March 2016.

[123] Bruno Schuler, Wei Liu, Alexandre Tkatchenko, Nikolaj Moll, Gerhard Meyer, Anish Mistry, David Fox, and Leo Gross. Adsorption Geometry Determination of Single Molecules by Atomic Force Microscopy. *Phys. Rev. Lett.*, 111(10):106103, September 2013.

[124] Qitang Fan, Liming Liu, Jingya Dai, Tao Wang, Huanxin Ju, Jin Zhao, Julian Kuttner, Gerhard Hilt, J. Michael Gottfried, and Junfa Zhu. Surface Adatom Mediated Structural Transformation in Bromoarene Monolayers: Precursor Phases in Surface Ullmann Reaction. *ACS Nano*, 12(3):2267–2274, March 2018.

[125] M. Lackinger. Surface-assisted Ullmann coupling. *Chem. Commun.*, 53(56):7872–7885, July 2017.

[126] James Bushell, Albert F. Carley, Mark Coughlin, Philip R. Davies, Dyfan Edwards, David J. Morgan, and Martin Parsons. The Reactive Chemisorption of Alkyl Iodides at Cu(110) and Ag(111) Surfaces: A Combined STM and XPS Study. *J. Phys. Chem. B*, 109(19):9556–9566, May 2005.

[127] S. Doniach and M. Sunjic. Many-electron singularity in X-ray photoemission and X-ray line spectra from metals. *J. Phys. C: Solid State Phys.*, 3(2):285–291, February 1970.

[128] Arne Almenningen, Otto Bastiansen, Liv Fernholt, Bjørg N. Cyvin, Sven J. Cyvin, and Svein Samdal. Structure and barrier of internal rotation of biphenyl derivatives in the gaseous state: Part 1. The molecular structure and normal coordinate analysis of normal biphenyl and pedeuterated biphenyl. *Journal of Molecular Structure*, 128(1):59–76, April 1985.

[129] Alex Saywell, Wojciech Greń, Grégory Franc, André Gourdon, Xavier Bouju, and Leonhard Grill. Manipulating the Conformation of Single Organometallic Chains on Au(111). *J. Phys. Chem. C*, 118(3):1719–1728, January 2014.

[130] C. Bürker, N. Ferri, A. Tkatchenko, A. Gerlach, J. Niederhausen, T. Hosokai, S. Duhm, J. Zegenhagen, N. Koch, and F. Schreiber. Exploring the bonding of large hydrocarbons on noble metals: Diindoperylene on Cu(111), Ag(111), and Au(111). *Phys. Rev. B*, 87(16):165443, April 2013.

[131] Iris Antes and Gernot Frenking. Theoretical Studies of Organometallic Compounds. XIV. Structure and Bonding of the Transition Metal Methyl and Phenyl Compounds MCH3 and MC6H5 (M = Cu, Ag, Au) and M(CH3)2 and M(C6H5)2 (M = Zn, Cd, Hg). *Organometallics*, 14(9):4263–4268, September 1995.

[132] Robert Lindner and Angelika Kühnle. On-Surface Reactions. *ChemPhysChem*, 16(8):1582–1592, June 2015.

[133] Qian Shen, Hong-Ying Gao, and Harald Fuchs. Frontiers of on-surface synthesis: From principles to applications. *Nano Today*, 13:77–96, April 2017.

[134] Mohamed El Garah, Jennifer M. MacLeod, and Federico Rosei. Covalently bonded networks through surface-confined polymerization. *Surface Science*, 613:6–14, July 2013.

[135] Leif Lafferentz, Francisco Ample, Hao Yu, Stefan Hecht, Christian Joachim, and Leonhard Grill. Conductance of a Single Conjugated Polymer as a Continuous Function of Its Length. *Science*, 323(5918):1193–1197, February 2009.

[136] Shigeki Kawai, Ondřej Krejčí, Adam S. Foster, Rémy Pawlak, Feng Xu, Lifen Peng, Akihiro Orita, and Ernst Meyer. Diacetylene Linked Anthracene Oligomers Synthesized by One-Shot Homocoupling of Trimethylsilyl on Cu(111). *ACS Nano*, 12(8):8791–8797, August 2018.

[137] Dmitry V. Kondratuk, Luís M. A. Perdigão, Ayad M. S. Esmail, James N. O'Shea, Peter H. Beton, and Harry L. Anderson. Supramolecular nesting of cyclic polymers. *Nature Chemistry*, 7(4):317–322, April 2015.

[138] Stefan Schlögl, Wolfgang M. Heckl, and Markus Lackinger. On-surface radical addition of triply iodinated monomers on Au(111)—the influence of monomer size and thermal post-processing. *Surface Science*, 606(13):999–1004, July 2012.

[139] Dmitry V. Kondratuk, Johannes K. Sprafke, Melanie C. O'Sullivan, Luis M. A. Perdigao, Alex Saywell, Marc Malfois, James N. O'Shea, Peter H. Beton, Amber L. Thompson, and Harry L. Anderson. Vernier-Templated Synthesis, Crystal Structure, and Supramolecular Chemistry of a 12-Porphyrin Nanoring. *Chem. Eur. J.*, 20(40):12826–12834, September 2014.

[140] Maria B. Wieland, Luis M. A. Perdigão, Dmitry V. Kondratuk, James N. O'Shea, Harry L. Anderson, and Peter H. Beton. Height dependent molecular trapping in stacked cyclic porphyrin nanorings. *Chem. Commun.*, 50(55):7332–7335, June 2014.

[141] Alex Saywell, Johannes K. Sprafke, Louisa J. Esdaile, Andrew J. Britton, Anna Rienzo, Harry L. Anderson, James N. O'Shea, and Peter H. Beton. Conformation and Packing of Porphyrin Polymer Chains Deposited Using Electrospray on a Gold Surface. *Angewandte Chemie International Edition*, 49(48):9136–9139, October 2010.

[142] Zhitao Deng, Nicha Thontasen, Nikola Malinowski, Gordon Rinke, Ludger Harnau, Stephan Rauschenbach, and Klaus Kern. A Close Look at Proteins: Submolecular Resolution of Two- and Three-Dimensionally Folded Cytochrome c at Surfaces. *Nano Lett.*, 12(5):2452–2458, May 2012.

[143] Alex Saywell, Graziano Magnano, Christopher J. Satterley, Luís M. A. Perdigão, Andrew J. Britton, Nassiba Taleb, María del Carmen Giménez-López, Neil R. Champness, James N. O'Shea, and Peter H. Beton. Self-assembled aggregates formed by single-molecule magnets on a gold surface. *Nature Communications*, 1:75, September 2010.

[144] Robert H. Temperton, James N. O'Shea, and David J. Scurr. On the suitability of high vacuum electrospray deposition for the fabrication of molecular electronic devices. *Chemical Physics Letters*, 682:15–19, August 2017.

[145] Stephan Rauschenbach, Markus Ternes, Ludger Harnau, and Klaus Kern. Mass Spectrometry as a Preparative Tool for the Surface Science of Large Molecules. *Annual Review of Analytical Chemistry*, 9(1):473–498, 2016.

[146] Simon A. Svatek, Luis M. A. Perdigão, Andrew Stannard, Maria B. Wieland, Dmitry V. Kondratuk, Harry L. Anderson, James N. O'Shea, and Peter H. Beton. Mechanical Stiffening of Porphyrin Nanorings through Supramolecular Columnar Stacking. *Nano Lett.*, 13(7):3391–3395, July 2013.

[147] Richard J. Baxter, Gilberto Teobaldi, and Francesco Zerbetto. Modeling the Adsorption of Alkanes on an Au(111) Surface. *Langmuir*, 19(18):7335–7340, September 2003.

[148] A. C. Bleszynski-Jayich, W. E. Shanks, B. Peaudecerf, E. Ginossar, F. von Oppen, L. Glazman, and J. G. E. Harris. Persistent Currents in Normal Metal Rings. *Science*, 326(5950):272–275, October 2009.

[149] M. D. Teodoro, V. L. Campo, V. Lopez-Richard, E. Marega, G. E. Marques, Y. Galvão Gobato, F. Iikawa, M. J. S. P. Brasil, Z. Y. AbuWaar, V. G. Dorogan, Yu. I. Mazur, M. Benamara, and G. J. Salamo. Aharonov-Bohm Interference in Neutral Excitons: Effects of Built-In Electric Fields. *Phys. Rev. Lett.*, 104(8):086401, February 2010.

[150] Stefan Fölsch, Jesús Martínez-Blanco, Jianshu Yang, Kiyoshi Kanisawa, and Steven C. Erwin. Quantum dots with single-atom precision. *Nature Nanotech*, 9(7):505–508, July 2014.

[151] Van Dong Pham, Kiyoshi Kanisawa, and Stefan Fölsch. Quantum Rings Engineered by Atom Manipulation. *Phys. Rev. Lett.*, 123(6):066801, August 2019.

[152] Axel Lorke, R. Johannes Luyken, Alexander O. Govorov, Jörg P. Kotthaus, J. M. Garcia, and P. M. Petroff. Spectroscopy of Nanoscopic Semiconductor Rings. *Phys. Rev. Lett.*, 84(10):2223–2226, March 2000.

[153] P. Offermans, P. M. Koenraad, J. H. Wolter, D. Granados, J. M. García, V. M. Fomin, V. N. Gladilin, and J. T. Devreese. Atomic-scale structure of self-assembled In(Ga)As quantum rings in GaAs. *Appl. Phys. Lett.*, 87(13):131902, September 2005.

[154] J. A. Vinasco, A. Radu, E. Kasapoglu, R. L. Restrepo, A. L. Morales, E. Feddi, M. E. Mora-Ramos, and C. A. Duque. Effects of Geometry on the Electronic Properties of Semiconductor Elliptical Quantum Rings. *Sci Rep*, 8(1):1–15, September 2018.

[155] O. Voskoboynikov, Yiming Li, Hsiao-Mei Lu, Cheng-Feng Shih, and C. P. Lee. Energy states and magnetization in nanoscale quantum rings. *Phys. Rev. B*, 66(15):155306, October 2002.

[156] Martin D. Peeks, Timothy D. W. Claridge, and Harry L. Anderson. Aromatic and antiaromatic ring currents in a molecular nanoring. *Nature*, 541(7636):200–203, January 2017.

[157] Michel Rickhaus, Michael Jirasek, Lara Tejerina, Henrik Gotfredsen, Martin D. Peeks, Renée Haver, Hua-Wei Jiang, Timothy D. W. Claridge, and Harry L. Anderson. Global aromaticity at the nanoscale. *Nat. Chem.*, 12(3):236–241, March 2020.

[158] Pernille S. Bols and Harry L. Anderson. Template-Directed Synthesis of Molecular Nanorings and Cages. *Acc. Chem. Res.*, 51(9):2083–2092, September 2018.

[159] Stefan Grimme, Christoph Bannwarth, and Philip Shushkov. A Robust and Accurate Tight-Binding Quantum Chemical Method for Structures, Vibrational Frequencies, and Noncovalent Interactions of Large Molecular Systems Parametrized for All spd-Block Elements (Z = 1–86). *J. Chem. Theory Comput.*, 13(5):1989–2009, May 2017.

[160] Frank Eisenhut, Tim Kühne, Fátima García, Saleta Fernández, Enrique Guitián, Dolores Pérez, Georges Trinquier, Gianaurelio Cuniberti, Christian Joachim, Diego Peña, and Francesca Moresco. Dodecacene Generated on Surface: Reopening of the Energy Gap. *ACS Nano*, 14(1):1011–1017, January 2020.

[161] Michel Rickhaus, Andreas Vargas Jentzsch, Lara Tejerina, Isabell Grübner, Michael Jirasek, Timothy D. W. Claridge, and Harry L. Anderson. Single-Acetylene Linked Porphyrin Nanorings. *J. Am. Chem. Soc.*, 139(46):16502–16505, November 2017.

[162] Patrick Parkinson, Christiane E. I. Knappke, Nuntaporn Kamonsutthipaijit, Kanokkorn Sirithip, Jonathan D. Matichak, Harry L. Anderson, and Laura M. Herz. Ultrafast Energy Transfer in Biomimetic Multistrand Nanorings. *J. Am. Chem. Soc.*, 136(23):8217–8220, June 2014.

[163] Chaw-Keong Yong, Patrick Parkinson, Dmitry V. Kondratuk, Wei-Hsin Chen, Andrew Stannard, Alex Summerfield, Johannes K. Sprafke, Melanie C. O'Sullivan, Peter H. Beton, Harry L. Anderson, and Laura M. Herz. Ultrafast delocalization of excitation in synthetic light-harvesting nanorings. *Chem. Sci.*, 6(1):181–189, December 2014.

[164] Patrick Parkinson, Dmitry V. Kondratuk, Christopher Menelaou, Juliane Q. Gong, Harry L. Anderson, and Laura M. Herz. Chromophores in Molecular Nanorings: When Is a Ring a Ring? *J. Phys. Chem. Lett.*, 5(24):4356–4361, December 2014.

[165] J. Hölz and F. K. Schulte. *Solid Surface Physics*. Springer Tracts in Modern Physics. Springer-Verlag, Berlin Heidelberg, 1979.

[166] David Nečas and Petr Klapetek. Gwyddion: an open-source software for SPM data analysis. *Open Physics*, 10(1):181–188, July 2011.

[167] Marcus D. Hanwell, Donald E. Curtis, David C. Lonie, Tim Vandermeersch, Eva Zurek, and Geoffrey R. Hutchison. Avogadro: an advanced semantic chemical editor, visualization, and analysis platform. *Journal of Cheminformatics*, 4(1):17, August 2012.

[168] You-Sheng Lin, Guan-De Li, Shan-Ping Mao, and Jeng-Da Chai. Long-Range Corrected Hybrid Density Functionals with Improved Dispersion Corrections. *J. Chem. Theory Comput.*, 9(1):263–272, January 2013.

[169] Florian Weigend and Reinhart Ahlrichs. Balanced basis sets of split valence, triple zeta valence and quadruple zeta valence quality for H to Rn: Design and assessment of accuracy. *Phys. Chem. Chem. Phys.*, 7(18):3297–3305, August 2005.

[170] Florian Weigend. Accurate Coulomb-fitting basis sets for H to Rn. *Phys. Chem. Chem. Phys.*, 8(9):1057–1065, February 2006.

[171] Stefan Grimme, Jens Antony, Stephan Ehrlich, and Helge Krieg. A consistent and accurate ab initio parametrization of density functional dispersion correction (DFT-D) for the 94 elements H-Pu. *J. Chem. Phys.*, 132(15):154104, April 2010.

[172] Stefan Grimme, Stephan Ehrlich, and Lars Goerigk. Effect of the damping function in dispersion corrected density functional theory. *Journal of Computational Chemistry*, 32(7):1456–1465, 2011.

[173] Frank Neese, Frank Wennmohs, Andreas Hansen, and Ute Becker. Efficient, approximate and parallel Hartree–Fock and hybrid DFT calculations. A 'chain-of-spheres' algorithm for the Hartree–Fock exchange. *Chemical Physics*, 356(1):98–109, February 2009.

[174] Frank Neese. Importance of Direct Spin-Spin Coupling and Spin-Flip Excitations for the Zero-Field Splittings of Transition Metal Complexes: A Case Study. *J. Am. Chem. Soc.*, 128(31):10213–10222, August 2006.

[175] Róbert Izsák and Frank Neese. An overlap fitted chain of spheres exchange method. *J. Chem. Phys.*, 135(14):144105, October 2011.

[176] Frank Neese. Software update: the ORCA program system, version 4.0. *Wiley Interdisciplinary Reviews: Computational Molecular Science*, 8(1):e1327, 2018.

List of Figures

1.1 Introduction to directing surface reactions 3

2.1 Molecular self-assembly 7
2.2 Ullmann-like coupling reaction scheme 11
2.3 Glaser coupling reaction scheme 12
2.4 Example of Glaser coupling 13
2.5 Additional on-surface coupling reactions 15
2.6 Inducing the on-surface Ullmann reaction with an STM probe . . . 16
2.7 Ullmann coupling of brominated porphyrins to form 2D molecular networks 17
2.8 On-surface synthesis of GNRs through Ullmann coupling reactions . 19
2.9 The role of halogen chemistry in the Ullmann reaction 21
2.10 The role of substrate chemistry on the Ullmann reaction 23
2.11 The role of substrate topography on the Ullmann reaction 24
2.12 Controlling reactions through surface templating: Cu-O 26
2.13 Controlling reactions through surface templating: Molecular networks 27

3.1 Quantum tunnelling through a potential barrier 29
3.2 Energy level diagrams for STM tip and sample at various biases . . 33
3.3 Tunnelling between states for a surface with an adsorbed molecular species 34
3.4 Scanning tunnelling spectroscopy theory 35
3.5 Principles of STM operation 36
3.6 Miller indices and surface topography 38
3.7 Au(111) surface reconstruction 39
3.8 The process of electrospray ionisation 42
3.9 Basic apparatus for electrospray deposition system 43
3.10 The generation of photoelectrons as employed within XPS measurements 44
3.11 Example of chemical shift observed in XPS 45
3.12 Principles of NIXSW 47
3.13 Using Argand diagrams to represent atomic adsorption positions . . 50
3.14 Principles of triangulation for NIXSW analysis 52
3.15 Orientations of the (111) and (200) reflecting planes 53

4.1 Reaction scheme for DITP 56
4.2 Adsorption of TP on Ag(111): Metal-organic phase 57
4.3 Overview of TP on Ag(110) 59
4.4 Iodine adsorption on Ag(110) after dissociation 60

4.5 Adsorption of TP on Ag(110): Metal-organic phase 61
4.6 Adsorption of TP on Ag(110) and Ag(110): Covalent phase 63
4.7 Additional hexagonal structures from DITP on Ag(111) 65
4.8 Overview STM images of DITP on Ag(111) and Ag(110) at different stages of the Ullmann reaction 67

5.1 Chemical structures and reaction scheme for DITP and TIPB . . . 72
5.2 Initial C 1s and I 3d XPS measurements 74
5.3 Methodology for applying fits to C 1s NIXSW measurements 75
5.4 NIXSW adsorption profile measurements for C 1s (111) reflection . 77
5.5 Argand diagrams modelling adsorption of MO carbon atoms relative to the (111) plane 78
5.6 Structural model for the conformation of TPB_{CC} on Ag(111) 79
5.7 Argand diagrams for models of aromatic carbon atoms from the (111) reflection 80
5.8 Vertical positioning of molecules above the Ag(111) surface 82
5.9 NIXSW adsorption profile measurements for I 3d 84
5.10 NIXSW adsorption profile measurements for C 1s (200) reflection . 87
5.11 Absorption profile comparison for MO carbon atom C 1s (200) NIXSW measurements 88
5.12 STM images of TPB structures on Ag(111) 90
5.13 STM images of TP structures on Ag(111) 92
5.14 Modelling methods for the lateral adsorption of molecules from NIXSW measurements of organometallic carbon atoms 94
5.15 TPB lateral adsorption modelling 96
5.16 TP lateral adsorption modelling 98

6.1 Chemical structures of TIPB and *c*-P40 molecular species 104
6.2 Preliminary STM investigations of TIPB and *c*-P40 nanorings . . . 105
6.3 Flattening factor measurements for *c*-P40 nanorings 107
6.4 Example STM images of TIPB inside *c*-P40 nanoring 108
6.5 Further STM images of TPB structures inside nanorings 109
6.6 Line profile of TPB structure unit separation 110
6.7 Effect of elevated temperatures on the *c*-P40 rings 112
6.8 STM images of co-deposited contaminant species 113
6.9 Schematic of tip-surface structure within a circular pore 114
6.10 Graphs of tip separation for various ring structures 116
6.11 Extended model of tip ring interactions to include a tip terminated with a single atom 117

7.1 Quantum confinement effects for a chain of assembled atoms 120
7.2 Quantum confinement effects for a ring of assembled atoms 122
7.3 Semiconductor quantum ring examples 123
7.4 *c*-P40 nanoring structure models 125
7.5 Comparison of xTB and DFT modelling methods for porphyrin chains 127
7.6 Electronic resonances observed in *c*-P40 nanorings on Ag(111) . . . 129
7.7 Differential conductance maps for a single *c*-P40 nanoring stack . . 131
7.8 Comparisons of stripe features observed in experiment and computational models of *c*-P40 133

B.1 Twisting angle model for TP and TPB NIXSW measurements . . . 141
B.2 Example Argand diagram for the ideal twisting model 142

C.1 Molecular orbital distribution calculations for linear porphyrin chains using xTB methods 146
C.2 Molecular orbital distribution calculations for linear porphyrin chains using DFT methods 147
C.3 Molecular orbital distribution calculations for *c*-P40 using xTB methods 148

List of Tables

2.1 Comparison of bond energies 10

4.1 Comparison of STM Image Measurements and Adsorption Model Unit Cells 66

5.1 Coherent fraction and position measurements for the C 1s (111) reflection 76
5.2 Coherent fraction and position measurements for I 3d NIXSW data 85
5.3 Coherent fraction and position measurements for the C 1s (200) reflection 86

B.1 Values used and results of end phenyl twisting calculations 144

C.1 xTB calculations of molecular orbital energies of linear and cyclic porphyrins 149
C.2 xTB calculations of HOMO and LUMO for linear and cyclic porphyrins 149
C.3 DFT calculations of molecular orbital energies of linear and cyclic porphyrins 150
C.4 DFT calculations of HOMO and LUMO for linear and cyclic porphyrins 150